



**HAL**  
open science

# Ion beam analysis of three dimensional (3D) structures for applications in nanotechnology

Lucien Penlap Woguia

► **To cite this version:**

Lucien Penlap Woguia. Ion beam analysis of three dimensional (3D) structures for applications in nanotechnology. Materials Science [cond-mat.mtrl-sci]. Université Grenoble Alpes, 2019. English. NNT : 2019GREAY015 . tel-02443991

**HAL Id: tel-02443991**

**<https://theses.hal.science/tel-02443991>**

Submitted on 17 Jan 2020

**HAL** is a multi-disciplinary open access archive for the deposit and dissemination of scientific research documents, whether they are published or not. The documents may come from teaching and research institutions in France or abroad, or from public or private research centers.

L'archive ouverte pluridisciplinaire **HAL**, est destinée au dépôt et à la diffusion de documents scientifiques de niveau recherche, publiés ou non, émanant des établissements d'enseignement et de recherche français ou étrangers, des laboratoires publics ou privés.

## **THÈSE**

Pour obtenir le grade de

### **DOCTEUR DE LA COMMUNAUTE UNIVERSITE GRENOBLE ALPES**

Spécialité : **PHYSIQUE DES MATERIAUX**

Arrêté ministériel : 25 mai 2016

Présentée par

**Lucien PENLAP WOGUIA**

Thèse dirigée par **Denis JALABERT**, Ingénieur-Chercheur,  
**CEA-INAC**  
et encadrée par **François PIERRE**, Ingénieur-Chercheur,  
**CEA-LETI**

Préparée au sein du **Commissariat à l'Energie Atomique et aux  
Energies Alternatives – Laboratoire de l'Electronique des  
Technologies de l'Information (CEA – LETI)**  
dans l'**École Doctorale de Physique**

**ANALYSES PAR FAISCEAUX D'IONS DE STRUCTURES  
TRIDIMENSIONNELLES (3D) POUR DES APPLICATIONS EN  
NANOTECHNOLOGIE**

**ION BEAM ANALYSES OF THREE DIMENSIONAL (3D)  
STRUCTURES FOR APPLICATIONS IN  
NANOTECHNOLOGY**

Thèse soutenue publiquement le **15 Mai 2019**,  
devant le jury composé de :

**Monsieur Ian VICKRIDGE**

Directeur de Recherche, Institut des NanoSciences de Paris, Université  
Pierre et Marie-Curie, Rapporteur

**Monsieur Esidor NTSOENZOK**

Professeur, Université d'Orléans, CEMHTI – Cyclotron, Rapporteur

**Madame Nathalie MONCOFFRE**

Directeur de Recherche, Institut de Physique Nucléaire de Lyon,  
Université de Lyon 1, Présidente

**Monsieur Patrice GERGAUD**

Ingénieur-Chercheur, CEA-LETI, Université Grenoble Alpes, Examineur

**Monsieur, Frédéric MAZEN**

Ingénieur-Chercheur, CEA-LETI, Université Grenoble Alpes, Examineur



Université Grenoble Alpes  
CNU: Génie Electrique, Electronique, Photonique et Systèmes

# ION BEAM ANALYSIS OF 3D STRUCTURES FOR APPLICATIONS IN NANOTECHNOLOGY

by

Lucien PENLAP WOGUIA

A thesis submitted in fulfillment of the requirements for the degree of Doctor of  
Philosophy

Nano Characterization Plat-Form (PFNC)-MINATEC European Campus  
Laboratory of Surface and Interface Analyses (LASI)  
Ion Beam Group

In the  
Doctoral School of Physics (EDPhys)  
Materials Department

And the  
Commissariat à l'Energie Atomique et aux Energies Alternatives (CEA)  
Laboratoire de l'Electronique des Technologies de l'Information (LETI)  
CEA-LETI

May 2019

# Declaration of Authorship

I, Lucien PENLAP WOGUIA, declare that this thesis titled, 'ION BEAM ANALYSIS OF 3D STRUCTURES FOR APPLICATIONS IN NANOTECHNOLOGY' and the work presented in it are my own. I confirm that this work was done wholly or mainly while in candidature for a research degree at the Université Grenoble Alpes. Where any part of this thesis has previously been submitted for a degree or any other qualification at this University or any other institution, this has been clearly stated. Where I have consulted the published work of others, this is always clearly attributed. Where I have quoted from the work of others, the source is always given. With the exception of such quotations, this thesis is entirely my own work. I have acknowledged all main sources of help.

Signed: *L. P W*

---

Date: May 2019

---

*"Science without social is just ruin of Man"*

*"Science sans social n'est que ruine de l'Homme"*

*Lucien Penlap*

## *Abstract*

With the aim of optimizing the performances of integrated circuits (ICs), the nanotechnology industry is carrying out intense research activities on the miniaturization at the sub-22 nm scale of their main constituents: the MOS transistors. Nevertheless, the shrinking of the gate size has reached the limits that make the control of the channel problematic. One of the most promising approaches to circumvent this dilemma and thus further the miniaturization of the future technological nodes, is the development of transistors of 3D architecture (Trigate or FinFET). The elaboration of such nanostructures requires increasingly fine characterization tools precisely at a key stage of their fabrication, namely the ion implantation doping. Given the ultra-shallow implantation depths, the medium energy ion scattering (MEIS) analysis technique is suitable for quantifying the implants and evaluating the doping conformity thanks to its good depth resolution (0.25 nm). However, the dimensions of the beam ( $0.5 \times 1 \text{ mm}^2$ ) being by far larger than those of the patterns, we had to develop an analysis protocol dedicated to such architectures. The samples studied in the framework of this thesis are considered as model systems. They are constituted of 3D silicon (Si) Fin – shaped line gratings, etched on the 300 mm wafers of silicon on insulator (SOI) types by using the electron beam (e-beam) lithography. The doping has been carried out at an energy of 3 keV by using the conventional (or beam line) and plasma immersion ion implantation (PIII) methods. The analyses of the MEIS spectra of the dopants implanted into each part of the patterns were possible thanks to the 3D Monte-Carlo simulations performed with the PowerMEIS software. We have thus developed a new method suitable for the characterization of the 3D doping. The measurements have shown that, contrarily to the PIII method, the dose implanted by the conventional method is as targeted. However, the distribution of the dopants inserted within the nanostructures by using the two doping methods is not uniform. In the PIII implanted samples, a large dopants' focusing at the tops of the patterns and low sidewalls' doping have been observed. This is less marked in the one implanted by the conventional method. By correlating the Transmission Electron Microscopy (TEM), synchrotron x – ray analyses and MEIS, we have also determined the dimensions of the implanted and crystal areas of the line gratings. The exploitation of the MEIS technique in channeling mode has permitted the full assessment of the impacts of the implantation in the non-etched layers. The investigations of the crystal qualities in the non-implanted areas were carried out with the same technique. The results show that the temperature conditions have a considerable influence on the defects and lattice deformations. The origin of the anomalies in the samples has thus been identified by correlating the MEIS and Time-of-Flight Secondary Ion Mass Spectrometry (ToF-SIMS) measurements.

**Keywords:** 3D – MEIS, 3D – doping, FinFET – like nanostructures, Cloud simulations (PowerMEIS), Synchrotron x-ray analyses, Structural damages.

## *Résumé*

Afin d'optimiser les performances des circuits intégrés, l'industrie de la micro et nanotechnologie mène d'intenses recherches sur la miniaturisation à l'échelle sub-22nm de leurs principaux constituants que sont les transistors MOS. La réduction de la taille de grille atteint néanmoins des limites qui rendent problématique le contrôle du canal. L'une des approches les plus prometteuses pour contourner ce dilemme et ainsi poursuivre la miniaturisation des futurs nœuds technologiques, consiste au développement des transistors d'architectures 3D (Trigate ou FinFET). La mise au point de telles structures requiert une caractérisation de plus en plus fine, surtout à une étape clé de leur élaboration, qui est celle du dopage par implantation ionique. Du fait des faibles profondeurs implantées, l'analyse par diffusion d'ions de moyenne énergie (MEIS) est tout à fait adaptée pour quantifier les implants et évaluer la conformité du dopage grâce à sa bonne résolution en profondeur (0.25 nm). Néanmoins, les dimensions de la sonde ( $0.5 \times 1 \text{ mm}^2$ ) étant très supérieures à celles des motifs, il nous a fallu développer un protocole d'analyse propre à de telles architectures. Les échantillons étudiés dans le cadre de cette thèse sont des systèmes modèles. Ils sont constitués de réseaux de lignes de silicium (Si) 3D, formées par gravure lithographique par faisceaux d'électrons (e-beam) sur des plaques 300 mm de types silicium sur isolant (SOI). Le dopage a été réalisé à une énergie de 3 keV par implantations conventionnelle (ou beam line) et immersion plasma (PIII).

L'analyse des spectres MEIS des implants insérés dans chaque facette des motifs a été possible grâce aux simulations 3D types Monte-Carlo effectuées avec le logiciel Power-MEIS. Nous avons ainsi développé une nouvelle méthode adaptée à la caractérisation du dopage 3D. Les mesures ont montré que, contrairement à la méthode PIII, la dose implantée par la méthode conventionnelle correspond à celle visée. Cependant la distribution des dopants introduits au sein des nanostructures par les deux méthodes de dopage n'est pas uniforme. Dans les échantillons implantés par PIII, on a observé une importante concentration des dopants aux sommets des motifs et un faible dopage des flancs. Ceci étant moins marqué dans celui implanté par la méthode conventionnelle. En corrélant les techniques de Microscopie Electronique en Transmission (MET), d'analyses par rayons x synchrotron et MEIS, nous avons également pu déterminer les dimensions des zones implantées ainsi que celles des zones cristallines dans les réseaux de lignes gravées.

L'exploitation de la technique MEIS en mode canalisation a permis une évaluation complète des couches non gravées. L'investigation des endommagements post - dopage dans les régions cristallines non implantées ont été menées toujours avec la même technique MEIS. Les résultats ont révélé une importante influence de la méthode d'implantation et la température sur les défauts et les déformations dans le cristal. L'origine des anomalies au sein des échantillons a ainsi été identifiée en corrélant les mesures MEIS et celles par

spectrométrie de masse des ions secondaires en temps de vol (ToF-SIMS).

**Mots - Clés:** 3MEIS – 3D, Dopage – 3D, Nanostructures types FinFET, Simulations cloud (PowerMEIS), Analyses rayons – x synchrotron, Défauts structuraux.

# *Acknowledgements*

This work could not be presented without the contribution of all the crew members, precisely the MEIS team. I realized how tough is the supervisors' work. A big thank to my thesis advisor, Denis Jalabert. I was always in your office just for one sake: to learn. Thank you very much for everything.

I remember the training for conducting the MEIS experiments under the supervision of François Pierre. If I have had good results, it is first because of your experience, advice and help. Thank you. The accelerator was always in perfect conditions to acquire nice spectra because of the hard work of Philippe Charrault, to whom I am grateful.

To all the ion beam group, with a particular thank to Jean-Paul Barnes, the leader and new scientific advisor of the department of technological plat-forms (DPFT). I wish you to achieve a job as great as that of the person you replace, François Bertin. All the best in your new responsibilities.

To all the members and the head (Nicolas Chevalier) of the Laboratory of Surface and Interface Analysis (LASI). I wish you all the best in your new responsibilities and missions.

To the Nano Characterization Plat-Form (PFNC) - team, for the moments we spent together and their support. A special star for the Ladies.

I had the opportunity to work with two different heads of department. I thanks Jean-Claude Royer who welcomed me in the former LETI/DTSI/SCMC department, then Nicolas Lhermet who is leading the new LETI/DPFT/SMCP department and who guided me until the end of my PhD studies.

To the PowerMEIS trainers: Dario F. Sanchez (Paul Scherrer Institute (PSI), Villigen) and Gabriel G. Marmitt (Netherlands) whom their help and assistance are non-measurable. I really appreciated working with you and my stay in PSI.

I will never forget the moments spent at ESRF, discovering the synchrotron world. I would like to say a great thank to the BM32 beam line team (Samuel Tardif, Joel Eymery & François Rieutord) for the nice measurements, help and advice.

I really enjoyed the unforgettable moments spent at the ESRF's BM05 beam line, looking for the rotation centers of the samples and the spinner with Jerome Reche and Tra Nguyen. Thank you guys for everything, it was amazing.

A special thank to the x-ray group of CEA-LETI, specially to the leader, to Frédéric Fillot, Nicolas Vaxellaire, for their availability, time, involvement and help. I will never forget the full implication of Jayanth Channagiri for the data processing, but also for his time, advice and strong support. Big thank to all of you.

I would like to thank Denis Mariolle and Łukasz Borowik for the nice moments shared in the same office.

To Remi Blinder for all his help and advice. It is difficult to find nice people like you.

To Mohamed-Ramzi Ammar (France), Mme. Kadidjatou Dramé Diop, Papa Diaw and Papa Dramé (Senegal) for all their advice and permanent support.

To all my family, brothers & sisters and all my friends all over the world.

I am Thankful towards any person who, near or far, have contributed to the achievement of my work.

This work, carried out on the PFNC of CEA-Leti & MINATEC european campus, was supported by the "Recherches Technologiques de Base" Program of the French Ministry of Research.

# Contents

<b>Declaration of Authorship</b>	<b>i</b>
<b>Abstract</b>	<b>iii</b>
<b>Résumé</b>	<b>v</b>
<b>Acknowledgements</b>	<b>vii</b>
<b>List of Figures</b>	<b>xii</b>
<b>List of Tables</b>	<b>xxii</b>
<b>Abbreviations</b>	<b>xxiii</b>
<b>Symbols</b>	<b>xxv</b>
<b>1 Technological context and state-of-the-art</b>	<b>3</b>
1.1 Introduction . . . . .	3
1.2 Silicon On Insulator (SOI) materials . . . . .	4
1.2.1 Fabrication techniques of SOI structures . . . . .	5
1.3 Semiconductor materials . . . . .	6
1.4 Evolution of the MOS transistors: from MOSFET to FinFET . . . . .	8
1.4.1 The structure of MOSFET . . . . .	8
1.4.2 The FinFET technology . . . . .	13
1.5 Ion implantation doping . . . . .	20
1.5.1 The conventional ion implantation method . . . . .	20
1.5.2 Plasma immersion ion implantation (PIII) . . . . .	23
1.6 Quantification methods of 3D doping in the FinFET-like structures . . . . .	26
1.6.1 Scanning Spreading Resistance Microscopy . . . . .	26
1.6.2 Atom Probe Tomography . . . . .	28
1.6.3 1.5D SIMS . . . . .	30
1.7 Sample descriptions . . . . .	33
1.8 Conclusion . . . . .	34

---

<b>2</b>	<b>Experimental techniques</b>	<b>35</b>
2.1	Introduction . . . . .	35
2.2	Medium Energy Ions Scattering (MEIS) . . . . .	36
2.2.1	Principle . . . . .	36
2.2.2	Description of the equipment . . . . .	38
2.2.3	Theory . . . . .	45
2.2.3.1	The kinematic factor K . . . . .	45
2.2.3.2	The Rutherford's scattering cross-section $\sigma(\theta_s)$ . . . . .	48
2.2.3.3	Energy loss in materials . . . . .	49
2.2.3.4	The straggling . . . . .	51
2.2.3.5	The channeling phenomena of ions and the random orientation of crystals . . . . .	53
2.2.3.6	Blocking and Shadowing in crystals . . . . .	56
2.2.4	Analysis protocol for 3D FDSOI nanostructures using MEIS . . . . .	57
2.2.4.1	Data acquisition . . . . .	65
2.2.5	Exploitation of data . . . . .	66
2.2.5.1	2D simulations of MEIS spectra . . . . .	68
2.2.5.2	3D simulations of MEIS spectra using PowerMEIS . . . . .	69
2.3	Ion beam analysis (IBA) . . . . .	74
2.3.1	IBA principles and techniques . . . . .	75
2.4	Time of flight-Secondary Ion Mass Spectrometry (ToF-SIMS) . . . . .	76
2.4.1	Principle . . . . .	76
2.4.1.1	Presentation of the instrument . . . . .	77
2.4.1.2	Depth and concentration profiling . . . . .	79
2.5	X-ray diffraction analysis technique . . . . .	80
2.5.1	Diffraction principle . . . . .	81
2.5.2	Bragg's diffraction . . . . .	81
2.5.3	Analysis methods employed in XRD . . . . .	82
2.5.3.1	Symmetrical and Asymmetrical scans . . . . .	83
2.5.3.2	High precision characterization of materials using state of the art XRD methods . . . . .	84
2.5.3.3	Definition of the momentum transfer coordinates for the asymmetric geometry in GIXRD . . . . .	86
2.5.4	X-ray sources and instruments . . . . .	87
2.5.4.1	X-ray laboratory source and instrumentation . . . . .	87
2.5.4.2	Synchrotron radiation source and instrumentation . . . . .	88
2.6	Conclusion . . . . .	91
<b>3</b>	<b>Doping conformity in 3D structures</b>	<b>93</b>
3.1	Introduction . . . . .	93
3.2	Preliminary studies on the non-patterned ultra-thin layers . . . . .	94
3.2.1	Quantification of the dopants by using MEIS and RBS . . . . .	94
3.2.2	Implanted depths of the dopants . . . . .	96
3.3	Conformity assessment by MEIS in the 3D sample implanted by the conventional method . . . . .	98
3.3.1	Simulation approach . . . . .	98

---

3.3.2	Calculations of the expected doses in the conventional implanted 3D sample. . . . .	99
3.3.3	Calculations for the conformal implantation in the conventional implanted 3D sample. . . . .	101
3.3.4	Measurements on the conventional implanted 3D sample . . . . .	102
3.4	Conformity assessment by MEIS in the plasma implanted 3D sample at room temperature . . . . .	107
3.5	Dimensions of the crystal and damaged areas by x-ray diffraction and TEM analyses . . . . .	115
3.5.1	Case of the sample (S1) implanted at room temperature by using the conventional method . . . . .	118
3.5.2	Case of the samples implanted by using the plasma immersion ion implantation method. . . . .	121
3.5.3	Confrontation with the MEIS measurements on ultra-thin layers . . . . .	124
3.6	Summary . . . . .	126
<b>4</b>	<b>Investigation of structural damages in ultra thin layers</b>	<b>128</b>
4.1	Introduction . . . . .	128
4.2	The MEIS experimental results on ultra thin layers . . . . .	129
4.3	Assessment of the crystal qualities in the non-implanted areas by MEIS . . . . .	131
4.3.1	Highlight of the presence of defects in the crystal by using MEIS . . . . .	134
4.3.2	Highlight of the existence of deformation gradients into crystals by MEIS . . . . .	136
4.4	Investigation of the co-implanted elements by ToF – SIMS . . . . .	137
4.5	Summary . . . . .	140
<b>5</b>	<b>General conclusion &amp; future works</b>	<b>141</b>
<b>A</b>	<b>Matrix models for 3D deconvolutions</b>	<b>144</b>
<b>B</b>	<b>Analysis Electron Microscopy (AEM)</b>	<b>147</b>
	<b>Bibliography</b>	<b>153</b>

# List of Figures

1.1	Schematic illustration of a stack of SOI type. . . . .	4
1.2	Illustration of two different types of doping of semiconductors. (a): p-type doping with boron (B) and (b): n-type doping with arsenic (As). . . . .	7
1.3	(a): Schematic description of the a MOSFET transistor, where we can see the three connection pads: $V_S$ , $V_D$ , $V_G$ , $V_{ground}$ . (b): is the characteristic curve $I_D = f(V_G)$ . . . . .	8
1.4	Evolution of the number of transistors in ICs according to the Moore's law[1] plotted with some of the other parameters key parameters[2, 3]. . . . .	10
1.5	Evolution with the gate leakage current in function of the gate length . Source: [2] and data from ITRS (2004 update). . . . .	11
1.6	Short channel effects graphical illustration[4].(a): illustration of the gate length reducing. (b): representation of the non-overlapping (bottom left) and the overlapping (bottom right) wave functions with the associated tunnelling probabilities. . . . .	12
1.7	Left: Image of the first non planar (double Gate or DELTA) transistor[5]. Right: top view SEM image of a FinFET where the drain, source and the channel region are highlighted[6]. . . . .	13
1.8	Comparison of a planar (left) and a trigate (right) transistor (source: Intel)	14
1.9	Comparison of the performances of a planar and a trigate transistor, for two different technological nodes. The left graph compares the leakage currents ( $I_{off}$ ) and the subthreshold slopes when the devices are in off-state, whereas the right graph compares the delay times in function of the operating voltage[7]. . . . .	15
1.10	The images show the different processes of obtaining the three dimensional transistors on bulk silicon and SOI. Top: Fully depleted SOI (FDSOI) technology and Bottom: totally strained silicon technology[8]. . . . .	16
1.11	28 nm node threshold voltages with respect to the body bias for the UTBB-FDSOI and Bulk[9]. . . . .	17
1.12	A demo of the power and temperature efficiencies of UTBB-FDSOI and bulk FinFETs[10]. . . . .	19
1.13	Schematic principle of a classical implantor. . . . .	21
1.14	Dopants concentration profile obtained with the conventional implantation method[11]. . . . .	22
1.15	Schematic diagram describing the ion implantation method by plasma immersion in pulsed mode. This drawing was inspired from[12] . . . . .	24
1.16	Schematic of the main signal's chronogrammes controlling the implantation in pulsion mode. . . . .	25

1.17	Schematic showing the measurement principle of SSRM (left). The probe is visible in the right image acquired by scanning electron microscopy (SEM)[13]. . . . .	26
1.18	Top-left: Schematic drawing of a FinFET device, top-right: top view of a test area design with multiple fins capped by a staggered gate. Bottom: example to the SSRM images along the measurement plane [14, 15]. . . .	27
1.19	SSRM images obtained by reconstruction of multiple-fin scans of the gate and source/drain regions of a bulk finFET. They show the well, channel, halo, extension and contact heavily-doped drain (HDD) regions[14, 15]. . .	28
1.20	Schematic principle of atom probe tomography. M, L and R are the magnification, path length and radius of the tip, respectively. (x, y) are the position coordinates of the atoms at the sample surface, derived from the coordinates of the ion impacts on the detector. The magnification is defined as $x = X/M$ & $y = Y/M$ [16]. . . . .	29
1.21	Left: mapping of the arsenic distribution (orange) in the silicon patterns (tops and sidewalls). The green points represent the oxide, the data corresponding to the silicon are not included. Right: comparison of the arsenic profiles measured by APT in the tops and bottoms of the patterns[17]. . .	29
1.22	Representation of an array of objects with composition C, width W, and pitch P for SIMS measurements. The incident primary beam is parallel to the z direction[18]. . . . .	30
1.23	Results of the 1.5-D SIMS analyses carried out on the patterned structures (right) with different tilt angles[19]. . . . .	31
1.24	Secondary Electron Microscopy (SEM) image measured on an etched sample showing the 3D silicon Fins in profile (a) and top (b) views. . . . .	34
2.1	Schematic illustration of the characterization of a sample using a beam of particles.[20]. . . . .	36
2.2	Evolution of the minima of the scattered yields observed in MEIS on Ge(111) with respect to the scattering angle. The scattering geometries were: [-1-10] & [001](a), and normal & [-111](b). . . . .	38
2.3	Principle schematic of the high voltage facility used for the medium energy ion scattering analysis technique. The whole compartment is principally constituted of a plasma source and the accelerator, the beam line with the set of collimators, and the MEIS end station. . . . .	39
2.4	Image of the MEIS setup with the different compartments, necessary for high resolution MEIS experimentations. . . . .	40
2.5	The 400kV MEIS accelerator system (left) and the model SO-55-1 ion source utilized for the MEIS measurements (right). . . . .	40
2.6	Picture of a sample holder bottom used for MEIS measurements. The adequate dimensions of a piece of sample should be $1 \times 1 \text{ cm}^2$ , but the holder can also host a sample of extra dimensions with a rectangular or circular shape. . . . .	42
2.7	Left image: interior of the analysing chamber, one can see the goniometer and the toroidal electrostatic analyzer (TEA). Right image: drawing of the principal axes of the goniometer. There are three translational (x, y, z) and three rotational (Theta, Phi and Tilt) axes. . . . .	42
2.8	Toroidal electrostatic analyser (TEA) used for the detection and analysis of scattered ions in the MEIS technique . . . . .	43

2.9	Illustrative example of the multiplication process of electrons that leads to the signal's amplification along a channel of the MCPs. . . . .	44
2.10	Schematic drawing of a pair of micro channel plates[21]. . . . .	45
2.11	Illustration of the collision processes between the projectile and the target atoms. The scattered energy can be deduced using the kinematic factor K. . . . .	46
2.12	Drawing of the kinematics of the elastic collision between the projectiles of mass $M_1$ , energy $E_0$ , momentum $\vec{p}_1$ , and the target atoms of mass $M_2$ , energy $E_2=0$ (at rest), momentum $\vec{p}_2$ . $\vec{p}'_1$ , $E'_1$ , and $\vec{p}'_2$ , $E'_2$ are the momentum, energy of the projectiles, and the momentum, energy of the target atoms after the collisions, respectively. . . . .	46
2.13	Evolution of the kinematic factor in function of the target mass, for a given scattering angle( $\theta_s$ ). Protons (graph(a)) and alphas (graph(b)) are used as incident projectiles. . . . .	47
2.14	Evolution of the kinematic factor with respect to the scattering angle for different target masses. Protons ( $H^+$ , graph(a)) and alphas ( $He^+$ , graph(b)) are used as incident projectiles. . . . .	48
2.15	Evolution of the stopping powers of protons (a)[22] and alphas(b)[23] particles in silicon. . . . .	50
2.16	Evolution of the total penetration depth of $H^+$ [22] and $He^+$ in silicon[23]. . . . .	51
2.17	Computed values of straggling for protons and helium used as projectiles[24]. . . . .	52
2.18	Illustration of the channeling of protons ( $H^+$ ) along a crystallographic direction . . . . .	53
2.19	Illustration of the angular aperture along a channeling direction. The value of the critical angle is obtained by taking the full width at half-minimum, as indicated on the curve. . . . .	54
2.20	Evolution of the critical angle of channeling $\psi_{1/2}$ in function of the energy of hydrogen $H^+$ and helium $He^+$ along the crystal direction $\langle 001 \rangle$ of silicon. . . . .	55
2.21	Representation of the blocking and shadowing phenomena in crystal. A shadow cone is observed at the entrance of the channeled ions inside the crystals. Indeed, the firsts atomic planes shadow those of the inner layers. The second blocking cone observed at their exit results from the inverse process. The atoms of the upper planes block the scattered ions during their exit from the sample. . . . .	57
2.22	TEM image of the 3D line grating . . . . .	58
2.23	Comparison of the penetration ranges of 200 keV hydrogen (left) and helium (right) into Si. The simulations were performed with SRIM[25]. The associated curve at the bottom are the profiles of the displaced Si atoms. . . . .	60
2.24	Stereographic projection of FCC silicon along the $\langle 001 \rangle$ crystal direction. The convention we adopted for the crystal axes orientation is (a,b,c), we have encircled the investigated crystal directions. . . . .	61
2.25	Comparison of the evolution of $\psi_{1/2}$ for $H^+$ and $He^+$ along the incidence directions $\langle 201 \rangle$ (a), $\langle 301 \rangle$ (b) and $\langle 332 \rangle$ (c) of the crystal Si. . . . .	62
2.26	Evolution of $\chi_{min}(\%)$ with respect to the thickness of the amorphous layer traversed by the incident ions: in channeling + blocking mode(a) and in channeling mode only (b). . . . .	63
2.27	Ideal protocol for the characterization of Si based patterned fin shaped nanostructures of SOI types. . . . .	64

2.28	Analysis geometry in normal incidence for the characterization of the Si-fin shaped nanostructures of SOI types. . . . .	65
2.29	Presentation of the MEIS results. From the 2D energy-angle image in the middle(b), one can obtain either a 1D energy spectrum(a) or a 1D angular spectrum(c) by performing the cuts at a fixed scattering angle or scattering energy. . . . .	66
2.30	illustration of the in-going and out going trajectories in a sample of thickness $t$ with the associated angles of: incidence ( $\theta_i$ ), scattering (TEA) and exit( $\theta_e$ ). . . . .	67
2.31	Example of the types of nanostructures one can simulate using PowerMEIS	69
2.32	Left: example of the 3D Fin-shaped nanostructure of SOI type that we want to simulate its MEIS spectrum. The analysis geometry in normal incidence is illustrated. Right: zoom on two Fins with their associated dimensions. The different possibilities of orientating the etching line at an angle ' $\varphi$ ' with respect to the horizontal axis in the azimuthal plane are represented. The Si-bulk substrate is not represented on the drawings. . .	70
2.33	Different implantation profiles of the initial SOI nanostructure obtainable by modellings. The Si-bulk substrate is not represented. The images were generated by Python codes. . . . .	71
2.34	Example of 3D simulations of the MEIS spectra of the FinFET-like nanostructures of three different technological nodes implanted with As. The azimuth angle $\varphi=0^\circ$ corresponds to the horizontal orientation of the etching line and $\varphi=90^\circ$ corresponds to the vertical orientation. . . . .	72
2.35	Image of the ToF-SIMS instrument provided by IonToF with the annotations of the different parts. The top-left drawing indicates the schematic principle of the ToF analysis mode. . . . .	77
2.36	Energy and wavelength scale for an extended range of electromagnetic radiations[26]. . . . .	81
2.37	Geometrical representation of the Bragg's condition for the interferences between the diffracted rays within a crystal, where the atomic planes are separated by a constant distance $d_{hkl}$ . . . . .	82
2.38	Different orientations of the crystal planes corresponding to precise types of scans with the orientation of the scattering vector $\vec{q}_v$ . (a): symmetrical scan, (b): asymmetrical scan (grazing incidence and large emergence). (c): asymmetrical scan (large incidence and glancing emergence). The two components of the scattering vector $\vec{k}_i$ and $\vec{k}_d$ represent the momenta of the incident and the diffracted rays, respectively. . . . .	83
2.39	Experimental geometry used for GIXRD measurements with the associated angles. . . . .	85
2.40	X'Pert PRO diffractometer used at the PFNC of CEA-LETI with a representation of the experimental principle of X-rays diffraction. The source of the incident x-rays is fixed. The holder which can host several samples that can rotate around three principle angles: omega( $\omega$ ), phi( $\phi$ ) and tilt( $\gamma$ ) and translate along the horizontal axis. The detector itself can also rotate out of the plane of the sample holder. . . . .	87

2.41	An overview of the storage ring of the ESRF synchrotron facility with all the beam lines represented around. The inset is the ensemble picture showing the linear accelerator (LINAC) from where the electrons are produced, the booster synchrotron of 300 m diameter where the electrons are pre-accelerated at a solicited velocity before being injected into the storage ring of 844.4 m circumference. . . . .	88
2.42	Picture of a part of the storage ring of the ESRF synchrotron, with a section showing the set of the focusing magnets, bending magnets (BM) and insertion devices (ID). . . . .	89
2.43	Picture of a part of an insertion device (or undulator) of the storage ring[27]. It illustrates how the electrons's intensity is amplified through the oscillation of their trajectories during their passage into the field established by the magnetic poles. . . . .	89
2.44	Illustration of the deflection of electrons when passing through the a bending magnet, followed by the emission of a synchrotron radiation[27]. . . . .	90
2.45	Experimental setup for HRXRD measurements of the ESRF's BM32 beam line end station. An image of a sample mounted on a holder fixed to the goniometer is shown. . . . .	91
3.1	MEIS measurements on the samples implanted with arsenic ( $\text{As}^+$ - S1) and arsine ( $\text{AsH}_3^+$ - S2, S3) with the associated fits. The incidence and scattering angles were $64^\circ$ and $135^\circ$ , respectively. The implantation methods are indicated in each graph. Samples S2 and S3 have been implanted by PIII at room and high ( $400^\circ\text{C}$ ) temperatures, respectively. . . . .	95
3.2	RBS experimental result with the associated fit, obtained on the arsine ( $\text{AsH}_3^+$ ) implanted sample. The incidence and the scattering angles were $62^\circ$ and $160^\circ$ , respectively. . . . .	95
3.3	MEIS experimental spectra of arsenic measured in the samples implanted by the conventional (S1) and plasma (S2 & S3) methods at 3 keV. The spectra were acquired in normal (open dotted circles) and off-normal ( $64^\circ$ - filled circles) incidences. The SRIM simulations of the arsenic spectra in the conventional implantation were carried out with mono-energy ions. However, those for the plasma methods were carried out by using the arsenic ions of multiple energies. The gridded parts represented in the graphs indicate the surface oxide's thicknesses. . . . .	97
3.4	Schematic illustration of the tops and sidewalls doping from a bidimensional SRIM simulation approach. The estimated implantation depths are indicated in the table. The implantation conditions as well as the nature and the energies of the dopants are indicated in the graph and the drawing. . . . .	98
3.5	Cross-sectional Transmission Electron Microscopy (TEM) images in scanning mode acquired on the 3D-nanostructured sample (S1) implanted with arsenic. The image shows the Si-Fins, buried oxide (Box) and the Si-bulk stacking and the dimensions. . . . .	99
3.6	Schematic illustration showing the geometrical projections of the implantation of As in the Fins of dimensions as indicated in the TEM image of Figure (3.5). The figure represents the sample (S1) implanted by using the conventional method, the width is represented by considering the presence of a native oxide. The estimated implanted depths in the tops (9 nm) and sidewalls (7 nm) are those deduced from the SRIM [25] simulations illustrated in Figure (3.4). . . . .	100

3.7	Illustration of a conformal implantation of arsenic ( $\text{As}^+$ ) by using the conventional method. The thicknesses $x$ and $y$ of the implanted layers in the tops and sidewalls are considered as the same. . . . .	102
3.8	Schematic illustration of the geometry where the scattered projectiles are detected laterally with respect to the silicon (Si) Fins during the analyses in inclined incidence (a) and in normal incidence (b). . . . .	103
3.9	Illustration of the PowerMEIS simulations of a MEIS experimental spectrum with the contribution of all the chemical elements (Si, O, As) constituting the matrix. The incidence and scattering angle are indicated on top of the graph. . . . .	103
3.10	Presentation of the MEIS experimental spectra and their associated PowerMEIS simulations, obtained on the sample (S1) implanted with arsenic by using the conventional method. The incidence and scattering angle of the 200 keV projectiles are indicated on top of each graph. The orientation of the line grating on the wafer was such that the scattered ions exit laterally with respect to the Fins (see Figure (3.8)). The best fit (Total) is represented by the solid curve. The simulation of the spectrum corresponding to a conformal implantation (red-dashed) and the one expected from the implantation conditions (green-dashed) are illustrated. The double peaks of arsenic in the patterns are highlighted in the top and bottom-left graphs (B & D). . . . .	104
3.11	3D deconvolutions of the arsenic spectra in the two analysis geometries. The first peak is labelled as 1 and the second as 2. . . . .	105
3.12	Illustration of the 3D deconvolutions of the simulated spectra for a conformal implantation, in the two geometries. The first and second peaks are also labelled as 1 and 2. . . . .	105
3.13	Illustration of the sidewalls - I and Sidewalls - II of the Fins. In inclined incidence ( $64^\circ$ ), the projectiles penetrate the Fins from the side directly facing the beam (sidewalls - I), then lose energy when crossing the core of the Fins, before reaching the sides opposite to their entrance (sidewalls - II). . . . .	106
3.14	Cross-sectional Transmission Electron Microscopy (TEM) image in scanning mode of the 3D-nanostructured sample (S1) implanted with arsine. The image shows the Si-Fins, buried oxide (Box), the Si-bulk and the dimensions of the patterns. . . . .	108
3.15	Presentation of the experimental spectra with their associated PowerMEIS simulations, obtained on the sample (S2) implanted by the plasma method at room temperature. The incidence and scattering angles of the 200 keV proton projectiles are indicated on top of each graph. The best fit (Total) is represented by the blue - solid curve. The simulation of the spectrum corresponding to a conformal implantation (red - dashed curve) is illustrated. The double peaks of arsenic in the patterns are highlighted in the top and bottom-left graphs (B) and bottom (D). The orientation of the line grating was such that the scattered ions exit laterally to the Fins (see Figure (3.8)). . . . .	109
3.16	3D - deconvolutions of the arsenic spectra of the sample implanted by plasma at 3 keV - room temperature. The first peak is labeled as 1 and the second as 2. The deconvolutions are performed in the two analysis geometries. . . . .	110

3.17	Simulations by 3D – deconvolutions of the arsenic spectra considered as conformally implanted by PIII at 3 keV - room temperature in each part of the nanostructure. The first peak is labeled as 1 and the second as 2. The deconvolutions are performed in the two analysis geometries. . . . .	110
3.18	Presentation of the experimental spectra with their associated PowerMEIS simulations, obtained on the sample (S3) implanted by the plasma method at 400°C. The incidence and scattering angles of the 200 keV proton projectiles are indicated on top of each graph. The best fit (Total) is represented by the green-solid curve. The simulation of the spectrum corresponding to a conformal implantation (red – dashed curve) is illustrated. The double peaks of arsenic in the patterns are highlighted in the top and bottom – left graphs (B & D). The orientation of the line grating was such that the scattered ions exit laterally to the Fins. . . . .	111
3.19	3D – deconvolutions of the arsenic spectra implanted in each single part of the nanostructure by plasma at 400°C, in the two analysis geometries. The first peak is labelled as 1 and the second as 2. . . . .	112
3.20	Simulations by 3D – deconvolutions of the arsenic spectra for an implantation by PIII at 400°C considered as conformal. The spectra are provided in the two analysis geometries. The first peak is labeled as 1 and the second as 2. . . . .	112
3.21	(a): Simulations of the arsenic spectra in the tops, sidewalls and bottoms of the patterns, when the scattered projectiles exit along the lines. (b): schematic illustration of the Fins where the azimuth $\varphi = 90^\circ$ is their orientation in the plane of the sample holder during the analyses. . . . .	114
3.22	X-ray reflectivity measurements carried out in the line grating of the samples around the (220) reflexion. The energy of the x – photons was 12 keV and the wavelength 0.103532 nm. The reference sample was obtained from a slot different from that of samples S1, S2 and S3, which could explain a thickness of the crystal area 55 nm $\neq$ 60 nm. . . . .	116
3.23	Raw experimental spectra measured by x-ray diffraction in grazing incidence (GIXRD) mode around the (220) reflexion. They were acquired on the samples implanted with arsenic by the conventional implanter and plasma immersion ion (PIII) methods, then compared with a non-implanted reference. The top-right drawing illustrates the geometrical conditions of the measurements. The wavelength of the x-photons was 0.103532 nm with an energy of 12 keV. . . . .	117
3.24	Model of the FDSOI line gratings used to calculate the diffracted intensities of the reference and the implanted samples. The term $\alpha$ represents the sidewalls angle to take into consideration a possible non-rectangular shape of the patterns. . . . .	118
3.25	Comparison of the measured and calculated transverse scan profiles around the (220) reflexion of a non – implanted reference sample. The initial values of the height and the pitch are 55.5 nm and 160 nm, respectively. The width and the sidewalls angle determined by the calculations are indicated in the graph. . . . .	118

3.26	Comparison of the measured and calculated transverse scan profiles around the (220) reflexion of a sample implanted with arsenic at room temperature by using the conventional implanter. The energy, temperature conditions and parameters corresponding to the best fit are indicated on the graph. The values of the height and the pitch used for the calculations were 50.6 nm and 160 nm respectively. . . . .	119
3.27	SRIM profiles of the displaced silicon atoms. They are used to estimate the damaging depths in the tops and sidewalls. . . . .	119
3.28	HAADF image of an isolated Fin of the sample implanted with arsenic at 3 keV-RT by the conventional method. The thickness of the implanted area on the top, the height of the pattern as well as the width of the crystal area are indicated. . . . .	120
3.29	HAADF image of an isolated Fin of the sample implanted with arsenic at 3 keV-RT by plasma. The dimensions as well as the thickness of the implanted areas on the top ( $\sim 6$ nm) are indicated. . . . .	122
3.30	Comparison of the measured and calculated transverse scan profiles around the (220) reflexion of a sample implanted with $\text{AsH}_3^+$ at room temperature by using the plasma method. The energy, temperature conditions as well as the parameters corresponding to the best fit are indicated on the graph. The values of the height and the pitch used for the calculations were 52.3 nm and 160 nm, respectively. . . . .	123
3.31	Comparisons of the measured and calculated transverse scan profiles around the (220) reflexion of a sample implanted with $\text{AsH}_3^+$ at $400^\circ\text{C}$ by using the plasma method. The energy, temperature conditions as well as the parameters corresponding to the best fit are indicated on the graph. The values of the height and the pitch used for the calculations were 60 nm and 160 nm, respectively. . . . .	123
3.32	MEIS experimental results acquired in channeling and random modes on the samples implanted with the conventional implanter (S1) and by plasma – room temperature (S2) and $400^\circ\text{C}$ (S3). The yield of the surface silicon damaged – peak in channeling mode serves to evaluate the amorphization level relatively to the yield in random mode. The top – right drawing shows the non-etched (2D) area on which the measurements were carried out. . . . .	125
4.1	Experimental results with the associated models obtained on the arsenic ( $\text{As}^+$ : S1) and arsine ( $\text{AsH}_3^+$ : S2 & S3) implanted samples. The spectra of the left – column were acquired at an incidence angle of $64^\circ$ so as to align the projectiles along the $\langle 332 \rangle$ crystal axis and detect the scattered ones at $135^\circ$ . Those of the right – column were measured at an incidence angle perpendicular to the sample's surfaces (normal incidence $\equiv \langle 001 \rangle$ ) with the scattering angle of $119^\circ$ . . . . .	130

4.2	Illustrations of how the existence of crystal damages lead to the increase of the yield in the Si-crystal region, due to the dechanneling of the ingoing projectiles which affects the minimum yield ( $\chi_{\min}$ ). The example of the corresponding MEIS spectra in channeling and random modes are illustrated. The graphs A & A' depict the case of a pure (virgin) crystal silicon, graphs B & B' are for an implanted silicon showing that the increase of the $\chi_{\min}$ is related to the thickness of the implanted area. Graphs C & C' are similar to those of graphs B & B', with the only difference that the damaged area is thicker. . . . .	131
4.3	Evolution of the minimum yield with respect to the amorphous layer traversed by the incident projectiles in the silicon crystal. . . . .	132
4.4	Normalized MEIS spectra of the damages in channeling mode, represented by the $\chi_{\min}$ plotted in function of the depth. They derive from the spectra of Figure (4.1) measured along the $\langle 332 \rangle$ channeling direction ( $64^\circ$ incidence) and in normal incidence ( $\langle 001 \rangle$ ). The Zones A and B refer to the implanted and non-implanted regions in the Si crystal. The $\chi_{\min}$ corresponding to thermal vibrations of the Si atoms is indicated. . . . .	133
4.5	Illustrative examples of how the incident projectiles penetrate a crystal containing different types of damages such as displaced atoms, distortions, interstitials, when they are channeled along an inclined $\langle 332 \rangle$ direction (A) and a vertical $\langle 001 \rangle$ crystal axis (B). . . . .	134
4.6	Determination of the expected min by using the calibration line giving the evolution of the minimum yield with respect to the amorphous thickness. The computed $\chi_{\min}$ in normal incidence ( $\langle 001 \rangle$ ) are equivalent for the two samples (10 %). The experimental values are indicated in their respective spectra. . . . .	135
4.7	Comparison of the values of the measured minimum yields (obtained from the experimental spectra) and those extracted from the calibration line in normal incidence ( $\langle 001 \rangle$ ). The notation IM refers to implanter method and PL refers to plasma method. . . . .	135
4.8	Determination of the expected $\chi_{\min}$ by using the calibration line giving the evolution of the minimum yield with respect to the amorphous thickness. The incidence angle of the projectiles was $64^\circ$ ( $\langle 332 \rangle$ ) with respect to the sample's normal. . . . .	136
4.9	Comparison of the values of the measured minimum yields (obtained from the experimental spectra) and those extracted from the calibration line in inclined incidence ( $\langle 332 \rangle$ ). The notation IM refers to implanter method and PL refers to plasma method. . . . .	137
4.10	Comparison of the ToF-SIMS profiles of hydrogen, measured in the $\text{AsH}_3^+$ – implanted samples at 3 keV. A $\text{Cs}^+$ beam of energy 500 eV was used for the abrasion and the elements were analyzed with a $\text{Bi}^+$ beam of 25 keV. The depth calibration was performed by profiling boron deltas in Si (the deltas being measured by TEM). The implanted and non-implanted areas are those determined by MEIS. . . . .	138
4.11	ToF-SIMS profiles of hydrogen in the 3 keV (A, B) PIII implanted samples with the associated SRIM simulations. The energies of the H ions used in the simulations were 3 keV. The concentrations corresponding to the residual contamination in the SIMS chamber are indicated by the arrows. The implanted and non-implanted areas are those determined by MEIS. . . . .	139

---

A.1	Representation of the matrice model used to simulate the MEIS spectrum of a 3D structure. The layers of different stoichiometries are introduced in the model to take the implantation of arsenic into account. . . . .	144
A.2	Representation of the matrix models of the nanostructures utilized to simulate the implantation of arsenic in the: tops, bottoms, sidewalls-I and sidewalls-II. . . . .	146
B.1	TEM image of the atomic columns represented by the white dots. . . . .	147
B.2	Schematic principles of the TEM (left) and STEM (right) analysis techniques. . . . .	148
B.3	Different detectors utilised in (S)TEM. The different angles $\theta$ correspond to the deviations with respect to the direct transmitted beam, and also to the limits of the detection angle with the other systems. . . . .	149
B.4	Example of an EDX image showing the chemical profiles of Si, As and O acquired on a 3D Fin-shaped silicon nanowire. . . . .	150
B.5	Left: Zoom of the two beams system of the sample preparation (the FIB gun generates $\text{Ga}^+$ for the sputtering and the SEM gun can be used for imaging the sputtered region. Right: preparation steps for the FIB cuts in question[28]. . . . .	151
B.6	Image of the traditional side-entry holder[28]. . . . .	151
B.7	Image of the FEI Titan Themis (S)TEM microscope column utilised for the analyses, available on the Leti's nano characterization platform (PFNC). . . . .	152

# List of Tables

1.1	Scaling rules of the MOSFETs in the CF hypothesis proposed by Dennard in 1974[3]. The parameters $W$ , $L$ , $C_{ox}$ and $X_j$ refer to the gate width, gate length, oxide thickness and the junction depth, respectively. $C_{gate}$ is the gate capacitance per channel. . . . .	11
1.2	Overview of the capacities of the above presented techniques regarding the characterization of 3D doping. . . . .	32
1.3	Part of the samples studied in this work labeled as S1, S2 and S3. The implantation methods as well as the parameters are indicated in each column. As indicated in the table, plasma refers to the PIII method which was employed in pulsed mode. . . . .	33
3.1	Comparison of the implanted arsenic doses measured by RBS and MEIS. The values obtained with the MEIS technique were computed through the simulations of the experimental spectra with the respective densities: $6.9 \times 10^{22}$ mol/cm <sup>3</sup> (for Si <sub>0.36</sub> O <sub>0.64</sub> ), $2.3 \times 10^{22}$ mol/cm <sup>3</sup> (for SiO <sub>2</sub> ) and $5 \times 10^{22}$ mol/cm <sup>3</sup> (for Si). . . . .	96
3.2	Calculated dose fractions and the expected local doses in the sample implanted by the conventional method. They were determined by considering the implantation conditions and the geometry of the sample. . . . .	101
3.3	Comparison of the normalized local dosages in the sample. The values of the measured and expected ones from calculations, as well as those deduced by simulations in the situation of a conformal doping are provided. . . . .	107
3.4	Comparison of the normalized local doses measured in the sample implanted by plasma at 3 keV – RT, with those deduced from the simulations based on the assumption of a conformal doping. . . . .	110
3.5	Comparison of the normalized local doses measured in the sample implanted by plasma at high temperature (400°C) – 3 keV, with those deduced by the simulation of a conformal implantation. . . . .	112
3.6	Comparison of the normalized local doses measured in the three samples. . . . .	113
3.7	Comparison of the vertical and lateral dimensions of the crystal and damaged-implanted areas in the patterns. The values determined by each technique are indicated, the dimensions of the overall nanostructures are provided as well. . . . .	120
3.8	Comparison of (A): the vertical and lateral dimensions of the entire patterns used in the MEIS simulations and determined by TEM imaging. There are not TEM data available for sample S3. (B): the damaged implanted and the crystal areas within the line grating of the two samples. . . . .	122

# Abbreviations

<b>ADC</b>	<b>A</b> nalog to <b>D</b> igital <b>C</b> onverter
<b>APT</b>	<b>A</b> tom <b>P</b> robe <b>T</b> omography
<b>Box</b>	<b>B</b> uried <b>o</b> xide
<b>CCD</b>	<b>C</b> harge <b>C</b> oupled <b>D</b> evice
<b>CMOS</b>	<b>C</b> omplementary <b>M</b> etal <b>O</b> xide <b>S</b> emiconductor
<b>cpm</b>	configurating <b>p</b> ower <b>m</b> eis
<b>Cz Si</b>	<b>C</b> zochalski <b>S</b> ilicon
<b>DOS</b>	<b>D</b> ensity <b>O</b> f <b>S</b> tate
<b>EDX</b>	<b>E</b> nergy <b>D</b> ispersive <b>X</b> -ray analysis
<b>ERDA</b>	<b>E</b> nergy <b>R</b> ecoils <b>D</b> etection <b>A</b> nalysis
<b>ESRF</b>	<b>E</b> uropean <b>S</b> ynchrotron <b>R</b> adiation <b>F</b> acilities
<b>eV</b>	electron <b>V</b> olt
<b>FDSOI</b>	<b>F</b> ully <b>D</b> epleted <b>S</b> ilicon <b>O</b> n <b>I</b> nsulator
<b>FinFET</b>	<b>F</b> in <b>F</b> ield <b>E</b> ffect <b>T</b> ransistor
<b>FIB</b>	<b>F</b> ocused <b>I</b> on <b>B</b> eam
<b>FWHM</b>	<b>F</b> ull <b>W</b> idth at <b>H</b> alf <b>M</b> aximum
<b>FWHm</b>	<b>F</b> ull <b>W</b> idth at <b>H</b> alf <b>m</b> inimum
<b>HAADF</b>	<b>H</b> igh <b>A</b> nge <b>A</b> nnular <b>D</b> ark <b>F</b> ield
<b>GIXRD</b>	<b>G</b> razing <b>I</b> ncidence <b>X</b> -ray <b>D</b> iffraction
<b>HRBS</b>	<b>H</b> igh <b>R</b> esolution <b>R</b> utherford <b>B</b> ack <b>S</b> cattering
<b>HV</b>	<b>H</b> igh <b>V</b> acuum
<b>HVEE B.V</b>	<b>H</b> igh <b>V</b> acuum <b>E</b> ngineering <b>E</b> uropa <b>B.V.</b>
<b>IC</b>	<b>I</b> ntegrated <b>C</b> ircuit
<b>I, V</b>	<b>I</b> nterstitial, <b>V</b> acancy (point defects)
<b>LEIS</b>	<b>L</b> ow <b>E</b> nergy <b>I</b> on <b>S</b> cattering

---

<b>MEIS</b>	<b>M</b> edium <b>E</b> nergy <b>I</b> on <b>S</b> cattering
<b>MOSFET</b>	<b>M</b> etal <b>O</b> xide <b>S</b> emiconductor <b>F</b> ield <b>E</b> ffect <b>T</b> ransistor
<b>NRA</b>	<b>N</b> uclear <b>R</b> eaction <b>A</b> nalysis
<b>PIII</b>	<b>P</b> lasma <b>I</b> mmersion <b>I</b> on <b>I</b> mplantation
<b>PSDA</b>	<b>P</b> osition <b>S</b> ensitive <b>D</b> etector <b>A</b> nalyzer
<b>Q-pole</b>	<b>Q</b> uadrupole
<b>RBS</b>	<b>R</b> utherford <b>B</b> ackscattering <b>S</b> pectrometry
<b>R<sub>p</sub></b>	<b>P</b> rojected <b>R</b> ange
<b>RT</b>	<b>R</b> oom <b>T</b> emperature
<b>SAXS</b>	<b>S</b> mall <b>A</b> ngle <b>X</b> -ray <b>S</b> cattering
<b>SEM</b>	<b>S</b> canning <b>E</b> lectron <b>M</b> icroscopy
<b>SIMS</b>	<b>S</b> econdary <b>I</b> on <b>M</b> ass <b>S</b> pectrometry
<b>SRIM</b>	<b>S</b> topping and <b>R</b> ange of <b>I</b> on in <b>M</b> atter
<b>(S)TEM</b>	<b>(S)</b> canning <b>T</b> ransmission <b>E</b> lectron <b>M</b> icroscopy
<b>SSRM</b>	<b>S</b> canning <b>S</b> preading <b>R</b> esistance <b>M</b> icroscopy
<b>TEA</b>	<b>T</b> oroidal <b>E</b> lectrostatic <b>A</b> nalyzer
<b>TED</b>	<b>T</b> ransient <b>E</b> nhanced <b>D</b> iffusion
<b>ToF</b>	<b>T</b> ime of <b>F</b> light
<b>TRIM</b>	<b>T</b> ransport and <b>R</b> ange of <b>I</b> on in <b>M</b> atter
<b>UHV</b>	<b>U</b> ltra <b>H</b> igh <b>V</b> acuum
<b>ULE</b>	<b>U</b> ltra <b>L</b> ow <b>E</b> nergy
<b>ULSI</b>	<b>U</b> ltra <b>L</b> ow <b>S</b> cale <b>I</b> ntegration
<b>USJ</b>	<b>U</b> ltra <b>S</b> hallow <b>J</b> unction
<b>VLSI</b>	<b>V</b> ery <b>L</b> arge <b>S</b> cale <b>I</b> ntegration
<b>XRD</b>	<b>X</b> - <b>R</b> ay <b>D</b> iffraction

# Symbols

Definition	syntax	unit or value
Angstrom	$\text{\AA}$	$= 10^{-10} \text{ m}$
Average atomic spacing along an atomic row	$d$	
Average atomic spacing between planes	$d_p$	
Avogadro constant	$\mathcal{N}_A$	$= 6.022 \times 10^{23} \text{ atom/mole}$
Bohr radius ( $\hbar^2/me^2$ )	$a_0$	$= 0.529 \text{ \AA}$
elementary charge	$e$	$1.60217622 \times 10^{-19} \text{ C}$
	$e^2$	$= 14.4 \text{ eV}\cdot\text{\AA}$
Vacuum permittivity	$\epsilon_0$	$= 8.854 \times 10^{-12} \text{ F/m}$
Silicon permittivity	$\epsilon_0^{Si}$	$= 1.04 \times 10^{-12} \text{ F/m}$
Silicon gap	$E_g^{Si}$	$= 1.12 \text{ eV}$
Silicon electron affinity	$\chi_{Si}$	$= 4.05 \text{ eV}$
Minimum yield	$\chi_{min}$	$\sim 4\%$ (pure crystal Si)
Plank constant	$h$	$= 6.626 \times 10^{-34} \text{ J}\cdot\text{s}$
	$\hbar$	$= h/2\pi = 1.054 \times 10^{-34} \text{ J}\cdot\text{s}$

*To my Father and beautiful Mother...*

## General Introduction

This manuscript is about the results of my work throughout these three years of PhD studies at the "Commissariat à l'Energie Atomique et aux Energies Alternatives (CEA)", in the "Laboratoire de l'Electronique des Technologies de l'Information (LETI)". The major part of my activities were carried out on the "Nanocharacterization Platform (PFNC)" of CEA-LETI and the "Micro-Nanotechnology (MINATEC)" European campus. CEA-LETI has been involved in several projects at the European or world level for years, in the domains of technological research (source: EU, Ion4SET H2020). Entitled 'Ion beam analysis of three-dimensional (3D) structures for applications in nanotechnology, my thesis is defined in the framework of one of them (*NO22 ENabTech*) initiated in the context of the 3D integrations of microelectronic devices. The main objective is to use ion beam analysis techniques to characterize the doping performed by ion implantation into 3D silicon (Si) nano-lines (or Fins) obtained by electron beam (e-beam) etching. One of the serious issues concerning the doping of the 3D structures is the evaluation of the concentration of dopants. Therefore, a good quantification requires state-of-the-art instruments of very high precision. With the advent of a third dimension in the non planar structures, the issue about the lateral resolution get in the play, thereby making things to be more complicated for some techniques such as Medium Energy Ion Scattering (MEIS) and Time of Flight Secondary Ion Scattering (ToF-SIMS) for instance. Since it is not only the matter of dealing with the multiple path lengths of the incident projectiles into the nanostructure[20, 29], but also the non homogeneous concentrations of the dopants within the different parts [18]. Hence efficient analysis methods are needed. Several approaches relying on different characterization techniques have been developed in order to propose solutions to this problem. Some of them are presented in section(1.6). Thanks to the analyses protocols which has been developed for these types of nanostructures, the MEIS technique has been used to quantify the dopants through the simulations of the spectra by using the PowerMEIS software[30]. The studies carried out have the goal of comparing the doping conformity. The types of the implants used are Arsenic ( $\text{As}^+$ ) introduced in the structure by using the conventional implanter method, and arsine ( $\text{AsH}_3^+$ ) introduced by the plasma immersion ion implantation (PIII) method. However, the quantification in the ultra thin (non-etched) layers has been assessed by MEIS and RBS so as to check the aptitudes of the two techniques in the compositional analysis of such samples. It is known that a foreign specimen cannot be introduced into a given material without influencing the equilibrium the crystal lattice of the structure receiving it. An important part of the studies has been consecrated to the impact of the arsenic and arsine implantations within the different specimens. During the investigations, it has been observed that the ion beam analysis techniques are certainly powerful in providing the key information concerning the elemental (MEIS & ToF-SIMS) and structural

(MEIS) characterization of materials. However, when it comes to the damaging impacts in 3D structures, MEIS is not yet able to provide that kind of information within the patterns. Consequently, we have looked for other complementary techniques that are more sensitive to the crystal orders even in such small volumes. For the sake of widening the analyses, so as to provide further explanations to the obtained results, we had the opportunity to access to some of the world-leading research institutions and facilities. The experiments on x-ray analyses (diffraction and reflectivity) at the European Synchrotron Radiation Facilities (ESRF) allowed us to achieve the goal. The final objective of the studies of these 3D Fin-shaped Si patterns of sub-nanometric dimensions, is to build the triple gate (Trigate) Fin field-effect transistors (FinFET) on fully depleted silicon on insulator (FDSOI) materials. First, it is important to define the technological context of the thesis and also to give a brief overview of the state-of-the-art of research concerning the 3D doping. This manuscript is therefore organized as follows.

The chapter 1 is consecrated to the technological context whereby the background on SOI materials, semiconductor and doping has been recalled. The current state-of-the-art concerning the characterization of 3D doping has been also discussed. In chapter 2, the experimental techniques used throughout this project are presented. In chapter 3, we present the results concerning the studies of the doping conformity in the patterned samples, followed by some comparisons based on the implantation methods. In chapter 4, the general idea is to know what are the consequences of the implantation methods employed in terms of damage creations in the crystal Si, i.e. beyond the implanted areas. Last, the chapter 5 is consecrated to the general conclusion followed by some perspectives. Each chapter ends-up with a short conclusion resuming the main information about the discussed results. An appendix (A) is provided for further information relative to the simulation methods of the MEIS spectra. Some basics on electron microscopy are provided in appendix(B).

# Chapter 1

## Technological context and state-of-the-art

### 1.1 Introduction

The nanotechnology industry is leading intense research activities on the miniaturization of the main constituents of integrated circuits (ICs), namely the Metal Oxide Semiconductor Field Effect Transistors (MOSFETs). The dimensioning of the devices' structure has a decisive impact on their operation and performances. As a consequence of the Moore's law[31], the performances will be improved but it appears that all the parts of the CMOS transistors can indefinitely not be shrunk, because of the occurrence of unexpected behavior. Mostly when these non desirable features take place at the key part of the device: the gate. The scaling down of the gate's size has actually reached the limits of physics. The main reason is that the low dimensions of the the gate length make the monitoring of the channel problematic for the infinitely small dimensions. One of the most promising approaches to circumvent this dilemma and thus improve the efficiency of the future technological nodes, is the development of transistors of 3D architectures. Many initiatives have been carried out for years to tackle an boost their integration. This is very important in the sense which it is tricky to imagine a far or even near future without the technological gadgets more and more thin, fast, powerful and environmental friendly. Nanotechnology is therefore at the crossroad of all the stages leading to such sophisticated and futuristic devices: lithography, doping, device engineering, design, packaging, integration, improvement, and hence innovation. The success in this approach requires state-of-the-art researches. First, in the field of fundamental physics for a better understanding of the laws governing the infinitely small dimensions. Secondly, in the field of material sciences, precisely in the sectors such as thin film engineering for instance.

Establishing itself as an European center of excellence for research in microelectronics, the MINATEC campus in partnership with corporates, is carrying out very intense research aiming at increasing the development of integrated circuits and to significantly contribute to the integration of 3D devices. The good realization of such semiconductor devices requires the materials' doping of high qualities, because doping is one of the crucial steps in the semiconductor manufacturing process. After we have described the materials from which the samples were fabricated, the doping techniques that are commonly used will be presented as well. We will highlight their main features and detail the most used one in the semiconductor industry.

## 1.2 Silicon On Insulator (SOI) materials

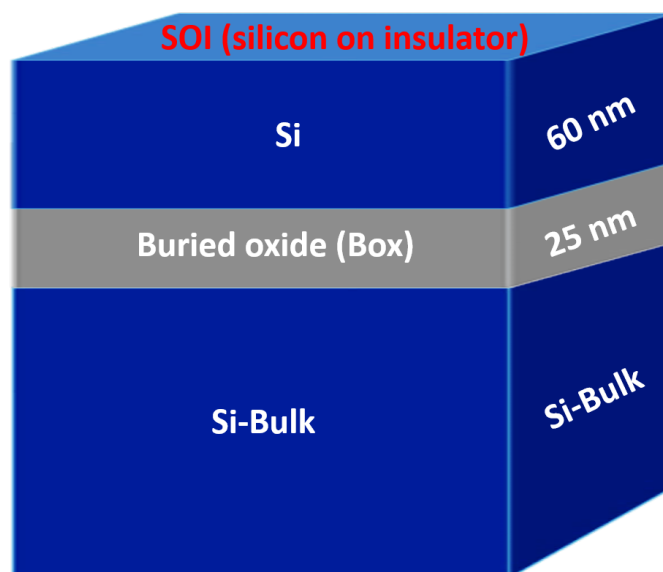


FIGURE 1.1: Schematic illustration of a stack of SOI type.

The structure of a SOI material consists of a silicon layer formed on an oxide ( $\text{SiO}_2$ ), which itself is laid on another silicon layer representing the substrate. As shown in figure (1.1), the two silicon layers are separated by a continuous oxide layer commonly called buried oxide (Box). The thickness of each of these layers varies depending on the technological needs. The intercalated  $\text{SiO}_2$  layer has thus as a role, to warrant the mechanical properties of the whole material [32] and avoid leakage currents. In contrast to the devices fabricated using bulk silicon, those made from SOI structures display better performances. This will be demonstrated with the three-dimensional ones, since we will focus on the trigate transistors. They find their applications in multiple technological domains such as microelectronics, optics, photonics, micro-electromechanical systems (MEMS), or biotechnology. Given that the studies conducted in this project are part

of the microelectronic framework, we are going to provide some interesting examples of the advantages that one can get from the microelectronic devices elaborated on FDSOI wafers. We have:

- \* High switching frequency: the automatic latching-up phenomena are significantly attenuated or often avoided, thanks to the good isolation of the p and n junctions.
- \* Reduction of the capacitance effects: this is possible due to the excellent isolation between the top mono crystal silicon layer and the substrate by the buried oxide.
- \* Reduction of the energy consumption thanks to the low leakages and low capacitance effects.
- \* The SOI nano-sensors are more efficient than those fabricated on bulk silicon thanks to the radiative strengthening that they afford.

### 1.2.1 Fabrication techniques of SOI structures

The SOI-based silicon wafers can be of different diameters depending on the adopted technologies. There are several SOI wafer production techniques. The most common being: SIMOX (separation by implantation of Oxygen), BSOI (bounded silicon on insulators), Eltran (Epitaxial layers transfer process).

The first method allows to obtain wafers of good quality but at relatively high production costs. In fact, it first requires the implantation of oxygen, which has a non negligible mass, and therefore requires a considerable energy budget. Despite all of this, it remains one of the main production methods used by the japanese fabricants like Toshiba for example. In the second technique (BSOI) was developed in the 1980s. It is about preparing the surface of two wafers by growing a hydrophilic oxide layer (native oxide obtained by chemical or thermal processes on both wafers). Then, they are bonded to each other, followed by a rapid thermal process which makes the adhesion to be completely effective[32]. The intercalated oxide obtained in that process serves to separate the top and bottom (substrate) silicon. The Eltran method also consists in a direct bonding of two wafers together. Comparatively to SIMOX, it offers many advantages such as the re-utilization of the remaining parts of each of the two wafers after they have been separated from the initial ones and chemically treated. The Eltran method also allows a good controllability of the thicknesses of the SOI stack formed (with the thicknesses ranging from few nanometers for MOSFET applications to few micrometers for MEMS applications), the obtention of a homogeneous buried oxide layer, etc. In spite of the wafers of good qualities that this fabrication method affords, it has been noticed that one of the most critical issues encountered is the production cost which remains very

high. A reason justifying this derives from the fact that the two wafers are used for the growing of all the stacks constituting the obtained final SOI structures. The quality of the final product obtained with this method also suffers from the existence of structural defects. They result from the strains generated during the mechanical separation of the porous silicon at either side of the wafers. The fabrication process employed in this method is similar to that developed in the Smart-Cut technique[33], since it also uses two separated silicon wafers. However, their bonding methodology being different from that of the Eltran and the other techniques[33]. The readers interested by the different steps describing the Smart-cut processes necessary for the fabrication of the SOI wafers can consult the following documents[32–34].

The SOI based microelectronic devices are known for their best performances comparatively to those elaborated on bulk silicon[32, 35]. It is thanks to the improvement of their intrinsic properties. Indeed, the fact that the active top silicon layer being separated from the one of the substrate, spares the devices from the anomalies such as energy losses and capacitance effects, thereby increasing the gains in performances. Actually, the voltage and current gains as well as the low energy consumption are among the many advantages afforded by the SOI technology. However, we think it is worth describing the semiconductor materials, then the CMOS devices such as MOSFETs and FinFETs fabricated from the SOI wafers. It is also important to understand why they seem to be better than the FinFETs on bulk Si. Indeed, unlike what is reported, FinFETs on bulk Si may allow better performances as claimed by some tech-giants like intel[7]. One should therefore consider such studies as the performance comparisons, because each technology (SOI or bulk Si) has actually its own application limits.

### 1.3 Semiconductor materials

A semiconductor (SC) material has similar properties with those of insulator materials, i.e. the valence and conduction band are separated from each other by a forbidden band (gap). The energy gap ( $\Delta$ ) can be defined as the energy the electrons should possess so that they can cross the forbidden band delimited by the conduction and valence bands: it is an energy barrier. What differentiates semiconductors from insulators is their shorter gap contrarily to those of insulators that are larger. In the case of SC, the electron's probability of transition from a lower to higher level, yielding to the generation of a current, is more significant than in insulators. Even though it may not be sufficient to make the transition totally effective.

There exists two types of semiconductors: intrinsics and extrinsics. A SC is qualified as intrinsic when it is defects free. Its electrical properties only depend on its structure, they

are very close to those of a pure monocrystal silicon[36]. The total number of electrons  $n$  present in the conduction band is equal to the total number of holes ( $p$ ) present in the valence band:  $n=p=n_i$ .  $n_i$  is defined as the total number of intrinsic carriers. In the case of silicon,  $n_i = 1.45 \times 10^{10} \text{ electrons/cm}^3$  at  $T=300\text{K}$ .

The extrinsic SC is the opposite of the previous type mentioned above, i.e, they contain defects. Consequently, the total number of electrons ( $n$ ) present in the conduction band is different from the total number of holes ( $p$ ) present in the valence band: ( $n \neq p$ ). However, the law of mass action ( $\bar{p} \times \bar{n} = n_i^2$ ) remains conserved. The difference in the number of charge carriers results from the fact that some extraneous atoms called impurities, have been introduced inside its structure. The direct consequence of their presence is the modification of the carriers' density. Indeed, the density of the majority carriers can be augmented when that of the minority carriers is decreasing, or vice-versa. This imbalance in the total number of both types of carriers, provoked by the doping process will induce a modification of the transport or electrical properties of the semiconductor such as the conductivity and resistivity. Almost the total quantity of impurity atoms will occupy the interstitial sites of the crystal without establishing any bond with the host atoms. They are thus electrically inactive. The schematics of figure(2.1) show the situations when two different types of impurity atoms (boron (B) & arsenic (As)) introduced inside a crystal silicon.

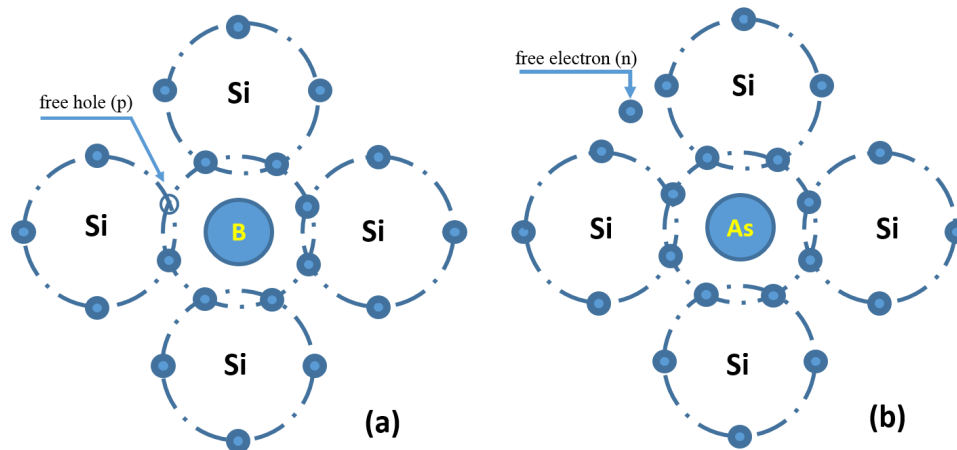


FIGURE 1.2: Illustration of two different types of doping of semiconductors. (a): p-type doping with boron (B) and (b): n-type doping with arsenic (As).

In order to make the doping more effective and efficient by activating the dopants, a thermal treatment (annealing) is needed. High temperature annealing is usually required at temperatures around  $\sim 1000^\circ\text{C}$  to make the impurity atoms migrate towards the substitutional sites. The insertion of impurity atoms inside crystals or non crystal materials not only find applications in semiconductors industry, but also in metallurgy for example[37]. This process is indeed utilized to strengthen metals by inserting foreign

atoms of mass smaller than those of the host matrix to modify their mechanical properties. For example, nitrogen is often introduced into the iron's structure to improve its wear resistance[37]. We are mainly interested in the doping processes of semiconductors performed for the uses in the microelectronic domain. The dimensions of the SC devices are continuously decreasing from a technological node to another, and this strongly influence the qualities of the junctions to elaborate. Therefore, there is a crucial need of performing the dopings at ultra shallow depths. Such doping characteristics are intensively investigated in the areas of nanoelectronics.

## 1.4 Evolution of the MOS transistors: from MOSFET to FinFET

### 1.4.1 The structure of MOSFET

Like the bipolar junction transistors (BJTs), the MOSFET represent another class of transistors which their operations rely on the field effects. It is, however, characterized by its very fast switching frequency from the off-state to On-state and low leakage, with an extremely low queue current. That is why it is recognized as the best devices for high frequency and low power consumption applications. Its structure thus needs to be explained so that one can understand how the entire MOS device operates.

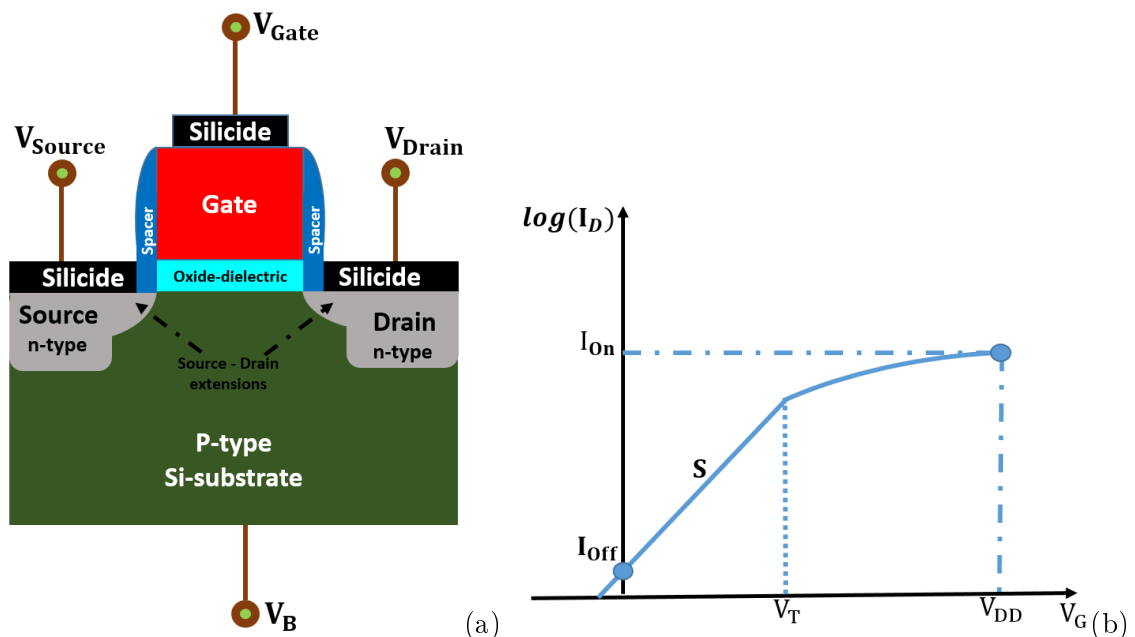


FIGURE 1.3: (a): Schematic description of the a MOSFET transistor, where we can see the three connection pads:  $V_S$ ,  $V_D$ ,  $V_G$ ,  $V_{ground}$ . (b): is the characteristic curve  $I_D = f(V_G)$ .

A MOSFET is constituted of four principle parts: the Source (S), the Drain (D), the gate (G) and the substrate (body). The first three are the mains parts that actively contribute to its operation and the gate is one of the most solicited part of the device. The channel can be assimilated to a corridor delimited by the drain and source. The polarisability of the channel will be defined by those of D and S. If D and S are n-type doped, the channel will take the name n-channel and If D and S are p-type doped, the channel will take the name p-channel. The charge carriers which are controlled from the gate, flow along the channel. The sense of their circulation will depend on both the polarisability of the substrate and the channel, since the sign of the latter also depends on that of D and S. When the substrate is of p-type (p doping) the channel must be of n type (n-channel MOSFET) and when the substrate is of n-type (n doping) the channel have to be of p type. This is important because it is the difference of potential established between the substrate and channel that allows the circulation of charges through the channel and hence generates a current. The graphs of the figure(1.3) present a schematic description of a MOSFET and the  $(I_D, V_G)$  characteristic curve. The dielectric contact between the source and drain is established via a MOS capacitance ( $C_{MOS}$ ) taking its origin on the substrate. The role of  $C_{MOS}$  is to control the formation of the desertion area appearing when the gate is biased.

### Factors limiting the scaling down of MOSFET transistors

Since the invention of integrated circuits in 1958, ten years after the first transistor was jointly created by Shockley, Brattain and Bardeen[4], their sizes have always been in continuous reduction. The famous empiric law predicting the size's miniaturization of these devices was enunciated by Gordon E. Moore in the mid sixties[31] derived from its observations, which stipulates that:

- the number of transistors in the integrated circuits must double every eighteen months
- the size of the integrated circuits in the electronic devices must decreases by a factor of 0.7 every three years

A direct advantage of the size reduction is the increase of the switching frequency of transistors by a factor of about 1.5 and the reduction in power consumption and cost[4]. Figure(1.4) shows the prediction in the evolution of the number of transistors inserted in ICs, which is almost constant since the 2000s. However, one can observe an absence of prediction from 2018. This can probably be justified by the issue encountered with the limitations in size for a simple reason that their allowed physical limits have been reached.

Several factors can explain this. However, we will dwell on the main ones, resulting from the quantum physical concepts, namely the tunneling and quantum confinement.

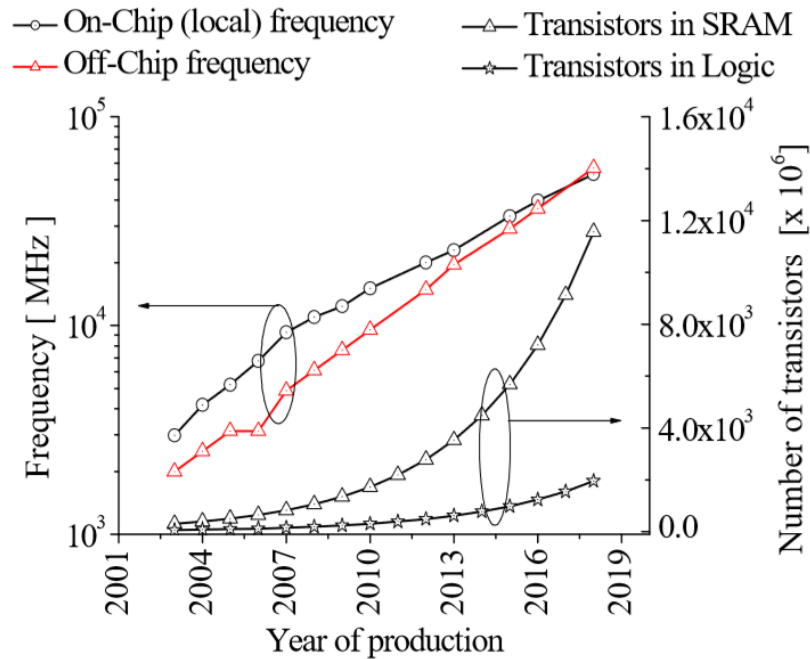


FIGURE 1.4: Evolution of the number of transistors in ICs according to the Moore's law[1] plotted with some of the other parameters key parameters[2, 3].

First of all, scaling is about linearly reducing three major design parameters such as the physical dimensions, the supply voltage ( $V_{DD}$ ) and the implants concentration  $N(\text{at}/\text{cm}^3)$ . When the two firsts parameters decrease by a scaling factor  $k$  (i. e. multiplied by  $1/k$ ), the concentration of implants will have its value augmented by a factor  $k$ . The table(1.1) below gives the relationships between the scaling factor and the transistor parameters to be reduced in constant field (CF) hypothesis[2, 3]. The quantum effects resulting from the miniaturization are due to the fact that the charges do not only behave like particle, but also as waves. This wave-corpussular nature can permit them to cross the potential barrier without any gate voltage influence because they can tunnel through the channel. The tunneling can happen through the border between the gate and the oxide (gate-oxide tunneling), the channel delimited by the drain and the source (source-drain tunneling) and from a band to a band (quantum confinement).

#### The gate-oxide tunneling:

It happens when the thickness of the oxide separating the gate and the substrate is very thin (of the order of  $< 2$  nm). The consequence of this oxide shrinking is the existence of an induced gate leakage current ( $I_g$ ), which increases as  $t_{ox}$  is shrunk. This can be seen on the graph of figure(1.5)(source ITRS 2004 data), which shows the variation of the gate leakage current with respect to the gate length for the 90 nm technological nodes. The increase of  $I_g$  has an exponential tendency. Because when  $l_g$  is inferior to

Physical parameters	Formula	Scaling factor
Dimensions: $W, L, t_{ox}, X_j$ (cm)	-	$1/k$
Chip active area: $A$ (cm <sup>2</sup> )	$W \cdot L$	$1/k^2$
Carriers' concentration: $N_a, N_d$ (ions/cm <sup>3</sup> )	-	$k$
Voltages: $V_{DD}, V_{Treshold}$	-	$1/k$
Normalised current: $I_{ON}$ ( $\mu A/\mu m$ )	-	1
Device's electric field: $E$ (V/cm)	-	1
Power dissipation: $P$ (W)	$V_{DD} \cdot I_{ON}$	$1/k^2$
Power density: $p$ (W/cm <sup>2</sup> )	$V_{DD} \cdot I_{ON}/S$	1
Circuit delay time: $\tau$ (s)	$C_{gate} \cdot V_{DD}/I_{ON}$	$1/k$
Inversion charge density: $Q$	-	1

TABLE 1.1: Scaling rules of the MOSFETs in the CF hypothesis proposed by Dennard in 1974[3]. The parameters  $W, L, C_{ox}$  and  $X_j$  refer to the gate width, gate length, oxide thickness and the junction depth, respectively.  $C_{gate}$  is the gate capacitance per channel.

20 nm,  $l_g$  starts to grow very significantly and the transistor will not be able to resist in high frequency applications. The device's efficiency is unfortunately affected in terms of power consumption.

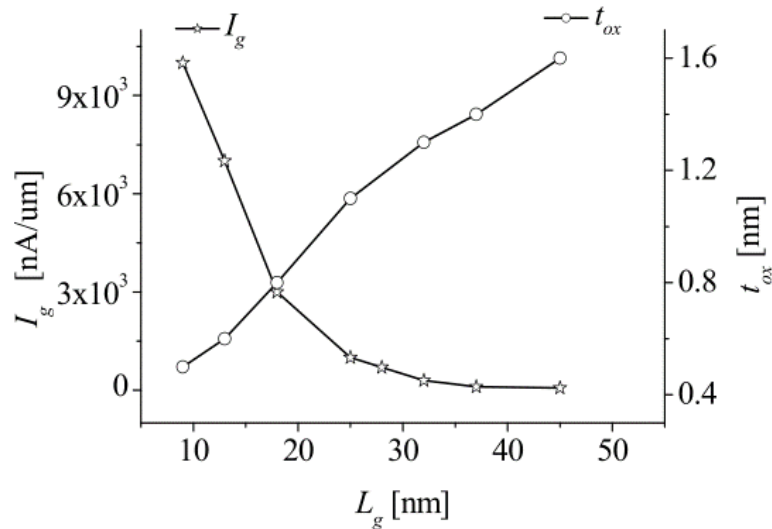


FIGURE 1.5: Evolution with the gate leakage current in function of the gate length . Source: [2] and data from ITRS (2004 update).

source-drain direct tunneling:

The shrinking of the whole transistor's size induces the down scaling of all the dimensions, namely that of the drain and source, hence the channel length. Indeed, when the area of both the source and drain are diminished, the short length of the channel is one of

the reason giving rise to the tunneling phenomena in that region, mostly when the gate length starts to become very short (from less than ten nanometer)[4]. Basically, if the gate length shrinks enough, there will be an overlap between the wave functions of the electrons in the drain and the source. Therefore the probability ( $p$ ) of the electrons' tunneling is large:  $p = \int (\chi_{e,drain} \cdot \chi_{e,source}) dx > 0$  (see figure 1.6).  $\chi_{e,drain}$  and  $\chi_{e,source}$  are the wave functions of the electrons in the drain and source, respectively. The device unexpectedly operates in the subthreshold mode when the leakage current induced by the quantum tunneling through the channel switches-on the transistor. This is not what we observe when the gate length is large, as it was demonstrated by Kauwura et al[38]. He experimentally compared the operations of two devices of lengths  $l_g=58\text{nm}$  and  $8\text{ nm}$  with the temperature and he showed that the drain current leakage significantly augments in the  $8\text{ nm}$  device, even at low temperature. This causes the device to switch on, even at the subthreshold voltage level since the slope is steeper (see the left graph of figure(1.3)). One can thus deduce the effect of a high drain current at the subthreshold level on the curve of figure(1.3(b)).

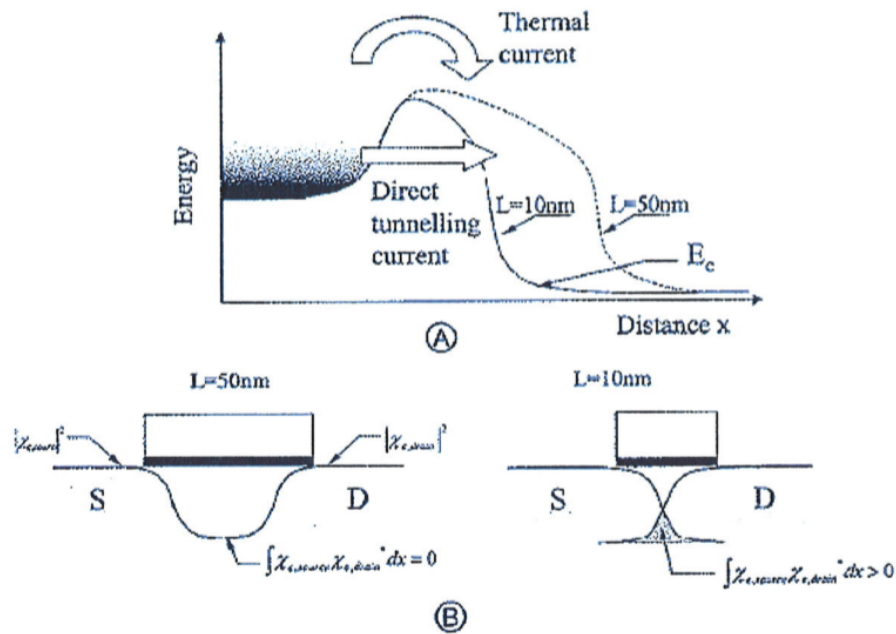


FIGURE 1.6: Short channel effects graphical illustration[4].(a): illustration of the gate length reducing. (b): representation of the non-overlapping (bottom left) and the overlapping (bottom right) wave functions with the associated tunnelling probabilities.

### 1.4.2 The FinFET technology

#### Definitions

A Fin-Field Effect Transistor (FinFET) is a MOS transistor whose, the source-drain region is formed with a silicon bar of nanometric dimensions (nano bar) commonly named as Fin, and the gate can be placed at the two sides or wrapped around that Fin. The first information about the non planar MOS transistors were provided in 1991 in an article jointly published by Toru Kaga, Eiji Takeda and Digh Hisamoto. These types of futurist transistors were known under the name of DELTA transistors[5]. The name 'FinFET' adopted to qualify such categories of non 2D-transistors was announced for the first time in 2001[6] by three researches from Berkeley university: Pr. Chenming HU, Tsu-Jae King-Liu and Jeffrey Bokor. They elaborated a P-type FinFET constituted of a double gate controlling the junction and the current flow. This alternative was undertaken due to the limitations in the scaling of planar MOSFETs beyond  $0.1\mu\text{m}$ , mostly the gate oxide thickness and the source/drain junction depth[39]. The first double gate transistor was elaborated on a SOI material where the active part of the transistor (top silicon) was isolated from the substrate by an oxide, as shown in figure(1.7). With such structure they claimed that the control of the channel will be effective with the help of self alignment of the two gates which reduces the parasitic gate capacitance effects and the series resistances. Also, the short channel effects can significantly be reduced or suppressed with this technology[6]. Nowadays, the non-planar MOSFETs are known under the term 'trigate' instead of double gate because of the exploitation of the three sides of the Silicon Fin on which the gate is built.

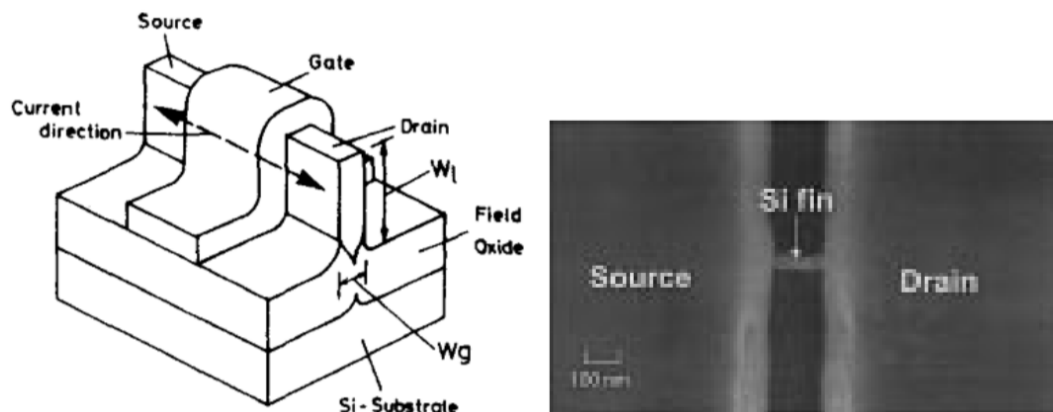


FIGURE 1.7: Left: Image of the first non planar (double Gate or DELTA) transistor[5]. Right: top view SEM image of a FinFET where the drain, source and the channel region are highlighted[6].

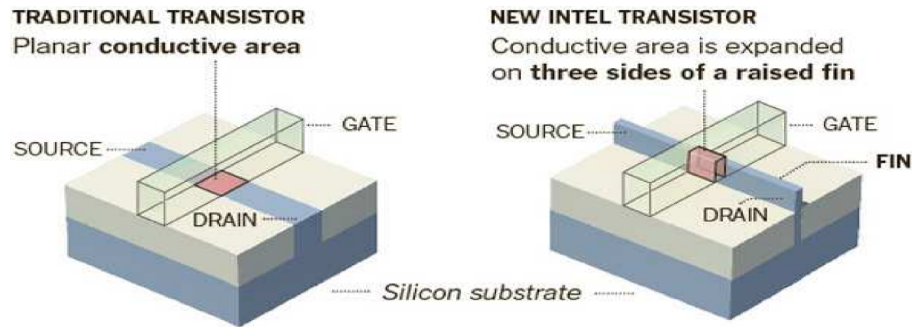


FIGURE 1.8: Comparison of a planar (left) and a trigate (right) transistor (source: Intel)

### Comparison of the performances of MOSFET transistors: planar $V_s$ trigate

The image of figure(1.8) presents an example of a FinFET compared to a planar (2D) MOSFET. If one of the most important performance criteria of the MOSFET devices is the  $I_{on}/I_{off}$  ratio, those which have an almost zero leakage are the most privileged ones. Indeed, the leakage current is related to the presence of an off-current ( $I_{off}$ ) when the device is switched off. From this ratio we can deduce that an important value of  $I_{off}$  will induce high consumptions and increase the delay. Therefore, the impact of the leakage current on the device's operation is a crucial information to obtain. By looking at both images of figure(1.8), theoretically speaking, it is obvious to see that the trigate transistor will presents the larger value of the on state current than that of the planar one. A direct advantage of this is its fast switching from the off-state to on-state, because almost three times the quantity of majority carriers cross the potential barrier lowered by the gate voltage. The delay time for the device's turning off is significantly shortened. An example comparing the delay times of the two different types of transistors for different technological nodes has been provided by Intel[7]. The graph at the right hand side of figure(1.9) shows that the trigate displays a better efficiency even at high operating voltage, than the planar transistor. The reason is that the slope of the ( $I_{ds}$ ,  $V_{gs}$ ) characteristic curve is steeper for the FinFET than that the 2D MOSFET. This second effect displayed at the left hand side of figure(1.9) reveals that the device can operate at lower voltage, and simultaneously presents few leakages at the subthreshold level.

Despite the incredible performances of ICs since the arrival of 3D transistors, however, the problem of leakages and the capacitance effects still remain in FinFETs elaborated on bulk silicon. A very good alternative developed in the microelectronic industry was to separate the top active part of the silicon from the bulk substrate by an intercalated oxide layer. So that the active layer of the transistor (where the gate and the channel are located) is insulated from the substrate by this oxide. This is the characteristics of

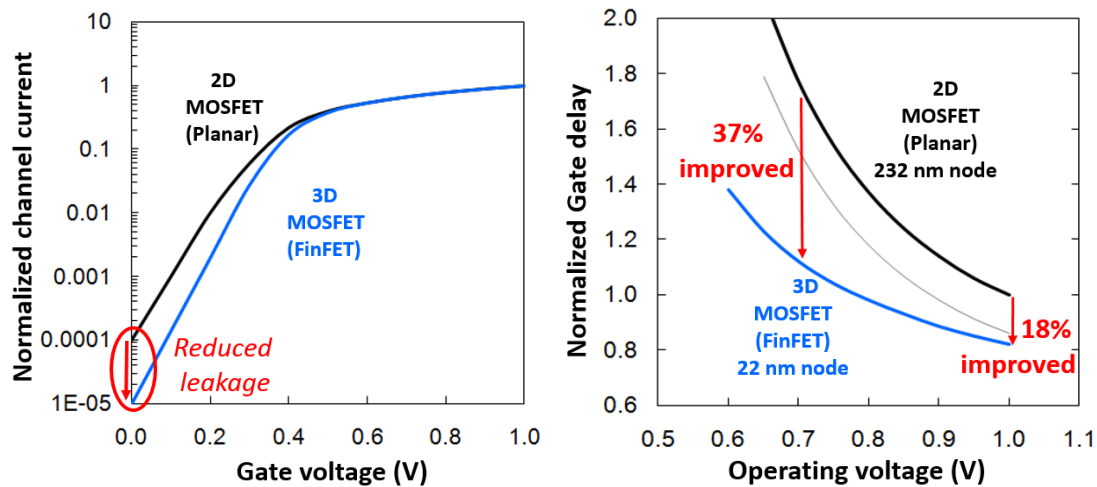


FIGURE 1.9: Comparison of the performances of a planar and a trigate transistor, for two different technological nodes. The left graph compares the leakage currents ( $I_{\text{off}}$ ) and the subthreshold slopes when the devices are in off-state, whereas the right graph compares the delay times in function of the operating voltage[7].

silicon on insulator (SOI) FinFETs. We will present the advantages of the 3D-transistors of this type compared to the 3D bulk FinFETs.

### FinFETs on SOI or FinFETs on bulk Silicon?

Face to the stringent requirements for energy consumption and performances of integrated circuits, in addition to the issues resulting from the limits in the size reduction of MOSFET transistors, it is imperative to find efficient alternatives to resolve these difficulties. This will allow to meet the predictions established by the different roadmaps for the implementation of the "More than Moore" concept. Resolving these crucial problems start by finding the right way of fabricating of 3D transistors, with the adequate technology that will afford the best performances, energy saving and the cost efficiency. In the following lines will present some key element of comparison that play a determinant role in the choice of a technology (SOI or bulk silicon) of the 3D transistor fabrications.

With the aim of comparing the 3D MOS transistors made on SOI materials by the industrials such as STMicroelectronics, IBM, AMD, we have investigated another model built on bulk silicon. It is developed by other industrial pioneers like Intel[7], TSMC Global Foundries for instance. The images of figure(1.10) present the two different technologies: SOI and bulk silicon. The process of fabricating a FinFET on SOI however, is quite different. As shown in the top image of figure(1.10), the etching is performed on the SOI wafer until the buried oxide is reached. Then the obtained Fin is implanted before wrapping the gate around it. In the latter technology however, the Fin is obtained by direct etching of the the bulk silicon, then implanted before mounting an oxide at either

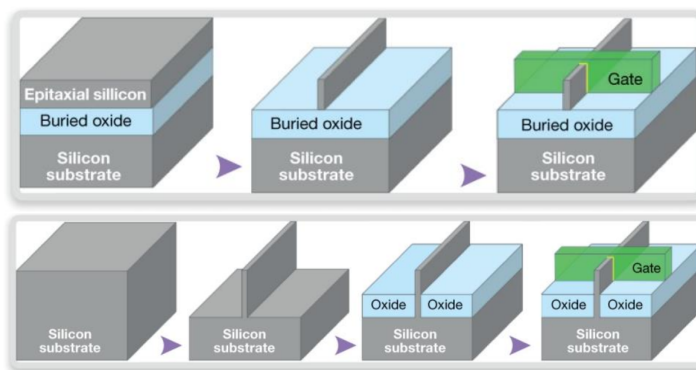


FIGURE 1.10: The images show the different processes of obtaining the three dimensional transistors on bulk silicon and SOI. Top: Fully depleted SOI (FDSOI) technology and Bottom: totally strained silicon technology[8].

sides of the Fin as indicated in the bottom image of figure(1.10). The gate can thus be mounted at the end of the process. Our comparisons will be principally based on the parameters affecting the performances or the power efficiency such as the capacitance effects, body biasing, threshold variability and the temperature effects for instance.

### The capacitance effects in the FinFETs

The problem or the difficulties encountered with the FinFETs on bulk silicon are numerous, as noticed in literature[5, 35, 40]. First, the substrate being directly in contact with the Fin forming the channel, the gate capacitance effects impact on the operation of the FinFET itself. Since the channel is in contact with the substrate (body), the leakages current emanating from the gate and substrate capacitance effects will reduce the charges' flow. This decreases the device's current and voltage gain and augments the power consumption. Let us also present the difficulties related to the short channel effects. As a consequence of the reduction of the channel length, the parasitic currents in the channel generated by the capacitance effects in the substrate exist. They will favour its auto-latch up even when the device is off,. Once again the consumption will peak up and the switching will be perturbed. The hypothesis found by the scientists to interpret these anomalies is that, the device is not completely in its off state because of the fact that the channel, even though narrow, is sharing a same area with the body. Where comes the issues related to the body effects that will be discussed in the next lines. From what precede concerning the consequences related to the capacitance effects, one can postulate that a FinFET which its active part (Fin) is isolated from the substrate (e.g. the FDSOI FinFETs) is spared or less suffer from these anomalies.

## Body biasing and body effects

The second main issue in bulk Si CMOS technology is related to the body biasing effects. They concern all the MOSFETs in general (planar or non-planar). An important fact to highlight is that, the response of FDSOI transistors to these effects are different from that of bulk silicon transistors. Actually, the body biasing is exploited to boost the performances and therefore to reduce the cost. It consists in biasing the substrate in order to establish a channel between the existing source and drain. In that case, the transistor acts as a double opposite gate transistor[40]. The advantage of the body biasing is fully exploited in the FDSOI technology, because the charges' flow through the channel controlled from the buried gate is preserved from the body effects. Therefore more voltage can be applied in the body, which leads to the possibility of dealing with many threshold voltages. The body bias voltage ( $V_{BB}$ ) that can be applied to the body ranges from -0.3 V to 0.3 V (for FDSOI) and the range for bulk technology is ten times lower (-0.3 mV to 0.3 mV) due to the body capacitance effects. This induces an increase in the threshold voltage for the UTBB-FDSOI as presented in the graph of figure(1.11), thereby boosting the current and the performances[9, 40].

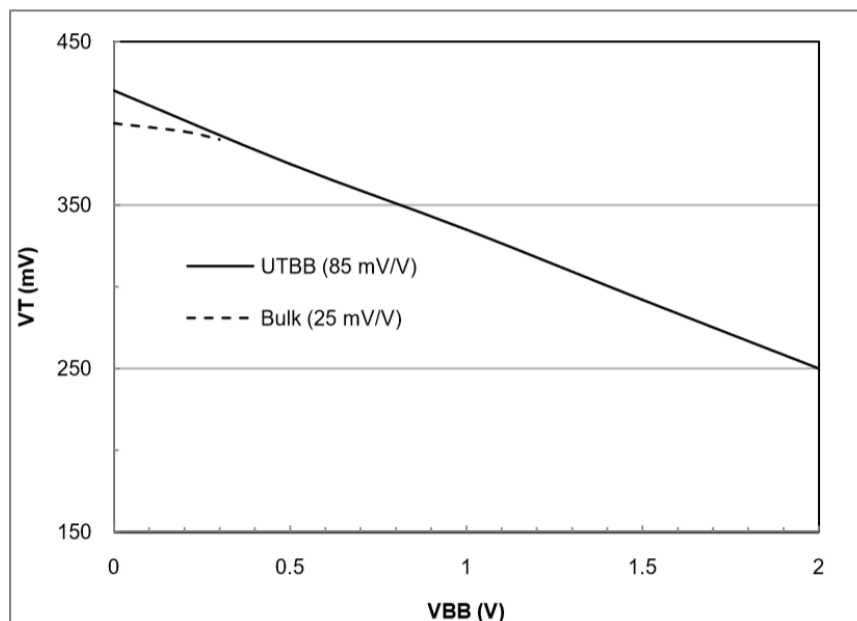


FIGURE 1.11: 28 nm node threshold voltages with respect to the body bias for the UTBB-FDSOI and Bulk[9].

## Threshold voltage variability: $\sigma V_T$

The scaling down of the channel length is very beneficial for the control of the charges' flow from the gate. Even though this appears as an important advantage in the implementation of the future CMOS technology nodes, another direct consequence arises. The

issue related to the reducing of the gate length  $L_g$  is also the threshold voltage variability  $\sigma V_T$ , arising at a certain limit of the silicon thickness  $T_{Si}$ . In the next lines, we will explain what does the threshold variability mean and what causes it. We will first present the situation in the planar bulk and FDSOI CMOS structures before establishing the links with the three dimensional CMOS.

The variability in the bulk MOSFET may arise from the different granularity in the gate and random dopants in the channel[41–43]. It is also reported that the presence of charges in the gate oxide have significant contribution on  $\sigma V_T$ . There is a crucial interest in reducing the voltage variability to benefit from their optimum operation. However, it appears to not be easy in bulk Si MOSFET[44]in contrast to FDSOI MOSFET[41] because of many reasons. In bulk CMOS, the number of dopants in the n-channel ( $N_{dop}$ ) increases nodes after nodes by a factor  $k$ , while the dimensions decrease by  $1/k$ , namely the active width ( $w$ ), gate length ( $L_g$ ) and the effective gate oxide thickness in the inversion regime ( $T_{inv}$ ). The threshold voltage standard deviation  $\sigma V_T$  actually varies as[35]:

$$\sigma V_T \propto T_{inv} \left[ \frac{N_{dop}}{(W \times L_g)^2} \right]^{\frac{1}{4}} \equiv T_{inv} \cdot k^{\frac{1}{4}} \quad (1.1)$$

Equation(1.1) tells that the intrinsic variability in bulk CMOS technology increases by a factor of  $k^{\frac{1}{4}}$  per technological node, which is unacceptable. Therefore a solution to avoid it is to slow down the reduction of  $L_g$  which means to damp the miniaturization. It thus looks that a 'continuous miniaturization' of integrated circuits by only using bulk CMOS technologies seems to be not guaranteed. Since one will have to face many difficulties arising from the electrostatic effects[35].

The FDSOI technology also displays the anomalies due to the threshold voltage variability, but which are less sensitive than in bulk CMOS technology, because one can use a non doped channel. Indeed, The size reduction in planar FDSOI is mostly governed by the thickness of the silicon film  $T_{Si}$  below the gate, in contrast to planar bulk CMOS where it is governed by the doping of the channel. The advantage is the good electrostatic behaviour of the device.

When it comes to 3D CMOS structures like FinFETs, the variability of the threshold voltage depends on the Fin's width  $W$  which induces a supplementary fluctuation. The threshold variability for FinFET will therefore be expressed as[35]:

$$\sigma V_{T,W} \propto \sigma_{Wfin} \left( \frac{dV_T}{dW_{fin}} \right)_{T_{inv}, T_{Si}, V_d} \quad (1.2)$$

The same conclusion will be drawn as we did for planar CMOS in the previous paragraph. The situation for  $\sigma V_{T,W}$  is better for 3D FDSOI structures than bulk Si CMOS because of the non doped channel.

### Temperature effects

The impact of the heat on the operation of a processor using bulk and UTBB-FDSOI FinFETs for the 28 nm technological nodes has been investigated in[10]. The image of figure(1.12) shows that the latter device displays low temperature effects than bulk silicon thanks to the reduced substrate leakage. On the same image, one observes a noticeable discrepancy between both devices in terms of power saving[10, 40].



FIGURE 1.12: A demo of the power and temperature efficiencies of UTBB-FDSOI and bulk FinFETs[10].

After all these comparisons, we would like to say that FinFETs on FDSOI are advantaged for certain relevant field of applications. Their advent have motivated all the actors from the microelectronics industry to think about the development of more and more powerful an smart devices. There is no transistor without doping. Many techniques are employed in the material industry to perform it, such as thermal diffusion, nuclear transmutation, laser doping and ion implantation. According to the technological needs as well as the different fields of applications of the doped materials, one doping technique can be preferred to another one. Even though all of them presenting advantages and drawbacks that are more or less attributed to their respective processes. We will only focus on the last one by presenting the different methods utilized with their respective characteristics.

## 1.5 Ion implantation doping

Nowadays, ion implantation doping is almost the principal technique employed to insert impurity atoms inside the materials. It consists in accelerating ionised atoms at relatively high voltage in order to confer to them a sufficiently high energy generated by an electric field, so that they can penetrate into the target. The doping techniques by ion implantation methods are at the basis of semiconductors' manufacturing. The ions introduced into the material will, depending on their energy, penetrate inside its structure up to a certain depth. During their penetration, they cause several atomic displacements in the crystal lattice of the target. These displacements result from the multiple collisions engaged between the incident ions and the host atoms. The cascade collisions are at the origin of the energy loss phenomena of ions until their final stop within the crystals. In the case of silicon for instance, an incident ions can kick a silicon atom out of its site, which in turn can also move another lattice silicon atom, and so on. These collisions cascade mostly caused by heavy ions ( $As^+$ ,  $Sb^+$ ,  $Xe^+$ ,  $Ge^+$ , etc.) are majoritarily responsible of structural defects in the lattice Si crystal[45, 46]. Indeed, the heavy atoms diffuse into the crystal by simultaneously creating the interstitial-vacancy (I-V) pairs. At a high degree of concentration of point defects, a continuous amorphous zone can form due to the agglomeration of these points defects, since the damaged zone is extended. The extension of that zone may depend on the implantation energy, the nature of the implants and their dose[47].

In the case of light ions such as boron (B) for example, it is not easy to obtain an amorphized zone in the crystal at low implantation energy and low dose because B does not diffuse into silicon in the same way like As for instance. Its diffusion mechanism give rise to the formation of boron-interstitial (B-I) pairs[48, 49]. A pre-amorphisation process is often performed using an atom heavier than boron like fluorine (F) in order to optimize a shallow implantation of B itself. The association of B with F to form molecules such as  $BF_2$  or  $BF_3$  is commonly employed in the semiconductor industry for the obtention of an amorphous layer with boron implanted at shallow depth. Thus, the higher the implantation energy, the larger the penetration of the ions and the extension of the crystal damages. The distribution of the implanted species being a purely random phenomenon, the law predicting the evolution of this distribution is generally the one established by Pearson[50].

### 1.5.1 The conventional ion implantation method

The operating principle of a conventional implanter is described in figure(1.13). The species to be implanted are produced by a source from gaseous compounds or metal

elements, introduced into an ionization chamber under vacuum then brought to a very high temperature. When leaving the chamber at an ionized state, the ions are accelerated at high energy (generally between 10 and 500 keV). A magnetic field deflector is employed to select only the ions of interest based on the mass analysis principle. The lateral dimensions of the ion beam to be implanted are defined by the size of the orifice placed at the outlet of the magnet. The beam is in turn guided and aligned by a set of collimators, then focused onto the sample (wafer) by a couple of electrostatic lenses. As a result of the interaction between the incident ions and the atoms of the target material, multiple collisions occur. This is at the origin of the energy loss phenomena experienced by the dopants as they penetrate the material and cause damages into its crystal structure. The undesirable species are magnetically deflected towards another direction. The trajectories are randomly distributed and the in-depth distribution of the implanted species follows a nearly Gaussian profile according to the nature of the implanted ions. As a consequence, it is preferable to define an average penetration known as 'projected range ( $R_p$ )', with a standard deviation  $\delta R_p$  (see Figure(1.14)[11]). The principal theoretical concept employed to interpret the energy loss phenomena of the ions inside the structure is given by the Lindhard Scharff Schiott (LSS) theory[51]. The LSS theory stipulate that the energy losses experienced by the ions are essentially due to two principle phenomena: the multiple collisions between ions and the target atoms (nuclear losses), then the collisions with the electron cloud (electron losses).

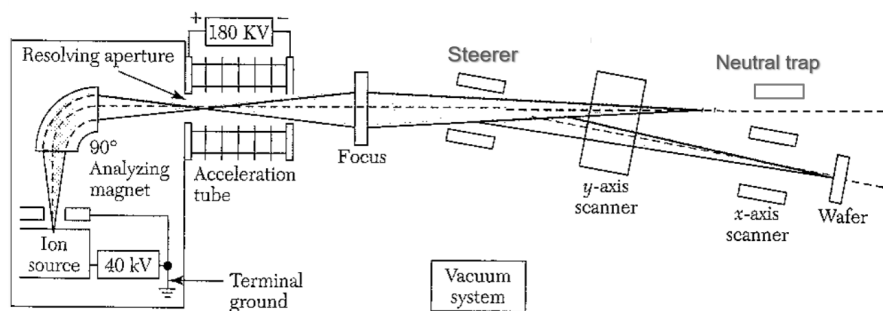


FIGURE 1.13: Schematic principle of a classical implanter.

The nuclear losses  $\left(\frac{dE}{dx}\right)_n$  are at the origin of the damages generated after the target atoms have been displaced from their lattice sites, and the electron losses  $\left(\frac{dE}{dx}\right)_e$  are responsible of the distributions of the ionized atoms. The latter can be computed using the standard tables available in the literature or by using TRIM simulations[25]. The energy range(50 keV to 500 keV) employed in the ion implantation domains being not too large (limited to an appropriate range to preserve the material properties as much as possible), the losses

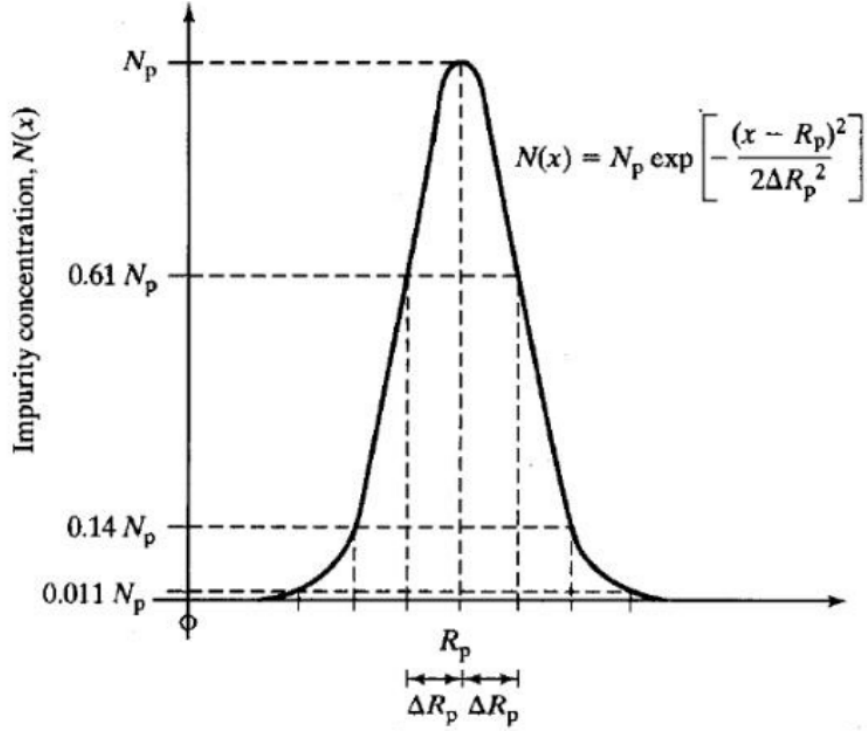


FIGURE 1.14: Dopants concentration profile obtained with the conventional implantation method[11].

due to nuclear collisions are usually negligible. Therefore, the energy losses experienced by the ions in the field of ion implantations are essentially due to electron collisions. The computation of the energy and range of an ion colliding with a host atom at rest during the implantation can be approached by using the formulae provided by the LSS theory[51], where two dimensionless variables ( $\varepsilon$  and  $\rho$ ) are introduced:

$$\varepsilon = E \frac{aA_2}{Z_1 Z_2 e^2 (A_1 + A_2)}$$

$$\rho = RN A_2 4\pi a^2 \frac{A_1}{(A_1 + A_2)^2}$$

$R$  is a path variable and  $E$  is an energy variable.  $N$  is the number of atoms per unit volume;  $A_1$  and  $A_2$  are the atomic masses of the incident ions and atoms of the material under doping, respectively.  $Z_1$  and  $Z_2$  are the atomic numbers of the incident ions and the target material, respectively.  $e^2$  being the elementary charge;  $a = a_0 \times 0.8853 \left( Z_1^{2/3} + Z_2^{2/3} \right)^{-1/2}$  is the screen length,  $a_0 = 0.529 \text{ \AA}$  the Bohr radius and the value 0.8853 is the Thomas Fermi constant.

There are many parameters influencing the implantation profile in this method. One has the twist angle defined by the rotation of the sample with respect to the horizontal plane of the sample holder (figure(1.13)). A tilt angle can be defined between the sample

normal and the beam if one would like to implant in inclined incidence. Both angles will have an important impact on the penetration depth of the implants, according to their nature and their energies, but also on the doping conformity. One of the main advantages of the conventional method is the control of the doping profile. This is possible thanks to the correct dose control and mass selectivity of the elements to implant. The advantage we just mentioned is fundamental for obtaining a good doping quality. This method affords a better amorphization rate of the implanted area according to the type of dopants, which is important for the recrystallization by rapid thermal processes (RTP) or high temperature annealings. One could also add the conservation of the properties of the substrate, a high solubility.

However, there are limits with this implantation method regarding the non-planar surfaces. The main issue is that this method requires a surface perpendicular to the ion beam. Consequently, the samples of non-regular geometry such as the 3D Fin-shaped structures or nanowires are not easily processable. Unless it is done in several steps, which increases the production costs and additional damages due to several repetitions of the process. Finally, given the constraints imposed by the structures of smaller dimensions such as FinFETs, it is imperative to implement the implantations at very shallow depths, in only one step, with very low damaging impacts. Hence the need of adopting another ion implantation method that can best meet all these requirements, like plasma immersion ion (PIII).

### 1.5.2 Plasma immersion ion implantation (PIII)

The plasma immersion implantation method uses a source in pulsed mode, emitting the ions at extremely short time intervals. This has the advantage of limiting the heating of the sample under implantation. Also, the advantage one can draw from the PIII method is that it can be used to perform implantations in the samples of non-regular geometries such as those we have mentioned above in only a single step. This is achievable thanks to its multidirectional character. Further more, it also affords implantation capabilities at very shallow depths, even at high energies and doses. The operating principle of a plasma implanter is as described by the diagram of figure(1.15).

The species to be implanted are emitted from a source in quartz. They are introduced in a chamber in which the sample (wafer) is immersed, as shown in the example of the figure. The plasma in question is obtained by introducing a precursor gas in the source, then by adjusting the correct pressure inside the chamber through the valve. The ionization of the gas is performed when the coil is on, so that a current can flow and start the RF generator which in turn, generates an energy that ionizes the atoms of the gas. The sample is mounted on a chuck which is negatively biased so that the potential

difference established between the positively charged ions and this one can attract them to penetrate into the sample. The species fall vertically onto the sample, but may have different trajectories during their travel between the source and the sample. Although we may have a selection of charges in this method, we do not have a mass selection of ions. The lack of mass selection is the main drawback of the PIII method. In order to ensure a good uniformity of implantation, the surface of the sample is scanned by the beam, by slowly moving the sample holder (chuck).

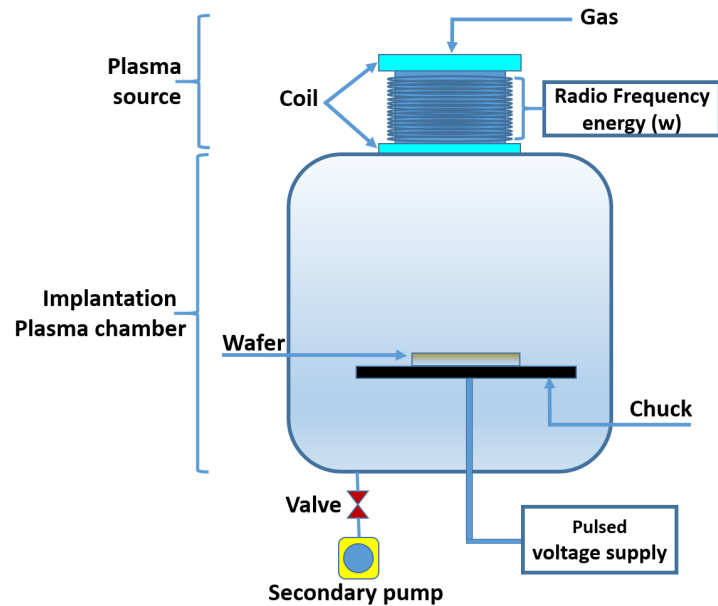


FIGURE 1.15: Schematic diagram describing the ion implantation method by plasma immersion in pulsed mode. This drawing was inspired from [12]

### Plasma parameters for ion implantation

In order to understand the issues related of the plasma implantation and to understand where the contaminants come from, we need to describe what are the parameters constituting the plasma. First of all, before the ions start to penetrate into the sample, the chuck first needs to be negatively biased. Therefore, the impurities potentially contained in the chuck will obviously implant in the sample. This is probably the first source of contamination during the implantation with this method, because it has been reported in [47] that the sample holder itself generates contaminants. Then, when the potential difference is established between the chuck and the ions, all the positively charged ions, including the non-solicited species are introduced into the sample. This is the second source of contamination. The graph of figure(1.16) highlights the operation cycles of the plasma implanter [12].

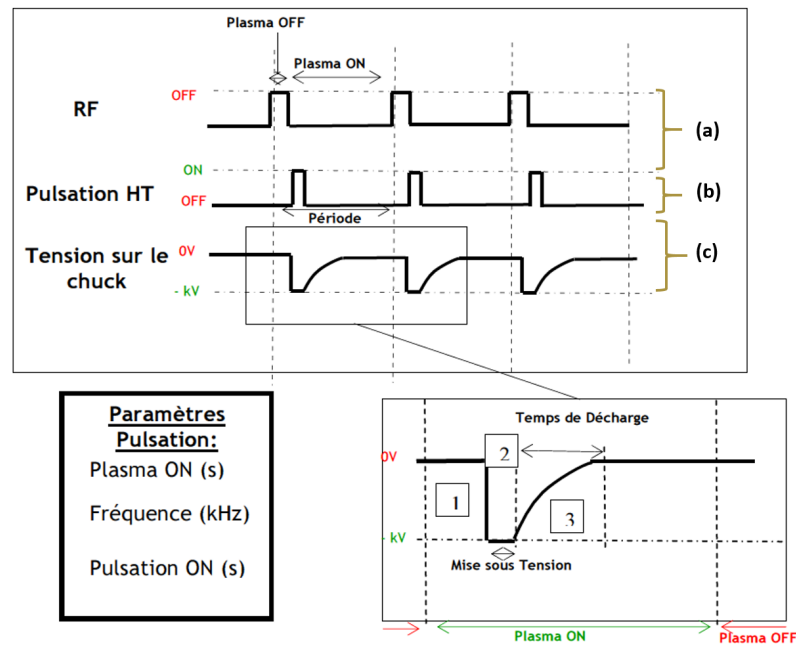


FIGURE 1.16: Schematic of the main signal's chronogrammes controlling the implantation in pulsion mode.

The RF generator that serves to ionise the ions is powered on, then it starts to emit pulsed signals (a) in short time intervals: the plasma is already created in the quartz source. An impulsion of the signal is emitted in the chuck (c) after the pulsed high power supply (b) is on. After the negative biasing of the sample holder, the implants start to flow and penetrate into the sample, because of the electric field. This last step can be divided into three other sub-steps: 1, 2 and 3 as displayed in diagram (c). The sub-step '1' shows that there is no signal onto the sample holder when the plasma is still under creation. As specified in the sub-step '2', the implantation begins when the chuck receives a negative voltage. Normally, at the end of a pulse in the high voltage supply, the signal in the chuck should instantaneously go to zero. However, it appears that the signal is delayed for a certain period of time as shown in the sub-step '3'. In this case, there are still some positive charges penetrating the sample, but with different energies. We think that this may be responsible or has an impact on the implantation profile in the pulsed plasma method, which is completely different from that obtained with the conventional implantation method. The fluence of the implants will depend on the exposure time of the wafer under the beam.

As a resume of this part, we need to bear in mind that the main issues generally encountered with the conventional beam line method is its limits to perform ultra shallow dopings, i.e. at energies less than 1 keV which is the main tendencies for the elaboration of USJs. Fortunately, the PIII method affords such performance, but it still suffers from the multi energy and multi elementary doping. Nevertheless it is the preferable alternative to the previous method since one can easily achieve a conformal doping,

even though progress still need to be made in order to improve this promising method. Given that the development of CMOS transistors is nowadays monitored by the design of devices of infinitely small dimensions and with non-simple geometries such as FinFETs, it is therefore essential to implement shallow implantations whatever the dose or the energies. One of the ideal and compatible structures made of silicon that can permit to reach such doping scale are elaborated on silicon on insulator (SOI) wafers. The devices built on SOI materials are supposed to have better performances because of the good isolation from the bulk. This does not stop us from saying that their successful operations first rely on the good characterization of their doping levels, which is the key issue to solve. Indeed, the 3D devices such as FinFETs are tricky to investigate, mostly when to it comes to count the number of dopants implanted within their structures. Their ultra-thin size requires state-of-the-art techniques.

## 1.6 Quantification methods of 3D doping in the FinFET-like structures

Nowadays, there exist many experimental techniques, which satisfy the requirements imposed by the structures of 3D architectures. But sometimes it lacks methodologies to extract the targeted information. Thereby making the quantification to become more and more challenging. Among many of these techniques and analysis methods including experimental and modeling, some of them were chosen in order to present their capabilities and limits in providing the expected information concerning the 3D doping. In the following line, three main techniques will be presented in comparison with the one (MEIS) chosen to investigate the samples studied in this project.

### 1.6.1 Scanning Spreading Resistance Microscopy

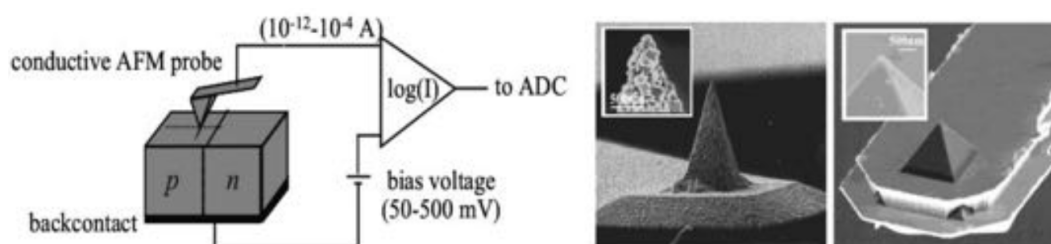


FIGURE 1.17: Schematic showing the measurement principle of SSRM (left). The probe is visible in the right image acquired by scanning electron microscopy (SEM)[13].

The scanning spreading resistance microscopy (SSRM) is a technique that was conceived by W. Vandervorst et al.[52–54] at IMEC and jointly developed with Peter De Wolf during

his Ph.D works. It consists in determining the spreading resistance  $R_{SR}$  established during the contact between a probe of radius ' $a$ ', and a doped semi-infinite sample of density  $\rho$ . However, the method to approach the real value of  $R_{SR}$  is to include a correction factor that in turn, takes into consideration the reality vis a vis of the environment defined at the contact point between the sample and the probe. Namely, the geometry of the probe and the non-uniformity of the doping of the sample. The formula regrouping all these parameters are provided in equation(1.3). From the value of the determined resistance one can thus get access to the carriers' concentration and plot their depth profiles.

$$R_{SR} = \frac{\rho}{Ra} \times CF(\rho a) \quad (1.3)$$

In order to explain the principle of SSRM, let us start by describing the scanning resistance probe (SRP) method, which is the precursor of SSRM [55–57]. In SRP, two probes of radius 0.01 mm are in contact with the extreme surface of the sample. Then the current of the probe is measured when a voltage about ( $\pm 50$  mV to  $\pm 500$  mV) is applied between the sample and the probe. The  $R_{SR}$  is thus determined when the probes exert a large force onto the sample. Otherwise (in the case when the action of the probes is not strong enough) the value of the measured resistance is just local. In SSRM however, only one thin probe of radius in the order of nm (see figure(1.17)) mounted on an atomic force microscopy (AFM) system from which it is brought into contact with the sample. The spreading resistance is now determined by measuring the current ( $\sim 10$  pA to 0.1 mA) with a logarithmic amplifier. In addition to the only one probe used in SSRM, the spatial resolution is by far improved compared to that in SRP since the dimension of the probe is roughly 1000 times smaller, thereby improving its measurement capabilities.

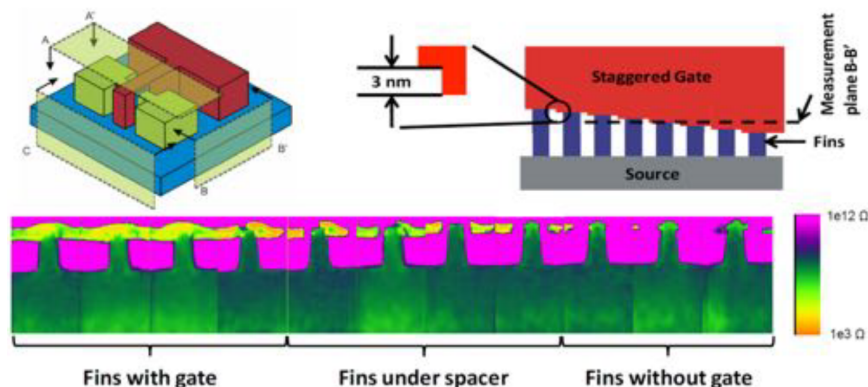


FIGURE 1.18: Top-left: Schematic drawing of a FinFET device, top-right: top view of a test area design with multiple fins capped by a staggered gate. Bottom: example to the SSRM images along the measurement plane [14, 15].

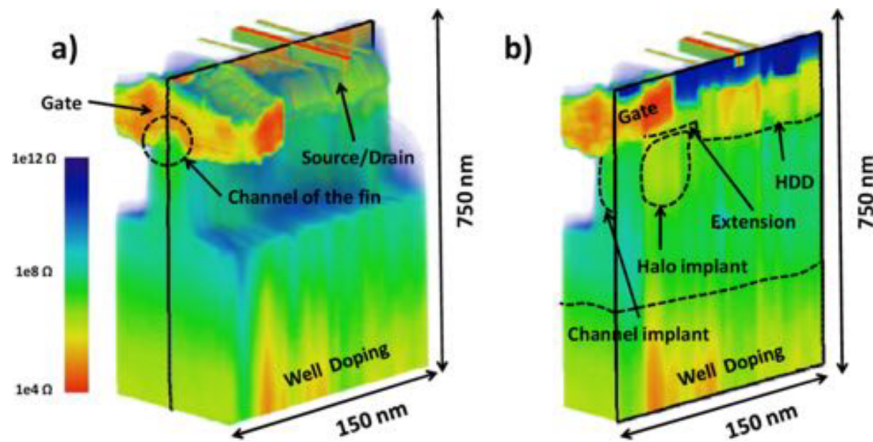


FIGURE 1.19: SSRM images obtained by reconstruction of multiple-fin scans of the gate and source/drain regions of a bulk finFET. They show the well, channel, halo, extension and contact heavily-doped drain (HDD) regions[14, 15].

From the definition and its principle, one understands that the accessible information in SSRM are purely electrical. It can produce the 3D map of the dopants' distribution and the concentration profiles of the charge carriers in the Fin-shaped patterns. The examples are shown in figures (1.18 & 1.19)[14, 15]. Indeed, the resistance levels in the 3D structure are sampled outside and inside the gate area. The resultant map of the doping levels is then obtained by reconstructing the images of all the scans. The depth profiles of the carriers' concentration in the 3D structure can be extracted from the mapping of the doping levels. This analysis is limited by its non-capability of determining the nature of the dopants, which affects the quantitativity. The outcomes of the measurements may be altered by the surface conditions such as the presence of a surface oxide. Therefore, the environment where the analyses take place should be well adapted. This technique can be associated to another one which is capable to provide information about the elementary composition, by identifying the nature of the dopants for instance.

### 1.6.2 Atom Probe Tomography

The principle of the atom probe tomography (APT) relies on the field evaporation of the atoms at the surface of the sample, and the elemental identification of the ions evaporated by the field through a mass spectrometer[16]. The sample hosting the region of interest (ROI) is a sharp cone-shaped needle of radius  $R \sim 50$  nm, obtained in general after a preparation by focused ion beam (FIB). A descriptive image is provided in figure (1.20)[16]. When the sample is under a sufficiently intense electric field  $E$  inversely proportional to its radius ( $E = \frac{V}{\beta R}$ ) where  $\beta$  is the field factor, the atoms are evaporated from its extreme surface and a 2D detector can record their coordinates and analyze

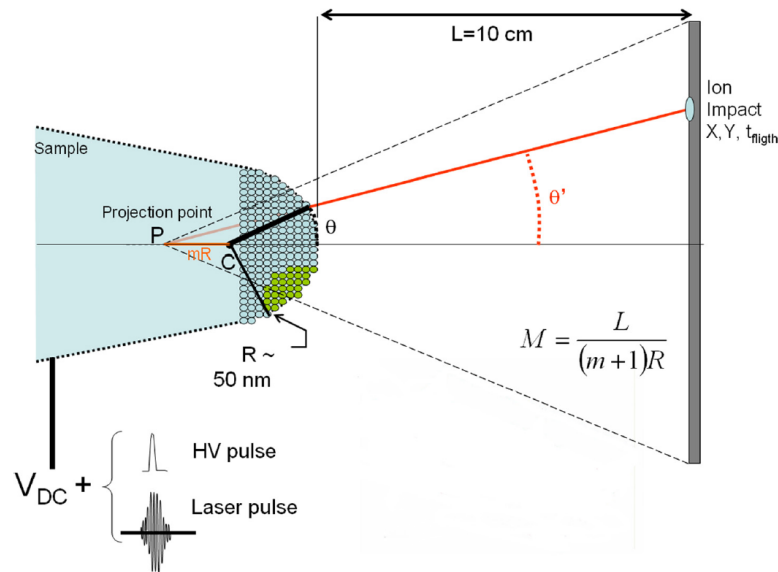


FIGURE 1.20: Schematic principle of atom probe tomography.  $M$ ,  $L$  and  $R$  are the magnification, path length and radius of the tip, respectively.  $(x, y)$  are the position coordinates of the atoms at the sample surface, derived from the coordinates of the ion impacts on the detector. The magnification is defined as  $x = X/M$  &  $y = Y/M$ [16].

their mass individually through the spectrometer. The images that forms on the screen with atomic resolution is the one of the evaporated surface.

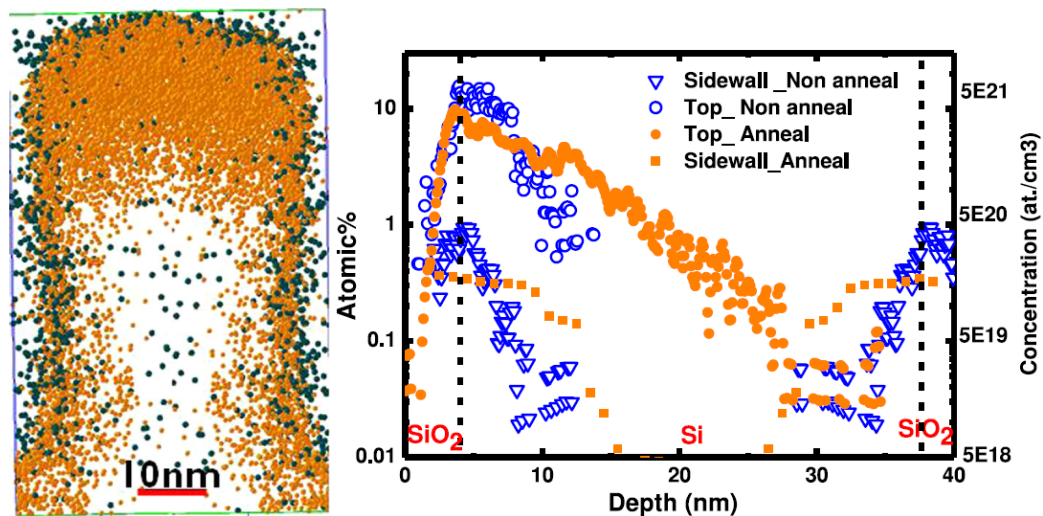


FIGURE 1.21: Left: mapping of the arsenic distribution (orange) in the silicon patterns (tops and sidewalls). The green points represent the oxide, the data corresponding to the silicon are not included. Right: comparison of the arsenic profiles measured by APT in the tops and bottoms of the patterns[17].

The strength of APT lies on its capability to measure the 3D distribution of the dopants implanted into a 3D volume, with a sub-nanometric depth resolution. At this scale it is one of the techniques of choice for the 14 nm technological nodes and below[16]. This technique possesses a high sensitivity to a wide range of elements, mostly light dopants such as boron, which is important for the p-type doping. The accessible information is

the concentration profile of the dopants as illustrated in figure (1.20)[17]. In APT, the quality of the outcomes depends on the quality of the sample preparation, which is the more critical step. The local dosage per surface unit is not easy to obtain, the effects such as clustering mostly in the case of boron and the low lateral resolution emanating from the field effects are among the phenomena that can perturb the outcomes.

### 1.6.3 1.5D SIMS

We are not going to detail the secondary ion mass spectrometry (SIMS) technique here because further descriptions are provided in the second chapter. This part focus on what information one can extract from the analyses of the doping into 3D Fin-Shaped structures by using SIMS. After that, they will be compared to those that can be obtained with the above presented techniques. Longly utilized to probe the dopants introduced into the bi-dimensional (2D) semiconducting thin films, SIMS is well known for its good depth resolution, precision and sensitivity [18, 58, 59]. The introduction of 3D or non – planar structures in the microelectronic world imposes a huge challenge to all the characterization techniques, precisely to SIMS. The problem in analyzing 3D structures with this technique is that, the distribution of the dopants and their profiles become very shape and dimensions dependent[18]. Therefore, there is an urgent need of finding new methodologies to analyze 3D structures with SIMS, because the one used for the analysis of 2D structures ceases to be efficient. This is first due to the limited spatial resolution of the beam relatively to non-planar architectures, but also to the fact that the concentration comes from all the parts. Because of these difficulties, a method to characterize 3D patterned samples with SIMS has been implemented.

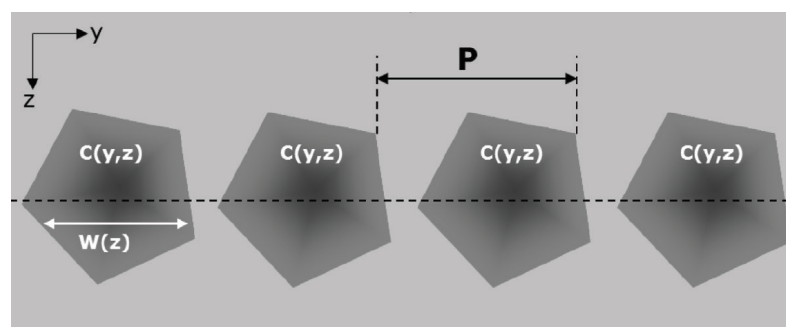


FIGURE 1.22: Representation of an array of objects with composition  $C$ , width  $W$ , and pitch  $P$  for SIMS measurements. The incident primary beam is parallel to the  $z$  direction[18].

1.5D SIMS is a method developed at IMEC for analyzing the non-planar devices with SIMS. It is capable to provide information in the transistor scale. Its principle relies on the change of the concentration at each level in the nanostructure, so as to trace the profile of the implants, as well as those of the associated chemical elements of the matrix. At a

position or coordinates within the matrix where there are no signal for a given element, the corresponding concentration just drop to zero. To illustrate this, let a 3D structure like the one in figure (1.22) constituted of the patterns which their shapes are distributed along the horizontal direction. If  $p$  is the distance between two consecutives patterns, the sputtering intensity  $I(z)$  will be influenced by the dimensions of the patterns (pitch ( $p$ ), width ( $w$ ), height ( $h$ )), but also by the variation of the concentration with respect to the depth  $z$ . The expression of the average concentration corresponding to this intensity is given by equation (1.4).

$$\langle C \rangle_y(z) = \frac{RSF}{I_m} \frac{I(z)}{w(z)} p \quad ; \quad \text{with} \quad RSF = C_0 \frac{I_m^0}{I_0} \quad (1.4)$$

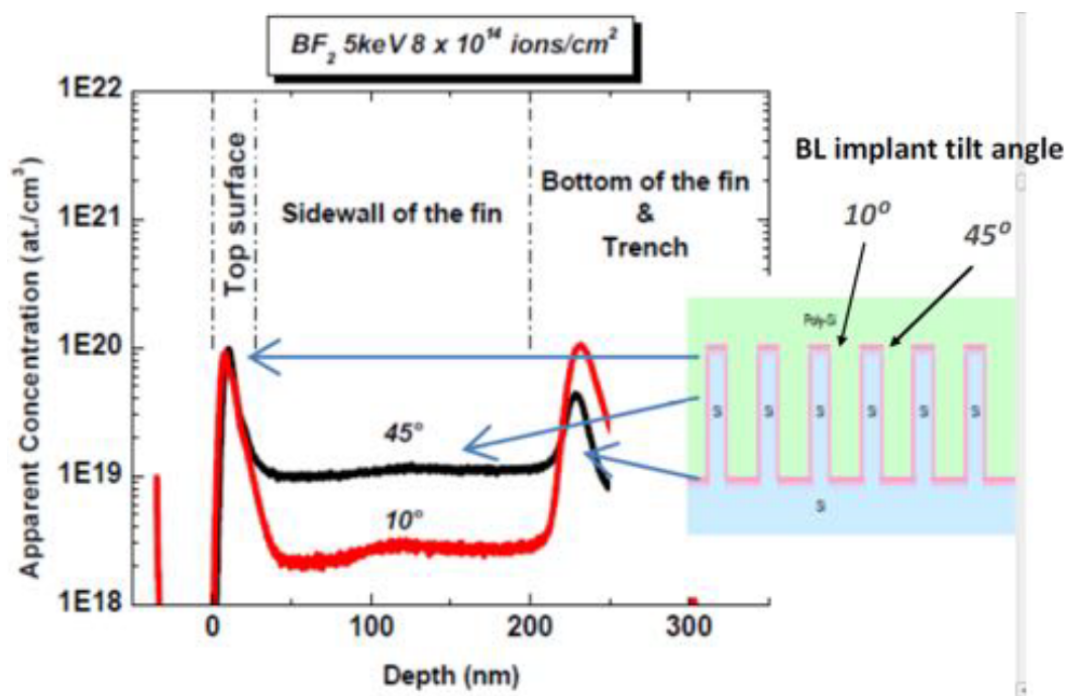


FIGURE 1.23: Results of the 1.5-D SIMS analyses carried out on the patterned structures (right) with different tilt angles[19].

As observed in this equation, the quantification in 1.5D SIMS depends on a relative sensitive factor (RSF) measured from a reference standard. Let us consider a concrete situation concerning the case of the Fins implanted with  $\text{BF}_2$  for example. Figure (1.23) illustrates the good sensitiveness in profiling light elements such as boron. The concentration profile is strongly influenced by the dimensions and the shape of the patterns, which make the extraction of the quantity of dopants in each part (tops, sidewalls and bottoms) very difficult. The SIMS experimental results obtained on 3D structures rely on a very good sample preparation. Indeed, the image of the sample in figure (1.23) shows that the patterns were encapsulated with polysilicon and the extremity was smoothed to obtain a flat surface. The encapsulation allows to have better profiles of the dopants

located at each part by avoiding their overlapping due to the altitude ( $z$ ) effects in patterns. The geometry of the measurements also influences the profile, more importantly in the parts difficultly accessible by the primary beam. Because it is observed how the intensity of the sidewalls varies with the incidence angle of the primary ions. With all these constraints related to the SIMS measurements, if one needs an accurate quantification so as to determine the correct profile in each parts for instance. Sophisticated developments are required as discussed in [18]. We have chosen to compare the advantages as well as the limits of all the above presented techniques with those of medium energy ion scattering (MEIS) in table(1.2). The quantification of the dopants in the 3D structures is a complex issue. None of the presented techniques permits to obtain the local number of atoms in each part, except MEIS. Which are important information to have. Because of this aptitude to compositionally analyze the doping of nanostructures, the MEIS technique has thus been chosen to investigate the 3D doping into the patterned samples as described in section(1.7).

Techniques	Characteristics	
	Strength	Limiting factors
Scanning Spreading resistance microscopy (SSRM)	<ul style="list-style-type: none"> <li>• 2D materials</li> <li>• Doping levels</li> <li>• Concentration profile</li> <li>• Electrical information (activation)</li> <li>• Spatial resolution (20 nm)</li> </ul>	<ul style="list-style-type: none"> <li>- Non easy quantification</li> <li>- Need reference sample</li> <li>- Nature of dopants</li> <li>- Atomic positions / Locations</li> <li>- Dopants distributions</li> <li>- Sample's architecture</li> <li>- Sample preparation (possible)</li> <li>- Back (sample) contact</li> </ul>
Atom Probe Tomography (APT)	<ul style="list-style-type: none"> <li>• Depth resolution (&lt;1 nm)</li> <li>• concentration profiles</li> <li>• Average quantification</li> <li>• Sensitivity to all elements</li> <li>• Conformity</li> <li>• No reference sample</li> </ul>	<ul style="list-style-type: none"> <li>- Sample preparation</li> <li>- Clustering (e.g. Boron)</li> <li>- Lateral resolution due to field effects</li> <li>- Dose in (<math>\text{at}/\text{cm}^2</math>)</li> <li>- Atom location</li> </ul>
1.5D Secondary Ion Mass Spectrometry (1.5D SIMS)	<ul style="list-style-type: none"> <li>• Sensitivity to all elements</li> <li>• Detection limit</li> <li>• Depth resolution</li> <li>• Concentration profile</li> </ul>	<ul style="list-style-type: none"> <li>- Sample preparation</li> <li>- Influence of the sample's architecture</li> <li>- Quantification in 3D sample</li> <li>- Reference sample</li> <li>- Dopant distributions</li> </ul>
Medium Energy Ion Scattering (MEIS)	<ul style="list-style-type: none"> <li>• Depth resolution ()</li> <li>• Local quantification in (<math>\text{at}/\text{cm}^2</math>)</li> <li>• Dopants distribution</li> <li>• Conformity</li> <li>• No sample preparation</li> <li>• No reference sample</li> <li>• Damages (2D architectures)</li> </ul>	<ul style="list-style-type: none"> <li>- Lateral resolution</li> <li>- Sample's architecture</li> <li>- Need accurate protocol</li> <li>- Non sensitivity to light elements</li> <li>- Dopants levels</li> <li>- Electrical information</li> </ul>

TABLE 1.2: Overview of the capacities of the above presented techniques regarding the characterization of 3D doping.

Samples	Implantation	Species	Energy (keV)	Dose (at/cm <sup>2</sup> )	Temperature (°C)
S1	Implanter	As	3	2 x 5,00E14	RT
S2	Plasma	AsH <sub>3</sub>	3	5,00E15	RT
S3	Plasma	AsH <sub>3</sub>	3	5,00E15	400

TABLE 1.3: Part of the samples studied in this work labeled as S1, S2 and S3. The implantation methods as well as the parameters are indicated in each column. As indicated in the table, plasma refers to the PIII method which was employed in pulsed mode.

## 1.7 Sample descriptions

The samples studied in this work were obtained on wafers of SOI types. Initially, the 300 mm diameter SOI wafers were fabricated by using the Smart Cut technology[33]. The structure consists of a stack of a Si film (60 nm) + SiO<sub>2</sub>(25 nm) over a Si(001) substrate. The crystal of the top Si film is initially non strained before any process. There are two categories of the FDSOI samples investigated in the framework of this thesis. The first one is constituted of ultra thin layers (bidimensionnal (2D) or full sheets), i.e., they are non etched. The samples of the second category represent the model systems adopted to investigate the 3D conventional and plasma doping by using MEIS principally, but other measurement techniques as well. They were etched by electron beam (e-beam) lithography in the clean room of CEA-Leti-MINATEC. The etching permitted to form patterns constituted of 3D rectangular lines of nanometric dimensions. They are periodically separated by a pitch of  $\sim 160$  nm, while the distance separating two consecutive Fins, named as the inter-Fin, is about hundreds of nanometers according to the Fins' width. The pitch is an important parameter for not only the process, but also for the theoretical computations before the measurements. The finishing at the Box leads to the height of about 60 nm. A secondary electron microscopy (SEM) image of the patterns obtained after the etching are presented in figure(1.24).

After the lythography processes, the ion implantations were then performed by using the two methods presented in the previous paragraphs and two different temperatures. The other parameters characterising the sample of each group (2D and 3D) are indicated in table(1.3). There are two additional parameters in the conventional implantation method: the tilt and the twist angles. The former refers to the angle between the incident ion beam during the implantation and the wafer's surface normal. The latter represents the rotation angle of the wafer after one implantation step of  $5.10^{14}$  (at/cm<sup>2</sup>) has been completed so that  $2 \times 5.10^{14}$  (at/cm<sup>2</sup>) =  $1.10^{15}$  (at/cm<sup>2</sup>). The targeted dose during the implantation of each sample is also indicated in the table.

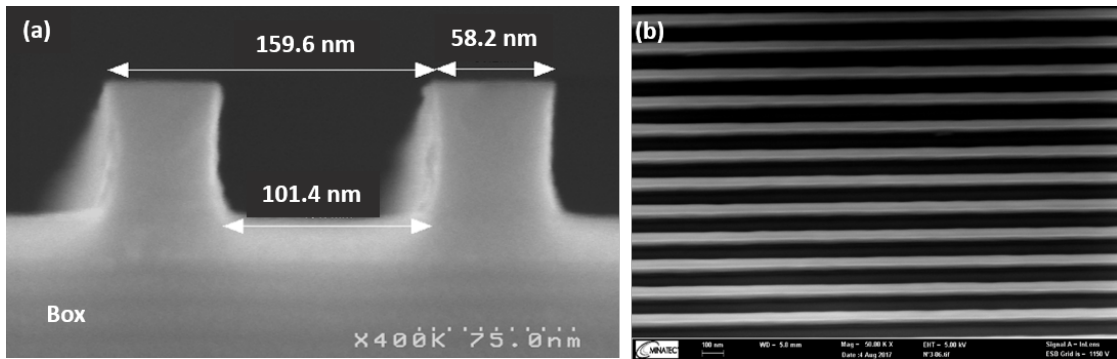


FIGURE 1.24: Secondary Electron Microscopy (SEM) image measured on an etched sample showing the 3D silicon Fins in profile (a) and top (b) views.

## 1.8 Conclusion

We have presented the technological context of this project in the first section. It partially recalls the steps illustrating the evolution of the MOS transistors. Knowing that they are by far better than the BJTs for low power electronics and high frequency applications, we have tried to highlight the advantages and the factors limiting their down-scaling. The reason justifying the miniaturization is that, the future technological nodes ( $< 10$  nm) require very stringent norms in terms of energy consumption and high performance ICs. There are many approaches undertaken to circumvent these issues. One of the most promising which is currently under intense developments, is the concept about 3D Fin-shaped field effect transistor (FinFET). Even at this level, the opinions about the elaboration methods and performances diverge. If some tech-giants like Intel claim that bulk-Si FinFETs are better than those built on SOI materials, which are the types of structures developed by CEA-Tech (Leti) and IBM, the SOI community is claiming the contrary. As shown by the investigations of this chapter, the fully depleted SOI nanostructures seem to afford better performances than the bulk-Si technology. Hence our interest for their study. One of the crucial stage in the fabrication process of SC devices being the doping, we discussed about each method employed in the ion implantation technique. The choice to focus on this technique has been justified by the advantages it affords, in comparison to the others. The samples that we have analyzed in this project are of non-etched and 3D types. We did not work on FinFETs really speaking, but on the FinFET-like models constituted of Fin-shaped line gratings. The goal being to bring our contribution in the resolving of the crucial issue related to 3D doping. Some elements related to their implantation are provided in table(1.3). The importance of the different characterization techniques that were employed is to quantify the dopants, determine their in-depth extensions and study the damages they generated. All these experimental techniques will be detailed in chapter 2.

## Chapter 2

# Experimental techniques

### 2.1 Introduction

In this chapter we present the techniques utilized to investigate the samples analyzed in the framework of this project. The information regarding the doping performed within their structures have been obtained via the ones based on ion beam analyses (IBA), x-ray analyses and electron microscopy. The specificities of each of them will be highlighted in details. We will have a principal focus on the medium energy ions scattering (MEIS) for the high resolution and also x-ray analyses.

### What does characterizing a material mean?

The characterization of a material consists in analysing its response when it is subjected to an external action. This external action can be either voluntarily provoked (experiments) or non provoked (natural phenomena). The physical nature of the action itself may be: mechanical (application of a force, a pressure), thermal (temperature effects), electrical (application of a current, voltage), wave (electromagnetic field, radiation), acoustic (ultrasounds), optical (light radiation), chemical (molecules, chemical solutions), corpuscular (particles beam), etc. Thus, according to the intrinsic properties of a given material, one can analyse its reactions and interpret the results with respect to the nature of the action at which they have been submitted. Further explanations can be provided during the interpretations with the help of simulations and modelings. The characterization can be very useful in the prediction of the reactions of a material or a system, based on what we already know about the other materials of the same class. Since the solicited information on a sample may differ from one experiment to another, one should therefore discriminate each type of characterization that needs to

be performed and classify them accordingly. In the domain of experimental sciences, one encounters several types of characterizations, namely: biological, chemical, physical, etc. Physical and chemical characterization may consist in sending a beam of particles (which can be of corpuscular nature or not) on a sample material. The incident particles can thus interact with the sample atoms before exiting from it. The response of the material vis-a-vis the incident beam can be known by analysing the re-emitted beam after interaction with the sample. The structure, morphology, chemical composition or the quantification are among many information we can obtain through such investigations. The schematic of figure(2.1) illustrates the characterization of a sample using a beam of particles (photons, ions, electrons, etc). The physical and chemical characterizations have been used in the framework of this thesis for our investigations. Initially, we have used ions beam analyses to investigate our samples. The next paragraph will be consecrated to the presentation of some ion beam based techniques. An entire section will be conferred to a detailed description of the medium energy ion scattering (MEIS) technique. Its physical principles including some key notions that are common to most of the IBA techniques will be developed as well.

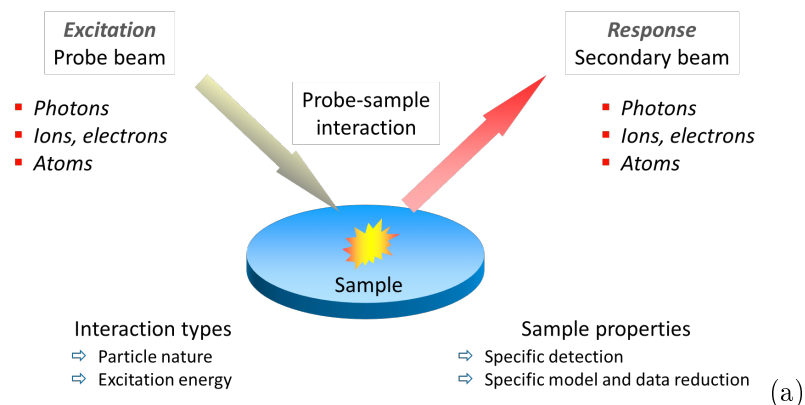


FIGURE 2.1: Schematic illustration of the characterization of a sample using a beam of particles.[20].

## 2.2 Medium Energy Ions Scattering (MEIS)

### 2.2.1 Principle

MEIS is a technique developed for analysing materials (e.g. semiconductors) in the medium energy ranges with high depth resolution. It uses light ions accelerated at energies in the range of about 50 keV to 500 keV. It shares the same physical principles with the RBS, namely the coulombian scattering of ions by the target nuclei. However, the acceleration energy in the latter technique ranging from 1 MeV to 10 MeV. The commonly used incident ions are protons ( $H^+$ ), alphas ( $He^+$ ). The possibly accessible

information among many are: the quantification of elements (concentration), defects, and the surface state.

- \* elemental composition: During the collisions between ions and the target nuclei, the kinetic energy is conserved. Therefore, the nature of the target atoms can be determined by evaluating the energy of the scattered particles.
- \* chemical concentration: It is obtained by analysing the yield of the scattered particles weighted to the scattering cross-section.
- \* defects: There are highlighted when the incident projectiles are aligned with a major crystallographic axis (channeling), so that they are more sensitive to the displaced Si atoms from their lattice sites. Because in this mode the yield is lowered in the crystal region.
- \* surface state: such information can also be obtained in MEIS in the same mode as in the precedent paragraph. When the incoming ions hit the material surface, a major part is scattered by the atoms of the extreme surface layer such that those in the sub-layers can not be seen by the ingoing ions. This phenomenon is called shadowing and the yield, comparable to that of the scattering events in an amorphous crystal contributes to the surface peak, defined as the signature of the chemical elements present at the surface of the analyzed material. Inversely, when the detector is aligned with an outgoing crystal direction, the scattered ions are blocked by the nuclei of the surface atomic layers along that direction. The consequence is that one observes a reduction of the yield at the corresponding scattering angle. This is the inverse of the shadowing phenomenon. The observation of the scattered intensity with respect to the scattering angle thus allows to evaluate the atomic displacements in the lattice with very high accuracy (in the order of pm), as presented in figure(2.2)[60].

The performances of microelectronics components rely on the quality of the materials they are constituted of. Such qualities derive from the results of high quality research in the material science areas by using state of the art facilities and techniques. The ion beam analysis techniques like those we mentioned in the previous paragraphs are part of them for instance. For the concerns of high precision in the investigations of their structures, one of the best technique to be employed is medium energy ion scattering (MEIS).

Thanks to its excellent depth resolution (0.25 nm at the surface), MEIS can be used to investigate structures of sub-nanometric dimensions such as 2D. However, the beam

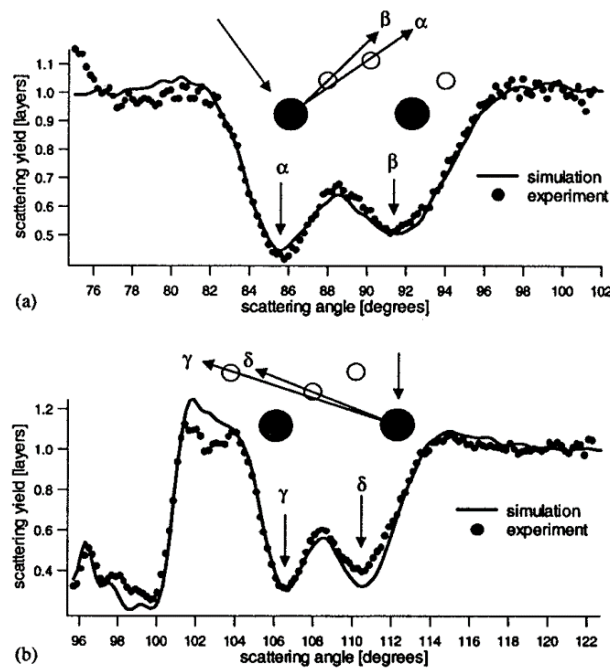


FIGURE 2.2: Evolution of the minima of the scattered yields observed in MEIS on Ge(111) with respect to the scattering angle. The scattering geometries were: [-1-10] & [001](a), and normal & [-111](b).

dimensions that are in the millimeter (mm) range can limit its fields of applications. Nevertheless, this technique has been employed to characterize structures of thin dimensions such as 2D thin films, quantum dots (q-dots)[61, 62]. In this work, we prove that MEIS is fully capable to probe 3D patterned samples such as the Fin shaped silicon, thanks to the suitable protocol which has been developed.

### 2.2.2 Description of the equipment

The medium energy ion scattering technique is limited to an energy range lower than that of RBS. It also consists in analyzing the energy and/or angle of the charged particles which have been scattered by the nuclei. The incident projectiles which are commonly used are protons ( $H^+$ ) and alphas ( $He^+$ ). However, the methodology and the analysis system are different. For example, the detector used in RBS is a surface barrier detector with a resolution of about 12-15 keV[61]. The samples of thicknesses of up to few microns can be probed in this technique with a depth resolution of the order of 10 nm at the surface. High resolution measurements are performed in MEIS with a detection system constituted of a toroidal electrostatic analyzer (TEA) coupled with micro-channel plates (MCPs). Such a device allows us to obtain an energy resolution of about 0.3% ( $\frac{\Delta E}{E}=3.3 \times 10^{-3}$ ) and an angular precision of  $0.1^\circ$ . The operating principle of this technique is as presented in figure(2.3).

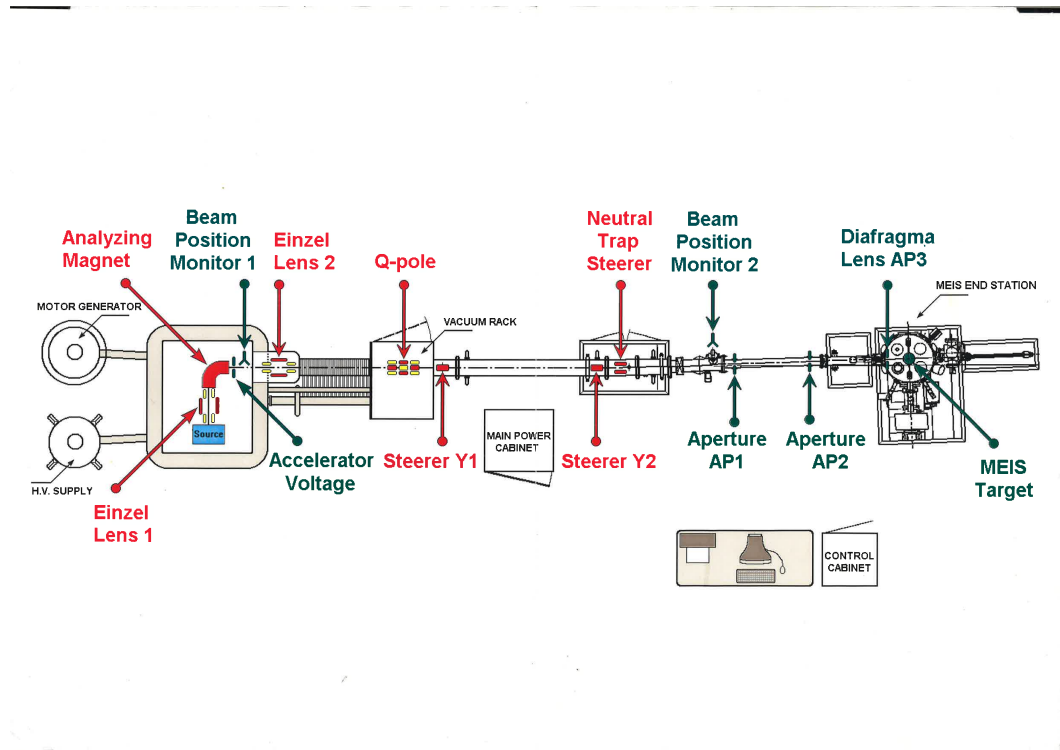


FIGURE 2.3: Principle schematic of the high voltage facility used for the medium energy ion scattering analysis technique. The whole compartment is principally constituted of a plasma source and the accelerator, the beam line with the set of collimators, and the MEIS end station.

The image of figure(2.4) presents an overview of the MEIS setup of the nano-characterization platform (PFNC) of CEA-Leti. It consists of three main parts: the ions' source production with acceleration system, the beam line and the end station. The main beam line is constituted by the set of collimators to focus and align the beam, while the end station hosts the main analysis chamber and the sample compartment. The next paragraph will be consecrated to the descriptions of the different parts of figure(2.4).

### The accelerator system and the ion source

The accelerator system of electrostatic type is capable of generating an ion beam of protons ( $H^+$ ) or helium ( $He^+$ ) in a voltage ranging from 50 to 400kV. The principal part constituting the acceleration system are: the HV terminal ('mini separator'), HV power supply, accelerator tube, resistor stack, vacuum rack and the main power cabinet. They are produced from a plasma formed in the source by electron bombardments, then accelerated at high voltage (HV) generated by the power supply. The energy of the projectiles should be sufficiently large in order to make the scattering event happens.

In general, the sources utilized for such experiments can produce either positive or negative ions. For protons used as incident projectiles, they are produced thanks to the

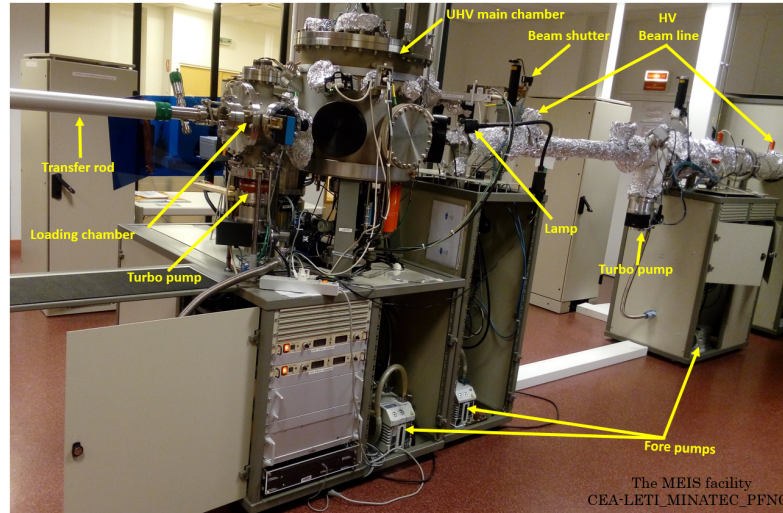


FIGURE 2.4: Image of the MEIS setup with the different compartments, necessary for high resolution MEIS experimentations.

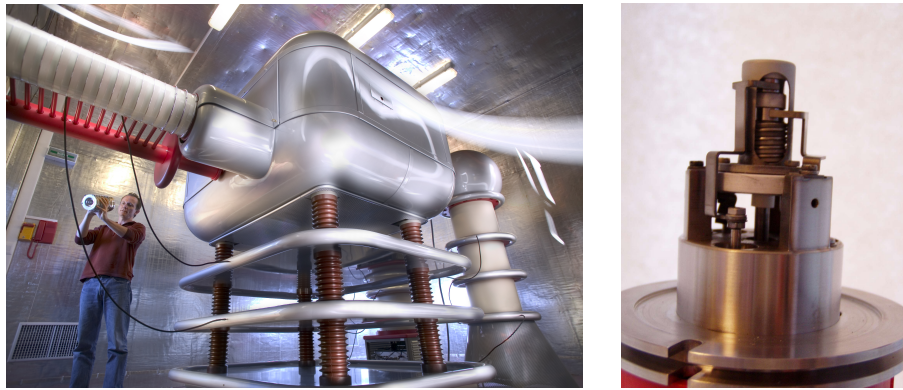


FIGURE 2.5: The 400kV MEIS accelerator system (left) and the model SO-55-1 ion source utilized for the MEIS measurements (right).

interaction between the atoms of the hydrogen gas introduced in the source and the electrons produced by a filament, heated at very high temperature ( $1700^{\circ}\text{C}$  at maximum) by injecting a current. The other principal constitutive elements present inside the MEIS accelerator displayed at the left hand side of figure(2.5) with their main functions are: the magnet (for electronic confinement in the plasma), anode (defines the beam's size at the exit of the source), the extraction (for the beam focusing).

In general, different types of sources can be employed to produce ions. The main drawback with the filament source (as in our case) is that the filament breaks down after a certain period of operating cycles. However, the other types such as radio frequency (RF) and microwave (MW) ions sources do not present such anomalies, despite their considerable cost. The advantage with these last two types of sources is the absence of the filament breaking down phenomenon when the measurements are going on[63].

## The beam line and the vacuum system

Just after exiting from the plasma source, ions are post-accelerated at a voltage of 15kV. The ion beam obtained at the exit of the accelerator is aligned and focused all along the line under high vacuum (HV) by a set of electrostatic lenses and collimators (figure(2.3)). Some of the main elements of the beam line are the: steerers, neutral trap, beam profile monitor (BPM) and beam apertures.

The steerers have as role to deflect the beam in the vertical (y) direction along the line. The neutral particles are removed from the beam thanks to the neutral trap system placed directly after the steerers, so that only the positive ions can follow the bend imposed by the DC voltage applied on its plates. When the dose is reached, a shutter close the beam on the the sample at the end of the measurements. The BPM allows to visualize profile of the beam in the x and y directions, by continuously checking its intensity, diameter and the positions. The lateral dimensions of the beam at the exit of the aperture in the main chamber are  $1 \times 0.5 \text{mm}^2$ .

## The loading chamber

The loading chamber is a cylindrical-shaped compartment made of stainless steel, and its interior environment is maintained under HV ( $10^{-9} \text{mbar}$ ). A maximum number of seven samples can be loaded on a carousel in the chamber. The analyzed sample in question is mounted on a sample holder. They are introduced in the loading chamber through an adapted aperture by using a transfer rod fixed on the ground as can be seen in the image. It is important to notice that there is no need to break the vacuum in the the main chamber for sample exchanges. This has the advantage of saving measurement times, it also help to avoid long pumping times to recover the required level of vacuum for measurements. Indeed the main and loading chambers are both isolated one another by an automatically controlled valve.

## The sample preparation and sample holder

The cleaning of the samples is done by using ethanol and acetone, one can also use ultrasounds. However, this depends on the nature of the sample. Thus, one should be very careful about the possible degradations they can induce when they are employed. After the samples have been cleaned, they are mounted on a sample holder made of molybdenum, before being introduced in the loading chamber. An image showing an example of a sample holder is presented in figure(2.6).



FIGURE 2.6: Picture of a sample holder bottom used for MEIS measurements. The adequate dimensions of a piece of sample should be  $1 \times 1 \text{ cm}^2$ , but the holder can also host a sample of extra dimensions with a rectangular or circular shape.

### The main chamber

It is a compartment of cylindrical form made in stainless steel, consisted of a removable top cover. The experiments take place in an ultra high vacuum (UHV) environment, where the minimum level of the vacuum is a few  $10^{-11}$  mbar. This level is permanently maintained constant by different pumps: primary, ionic and turbo. It is not excluded to have secondary electrons emitted during the scattering phenomena, and their presence can affect the current count. To avoid their perturbations during the measurements, there is an electrode fixed in the chamber which is in charge of suppressing their contributions.

### The sample manipulator: the goniometer

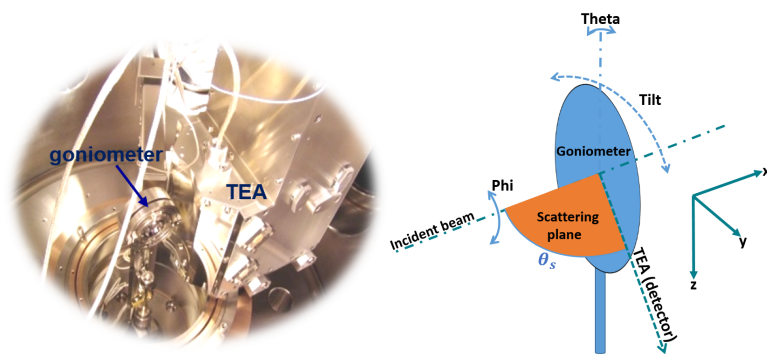


FIGURE 2.7: Left image: interior of the analysing chamber, one can see the goniometer and the toroidal electrostatic analyzer (TEA). Right image: drawing of the principal axes of the goniometer. There are three translational ( $x$ ,  $y$ ,  $z$ ) and three rotational (Theta, Phi and Tilt) axes.

The sample to be analysed is mounted on a high angular precision goniometer, connected to the center of the analysing chamber via a conflat flange. The system (goniometer + sample) is monitored via stepper motors. The sample itself can rotate around three angles (Theta, Phi and Tilt) used for alignments. Theta is the polar angle, defined with respect to the sample normal in an interval from  $-180^\circ$  to  $+30^\circ$  in steps of  $0.013^\circ$ . Phi is

the azimuthal angle defined in the sample plane and it can fully rotate at  $360^\circ$  around the vertical axis. For experimental conveniences, it was set to rotate from  $-100^\circ$  to  $+100^\circ$  in steps of  $0.013^\circ$ . Last, the third angle (Tilt) is perpendicular to both Theta and Phi. It has a narrower interval, where the only accessible angles are delimited between  $-3.5^\circ$  and  $+3.5^\circ$  in steps of  $0.007^\circ$ . In addition to these three rotational axes, the UHV sample manipulator can also translate along three principle axes: two in-plane axes (x, y) and one out of plane axis (z) which is perpendicular to the sample. With a precision of 0.01 mm, the translations along the three axes are fixed in a range between -10 mm and 10 mm. The z axis allows the acquisitions on different points on the sample without any change of the alignment and without shifting the target out of the beam direction. In the previous paragraph, we mentioned that the sample exchange can be operated between the loading and main chamber, which is made possible thanks to the goniometer placed in the center of the chamber.

### The Toroidal Electrostatic Analyser: detector

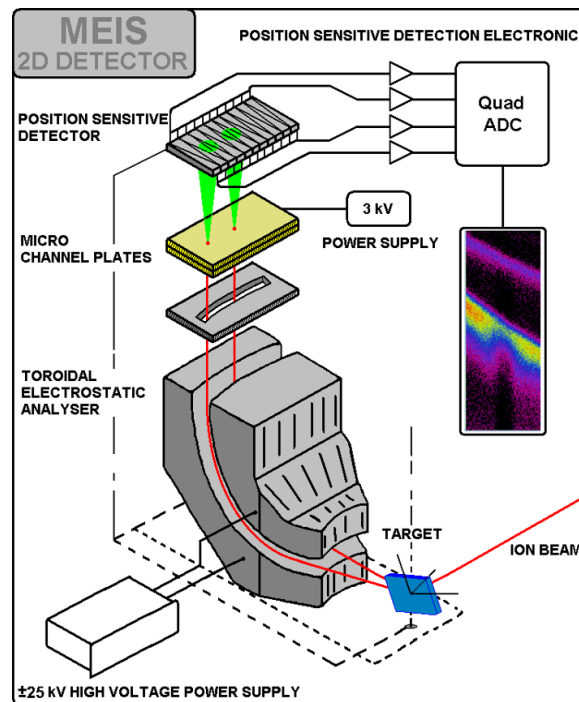


FIGURE 2.8: Toroidal electrostatic analyser (TEA) used for the detection and analysis of scattered ions in the MEIS technique

The toroidal electrostatic analyser (TEA) is a detection system which has been designed for scattering experiments in the energy range between 50 to 400 keV. The scattered ions are measured over a  $\sim 20^\circ$  angular window corresponding to the angular aperture of the TEA. It can be positioned between the angular values of  $-140^\circ$  and  $-20^\circ$  with an

acceptance window of  $\pm 10^\circ$ , and an angular precision of less than  $0.3^\circ$ . The TEA is a system developed for both angular and energy analyses of the scattered ions. The incident ions being initially emitted at low and controllable current doses by an accelerator. The advantage is thus to reduce the measurement time and the sample exposure to the beam.

As described in figure(2.8), the TEA consists of two toroidal electrodes, circularly separated to allow the projectiles to flow in between. Only the ions scattered over an energy window corresponding to the voltage applied between the toroidal electrodes are allowed to pass through the slit and they are detected by the micro channel plates (MCPs) placed at the exit.

### The Micro Channel Plates (MCPs)

The micro-channel plates are made of two identical plates, both assembled in a Chevron configuration. Their main roles are to amplify the signal. Thus, those 'particle amplifiers' operate as follows. After their surface has been hit by the incident ions, each of these ions extract few electrons. The secondary electrons are accelerated along the channel by the potential gradient established by the voltage applied across both plates, then hit the opposite wall of the channel by extracting other secondary electrons, and so on. As a consequence of these multiplication cascades, there is a creation of a charge cloud presents at the exit slit. The conversion of information related to their energies and scattering angles is performed by a position sensitive detector (PSD) via an analog to digital converter (ADC). Figure(2.9) highlights the amplification processes of the electrons through a channel of the MCPs[64]. An example of a bi-dimensional image of a pair of MCPs, indicating the electrons entering into the channels is provided in Figure(2.10)[21].

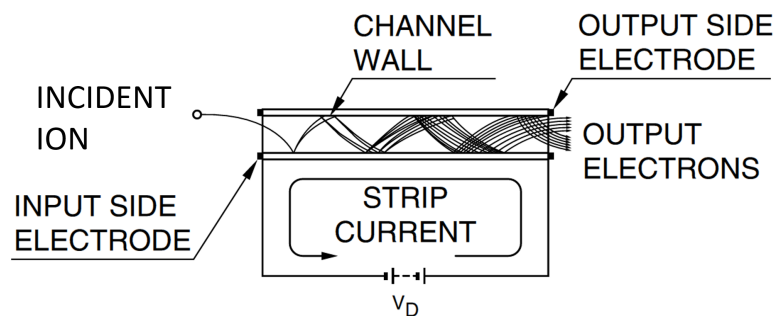


FIGURE 2.9: Illustrative example of the multiplication process of electrons that leads to the signal's amplification along a channel of the MCPs.

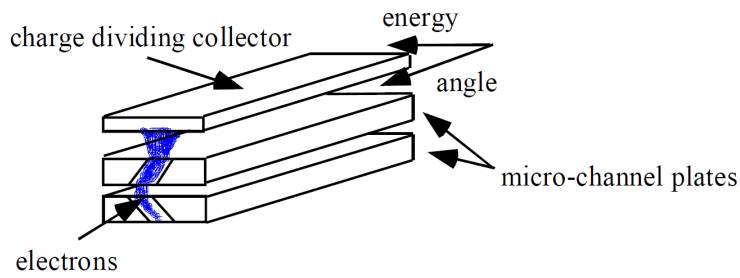


FIGURE 2.10: Schematic drawing of a pair of micro channel plates[21].

### 2.2.3 Theory

MEIS is a technique simply based on the scattering of ions by the nuclei in the keV ranges. Indeed, when the mono-energetic ions ( $H^+$  or  $He^+$ ) are very close to the atomic nuclei, they are scattered at different directions. The principle consists in analyzing the energies or angles of the scattered projectiles, by knowing the relationship between the scattering angle  $\theta$ , the incident energy  $E_0$  and the mass ratio of the target  $M_1$  and projectiles  $M_2$ .

#### 2.2.3.1 The kinematic factor K

It establishes the relationship between the incident energy  $E_0$  of ions and the one they have ( $E_1$ ) after they have been scattered by the nuclei of the target atoms (see figure(2.11)). When the incident projectiles of mass  $M_1$  collide with the target nuclei of mass  $M_2$ , they lose energy through a momentum transfer to the target atoms. The larger the mass of the target, the smaller the amount of energy lost by the projectiles. However, all the energy lost by the projectiles is indeed absorbed by the atoms of the target (elastic collisions). Figure(2.12) illustrates the dominant processes that take place during and after the interactions. Those processes are: the scattering of the projectiles (green circle) by the target atoms (red circle) and their possible recoil (orange dotted circle). Thus the K factor results from a momentum transfer from the projectiles to the target atoms, during the collision processes.

According to the fundamental principle of dynamic described within a pure classical context, one supposes that the momentum conservation as well as the relationship between the energy and the mass are always verified. Therefore:

$$\begin{aligned}\vec{p}_1 + \vec{p}_2 &= \vec{p}'_1 + \vec{p}'_2 \\ E_1 &= E_1 + E'_2\end{aligned}\tag{2.1}$$

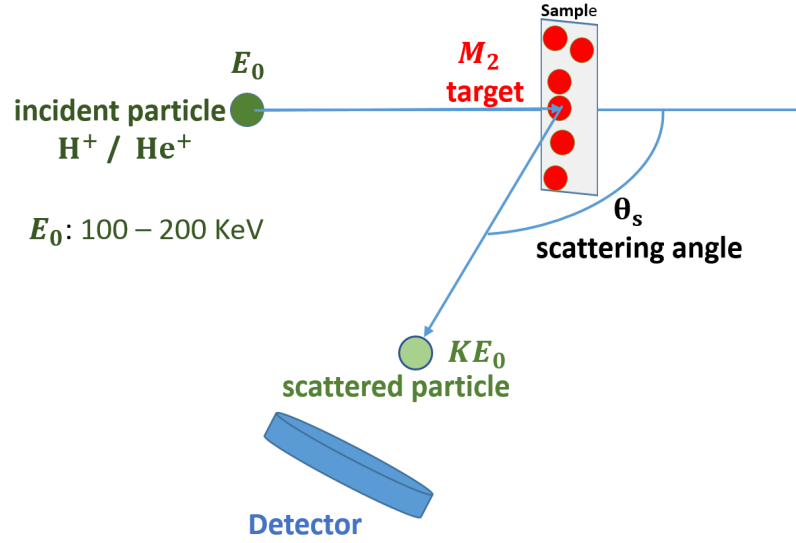


FIGURE 2.11: Illustration of the collision processes between the projectile and the target atoms. The scattered energy can be deduced using the kinematic factor  $K$ .

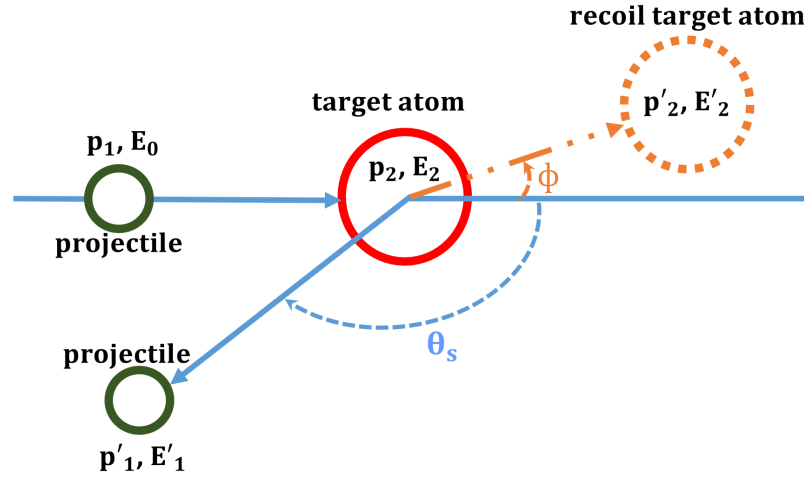


FIGURE 2.12: Drawing of the kinematics of the elastic collision between the projectiles of mass  $M_1$ , energy  $E_0$ , momentum  $\vec{p}_1$ , and the target atoms of mass  $M_2$ , energy  $E_2=0$  (at rest), momentum  $\vec{p}_2$ .  $p'_1, E'_1$ , and  $p'_2, E'_2$  are the momentum, energy of the projectiles, and the momentum, energy of the target atoms after the collisions, respectively.

By assuming that all the ongoing collisions within the target are of elastic nature, the kinetic energy is therefore conserved. From the projections along the different axes (in the frame of the laboratory) as described in figure(2.12), with  $\vec{p}_1 = M_1\vec{v}_0$ ,  $\vec{p}_2 = 0$ ,  $\vec{p}'_1 = M_1\vec{v}_1$  and  $\vec{p}'_2 = M_2\vec{v}_2$ , then  $\vec{E}_1 = \frac{1}{2}M_1v_0^2$ ,  $\vec{E}_2 = 0$ ,  $\vec{E}'_1 = \frac{1}{2}M_1v_1^2$  and  $\vec{E}'_2 = \frac{1}{2}M_2v_2^2$  have the following equation(2.2):

$$\begin{cases} M_1v_0 = M_1v_1 \cos(\theta_s) + M_2v_2 \cos(\phi) \\ M_1v_1 \sin(\theta_s) = M_2v_2 \sin(\phi) \\ \frac{1}{2}M_1v_0^2 = \frac{1}{2}M_1v_1^2 + \frac{1}{2}M_2v_2^2 \end{cases} ; \quad (2.2)$$

The elimination of the recoil angle  $\phi$  in order to obtain an expression that only depends on the scattering angle  $\theta_s$  and the masses  $M_1$  and  $M_2$  in equation(2.2) yields to the obtention of the kinematic factor given by equation(2.3).

$$K = \left\{ \frac{\sqrt{1 - \left(\frac{M_1}{M_2}\right)^2 \sin^2 \theta_s} + \left(\frac{M_1}{M_2}\right) \cos \theta_s}{1 + \left(\frac{M_1}{M_2}\right)} \right\}^2 \equiv \frac{E_1}{E_0} \quad (2.3)$$

The graphs of figure(2.13) shows the evolution of the kinematic factor for protons and alphas in function of the mass of the target ( $M_2$ ) for a given scattering angle  $\theta_s$ . For a large scattering angle (e.g.  $\theta_s=135^\circ$ ), one observes a significant variation of K for the small values of  $M_2$ . However, it is not the case when the target is constituted of heavy elements, even if the scattering angles are quite large. Even though the mass separation is always favourable to large scattering angles, nevertheless, the ideal case would be to deal with light elements for an experiment at large scattering angle.

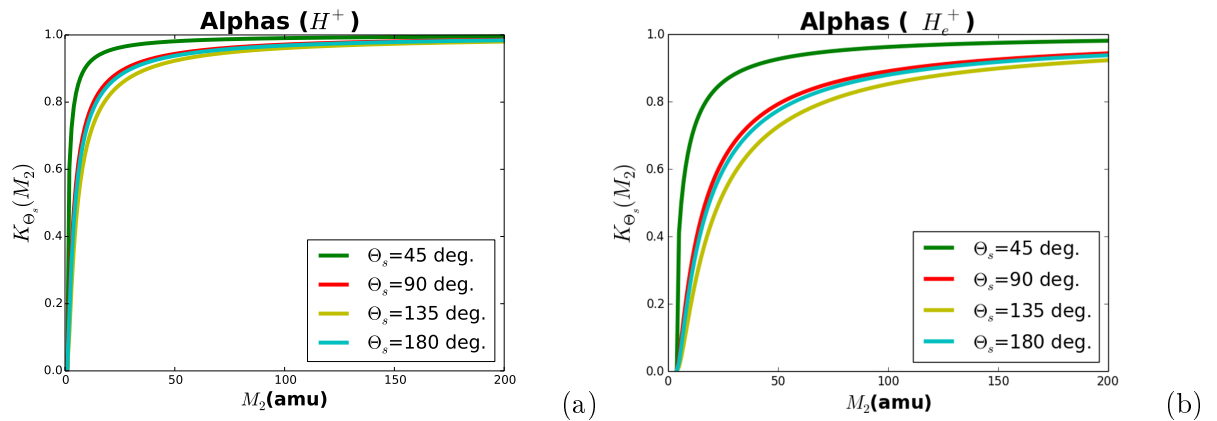


FIGURE 2.13: Evolution of the kinematic factor in function of the target mass, for a given scattering angle( $\theta_s$ ). Protons (graph(a)) and alphas (graph(b)) are used as incident projectiles.

From the point of view of the kinematics of elastic collisions, the factor K can be described as a mediator of the energy exchange between the projectiles and the target. Because, from the relationship  $E_1 = KE_0$  and thanks to the conservation of the kinetic energy, one can find the mass  $M_2$  of the target atom. In equation(2.3) we see that K is expressed in terms of the ratio between  $M_1$  and  $M_2$ , and the scattering angle  $\theta$ . Figures(2.14(a) and 2.14(b)) show the evolution of K with respect to the scattering angle for different targets. Protons ( $H^+$ ) and alphas ( $He^+$ ) are used as incident projectiles.

This variation is significant with the use of alpha particles as projectiles (see figure(2.14)(b)) because of their greater mass than those of protons. From an experimental point of view, the kinematic factor is exploited in the context of mass separation, which is useful for

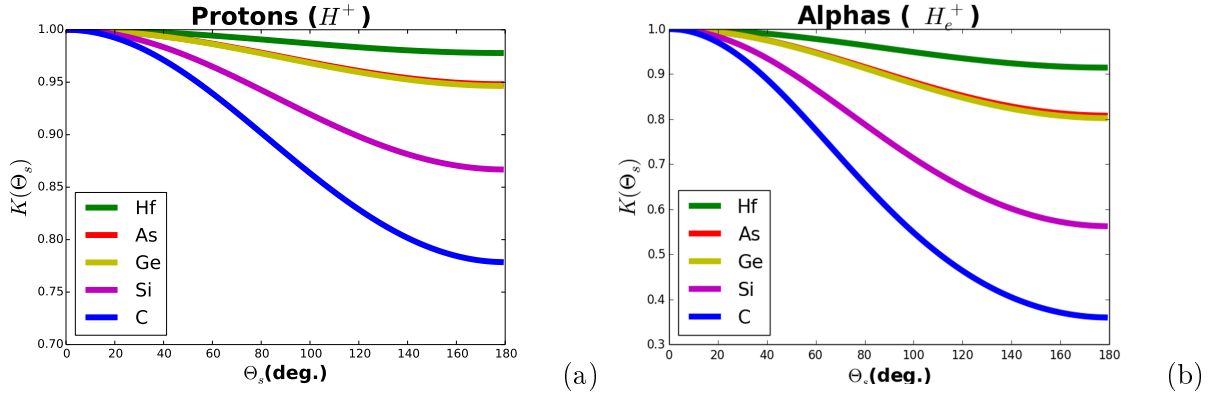


FIGURE 2.14: Evolution of the kinematic factor with respect to the scattering angle for different target masses. Protons ( $H^+$ , graph(a)) and alphas ( $He^+$ , graph(b)) are used as incident projectiles.

the discrimination of the scattering peaks of the chemical elements of interest. For example, the higher the scattering angle, the better the mass separation. In consequence, the identification of the elements in presence in a given material is much easier. Even though things still remain more or less tricky when two atoms of close masses are present in the material (e.g. As and Ge), as clearly presented in figure(2.14).

### 2.2.3.2 The Rutherford's scattering cross-section $\sigma(\theta_s)$

Employing a simple vocabulary, the scattering cross section  $\sigma(\theta_s)$  can be defined as an effective surface restricted to microscopical events. In the previous paragraph, we provided the expression of the kinematic factor  $K$ , which establishes the relationship between the incident energy ( $E_0$ ) of the particles, and the one they possess ( $E_1$ ) after they have been scattered by a target atom of mass  $M_2$  at a given scattering angle  $\sigma(\theta_s)$ . Thus, if  $K$  refers to a deterministic aspect, the scattering cross section  $\sigma(\theta_s)$ , however, refers to a probabilistic aspect. We would like to mention that all the scattering events taking place within the material may not lead to a detection. This means that it is not possible to detect and analyze all the particles which have been scattered. It depends on the solid angle at which they are seen by the detection system. Therefore, the scattering cross section as defined in equation(2.4) with  $x = \frac{M_1}{M_2}$ , might also be interpreted as the probability that a scattering event gives rise to a detection.

$$\frac{d\sigma}{d\Omega} = \left( \frac{Z_1 Z_2 e^2}{4E} \right)^2 \left[ \frac{4}{\sin^4(\theta)} \right] \frac{\left\{ \left[ 1 - (x \sin \theta)^2 \right]^{1/2} + \cos \theta \right\}^2}{\left[ 1 - (x \sin \theta)^2 \right]^{1/2}} \quad (2.4)$$

From the expression of  $\frac{d\sigma}{d\Omega}$ , we can draw some important remarks:

- \*  $\frac{d\sigma}{d\Omega} \propto Z_1^2$ : The scattering cross section obtained with heavy incident ions is larger than the one we get with light ions. For example,  $\left(\frac{d\sigma}{d\Omega}\right)_{He^+} = 4 \left(\frac{d\sigma}{d\Omega}\right)_{H^+}$
- \*  $\frac{d\sigma}{d\Omega} \propto Z_2^2$ : High sensitivity to heavy target atoms (large  $Z_2$ ) than to light ones (small  $Z_2$ )
- \*  $\frac{d\sigma}{d\Omega} \propto E^{-2}$ : The scattering intensity significantly increases with the diminution of the incident energy of ions.
- \* The fact that  $\frac{d\sigma}{d\Omega} \propto \sin^{-4}\left(\frac{\theta}{2}\right)$  may contribute to a rapid augmentation of the scattering intensity when the scattering angle diminishes.

The concentration or the number of atoms of a given chemical species in the target is determined by using the formula of the scattering yield given in equation(2.5)[65]. It means that the exact values of the scattering cross section related to that element of interest are supposed to be known for its quantification.

$$Yield = \frac{d\sigma}{d\Omega}(\Omega.Q.Nt) \quad (2.5)$$

$\Omega$ ,  $Q$  and  $Nt$  are: the detector solid angle, the number of incident ions and the density per unit area, respectively.

### 2.2.3.3 Energy loss in materials

When passing through a material of a given thickness  $x$ , the projectiles progressively lose energy as they penetrate the medium. Their slowing down is related to the physical properties of the medium. For a material of density  $N(\text{at}/\text{cm}^3)$ , one can define a parameter  $\epsilon(E)$  called the stopping power. It is the ability of a material to slowdown the ions during their travelling within its structure until their definitive stop. This energy loss mainly results from the collisions with the electron cloud. There exists also the losses due to collisions with the nuclei, but which are two orders of magnitude smaller comparatively to the electron losses. Therefore they are negligible in the energy range of RBS, comparatively to other techniques using lower impact energy (keV) such as low energy ion scattering (LEIS) or MEIS for example. For a given material, the energy loss will directly depend on the incidence energy and the nature of the projectiles. Its expression is given in equation(2.6):

$$\varepsilon = -\frac{1}{N} \frac{dE}{dx} \quad (2.6)$$

In the case of a material constituted of atoms of different types  $i$ , each of them having a proportion  $b_i$  in the compound such that  $\sum_i(b_i)=1$ , the stopping power of such a compound is a sum of all the stopping powers of the elements in presence. Its given by the Bragg's law as follows  $\varepsilon = \sum_i b_i \varepsilon_i(E)$ . The evolution of the stopping power of protons and alphas in silicon is given by figures(2.15(a) and 2.15(b)).

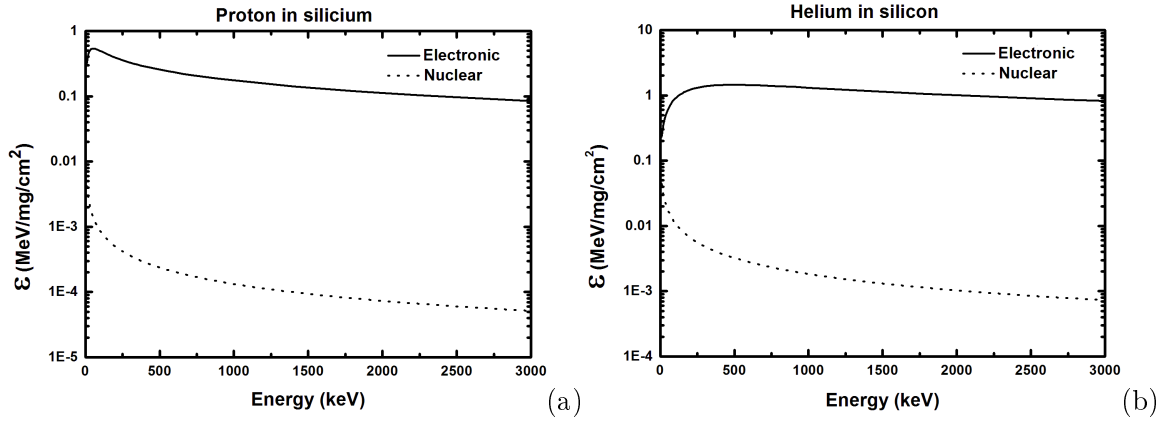


FIGURE 2.15: Evolution of the stopping powers of protons (a)[22] and alphas(b)[23] particles in silicon.

There exist several empiric relationships that have been established to determine the stopping powers of all the elements of the periodic table, where protons and alphas were used as incident projectiles[22, 23]. These relationships were deduced thanks to several measurements that have been carried out and filed in some documents available in the literature[23]. The term  $dE/dx$  in equation(2.6) can be described as the rate of the energy lost by the ions per unit path length  $x$ , due to the multiple collisions with the target atoms. The measurement of  $\varepsilon(E)$  obtained per unit of superficial mass ( $\text{eV/mg/cm}^2$ ) allows us to determine  $dE/dx$ , but there are several relationships that can be exploited to compute this term, like the one proposed by Bethe[66] in equation(2.7):

$$\frac{dE}{dx} = \frac{4\pi (Z_1 e^2)^2}{m_e v^2} Z_2 N L \quad (2.7)$$

with  $L = \ln\left(\frac{2m_e v^2}{I}\right)$  et  $I = 10Z_2$ . Equation(2.7) is a semi-empirical formula used to evaluate the energy lost by the projectiles, nowadays there are data bases produced by Ziegler and Biersack available in the literature to do it.

Knowing the expression of  $\epsilon(E)$ , one can deduce the total penetration depth of ions in the traversed medium:

$$D = -\frac{1}{N} \int_{E_0}^0 \frac{dE}{\epsilon_i(E)} \quad (2.8)$$

Figure(2.16) presents the evolution of the penetration D of hydrogen and helium particles in silicon.

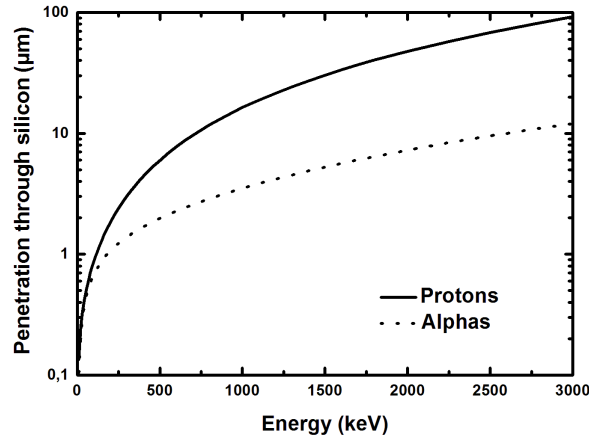


FIGURE 2.16: Evolution of the total penetration depth of  $H^+$ [22] and  $He^+$  in silicon[23].

#### 2.2.3.4 The straggling

When a beam of particles (having initially the same energy  $E_0$ ) traverses a material of a given thickness  $L$ , the incident beam loses energy in a similar process as described in paragraph(2.2.3.3). This loss gives rise to fluctuations of the trajectory of each particle of the packet, because they are more likely to collide with the target atoms when their energy decreases. These random fluctuations of trajectories is at the origin of the straggling phenomenon.

To these trajectory fluctuations, one can reciprocally associate other fluctuations during the losses in the kinetic energy of the ions, defined by  $\Delta E$ . However, it appears that the quantity  $\Delta E$  of the energy lost from one particle to another, within the same beam, is different. Therefore the total energy lost  $\delta\Delta E$  results from a purely probabilistic phenomenon. The distribution law of their kinetic energy can be assimilated to a Gaussian with a standard deviation  $\Omega$  and  $FWHM=2\sqrt{2\ln 2}\Omega=2.355\Omega$ . An expression of  $\Omega$  was proposed in 1948 by Niels Bohr[67], based on the model of collisions of the incident ions with free electrons. This model stipulates that the standard deviation does not depend on the energy of the ions. The expression of the Bohr's standard deviation  $\Omega_B$  is thus

given by equation(2.9). Where  $Z_1, Z_2$  are the atomic numbers of the projectile and the target atoms, respectively.  $e$  represents the elementary charge of electron.

$$\Omega_B^2 = 4\pi Z_1^2 Z_2 e^4 NL \tag{2.9}$$

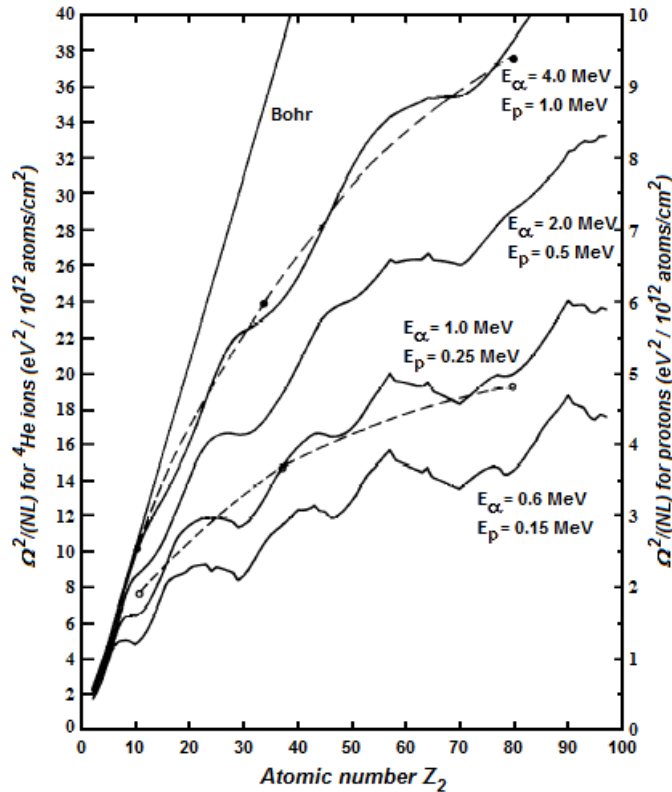


FIGURE 2.17: Computed values of straggling for protons and helium used as projectiles[24].

The straggling phenomenon can be resumed as the differences in the energy losses of the ions (that initially had the same incidence energy  $E_0$ ), after they have traversed a same medium of thickness  $L$ . This phenomenon is responsible to the degradation of the depth resolution as the ions penetrates inside the sample. Nevertheless, one can still gain in depth resolution if the targeted range is around the first 10 nm. At such a short penetration depth, the straggling is very negligible in RBS whatever the employed projectiles (protons or alphas), which is not the case in MEIS because of the detector resolution. Figure(2.17) shows that as the depth increases, the energy straggling also increases, but more importantly when using alpha particles. A quantum concept of this phenomenon was also proposed by W.-K. Chu[24]. In this formalism, the binding energy of the electrons and the nuclei is taken into account. Consequently, the expression of the energy straggling that they found was energy dependent, in contrast to the one proposed by N. Bohr.

### 2.2.3.5 The channeling phenomena of ions and the random orientation of crystals

In practice, channeling means to align the incident beam along a major crystallographical axis, so that the ions can flow between the atomic rows without meeting the nuclei thanks to the Coulomb interaction. Indeed, the electric field of the nuclei acts like a guide, thereby avoiding the positively charged ions from meeting the nuclei along the rows. However, the different impact parameters ( $b$ ) of each incident projectiles approaching the coulomb field, make that some of them may undergo slight deviations from their in-going trajectory. Actually, the trajectory of the ions are not strictly linear. As they penetrate the structure, they oscillate along their incidence direction due to multiple scatterings at small angles (large impact parameters). Figure(2.18) illustrates the channeling phenomenon of ions along a crystal axis.

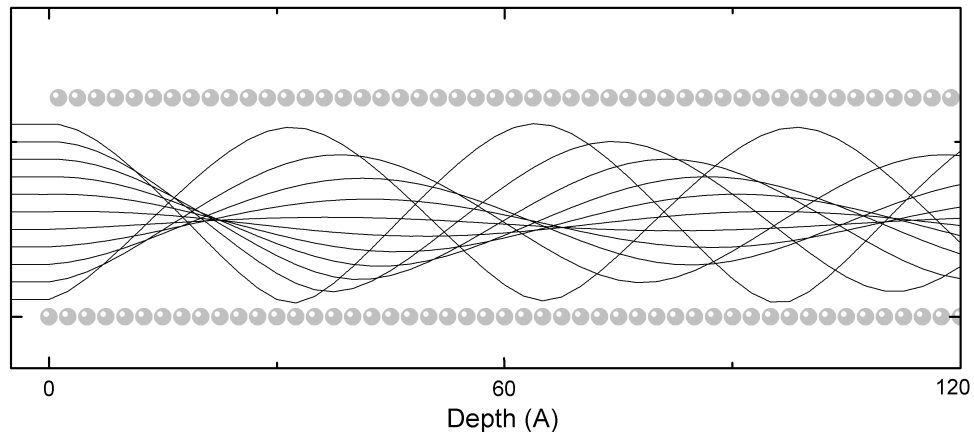


FIGURE 2.18: Illustration of the channeling of protons ( $H^+$ ) along a crystallographic direction

[20]

An experimental observation of the channeling effect is the significant reduction of the yield at a given depth inside the sample. In the case when the probed sample is silicon for instance, the reduction factor of the intensity is of the order of 25 at room temperature[20]. One of the great interest of using the channeling mode is its ability to probe defects and provide their depth profiles, in condition to have a good resolution. Indeed, the defects in crystal may arise from several effects such as the presence of impurities, displaced lattice atoms from their sites, lacuna, dislocations, etc. Thus, if the channeled ions encounter one of these anomalies during their penetration inside the crystal, they will face significant deviations from their initial direction. Their close encounter with the atoms along the rows (small impact parameter) may give rise to many scattering events. This is why the channeling of ions is employed to profile structural defects in materials with a very good accuracy.

## The critical angle of channeling and the minimum yield

### The critical angle of channeling

It is possible that a beam initially oriented along a crystal direction be not correctly aligned with the atomic rows if the incidence angle is slightly above or below the value corresponding to that of the targeted rows in the crystal. In this case, the channeling of the ions is not perfect. The fact that the incident projectiles still remain channeled is due to the angular tolerance which is still favorable for their channeling. Indeed, at the entrance of the atomic rows, there is a small angular gap allowed to the ions to still remain channeled, in condition that this gap be always inferior to the value of the critical angle ( $\psi_{1/2}$ ). From the figure(2.19) which gives the evolution of the angular aperture along a targeted crystal direction, we see that it tolerates an alignment error, but only at a certain limit. The full width at half minimum (FWHM) is equal to the critical angle ( $\psi_{1/2}$ ) that should not be exceeded if the ions have to be channeled. It is worth precisizing that the limits of the angular aperture are not the same for all the crystallographic directions. Above the limit of the tolerated angular errors, the conditions for a good channeling are no longer met. Consequently, the beam is disoriented from its initial direction and the projectiles can closely approach the atomic rows and scatter. In this case, the yield of the scattering intensity in the crystal will augment. This unexpected augmentation observed in the spectrum is attributed to a phenomenon called dechanneling. The formula used to compute the value of the critical angle is given by equation(2.10).

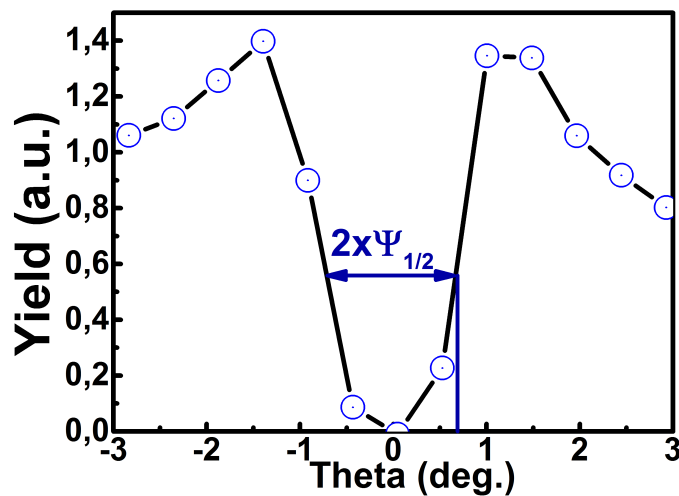


FIGURE 2.19: Illustration of the angular aperture along a channeling direction. The value of the critical angle is obtained by taking the full width at half-minimum, as indicated on the curve.

$$\psi_{1/2} = \sqrt{\frac{Z_1 Z_2 e^2}{Ed}} \quad (2.10)$$

The E dependence of  $\psi_{1/2}$  shows that one can study its evolution with the projectile energy (E) along a crystal axis, as highlighted in Figure(2.20). In this expression, d represents the distance between the atoms along the targeted crystal direction,  $Z_1$  and  $Z_2$  are the atomic numbers of the projectile and the target atom, and e is the elementary charge of the electron.

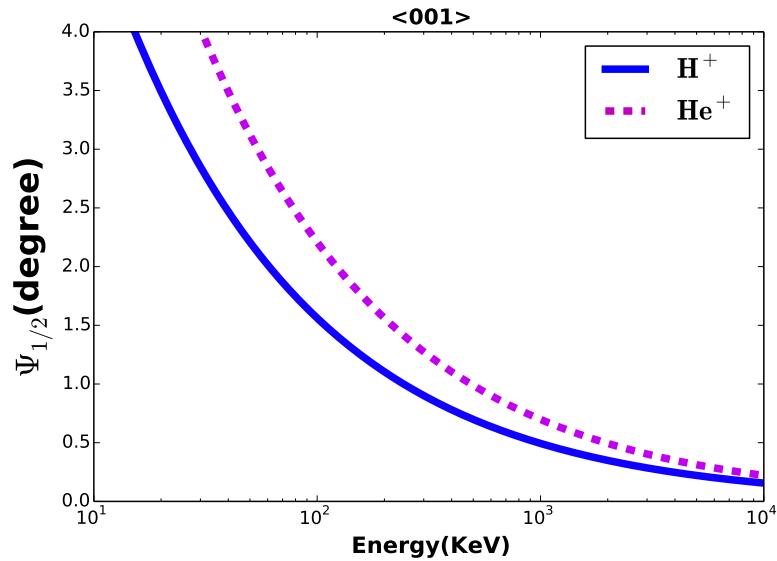


FIGURE 2.20: Evolution of the critical angle of channeling  $\psi_{1/2}$  in function of the energy of hydrogen  $H^+$  and helium  $He^+$  along the crystal direction  $\langle 001 \rangle$  of silicon.

### Random orientation of crystals

When the crystal axis is not oriented with the incident beam, a fraction of the ions will be scattered at a same yield as they were scattered in a material containing non ordered or randomly arranged atoms. This random orientation favors the close encounters between the target atoms and the incident particles. Basically, a perfect random orientation of crystals do not exist, consequently, it may happen that some of the incident projectiles face a weak channeling effect even in a random orientation of the crystal. Since almost all the incident projectiles are more likely to collide with the target atoms, the signal of any chemical element presents in the sample at a given depth will appear in the energy spectrum. The area under their peak in random mode can be used to evaluate their quantity in the sample. In paragraph(2.2.2), it has been mentioned that the channeling mode is employed to investigate defects in crystals. Therefore, the exploitation of both the channeling and random modes can be used to profile the displaced atoms and quantify the impurities as well the chemical element.

## The minimum yield

The minimum yield ( $\chi_{min}$ ) is obtained by computing the ratio of the aligned to the random yield. This is used to estimate the dechanneling rate of the ions in a crystal. Thus, the quantity attributed to the dechanneling rate is obtained by taking the value after the surface peak towards the low energy ranges in the normalized spectrum obtained from the ratio that we just described. In first approximation, the crystal quality of the subsurface region can be estimated by evaluating the intensity level of the part of the spectrum located at the low energy side of the surface peak. A mathematical expression of the minimum yield as we described above can be written as follows:

$$\text{minimum yield(\%)} = \frac{\text{yield}(\text{non damaged part in channeling mode})}{\text{yield}^{model}(\text{random mode})}$$

In the above expression, the 'yield' refers to the level of the scattered intensity, which is expressed in arbitrary units (a.u.). The larger its value, the higher the dechanneling degree. This augmentation can relate on the level of structural damages inside the crystal. The concept of dechanneling was first introduced by Lindhard in 1965[68]. It can also be observed in pure crystals material due to the thermal vibrations of atoms around their equilibrium positions, with very low values in general ( $\sim 4\%$ ). Further details on the use of  $\chi_{min}$  are provided in the third chapter.

### 2.2.3.6 Blocking and Shadowing in crystals

At the entrance of ions in the crystal, some of them are deflected by the atoms of the extreme surface planes, so that they cannot meet the others beneath. Therefore they are deviated on either sides of their ingoing trajectory and one observes the formation of a shadow around the initial deviation point. Actually, a fraction of the incident ions have closely approached the nuclei due to the distribution of their impact parameters, and are repelled at different angles because of the coulomb interaction. The cone thus formed at the entrance of the ions called 'shadow cone', results from the distribution of their deviated trajectories (figure(2.21)).

At their exit from the sample, the scattered ions can meet other upper layer atoms and undergo more deviations on either side of their exit trajectory. If the detector is aligned with the corresponding outgoing crystal axis, one observes a drastic reduction of the scattering intensity at the scattering angle identifying that crystal direction. This phenomenon is called blocking and is also represented on figure(2.21). In this case, one observes the formation of a cone called 'blocking cone'. This phenomenon is the inverse process of channeling because it takes place during the exit of the ions.

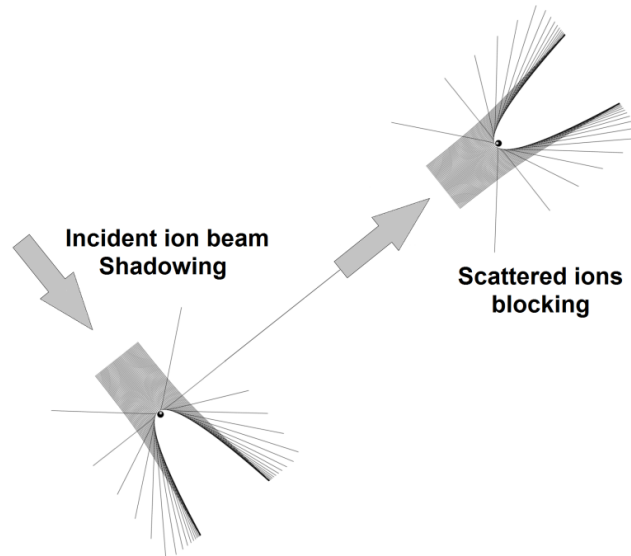


FIGURE 2.21: Representation of the blocking and shadowing phenomena in crystal. A shadow cone is observed at the entrance of the channeled ions inside the crystals. Indeed, the first atomic planes shadow those of the inner layers. The second blocking cone observed at their exit results from the inverse process. The atoms of the upper planes block the scattered ions during their exit from the sample.

The position of the detector has to be adjusted in consequence, in order to experience such a phenomenon. The evolution of the minimum intensity (blocking dip) with the energy can be associated to the deformation of the crystal with the depth. It relates on the atomic positions at a selected depth inside the crystal. It is not mandatory to channel the ions if we want to investigate the blocking in a crystal.

The discovery of the blocking phenomenon of ions in the 1960s was first employed for measuring the short nuclear lifetimes by measuring asymmetries in the axial blocking patterns[69, 70]. Then it was proposed to investigate lattice disorders in crystals[71]. Nowadays, it can accurately be exploited to investigate thin films with a medium energy technique like MEIS thanks to the detection systems of sub-nanometric depth resolution, contrary to RBS where it is around 10 to 20 nm. Blocking is also a useful way of investigating micro-strains in crystals[62]. Actually, this analysis mode is possible if one focuses on the analysis of the ions scattered at a fixed energy (i.e. fixed depth) along a selected crystal direction (or blocking direction). The combination of channeling and blocking (named as double alignment) for instance helps reduce the contribution of the ordered crystal in order to investigate the existence of structural defects[72].

#### 2.2.4 Analysis protocol for 3D FDSOI nanostructures using MEIS

In the previous paragraph we have presented the characterization methods of materials using ion beam analyses. When we are dealing with the samples of relatively simple

geometrical structure such as 2D materials, some of the constraints we can worry about may be their preparation or conservation conditions. Also, the analysis conditions have to be taken into consideration, mostly in the case when we are working with the samples which are very fragile or sensitive to some facts like a long beam exposition time for instance. But when it comes to 3D structures, in addition to all the constraints we just mentioned, we have to pay attention on the methodology we should adopt for their investigations. Because we will have to deal with several critical parameters such as the non regularity of the geometry, their shapes, dimensions, their chemical compositions, etc. Given that we are looking for information concerning the implantation profiles of the dopants in our 3D structures, we think that it is necessary to establish a suitable analysis protocol.

### Presentation of the problem

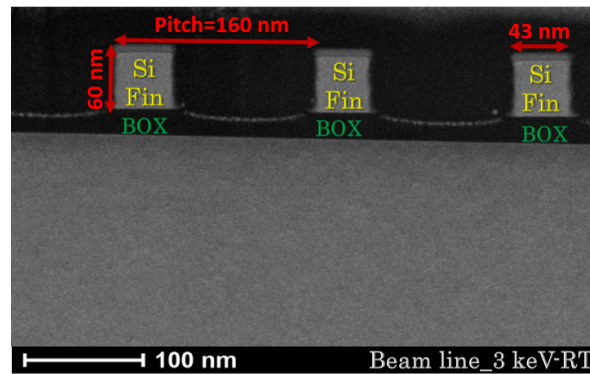


FIGURE 2.22: TEM image of the 3D line grating .

The aim of using the MEIS technique is to analyze the doping conformity, assess the total dose of the dopants in each face of the Fins, and possibly the damaging rate caused by the implantation. The good depth resolution available with this technique affords the study of these types of nanostructured samples. However, the weak lateral resolution is not sufficient to allow easy analyses. Because the dimensions of the beam ( $0.5\text{mm}\times 1\text{mm}^2$ ) are by far larger than those of the lines as can be seen in the image of figure(2.22).

We mainly want to investigate the implantation of the dopants and the induced damages at the sidewall faces, simultaneously with those of the top faces. By looking at figure(2.22), we see that it will require an adequate methodology of analysis if we want to highlight the spectra of the dopants. The idea is to minimize the scattering signal of the bottoms so that it can not merge with those of the top and sidewall faces. That is why the geometry of the analysis should be affordable for the sidewall and top faces. The implantation also being performed at the bottoms, the analysis geometry should at the same time afford it. One of the best approach is to hit the patterns from the

sidewalls, by choosing the experimental parameters accordingly. It means that we have to incline the sample at a certain angle of incidence so that the beam can hit a wide area of the sidewalls, by discriminating the scattering events in the buried oxide as much as possible. By doing this, we should be able to separate the dopants' peak of the tops and sidewalls from that of the dopants located at the bottoms. This means that one should carefully think about the incidence angle. Also, the scattering angle should be chosen such that only the ions scattered by the As atoms from all over the Fins can contribute to the surface edge of the As peak, and those scattered by the As atoms implanted at the bottom be shifted towards the lower energy range. Furthermore, if we want to highlight the damages' peak of the top SOI-Si film of the patterns it will certainly encompass the signals of the top and sidewall faces when the lines are inclined. We can nevertheless achieve this by choosing an incidence direction of the projectiles that matches with a crystallographic axis of silicon.

Although the incident ions will not directly hit the bottom during their penetration inside the nanostructure because of the shadowing effects by the neighbouring Fins, the scattered ions from that part of the sample will also contribute in the scattering event. The projectiles should be oriented at an incidence angle  $\theta_i$  chosen between  $0^\circ$  and  $\arctan(\text{height}/(\text{pitch} - \text{width}))^\circ$ , and that should allow: a good channeling, a large coverage of the sidewall faces and the minimization of contribution of the bottom.

### Solving attempt

#### Choice of the incident projectile: $\text{H}^+$ or $\text{He}^+$

The incident particles we shall use should help us to take a full advantage from the properties of the ion-solid interactions. For example, the damaging effects resulting from the interactions of high energy charged particles with the atoms by traversing the extreme surface of a material should significantly be minimized. Since the material we are dealing with is Si, we have to check what could be the best choice between the proton ( $\text{H}^+$ ) and alpha ( $\text{He}^+$ ) particles to probe it. The dimensions of the patterns as presented in figure(2.22) impose a careful choice of the probing projectiles so that the Fins do not suffer from the impacts of the beam when it probes the whole 60 nm (height).

The 200 keV protons ( $\text{H}^+$ ) used as incident particles for the investigations of these thin and fragile Si-Fins appears as the best choice because of some significant advantages they afford from a physical point of view. For example, protons have a large stopping power and low energy straggling into silicon (see section2.2.3.3). The top images of figure(2.23) display the ranges of 200 keV hydrogen (left) and helium (right) used as projectiles into

silicon of  $2.5\mu\text{m}$  thick. It can clearly be seen that hydrogen has the largest penetration depth. From these same images, we can obviously deduce that the damages generation in the near surface region is significantly few when employing protons, compared to alpha particles. The 'cloud' formed by the incident He projectiles as displayed in the graph (b) of figure(2.23) evidences their low penetration ranges, and the graph (c) of the same figure indicates the accumulation of the damages that they generate at shallower depth, mostly in the region of interest. From an experimental point of view, protons have a very weak damaging impact on the sample in contrast to alphas, nevertheless they create damages beyond the first 60 nm of interest. The pictures to fuel our arguments are given in the curves of figure(2.23(c)), corresponding to the damages' profile resulting from the displaced silicon atoms caused by the incident proton and alpha projectiles, respectively.

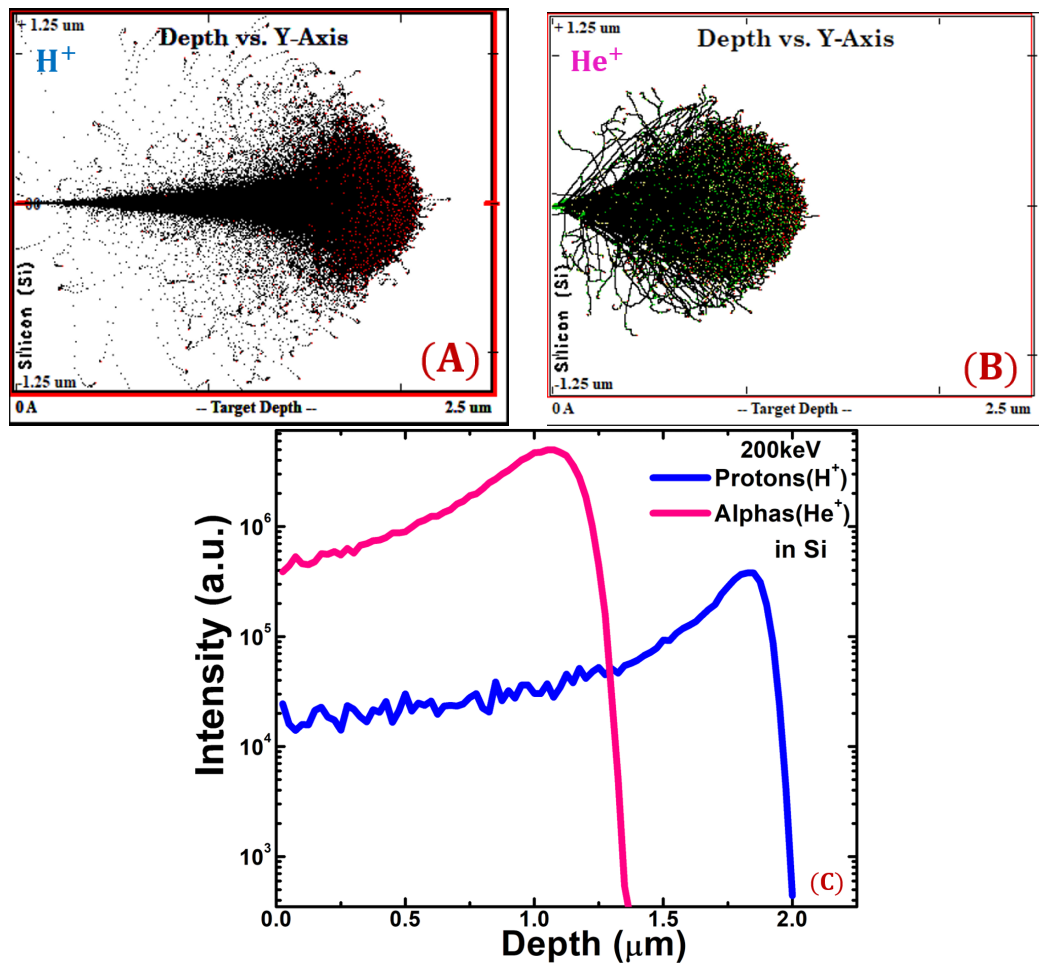


FIGURE 2.23: Comparison of the penetration ranges of 200 keV hydrogen (left) and helium (right) into Si. The simulations were performed with SRIM[25]. The associated curve at the bottom are the profiles of the displaced Si atoms.

Choice of the incidence direction and the scattering angle

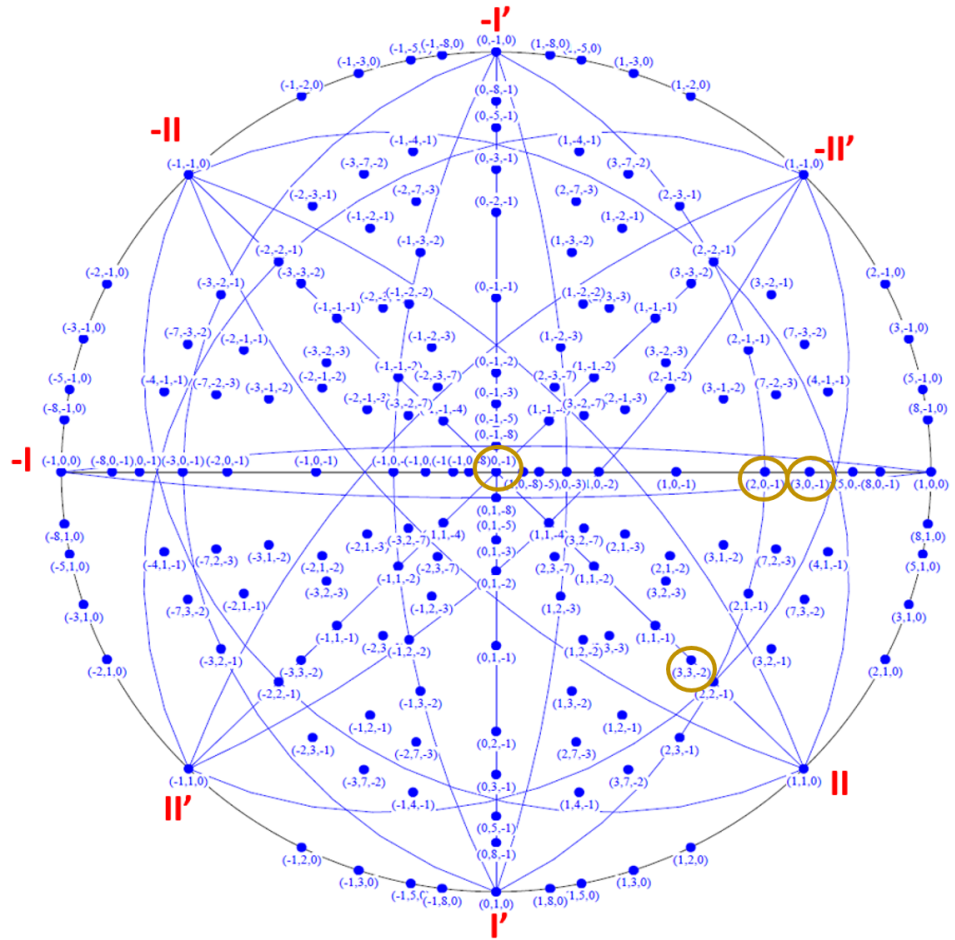


FIGURE 2.24: Stereographic projection of FCC silicon along the  $\langle 001 \rangle$  crystal direction. The convention we adopted for the crystal axes orientation is (a,b,c), we have encircled the investigated crystal directions.

The geometry as well as the dimensions of the patterns do not allow an easy choice of the incidence angle. Moreover, the investigation of defects using channeling will certainly limit the crystal direction to target. In the crystallographic projection of figure(2.24), we observe that as the indices increase, the crystal directions are getting close. Consequently, the ions channeling becomes difficult because the critical angle of channeling ( $\Psi_{1/2}$ ) is reduced. Therefore, we need to choose a particle which, in function of its incident energy, has a value of  $\Psi_{1/2}$  much smaller than the one imposed by the atomic directions, so that it can discriminate each of them. The curves of figures(2.25(a-c)) show the evolution of  $\Psi_{1/2}$  with respect to the incidence energy for protons and alphas particles channeled along the  $\langle 201 \rangle$ ,  $\langle 301 \rangle$  and  $\langle 332 \rangle$  directions for example. In the three graphs, the advantage is given to the 200 keV protons because they provide the smaller value of  $\Psi_{1/2}$ . However, it is not the case when the alpha particles are employed for the same incidence energy because at 200 keV, their  $\Psi_{1/2}$  is larger. If one would like to have a value of  $\Psi_{1/2}$  equivalent to that obtained with protons by employing  $\text{He}^+$  as incident projectiles,

their incident energy has to be augmented up to about 300 keV, but the inconvenience of this increase in the incidence energy is the degradation of the depth resolution (see section(??)).

We have investigated several crystal directions along which they should be oriented by exploiting the stereographic projection of figure(2.24). Precisely, the investigated directions were  $\langle 201 \rangle$ ,  $\langle 301 \rangle$  and  $\langle 332 \rangle$ . The two firsts channeling directions originate from the (100) azimuthal plane, labelled by the red Roman number as 'I' in figure(2.24) which is easy to localize experimentally in Si(001). While the third crystal axis takes its origin in the (110) azimuthal plane, labelled as 'II' in the figure(2.24) which is at  $45^\circ$  from the precedent one. The incidence angles corresponding to the  $\langle 201 \rangle$  and  $\langle 332 \rangle$  is  $64^\circ$  and the one corresponding to  $\langle 301 \rangle$  is  $72^\circ$ , respectively. These angles correspond to large inclinations of the sample so that the beam can hit a large area of the sidewalls by simultaneously covering the top surfaces.

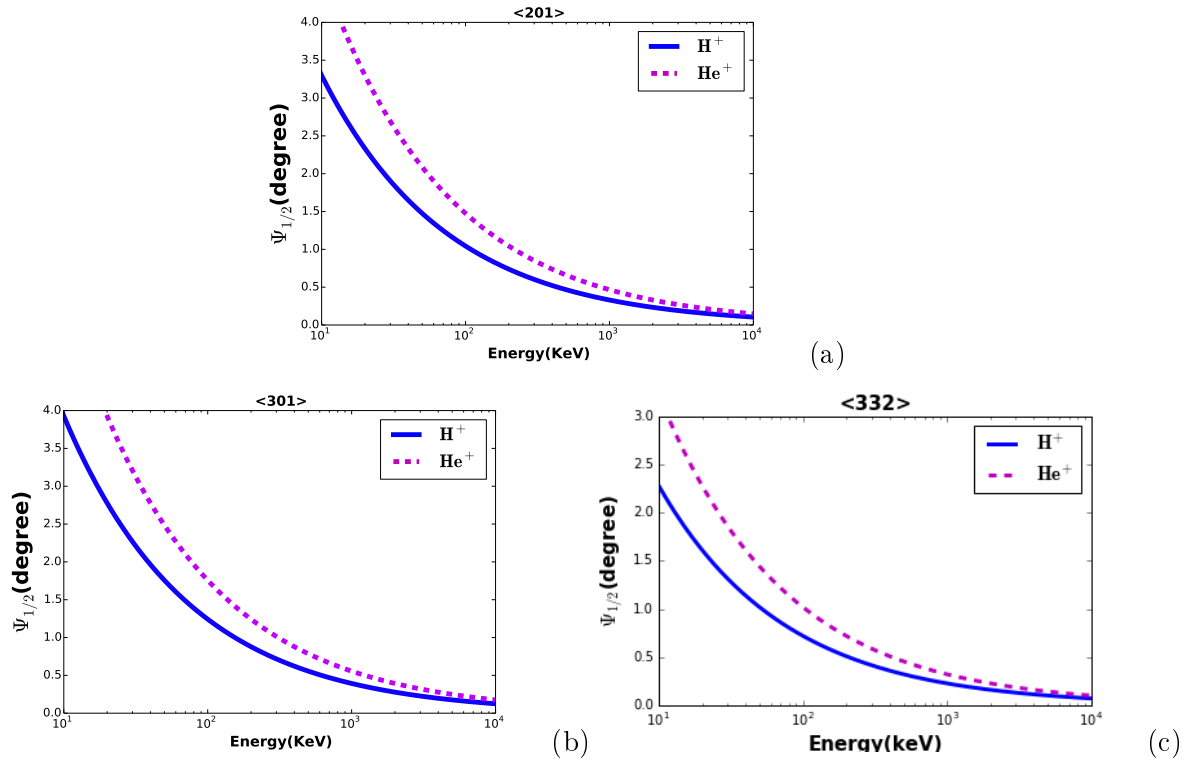


FIGURE 2.25: Comparison of the evolution of  $\psi_{1/2}$  for  $H^+$  and  $He^+$  along the incidence directions  $\langle 201 \rangle$  (a),  $\langle 301 \rangle$  (b) and  $\langle 332 \rangle$  (c) of the crystal Si.

As the ions penetrate the surface of a material containing defects, they are more likely to be deviated from their incidence direction because of the displaced atoms from the lattice sites that they encounter. Since the ingoing path length increases proportionally to the incidence angle ( $\theta_i$ ), in the law of  $1/\text{Cos}(\theta_i)$ , a direct consequence is also the drastical increase in the deviations of the projectiles' trajectories along their in-going channeling direction. This is also known as the ions' dechanneling that has an influence

on the minimum yield too. It leads to an incredible augmentation of the scattering yield in the subsurface (non implanted) regions inside the Si-crystal. A deeper study on the choice of an incidence direction by tacking these effects into consideration, brought us to draw the evolution of the minimum yield in function of the thickness of the amorphous layer traversed by the ions within the Si-film. These curves are displayed in the graphs of figures(2.26(a) & 2.26(b)). They were obtained on a bulk unimplanted (virgin) silicon and on an implanted SOI Si, however, having a good crystal quality beneath the implanted region. We see that whether in channeling + blocking or only in channeling modes, the incidence of  $64^\circ$  corresponding to the crystal directions  $\langle 201 \rangle$  and  $\langle 332 \rangle$  displays a lower minimum yield compared to that of the  $\langle 301 \rangle$  direction. This indicates that it will not be easy to obtain good channeling conditions if one choose to work at an incidence of  $72^\circ$ . Therefore, we have chosen to focus on the incidence angle of  $64^\circ$  corresponding to the crystal direction  $\langle 201 \rangle$  or  $\langle 332 \rangle$  according to the azimuth plane and which matches with the horizontal orientation ( figure(2.32)) of the line gratings, and a scattering angle of  $-135^\circ$ . This scattering angle has been chosen in consequence, since it favors a maximum contribution from the sidewalls too.

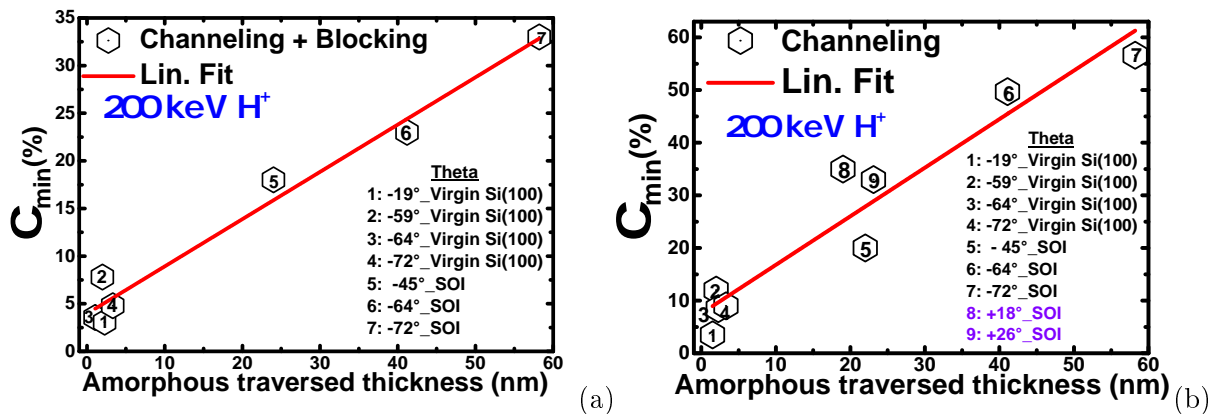


FIGURE 2.26: Evolution of  $\chi_{min}$ (%) with respect to the thickness of the amorphous layer traversed by the incident ions: in channeling + blocking mode(a) and in channeling mode only (b).

Indeed, the experimental conditions require that the etching line of the Fins should be strictly parallel to the horizontal direction, in order to have the line grating strictly vertical. This means that the channeling plane in which we will be working should also meet these conditions. We found that the one matching with all these requirements in the case of the 3D patterns studied in the present work is the (110) plane. The crystal direction corresponding to the angle of  $64^\circ$  in that plane is  $\langle 332 \rangle$ . The objectives of these preliminary studies were to find a suitable protocol for the characterization of these 3D nanostructures using MEIS.

## Summary of the protocol

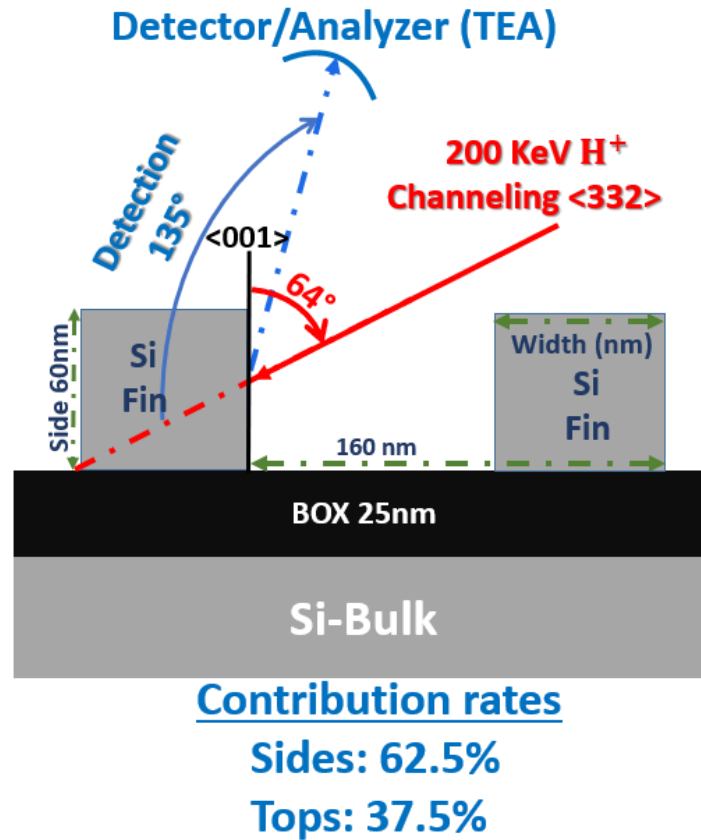


FIGURE 2.27: Ideal protocol for the characterization of Si based patterned fin shaped nanostructures of SOI types.

The drawing of figure(2.27) resumes all the steps of our investigations for the establishment of this protocol. It has been adopted for the analysis our 3D nanostructured samples. The sample should be inclined at  $-64^\circ$  so that the incident 200 keV  $H^+$  particles be channeled along the  $\langle 332 \rangle$  crystal direction. The scattered ions are collected at  $135^\circ$ , which is an angle corresponding to the blocking directions either along  $\langle 114 \rangle$ . The contribution rates of each faces are displayed on the drawing. They were computed by taking all the parameters of this protocol into consideration. In this case, we found that the flank surfaces will be contributing the most in the scattering geometry.

Alongside the previous protocol aiming at investigating the whole Fins by favoring the scattering events at the sidewalls, we also studied another geometry in normal incidence where the ions hit the structure vertically. The targeted objectives are thus to probe the dopants' profile all along the sidewalls and those eventually inserted deeper inside the Fins, and the total contribution of the tops. We will then compare the profiles of dopants in these two geometries. The scattering angle is also chosen in consequence so that one can collect the maximum scattered ions from the sidewalls while the signal resulting from

the scattering off arsenic atoms implanted inside the Box be shifted towards the lower energy ranges. The schematic drawing of this geometry is displayed in figure(2.28). The results of the measurements that were obtained will be presented and discussed in the next chapter.

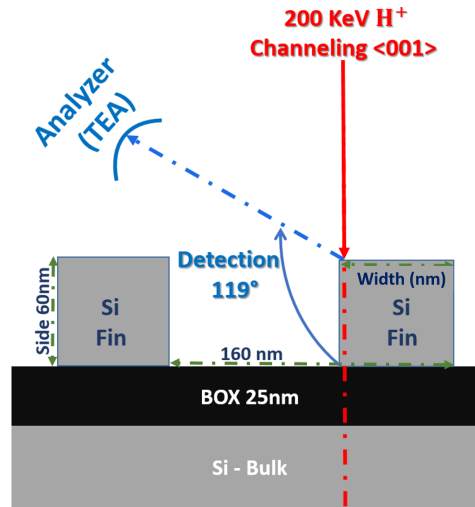


FIGURE 2.28: Analysis geometry in normal incidence for the characterization of the Si-fin shaped nanostructures of SOI types.

#### 2.2.4.1 Data acquisition

##### Energy-Angle acquisition

With an acceptance angle of  $20^\circ$  allowed by the detection system as described in section(2.2.2), the data can be acquired by sweeping the energies or angles (Theta, Phi and Tilt) in a pre-defined window, for a fixed number of scans. A scan is itself divided into a given number steps to sweep all the values defined over a fixed.

##### Energy scan

The energy sweep is realized at a fixed scattering (or TEA) angle. In this case, the number of steps that allow to fulfill one scan is delimited between a minimum and maximum energy ( $E_{Min}$  and  $E_{Max}$ ). These energies are assigned from the configuration window where the operator enters all the parameters of the acquisition. The measurement time will depend on the assigned dose for each step and obviously the number of scans to run before getting a correct image.

The energies to be scanned in order to obtain an image are proportional to the voltage applied to the electrodes of the analyzer. Indeed, it is the voltage applied to the electrodes which is step by step varied, so as to correspond to all the energies fixed in the scanned energy window. All the ions scattered with an energy included in that interval will be counted. A step is ended up when the integral dose is reached. This dose is computed by the time integration of the current received by the sample. This integration is executed by calculating the area defined by a curve described during a scan. The current received by the sample is proportional to the number of incident ions and the secondary electrons emitted.

### Angular scan

The angular sweeps are realized at a constant TEA energy. It consists in following the angular distribution of the ions which are scattered at a fixed depth into the sample. In our experimental setup, the possible angular scans can be achieved around Theta, Phi and Tilt. The energy is fixed for an angular scan, and its choice is related to the in-depth location at which the scattering events take place. The parameters to enter from the configuration window are: the type on ions (H or He), the incident energy, the total dose per each angular steps, the number of scans. There are also parameters that are specific to the angular scans, they are introduced from the angular window. We have: the initial angle ( $\alpha_{begin}$ ), aperture resolution ( $\delta\alpha$ ), sweeping step  $h$ , final angle ( $\alpha_{end}$ ) and the total number of scans.

### 2.2.5 Exploitation of data

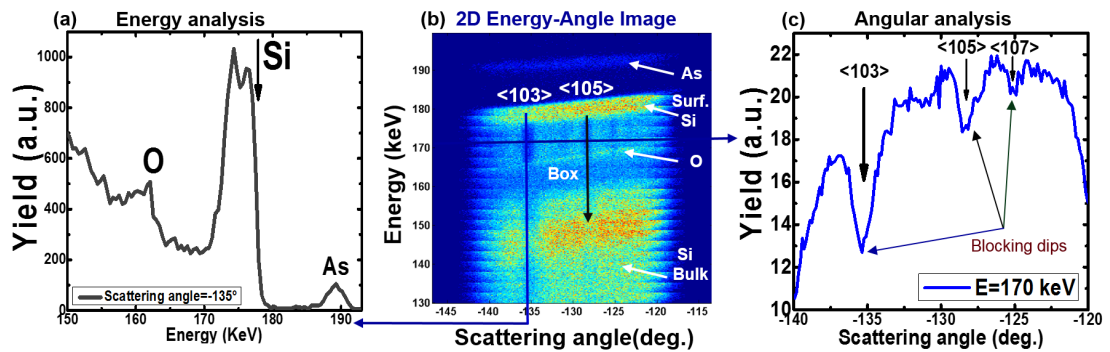


FIGURE 2.29: Presentation of the MEIS results. From the 2D energy-angle image in the middle(b), one can obtain either a 1D energy spectrum(a) or a 1D angular spectrum(c) by performing the cuts at a fixed scattering angle or scattering energy.

The data acquired during a MEIS experiment are represented by a 2D energy-angle image like the one displayed in figure(4.3(b)). It shows the results of the energy analysis of a

sample with the procedure that we described in the previous paragraphs. As we can see, we have one energy (vertical) axis and one angular (horizontal) axis. A third axis (color bar) can be defined as the scattered intensity axis (Yield). From the top to bottom of this image, we observe some parts having different intensity yields throughout the entire scattering angle window. They represent the signatures of any chemical element contained in the analyzed zones in the sample.

In the same image, we observe a drastic reduction of the yield all along the energy axis, at certain fixed values of the scattering angle, thus indicating the signature of blocking dips. The indexation of each of these crystal directions is made with the help of the stereographic projection and by using the equation  $|\theta_e| = |\pi - \theta_i - TEA(^{\circ})|$  (see figure(2.30)). The blocking dip is more marked at  $-135^{\circ}$  and  $-127^{\circ}$  because of the small critical angle, since the atomic positions at each of these angles within the crystal are favorable to its observation. Thereby reducing the eventual encountering with the other atoms during their exit from the crystal. In the case when we want to quantify the chemical elements and the damages, we have to perform a cut at a fixed scattering angle in the image, to obtain a 1D energy spectrum like the one shown in figure(4.3(a)). The concentration of each entities is obtained by simulating the experimental spectra. Also, by converting the energy axis to depth (in nm) we are able to give the depth profile of the chemical elements and damages.

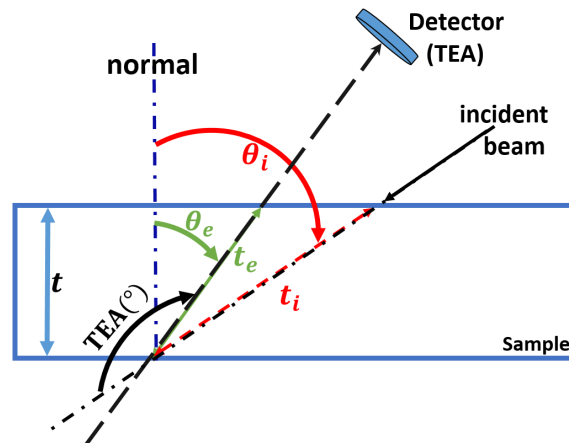


FIGURE 2.30: illustration of the in-going and out going trajectories in a sample of thickness  $t$  with the associated angles of: incidence ( $\theta_i$ ), scattering (TEA) and exit ( $\theta_e$ ).

The information regarding the surface structure or the atomic positions in the first 10 nm from the material surface, can be obtained by performing an angular cut at a given scattering energy (at a selected depth), then follow (for a given element) the evolution of the minima with respect to the scattering energy for instance. An example obtained from a cut in the 2D image of figure(4.3(b)) is displayed in figure(4.3(c)). Those we observe in the graph are the representations of the blocking dips.

### 2.2.5.1 2D simulations of MEIS spectra

To obtain complete information from the acquired data, the simulations of the spectra are of great help, they stand as deeper exploitations of the data presented in the previous paragraph. To achieve this goal, a software has been developed by D. Jalabert for the analyses of MEIS experimental spectra. The simulations are based on the calculation of the energy loss of the projectiles as they penetrate and exit from the sample.

The total quantity of the ions scattered from each layer in the sample is computed with respect to the experimental parameters presented below. One only detects charged particles with respect to their passing energy between the electrodes. For the simulations, a function considering the fraction of singly charged ions is used when computing the scattered intensity. Because it has an effect on the yield, mostly for the scattering off elements of low atomic number, due to the degradation of the ionization degree and the exit energy[73]. One thus obtain a 1D simulated spectrum by an iterative process, which can be compared with the experiment. In MEIS, the detector is of electrostatic type which deals with the charge of ions. The comparison of the simulated and experimental spectra will be presented in the next chapter.

One of the particularities of that software is that one can introduce a coefficient ( $<1$ ) which takes into consideration the morphology of a crystal layer. The approach we adopt to simulate a channeling spectrum for instance, is as follows: we introduce a factor representing the percentage of order in the crystal layer, in relation with the damages due to displaced atoms in the lattice. There are several information that we can get from the simulations of the spectra using this software. Namely, the thickness (by considering the appropriate density) of the crystal layer, the depth profiles of the damages, the percentage of the damaged layer, the quantity of elements. We would like to point out that the software only deals with 2D structures, and according to the number of layers they are constituted of, the procedure of building the input file for simulation is as described below.

- Experimental parameters
  - Incident particle(H/He):
  - Incidence ions energy(keV):
  - Scattering angle(degree):
  - Horizontal target angle(Phi)
  - Vertical target angle(Theta)
  - Detector resolution(%):

- Charge correction(Y/N):
- Number of layers:
- Parameters of each layer in the sample
  - Composition layer 1:
    - Density( $\times 10^{22}$  mol/cm<sup>3</sup>):
    - Layer thickness(nm):
    - Channeling rate (%):  $\vdots$

### 2.2.5.2 3D simulations of MEIS spectra using PowerMEIS

PowerMEIS is a software able to simulate the MEIS spectra of 3D structures of any geometrical shape such as the legos or cubes represented in figure(2.31), including their size distribution[74, 75]. The non uniformity in their shapes makes that the energy-depth relationship be no longer simple to express. Therefore, the spread in the ion energies and directions may lead to multiple scattering effects which degrade the depth resolution[76]. They are taken into consideration in the software in addition to the asymmetry in the energy loss underwent by the ions [77].

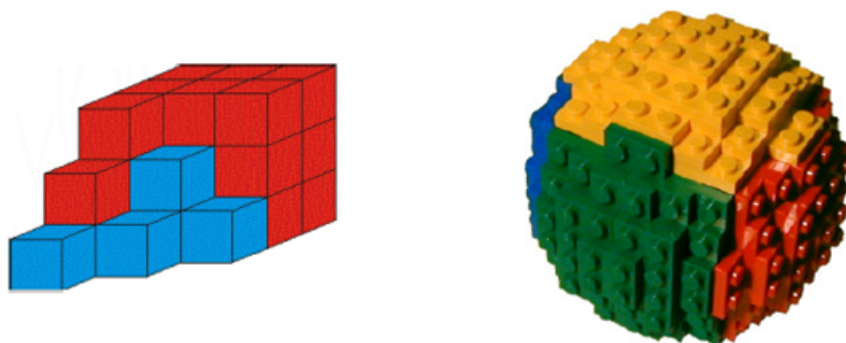


FIGURE 2.31: Example of the types of nanostructures one can simulate using PowerMEIS

### Principle of the simulations

The simulation of a MEIS spectrum obtained on a 3D structure by using this programme is performed in two steps. The first consists in generating a model matrix that best represents the whole sample. In the second step, one should build up the 'input file' that will be used to run the simulation via a simulation file. This file indeed contains the one of the matrix-model obtained in the first step and the other input parameters.

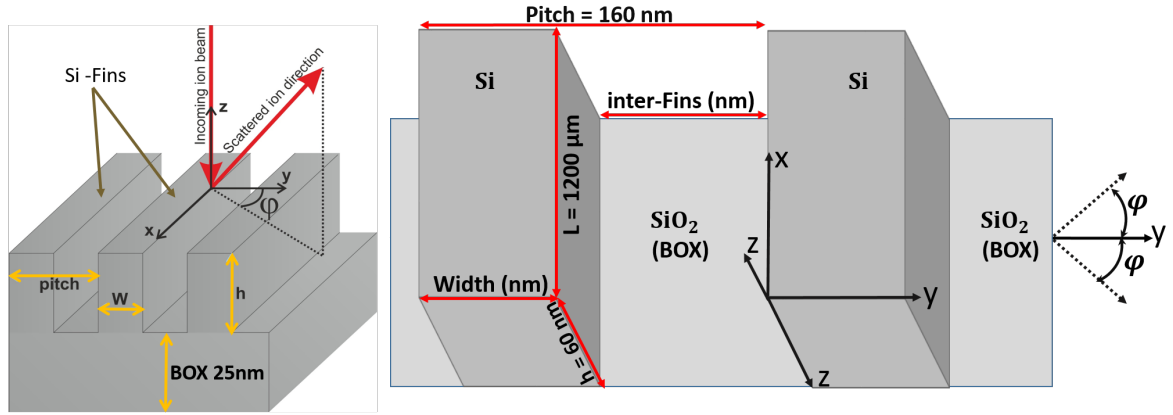


FIGURE 2.32: Left: example of the 3D Fin-shaped nanostructure of SOI type that we want to simulate its MEIS spectrum. The analysis geometry in normal incidence is illustrated. Right: zoom on two Fins with their associated dimensions. The different possibilities of orientating the etching line at an angle ' $\varphi$ ' with respect to the horizontal axis in the azimuthal plane are represented. The Si-bulk substrate is not represented on the drawings.

### -Modelling of nanostructures for PowerMEIS simulations

A 3D nanostructure can be modelled by the set of cubic bricks like those of figure(2.31) for example, where each color is attributed to a material or compound constituted of: chemical elements, a stoichiometry and density. In our case, the type of nanostructure we actually want to model is like the one presented in figure(2.32). In this figure, we observe that the nanostructure is made of different compounds (Si, SiO<sub>2</sub> or Box). The letters W, L, h and  $\varphi$  stand for the width, the length, the height and the azimuth angle, respectively. All these parameters are crucial for the generation of the matrix model of the nanostructure. There is no need to consider a large value of the Fins length, i.e. the dimension along the 'x' axis for the generation of the matrix. A small dimension along x will help save the computing time and the size of the file. This is an overview of the first step showing how the sample can be modelled.

In this project, we are dealing with 3D patterns that were implanted with arsenic by employing two different implantation methods (plasma and conventional implanter). Therefore, the next step (the most important) consists in modelling the implantation layers containing the dopants inside the Fins and the bottoms. The most efficient way of doing this is to use electron microscopy images in order to better represent them as well as the distribution of the dopants, if they are visible. This also stands for the previous step concerning the dimensions to use for the generation of the unimplanted nanostructure.

The modelling of the implantation layers consists in building small matrices of small volumes (thin layers) in the structure matrix. These thin layers (as shown in figure(2.33)) are elaborated at the surface of the Fins and the bottoms, in order to represent the

implantation in each part of the sample. Thus, figure(2.33) presents some examples of implanted nanostructures with the different cases that can be encountered. Let us suppose that arsenic was implanted at 9 nm at the top faces. If we want to model it with 6 thin layers like in the second image of figure(2.33) for instance, the thickness of each of them (defined from the script) will be  $9 \text{ nm}/6 = 1.5 \text{ nm}$ . However, those layers have the same thickness but not necessarily the same percentage of dopants. As indicated on the images of figure(2.33), each layer has its own color to which one can attribute a specific compound with a given stoichiometry. In the matrix file, each compound is represented by a number. The thickness of the whole implanted area, from one part to another in the nanostructure (as indicated by the arrows) is different. This particularity of the code is very important, mostly when we want to model the non conformity of the implantation.

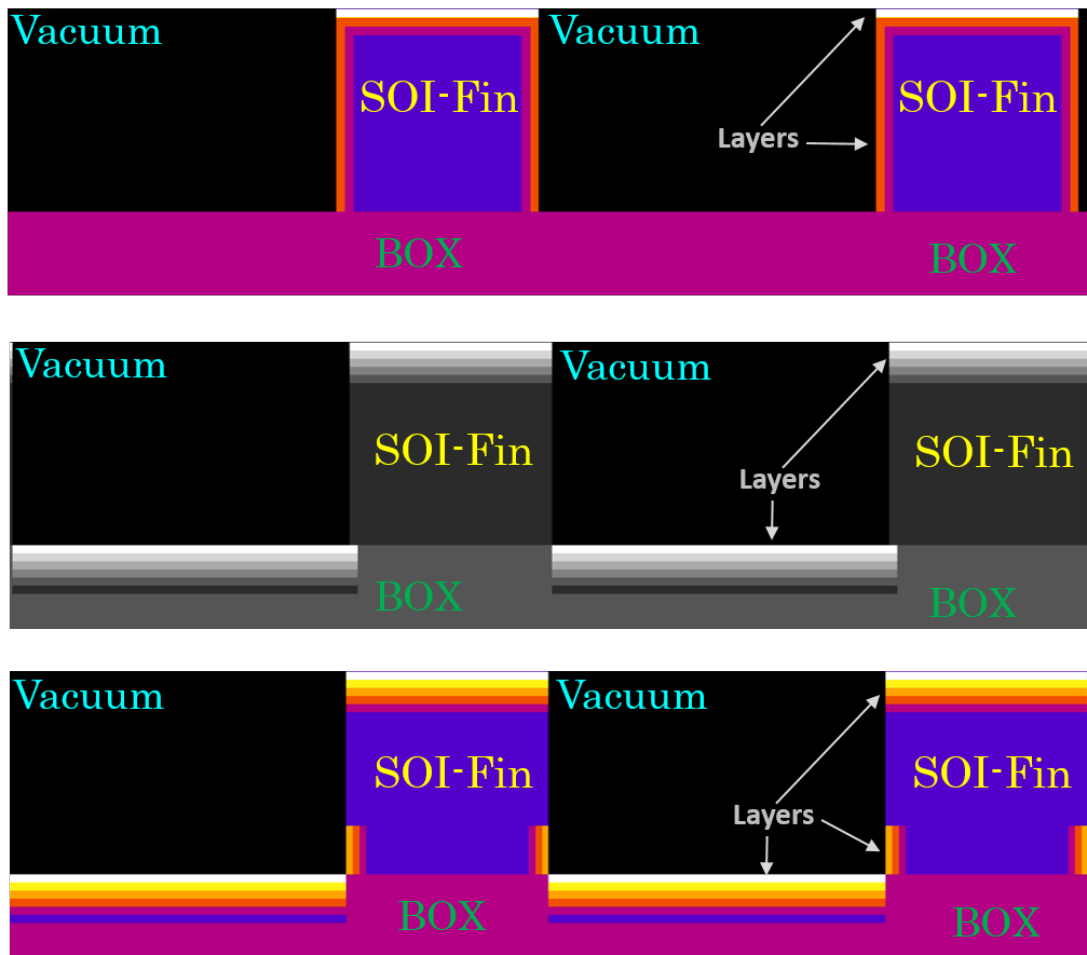


FIGURE 2.33: Different implantation profiles of the initial SOI nanostructure obtainable by modellings. The Si-bulk substrate is not represented. The images were generated by Python codes.

At this stage, we have terminated with the building of the matrix model and the implanted layers. Each dimension in nm should be converted into pixel by computing its ratio with the size of the smallest cubic volume (voxel) of lengths  $n_x$ ,  $n_y$  and  $n_z$  (along

the x, y & z directions) previously defined. The numerical files are of extension '.mtx'. It remains to elaborate the input file for the simulations.

The azimuth angle ( $\varphi$ ) is a fundamental parameter, describing the orientation of the line grating during the experimentations. Figure(2.34) shows that different orientations of the patterns lead to different features of the experimental spectra. One also observes the importance of choosing a good  $\varphi$  for a better analysis of the spectrum of the dopants. As shown in the image, their signal may display either a single peak or more, according to the orientation of the lines vis-à-vis to the incident beam. When the scattered ions exit across the lines one may observe two peaks that are better discriminated when the widths of the patterns are larger. But when the scattered ions exit from along the lines, one observes only one peak no matter their dimensions. If the beam spot is not totally focused on the line grating, it will also hit the 2D area surrounding the 3D patterns. This will be more significant in large incidence angles because the beam spot extends in the low of  $1/\cos(\theta_i)$ . The consequence is that the ions scattered from both the 2D and 3D areas will be collected, which affects the processing of the experimental results. The ideal case is to have  $\varphi = 0^\circ$  if one needs to investigate the contribution of each part of the nanostructure in the formation of the dopants' signal in the energy spectrum.

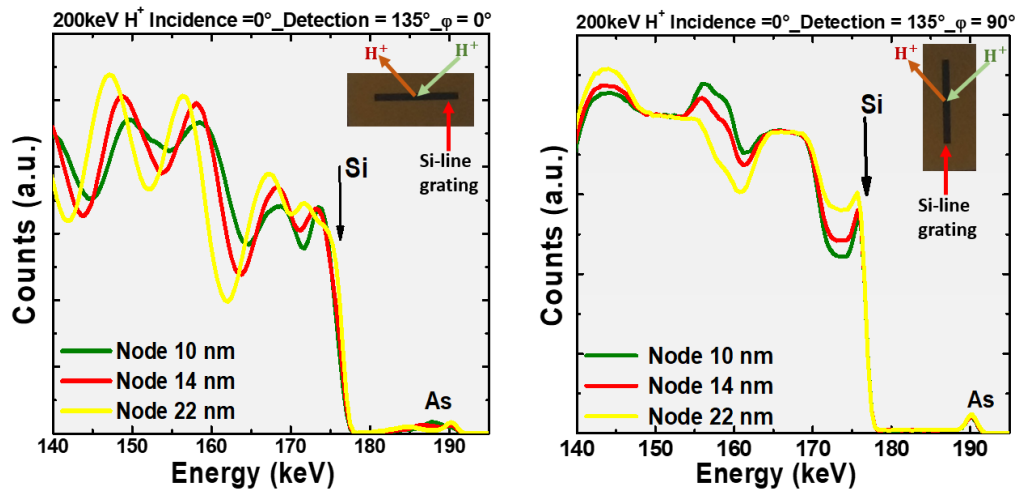


FIGURE 2.34: Example of 3D simulations of the MEIS spectra of the FinFET-like nanostructure of three different technological nodes implanted with As. The azimuth angle  $\varphi=0^\circ$  corresponds to the horizontal orientation of the etching line and  $\varphi=90^\circ$  corresponds to the vertical orientation.

### -Building up of the input file for PowerMEIS simulations

This is where the parameters for the simulation of the matrix generated as indicated in the previous sections are introduced. The name of the file is defined as 'configuringpowermeis', with the extension '.cpm'. A detailed description of the .cpm file can be found in [74, 75].

However, some important parts that are primordial for the simulations will be defined in the following lines.

**Header:** here we indicate the total number of compounds (*ncp*), chemical elements (*nEl*), their associated indexes as well as those of the layers, the simulation file name with the *.zip* extension. One will also find the analysis mode used, which is MEIS in our case. Indeed, the software is now capable to simulate the RBS, NRA and ERBS spectra.

**Matrix:** the dimensions *nx*, *ny*, *nz* (in pixel) of the matrix representing the nanostructure we want to simulate are indicated here. The name of the matrix file with the extension *.mtx* and the azimuth angle represented in drawing of figure(2.32) are provided here as well as.

**Simulation:** here we find some approximations taken into account for the computations in the software. We have the type of the algorithm (to choose), the number of iterations, the size of a voxel, the curve's line shape (e.g. EMG = Exponential Modified Gaussian), the cross-section correction, surface approximation (Y/N).

**Calculations:** this part of the input file indicates the physical principle on which the calculations and the simulations are based. One has to choose the model of the stopping power, straggling and the charge correction.

**Output:** this is where we fix the limits of the energy scale corresponding to the experimental spectrum we want to simulate. There are also the energy per channel (*dEnergy*) and the angle per channel (*dAngle*). All the other elements of this section can be introduced and/or modified via the PowerMEIS software during the simulations.

**Beam:** all the parameters regarding the beam are introduced here: the nature of incident projectiles (protons or alphas), atomic number, mass, incident energy and angle.

**Detector:** choose the type (electrostatic, ToF or magnetic), the resolution, the scattering angle.

**Element *i*** this is the part conferred to fill-in the information concerning any chemical elements *i* constituting the matrix and a compound, such as the: symbol (as in the periodic table), the atomic number and mass.  $i = 1, \dots, M$ , where *M* is the maximum number of elements.

**Compound *j***: here we introduce the information regarding the name, the stoichiometry of the compound '*j*' with the percentage of each chemical element '*i*' constituting that compound, the atomic density (in  $\text{g}/\text{cm}^3$ ). The indice  $j = 1, 2, \dots, M$ , where *M* is the maximum number of compounds. For example, the name of a compound can

be SiAs<sub>0.99</sub>, for a compound constituted of an oxide SiO<sub>2</sub> rich of 0.1% of As. We can choose to fix the density of this compound equals to that of silicon (2.3212 g/cm<sup>3</sup>).

Once the input file is filled-in, it remains to build up the simulation file with the extension *.zip*.

### The simulation software

If the matrix-model can be generated locally by a code using a known programming language, the simulations, however, take place in the online software. The open access version was used to perform all the simulations that will be presented in the third chapter of this manuscript. An overview of the online software is available accessible here [30] where one can find all the above mentioned contents of the input file. Some of the parameters concerning the beam, detector, physics, etc can be modified online. The thickness of the thin layers representing the implantation areas and constituting the matrix of the whole nanostructure should be defined from the modelling code, not online. Otherwise it will not be realistic and will not yield to good results. Last, one can choose the analysis technique with which the experimental spectrum was acquired. Some of the other ion beam analysis (IBA) techniques that can be simulated with PowerMEIS will be introduced in the next section.

## 2.3 Ion beam analysis (IBA)

The scientific discovery of the electron by J. J. Thomson in the 1897 and the atomic nucleus by Sir. Rutherford (assisted by H. Geiger and E. Marsden) in 1911, has permitted to think on several ways of efficiently exploiting charged particles in the areas other than nuclear physics, military, space[78], etc. The rapid expansion of nanosciences, principally in the domain of materials science research, has brought scientists to explore new techniques that could better analyze materials in the sub-micrometer scale.

Thus, the application of the ion beam analysis techniques for surface and interface investigations of materials in the second half of the 20<sup>th</sup> century has been of great importance. It has given another view to nuclear physics and ions beam, which was more or less employed for energy production[65, 66], in medicine or space. The fact that one can probe the structure of materials by just making them interacting with a beam of energetic particles was already a great breakthrough in the fields of particles physics and materials science. For example, the scattering of ions at the surface or beneath the surface of a

material can inform us on the atomic positions, crystallinity and even on its composition. However, the knowledge that we get from the samples analysis using ions beam may differ according to the nature of the interactions and the reactions that take place into the sample. Therefore, several techniques have been developed in order to collect information relatively to a targeted experiment using ion beam analysis. Having as origin the interaction between the incident ions and the target atoms, some of the techniques that will be presented in the following sections are classified in terms of the type of phenomena. We have:

- elastic scattering by the nuclei: MEIS, Rutherford Backscattering Spectrometry (RBS) and Energy Recoil Detection Analysis (ERDA).
- nuclear reactions: Nuclear Reaction Analysis (NRA),
- mass analysis: Time of Flight-Secondary Ion Mass Spectrometry (ToF-SIMS)

### 2.3.1 IBA principles and techniques

Ion beam analysis consists in sending a beam of monoenergetic particles onto a target material, then collect information resulting from its responses to the beam through the analysis of the emitted entities. The flux of the incident ions should be low enough in order to avoid the target damaging. During their interactions with the nuclei, ions lose a part of their incidence energy. At this level, several situations can happen. The incoming ions can be scattered by the target nuclei with an energy  $E$  proportional to their initial energy  $E_0$ . The study of the scattered energy  $E$  is at the basis of Rutherford backscattering (RBS) techniques and MEIS. The elastic collisions between ions and the target nuclei may either induce the recoil of the atoms or give rise to an emission of other particles due to nuclear reactions provoked by the incident ions of energy in MeV range that have defeated the coulombian barrier. The former process is at the origin of the elastic recoil detection analysis (ERDA) and the latter one is exploited in nuclear reaction analysis (NRA). There exist other IBA experimental techniques (e.g. ToF-SIMS) using very low energy ranges comparatively to those mentioned in the previous lines. In ToF-SIMS however, it is the masses of the ejected secondary ions that are analyzed for the depth profiling of all the chemical elements in presence and possibly their quantifications. Some of these experimental techniques have been presented in the next paragraphs.

#### Rutherford Backscattering Spectrometry (RBS)

The measurement principle of the RBS technique is also based on the detection and analyses of the angles and/or energies (in MeV) of the scattered  $H^+$  or  $He^+$  particles.

RBS is capable to provide the surface composition of the samples. It is one of the best technique utilized to quantify heavy elements in light matrices. The high energy range of RBS does not allows this technique to reach a good energy resolution, consequently with a depth resolution  $\sim 10$  nm because of its detector is not sufficient for a full study of the materials surface. But a technique such as MEIS is very performant in such investigations thanks to its good depth resolution. When it comes to evaluate light elements either in heavy or light matrices, this technique is limited by its low sensitivity in their detection. The complementary techniques to study this particular situation in the field of ion beam analyses in the high energy ranges are nuclear reaction analysis (NRA) and elastic recoil detection analysis (ERDA) for instance. Time of Flight secondary ion mass spectrometry can provide same information regarding the quantification as well as the depth profiles of the elements in the very low energy ranges (keV) with good detection limit.

## 2.4 Time of flight-Secondary Ion Mass Spectrometry (ToF-SIMS)

A complementary technique for chemical element analyses with good depth resolution is secondary ions mass spectrometry (SIMS). The detection limit can be improved (down to particle per billion (ppb)) by focusing on the time of flight (ToF) of the secondary ions. The association of the ToF analysis method and SIMS (ToF-SIMS) makes this technique highly sensitive to a very large majority of the chemical elements available in the periodic table and their isotopes.

### 2.4.1 Principle

ToF-SIMS is a technique based on the analysis of the mass of the secondary ions ejected from the surface of a sample of solid matrix, after it has been struck by the incident ions. Monoatomic ions or molecules (clusters) can be employed as primary beam. The interaction between the primary ions and the first atomic layers induce several collision cascades, which in turn give rise to the sputtering of the surface from which secondary ions are extracted along an 'analysis column'. The sputtering in question can be explained through the model developed by Sigmund for example [79]. The dimensions of the irradiated area are defined in the micrometer ( $\mu\text{m}$ ) range and also depend on those of the primary beam. The information on the material's composition as well as the in-depth profile of any chemical species result from the detection and the analysis of the different masses of the secondary ions. An overview of the ToF-SIMS instrument equipped with a dual beam column as well as the sample environment is presented in figure(2.35).

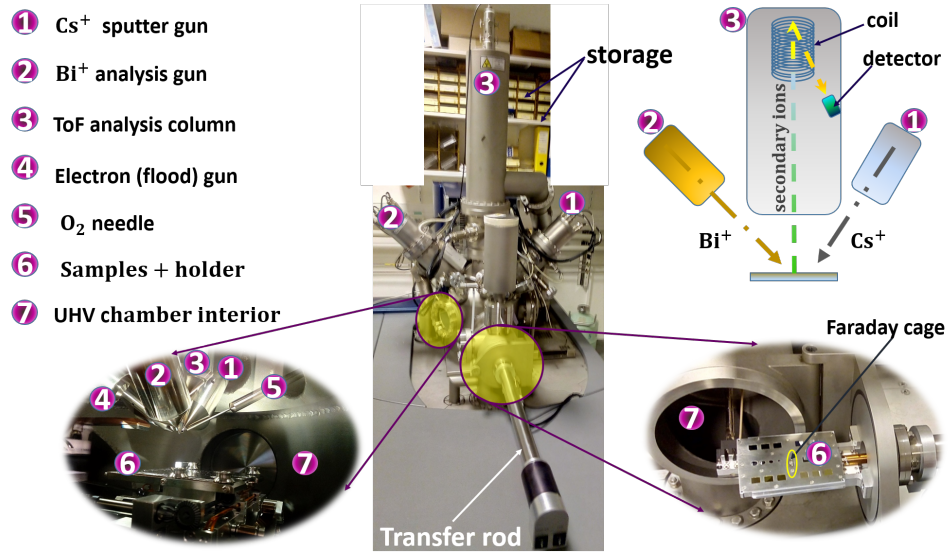


FIGURE 2.35: Image of the ToF-SIMS instrument provided by IonToF with the annotations of the different parts. The top-left drawing indicates the schematic principle of the ToF analysis mode.

#### 2.4.1.1 Presentation of the instrument

##### Primary ions sources

The ToF-SIMS setup of figure(2.35) hosts two different ion guns that play different roles: a sputtering gun and an analysis gun. The former has the role of profiling the specimen's surface in order to provide a large sputtering efficiency[80]. It defines the size of the area hit by the sputtering beam that forms a crater on the surface. The latter employs a Bi<sup>+</sup> beam to ensure a good lateral resolution during the analysis of the secondary ions extracted from the area delimited within the crater. The sputtering beam is emitted sequentially with a current of few dozens of nA[80] to abrade the surface. While the analysis column generates the beam in pulsed mode with a pulse period  $\leq 1$  ns. The shorter the pulse period, the better the resolution. However, a too short pulse period affects the sensitivity of the ToF-SIMS instruments because the number of the incident primary ions is reduced. The beams delivered by the two guns are oriented onto the sample at an incidence angle of  $45^\circ$  with respect to its surface normal. The type of the primary ion sources one would like to use depends on the targeted information, the nature and the sign of the secondary ions or the desired lateral resolution. In general, the ion sources utilized on the SIMS instruments are designed to generate beams of high brilliance and ion density, with the acceleration energy ranging from  $\sim 0.5$  keV to  $\sim 25$  keV. The incident projectiles that are frequently used are Ar<sup>+</sup>, Bi<sup>+</sup>, Ga<sup>+</sup>, Cs<sup>+</sup>, O<sub>2</sub><sup>+</sup> and O<sub>2</sub><sup>-</sup>. One can also find the sources emitting the beams constituted of polyatomic ions such as Ar<sub>n</sub><sup>+</sup>, C<sub>60</sub><sup>+</sup>, Bi<sub>3</sub><sup>+</sup>, etc.

The  $O_2^+$  ions are often utilised for the detection of the positively charged species of weak ionisation energy like silicon and carbon[81]. While the sources of alkali  $Cs^+$  are used to investigate negatively charged secondary ions of large electrons affinity such as H, C, O and S[81]. They are also efficient in the analyses of secondary ions of  $MCs^+$  types, where M is the mass of the ejected element that associated with the incident  $Cs^+$  when exiting the sample[80]. Nowadays,  $Bi^+$  is more employed in the place of  $Ga^+$  because of the better lateral resolution they afford. For the sake of optimizing the detection and analysis of organic species, polyatomic sources are often preferred to monoatomic because of the good sputtering efficiency and extraction of molecular ions.

### Sputtering regimes

There are two different sputtering regimes in SIMS analysis, dynamic and static. In dynamic regime, the analysis is carried out under a continuous primary beam of current of few nA, hitting an area defined within the crater. The surface is constantly renewed but the depth range is restricted to the firsts atomic layers. The achievable depth resolution can be down to sub-nm in the low energy range ( $\sim 0.1$  keV) corresponding to this technique. This regime is useful for the depth profiling of the elements below the surface, it is employed on magnetic and ToF-SIMS spectrometers.

In static regime, the primary beam is emitted in pulsed mode, i. e., it is no longer continuous but rather hits the sample discontinuously with a very short time interval. It thus consists in reducing the flux of the primary ions to the doses less than  $10^{13}$  ions/cm<sup>2</sup> for instance, thereby preserving the sample surface from heating. This is achieved either by reducing the current directly generated by the sputtering gun or by diminishing the pulse periods. Thus, one optimizes an extreme surface analysis at monolayer scale, by minimizing the degradation by the ion beam. This regime is mostly exploited in the ToF-SIMS instruments.

### The ToF-secondary ions analyser and detector

The secondary ions are analysed through the vertical column (figure(2.35)) by computing their time of flight  $t$  from the specimen to the detector with the formula given by equation(2.11). The analysis is performed in micro-probe by correcting the drift along the distance between the secondary ions and the detector. This mode consists in synchronizing their detection with the primary sweeping such that the detected signal corresponds to that of the beam on the sample surface. The top-right drawing of figure(2.35) illustrates the sequencing of both the sputtering and analysis beams. The achievable mass resolution (equation(2.12))[80] varies with the mass of the analyzed species, the detection

time and the pulse period. Thus, it will be better to identify species of light masses than those of large masses.

$$t = x \sqrt{\frac{m}{2qU_e}} \quad (2.11)$$

$x$  is the analyser's length,  $U_e$  is the acceleration voltage applied to charged particles,  $m$  and  $q$  are the mass and charge of the secondary ions, respectively.

$$\frac{\Delta M}{M} = \frac{t}{2} [(\Delta t_p)^2 + (\Delta t_{drift})^2 + (\Delta t_{res})^2] \quad (2.12)$$

$\Delta t_p$  is the length of a primary pulse,  $\Delta t_{drift}$  is the analyser drift and  $\Delta t_{res}$  is the analyser resolution.

The detector utilized in the instrument is of electron multiplier type. Actually, it is equipped with dynodes that have as role to multiply the number of electrons emitted by each secondary ions impinging on the first dynode, which is considered itself as an ion-electron converter[80].

### The sample environment and holder

The environment surrounding the sample in the chamber (see figure(2.35)) is maintained under ultra high vacuum at a level ranging from  $10^{-9}$  down to  $10^{-10}$  mbar. A maximum number of 17 samples can be mounted on a holder which in turn, is able to move along the horizontal and vertical axes and affords an out of plane tilt at an angle defined with respect to the sample normal. The computer controlled navigation of the holder is assisted by a CCD camera that allows the monitoring of the analyzed areas and the abrasion crater. The measurement of the beam current is possible thanks to a Faraday cage. A low energy electron gun (flood gun) is used to compensate the charging effects that happen in the chamber environment in the case when the analyzed sample is an insulator. In the context of SIMS analysis, these effects result from the modification of the local surface potential due to the secondary electron emissions that leads to a localized positive discharge. The consequence of the surface charging is the alteration of the energy of the secondary ions, hence their time of flight and trajectory.

#### 2.4.1.2 Depth and concentration profiling.

The intensity  $I^m$  acquired during a measurement on a sample containing a species  $m$ , can be expressed by the formula given in equation(2.13).

$$I^m = I_p \cdot Y_{tot} \cdot \gamma^m \cdot \tau \cdot \eta \cdot c^m \quad (2.13)$$

Where:  $I_p$  is the primary current,  $Y_{tot}$  the total sputtered yield,  $\gamma^m$  the ionization probability,  $\tau$  the transmission of the analysis system,  $\eta$  is the detection efficiency and the  $c^m$  is the fractional concentration of the species  $m$ . To avoid errors in the concentration calculation, the intensity of the species of interest  $m$  is often 'point-to-point' normalized to the matrix signal[82]. The conversion of the intensity into concentration, as well as the sputtering time into depth can be achieved by using calibration samples of known concentration of the species  $m$  and its depth distribution. This helps profile and possibly quantify the species of interest in the analyzed sample. This approach was adopted for the depth profiling of the elements such as hydrogen and carbon into the FDSOI ultra thin layers studied in this project. Another alternative for the calibration is to use the relative sensitive factors (RSF). The RSF can be literary defined as the ratio of the signal intensity to the concentration of the elements, its mathematical expression is proposed in equation(2.14)[83].

$$RSF = \frac{\text{impurity ion intensity (counts/s)}/\text{impurity density (atoms/cm}^3\text{)}}{\text{reference ion intensity (counts/s)}/\text{reference density (atoms/cm}^3\text{)}} \quad (2.14)$$

If the RSF method is adopted for the depth or concentration profiling, its values have to be measured on standard samples. Consequently, a successful calibration requires that one uses the same experimental conditions as for the specimen studied.

## 2.5 X-ray diffraction analysis technique

X-ray radiations were discovered by Wilhelm Conrad Röntgen in 1895. They were identified as such because of their unknown nature from the principles of physics[84]. In 1912, Von Laue discovered the diffraction of x-rays by the crystals and this breakthrough in the field of materials research also served as a proof of the wavy nature of the x-rays[26, 85]. W.H. and W.L. Bragg pioneered the use of x-ray diffraction to characterize the crystal structure, this category of energetic radiation was thereafter adopted as a new tool for studying crystals. X-rays are electromagnetic radiations with the wavelengths that can correspond to different energy ranges: low and high energy x-rays for example. Figure(2.36) shows the position in energy and wavelength of the x-ray within the full electromagnetic spectrum. Nowadays, they are considered as one of the best tool for

investigating the structure of materials at the atomic scale. There are employed in different areas such as microelectronics, biology, medicine, crystallography, metallurgy, space, etc. Actually, in the case of solid samples, the x-rays are used to probe the electronic density and reveal their crystallographic structures with high precision. This is possible by exploiting the diffraction phenomenon that will be explained in the next paragraph.

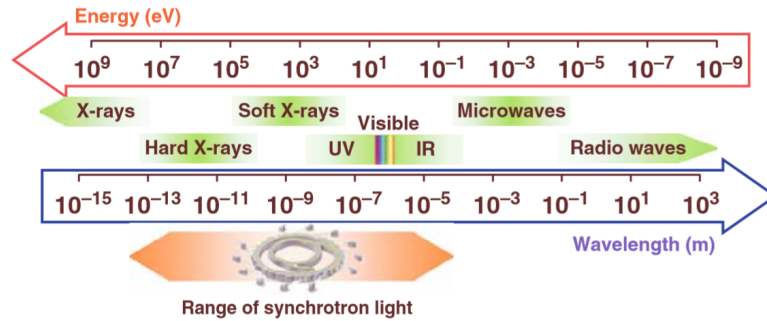


FIGURE 2.36: Energy and wavelength scale for an extended range of electromagnetic radiations[26].

### 2.5.1 Diffraction principle

When an incident electromagnetic radiation interacts with matter, it interferes with the atoms of the medium and several situations such as its scattering and diffraction can occur. In optical physics, diffraction means that the light, when approaching an obstacle, is deviated linearly in the directions predicted by the laws of the optical geometry. In the context of x-rays diffraction, the photon is deviated from its initial direction without losing its initial energy. It can be explained by the kinematic theory through some simple geometrical considerations as reported in the literature[86]. An overview of this phenomenon, tools and methods employed will be described in the following sections.

### 2.5.2 Bragg's diffraction

In 1913 W.L. Bragg described the diffraction as *the reflection of the crystal lattice at the atomic planes*[87]. It takes place when the scattered waves constructively interfere within the crystal. For the periodically separated planes with a constant distance  $d_{hkl}$ , two diffracted x-rays interfering constructively, will satisfy the Bragg's condition if the optical path length  $p'+p''=2d_{hkl}\sin\theta_B$ , is a multiple of the wavelength  $\lambda$ . The expression of  $p'+p''$  are provided on the drawing of figure(2.37). Therefore the Bragg's law can be written with the help of the geometrical projection of figure(2.37), as:

$$\lambda = 2d_{hkl}\sin\theta_B \quad (2.15)$$

$-\theta_B$  is the Bragg's angle

$-d_{hkl}$  is the inter-planar spacing where  $h,k,l$  represent the Miller indices. They also serve to determine the order of the planes.

$-\lambda$  is the wavelength

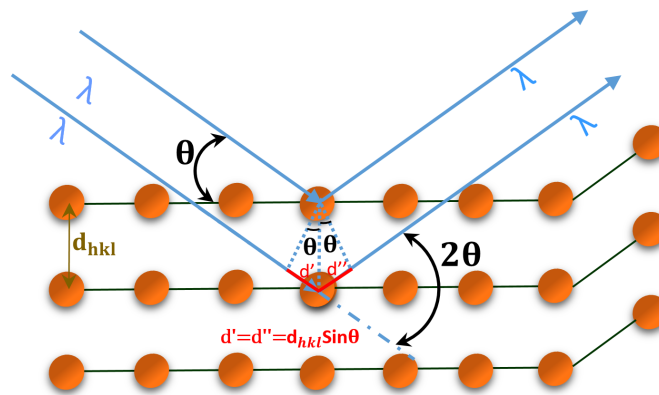


FIGURE 2.37: Geometrical representation of the Bragg's condition for the interferences between the diffracted rays within a crystal, where the atomic planes are separated by a constant distance  $d_{hkl}$ .

The Bragg's condition requires that the diffracting planes should be regularly distanced and that the interference of two waves coherently scattered by the crystal planes should be constructive. This means that the oscillations of those waves should be of the same phase. If they have opposite phases, one will observe an extinction because they are interfering destructively. There are several methods of performing x-ray diffraction analyses in order to study the crystal structure or composition of materials and highlight the presence or not of these anomalies. We will present some of these methods.

### 2.5.3 Analysis methods employed in XRD

XRD is a non destructive technique of choice for materials characterization of several types, ranging from ultra thin films, nanostructured to bulk crystals. The interaction of x-rays with matter being sufficiently low so that the multiple scattering event can be neglected, the kinematic theory can satisfactorily be applied. This is made possible by using the Fourier transform (FT) of the electron density. In a XRD experiment, the orientation of the diffracting planes is exploited to determine their  $d_{hkl}$  spacings using the Bragg's law. Depending on the geometry of the analysis (defined by the incidence and diffracted angles) and the reflections of a given family of crystal planes we want to analyze, the expected information may differ. For example, Figure 2.38 below presents the different orientations of the crystal planes that give the possibility to perform different types of scans in order to obtain the information of interest.

### 2.5.3.1 Symmetrical and Asymmetrical scans

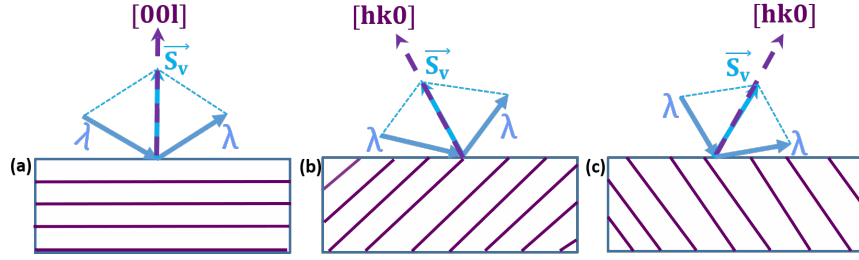


FIGURE 2.38: Different orientations of the crystal planes corresponding to precise types of scans with the orientation of the scattering vector  $\vec{q}_v$ . (a): symmetrical scan, (b): asymmetrical scan (grazing incidence and large emergence). (c): asymmetrical scan (large incidence and glancing emergence). The two components of the scattering vector  $\vec{k}_i$  and  $\vec{k}_d$  represent the momenta of the incident and the diffracted rays, respectively.

- Symmetrical scans: The diffracting planes that are probed here are parallel to the sample surface. The scattering vector  $\vec{q}_v$  is parallel to the crystal direction  $[001]$  of the analysis, which is also aligned with the surface normal. The accessible information in such a geometry are the  $d_{hkl}$  spacing between the parallel planes, the lattice constant along the vertical (out of plane) direction, defects, deformation gradients along that direction, etc.
- Asymmetric scans: the sample can be tilted so that one can probe the other crystal directions that are non parallel to the surface normal of the material. This is possible because the Bragg's condition requires that the scattering vector  $\vec{q}_v$  be aligned with the probed  $[hk0]$  direction. The advantage of this type of analysis is that the lattice constants along the vertical and horizontal directions can be determined. Figure 2.38 also displays the different situations that require asymmetric scans.

The scattering vector  $\vec{q}_v$  is the vector difference between the momenta of the diffracted  $\vec{k}_d$  and the incident  $\vec{k}_i$  x-rays. It describes the momentum transfer between the incident and the diffracted radiations, due to the elastic scattering of light by the atoms of the planes. Therefore, the momentum exchanges during the scattering of the x-rays writes as:

$$\vec{q}_v = \vec{k}_d - \vec{k}_i \quad (2.16)$$

Equation (2.17) represents the Bragg's law in the reciprocal space coordinates,  $|\vec{q}_v| = 2\pi/\lambda = k_0$ .

### 2.5.3.2 High precision characterization of materials using state of the art XRD methods

#### High resolution x-ray diffraction (HRXRD)

High resolution x-ray diffraction is a term adopted to qualify a highly collimated x-ray beam, by using an instrumentation of very good precisions. Therefore, both the spectral and lateral resolutions are the required conditions for XRD analyses in high resolution. The last sentence finds its full explanation in the derivative of the Bragg's law expressed as follows:

$$\frac{\Delta\lambda}{\lambda} = \frac{\Delta d_{hkl}}{d_{hkl}} + \frac{\Delta\theta}{\tan\theta_B} \quad (2.17)$$

$\theta_B$  is the Bragg's diffraction angle. HRXRD is one of the best analysis methods allowing a precise characterization of strains as well as the crystal structure of thin films. This is possible by assessing the main peaks appearing in the diffraction diagram acquired on an investigated sample. The other information we can get through this technique is the composition and the super lattice period.

#### Grazing incidence XRD (GIXRD)

GIXRD is a method that allows to enhance the weak diffracted signal originating from a thin film laid on a bulk substrate. It favours the diffraction into an extremely reduced volume or within the near surface region during the analyses. As can be understood from the definition, this method employs incidence angles that are very close to the critical angle of total external reflection  $\alpha_c = \lambda \sqrt{\frac{\rho r_0}{\pi}}$ . For a given incidence energy (E) of the x-rays, the critical angle of incidence will depend on the analysed material because it is proportional to the density  $\rho$ .

In the case of a film grown or deposited on a substrate of same material (homo-epitaxy), GIXRD is helpful when only the film needs to be analysed. This is possible thanks to the significantly reduced in-depth penetration of the x-rays into the whole sample until they reach the substrate, since the length of the rays inside the film is prolonged. This method has many other advantages like the reduction of the diffracted intensity of the substrate, or its total suppression. Thus, the beam is completely confined within the film. GIXRD is therefore a good method to accurately measure the  $d_{hkl}$ -spacing in thin crystal films.

Through this method, one can determine the damaging rates and strains in epitaxial thin films. Consequently, this method is also an efficient tool for comparing the different doping processes of SC through the evaluations of the crystal quality beneath an amorphous layer. GIXRD has widely been used among many methods to investigate the 2D as well as 3D (Fins) SOI samples[88], like those studied throughout this project. We will present the experimental geometry that was adopted for the measurements at grazing incidence.

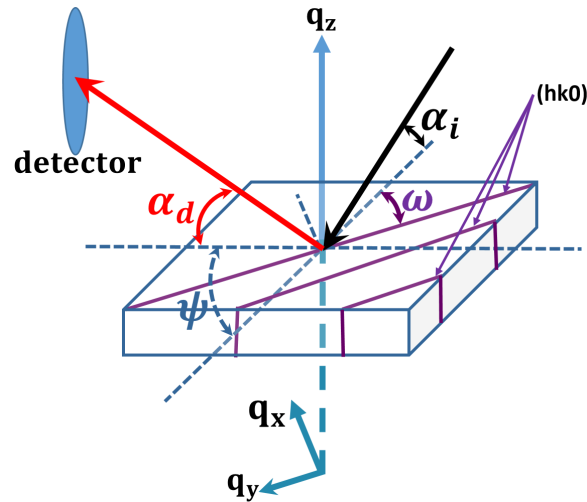


FIGURE 2.39: Experimental geometry used for GIXRD measurements with the associated angles.

Let  $\alpha_i$  the angle defined between the incident beam and the horizontal dotted line in the plane of the sample. In general, this angle is very small and kept constant. The horizontal dotted line is the projection of the beam in the plane of the sample. As indicated on figure(2.39), the geometry of the detection should also be explained. Let  $\alpha_d$  the emergence angle defined between the detector and the dotted line perpendicular to the previous one that we precedently mentioned.  $\psi$  is the angle between the two perpendicular dotted lines, therefore it is the angle between the diffracted and the incident beam in the plane of the sample. For  $\alpha_i$  and  $\alpha_d$  small enough,  $\psi$  is equivalent to the Bragg's angle  $\theta_B$  and  $\omega$  is an angle defined by the rotation of the sample around its normal. Before engaging the measurements, the alignments are performed so that the precession of the sample normal around  $\omega$  is avoided during the analyses. This is performed by checking the variation of the spot of a focused laser (assimilated to the beam) with the rotation center of the sample mounted on the holder.

### 2.5.3.3 Definition of the momentum transfer coordinates for the asymmetric geometry in GIXRD

Following the geometrical projections of figure(2.39), the coordinates for the momentum transfer are given by:

$$\left. \begin{aligned} q_x &= k_0 [\cos(\alpha_d) \cos(2\theta) - \cos(\alpha_i)] \\ q_y &= k_0 \cos(\alpha_d) \sin(2\theta) \end{aligned} \right\} \Leftrightarrow q_{\perp}$$

$$q_z = k_0 [\sin(\alpha_d) + \sin(\alpha_i)] \Leftrightarrow q_{\parallel} \quad (2.18)$$

It is the representation of the Bragg's condition in the reciprocal space coordinates for the perpendicular ( $q_{\perp}$ ) and parallel ( $q_{\parallel}$ ) planes of the sample. A simple way to determine the (hk0) planes is to consider  $\alpha_i$  and  $\alpha_d$  as nil. In that case,  $\omega$  becomes the incidence angle of the beam with respect to sample. Therefore, by restricting ourselves in the  $\perp$  plane where the z coordinate of the momentum is also nil, which means that we are only dealing with the angles  $\psi$  and  $\omega$ , the coordinates of equation(2.5.3.3) become:

$$\left\{ \begin{aligned} q_x &= \frac{4\pi}{\lambda} [\sin(\xi) + \sin(\omega)] \\ q_y &= \frac{4\pi}{\lambda} [\cos(\xi) - \cos(\omega)] \end{aligned} \right. ; \quad \underbrace{\xi(^{\circ}) = \psi(^{\circ}) - \omega(^{\circ})} \quad (2.19)$$

The x and y axes are perpendicular and parallel to the (hk0) planes, respectively.  $\xi(^{\circ})$  is the angle between the diffracted rays and those planes. Since they are not parallel to the surface, their analyses require that the sample be tilted at an angle ( $\gamma$ ) so that the scattering vector  $\vec{q}_v$  is parallel to the associated [hk0] crystal direction. Their analyses is achievable by running asymmetric scans that allow the determination of the in-plane lattice constant. The  $\omega$  scans called 'transverse scans', are exploited to determine the mosaic spread of the a layer, but also the structure factor of the patterns. The twist angle between the planes of the substrate and the top film can be deduced by computing the difference  $\Delta\omega$ . The determination of the respective inter planar distances  $d_{hk0}^{film}$  and  $d_{hk0}^{Subst.}$  within the film and substrate is possible by performing coupled scans ( $\omega$ ,  $\psi$ ) also known as radial scans. The use of a source of highly collimated beam such as a synchrotron radiation, combined with a goniometer of angular precision of about  $10^{-4}^{\circ}$ , one can realise all the above experiments with a high accuracy in the results. We will present the two different types of x-ray sources that were used for the measurements in the framework of this project.

## 2.5.4 X-ray sources and instruments

The generation of x-rays can be done by using several methods. There are classical sources constituted of anodes made with different materials that are able to produce radiations of sufficient intensities for the measurements. The rays produced by a synchrotron source are characterised by their strongly focused and very high brilliance. The large energy range delivered by a x-ray source can indeed be split into three categories: soft x-rays (low energy ranges), tender x-rays and hard/high energy x-rays (high energy ranges, see Figure(2.36)).

### 2.5.4.1 X-ray laboratory source and instrumentation

The production of x-rays in modern laboratories is performed under vacuum by bombarding a metallic target anode with a focused electron beam accelerated at high voltage. The intensity limit achievable is defined by the maximum power available with the experimental setup. These so called x-ray tubes are found in many research institutions like those utilised at the nano characterization plate-form (PFNC) of CEA-LETI for instance. The diffractometer used was a X'Pert PRO one provided by PANalytical. A picture is presented in figure (2.40) with a representation of the experimental principle.

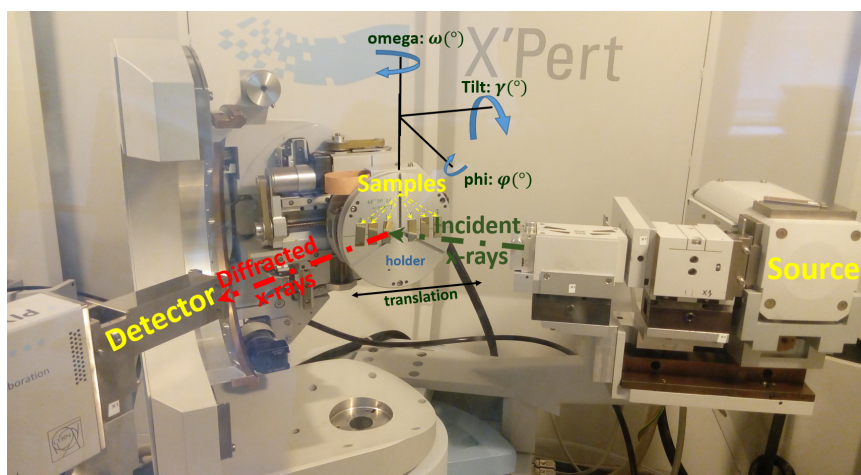


FIGURE 2.40: X'Pert PRO diffractometer used at the PFNC of CEA-LETI with a representation of the experimental principle of X-rays diffraction. The source of the incident x-rays is fixed. The holder which can host several samples that can rotate around three principle angles:  $\omega(\omega)$ ,  $\phi(\phi)$  and tilt ( $\gamma$ ) and translate along the horizontal axis. The detector itself can also rotate out of the plane of the sample holder.

### 2.5.4.2 Synchrotron radiation source and instrumentation

Synchrotron is a light source characterised by its strong collimation and very high brilliance, delivering photons of intensities by far larger than those produced by the laboratory sources. The x-ray radiations are emitted after the accelerated electrons moving circularly along an orbit, be deflected from their initial trajectory. The accelerated particles move with a velocity close to the speed of light. The deflection in question is operated by an intense magnetic field produced by a set of magnets, circularly placed in order to impose an orbital trajectory to the electrons, so that they can move into the field of the ring formed by those magnets. The emission of light results from the fact that the electrons when moving with a very high energy (in the order of about 6 GeV), are deviated very fastly. Thereby emitting radiations ranging from microwaves to high energy x-rays. One can refer to the diagram of figure(2.36) to check the energy and wavelength of the generated radiations. The principle schematic of a synchrotron is presented in figure(2.41)[89], which is the one available at the European Synchrotron Radiation Facility (ESRF).

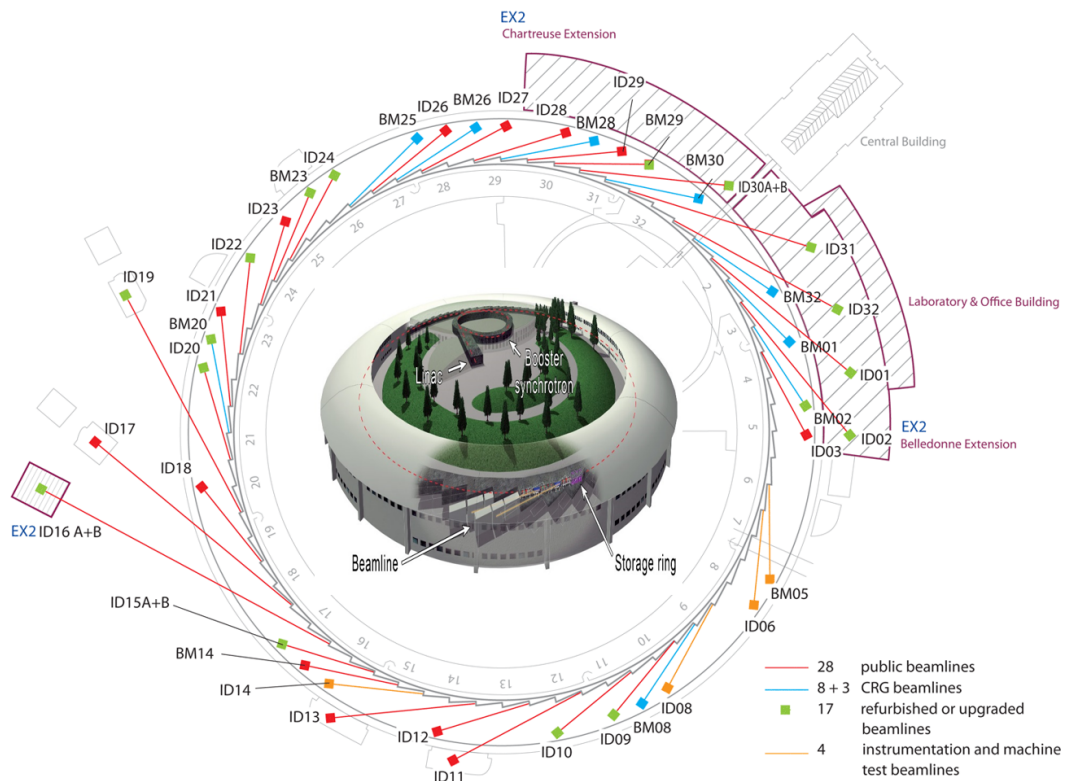


FIGURE 2.41: An overview of the storage ring of the ESRF synchrotron facility with all the beam lines represented around. The inset is the ensemble picture showing the linear accelerator (LINAC) from where the electrons are produced, the booster synchrotron of 300 m diameter where the electrons are pre-accelerated at a solicited velocity before being injected into the storage ring of 844.4 m circumference.

### The storage ring:

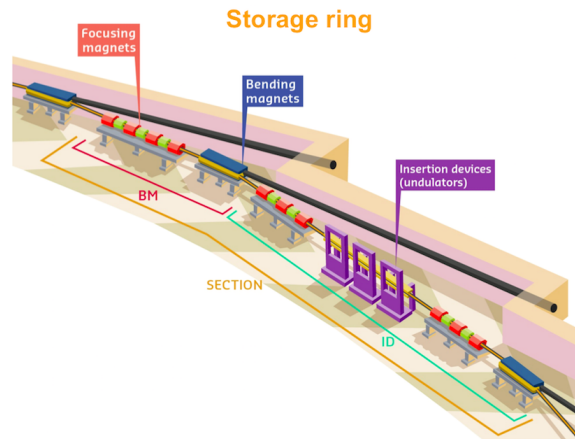


FIGURE 2.42: Picture of a part of the storage ring of the ESRF synchrotron, with a section showing the set of the focusing magnets, bending magnets (BM) and insertion devices (ID).

It consists of a couple of 32 alternating straight and curved sections of magnets. Its circular environment is kept under high vacuum with a pressure level of about  $10^{-9}$  torr. The curved sections are constituted of 32 bending magnets (BM) having as role, to change the trajectory of the electrons into the circular orbit. While the straight magnets host an ensemble of 43 focusing devices, their main function is to maintain the electrons on their forced orbit.

### Insertion devices (ID):

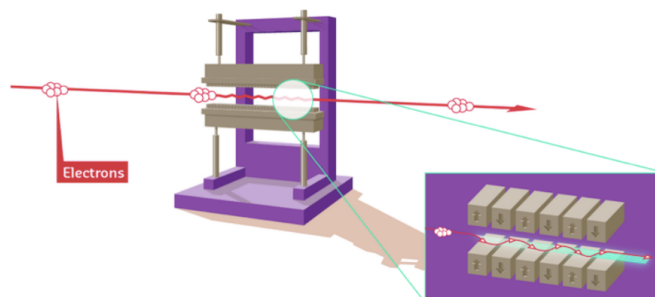


FIGURE 2.43: Picture of a part of an insertion device (or undulator) of the storage ring[27]. It illustrates how the electrons's intensity is amplified through the oscillation of their trajectories during their passage into the field established by the magnetic poles.

Their role is to provide the solicited radiation characteristics such as a narrow or broad band, the desired energy of the photon beam for instance. They are constituted of magnetic poles of opposite polarities. Indeed, when passing through the magnetic field of the insertion devices, the electrons are under the influence of a magnetic force that obliges them to follow a wavy trajectory. The consequence is that, the radiations emitted

during the oscillations of their trajectories at each consecutive bend, overlap and interfere with the radiations of the other bends[27]. The advantage is to avoid any variation of the beam's trajectory and consequently, to have a strongly focused and brilliant radiation.

### The bending magnets (BM):

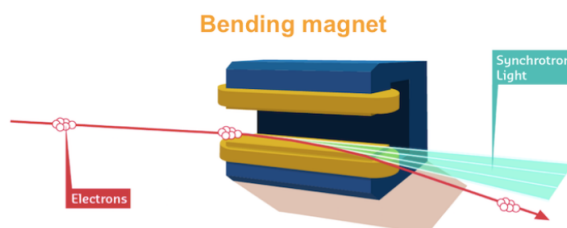


FIGURE 2.44: Illustration of the deflection of electrons when passing through the a bending magnet, followed by the emission of a synchrotron radiation[27].

The role of the bending magnets is to force electrons to follow their circular orbit, when passing through their magnetic field. When the electrons are deviated as they are passing through a BM, they emit a radiation: this is the origin of the synchrotron radiation. At the exit of each BM there, is a beam line with an attributed number  $xx$  (BM $xx$ ) that exploits the radiation emitted according to the solicited energy range. As can be read on the image of figure(2.41), the numbers range from  $xx=01$  to  $xx=32$ . This corresponds to the 32 bending magnets and 32 insertion devices that were available few years ago, because the facility has been extended to host a total of 44 beam lines. The wavelength of the x-rays that result from the emitted radiation can be used for a various category of measurements.

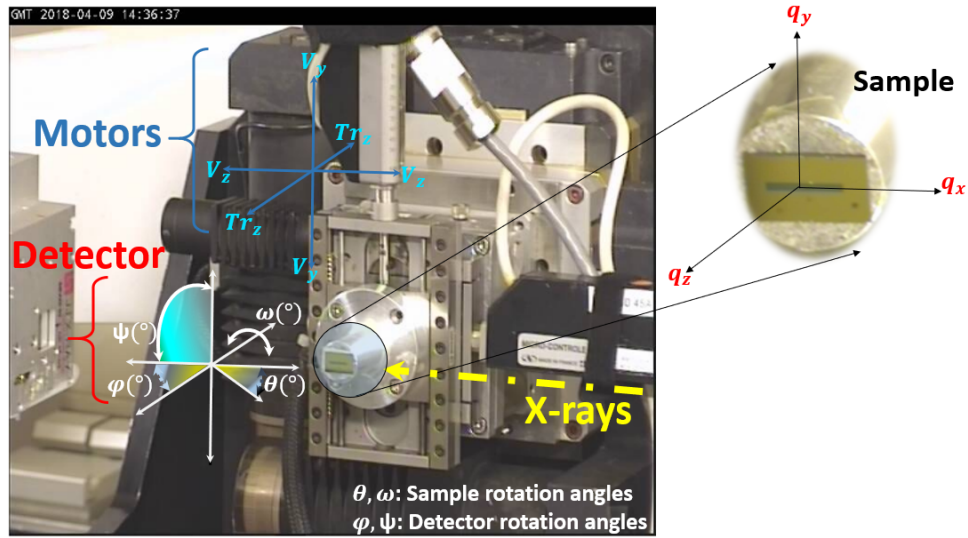
**The beam line end-station:**

FIGURE 2.45: Experimental setup for HRXRD measurements of the ESRF's BM32 beam line end station. An image of a sample mounted on a holder fixed to the goniometer is shown.

The image of figure(2.45) presents the BM32 beam line end-station. The 1D detector is placed at the left hand side to record the diffraction patterns of the x-rays delivered by the beam line from the right hand side of the figure. The moving motors and the detector axes are indicated with the associated directions and corresponding angles. The couples of angles  $(\theta, \phi)$  &  $(\omega, \psi)$  correspond to the respective out of plane & in-plane incidence and detection angles of the x-rays. A zoom of a sample hosting an etched line of 3D patterned nanostructures is highlighted. The coordinates of the reciprocal space vectors  $(q_x, q_y, q_z)$  represented on the figure correspond to those of the line grating.

## 2.6 Conclusion

We have presented all the techniques that were utilized for all the investigations in the framework of this project. Some of them like RBS and SIMS are efficient in the chemical composition analysis and the quantification of the elements in presence. The XRD and TEM (appendix(B)) techniques are among the best when it comes to find relevant information regarding the crystal quality, dimensions, composition, and the morphology. Medium energy ion scattering is a particular analysis technique because its strength relies on the fact that it can be employed to provide several of these information and the quantification with good accuracy. This is the reason why we had a particular focus on it. The physical principles which are nothing than the Coulombian interactions have been presented in a dedicated section. The next chapter is consecrated to the

analysis of the doping conformity into the 3D structures, by analyzing the spectra of the implants, their implantation depths and by providing their quantity. In contrast, the consequences of their insertion, i.e. the implantation induced damages and the impact of the processes will be presented in [chapter 4](#).

## Chapter 3

# Doping conformity in 3D structures

### 3.1 Introduction

The objective of this chapter is to investigate the doping conformity in the samples constituted of 3D silicon (Si) Fin-shaped line grating. The doping was performed by the conventional implanter (IM) and plasma immersion ion implantation (PIII) methods. The conventional implantation process was carried out by using arsenic ( $\text{As}^+$ ) at room temperature on a VIISTA HCP setup at the energy of 3 keV, with a tilt angle of  $25^\circ$  off the sample normal. While the plasma doping was made on a PULSION Nano tool machine manufactured by Ion Beam Services (IBS). The implantation was performed using the arsine ( $\text{AsH}_3^+$ ) gas at room and high temperatures, with the same energy as in the precedent method. It is reported that arsenic is frequently employed for n-type doping because of its high solid solubility[45]. Its quantity has been measured by using the Medium Energy Ion Scattering (MEIS) technique. For the sample implanted by the conventional method, a bi-dimensional approach was adopted to simulate the implantation depths in the patterns by using SRIM[25]. It is a software that uses Monte-Carlo calculation methods to predict the implantation ranges of the ions into crystals and assess the damage profiles they induce. However, SRIM does not take into consideration the 3D structures. In contrast, by simple geometrical considerations, the implantation can be evaluated by overlaying a set of 2D simulations.

Concerning the analyses of the MEIS experimental data, the PowerMEIS software[30] was used. It is also based on the Monte-Carlo simulations methods which, in contrast to the former one, considers the trajectories of the ions in the 3D structures of any shape. It was possible to evaluate the quantity of the dopants implanted in the patterns. Thus, the MEIS measurements and simulations were confronted in order to analyze the distribution of the dopants introduced by the conventional implantation. Concerning

the PIII implanted samples, the same 3D simulation software has been exploited to treat the experimental results so as to evaluate the doping conformity and compare with the results obtained by pure theoretical considerations. The determination of the thicknesses of the implanted layers in the patterns has been made by combining grazing incidence x-ray diffraction (GIXRD), x-ray reflectivity (XRR), Transmission Electron Microscopy (TEM) and MEIS. Prior to undertake the discussions on the results obtained on the implanted 3D line gratings, those of the preliminary studies that have been carried out on the ultra-thin layers implanted with the same methods will be presented.

## 3.2 Preliminary studies on the non-patterned ultra-thin layers

### 3.2.1 Quantification of the dopants by using MEIS and RBS

The MEIS spectra were measured in random mode by using 200 keV protons ( $H^+$ ) beam, penetrating the samples at an incidence angle of  $64^\circ$  with respect to their surface normal. The analyses at such inclined angle allows the improvement of depth resolution. The scattered projectiles were detected at an angle of  $135^\circ$ . The analysis in random mode allows the quantification of chemical elements. The Rutherford Backscattering (RBS) analyses using 2 MeV alpha particles ( $He^+$ ) were carried out for complementary measurements, so as to compare the result of the measured quantities of arsenic. This technique has also been presented in the previous chapter. The experimental results obtained from these two techniques are displayed in Figure (3.1) for MEIS and Figure (3.2) for RBS. The information regarding the quantities of arsenic are obtained by confronting the simulations as depicted by the solid curve (model) with the experimental spectrum.

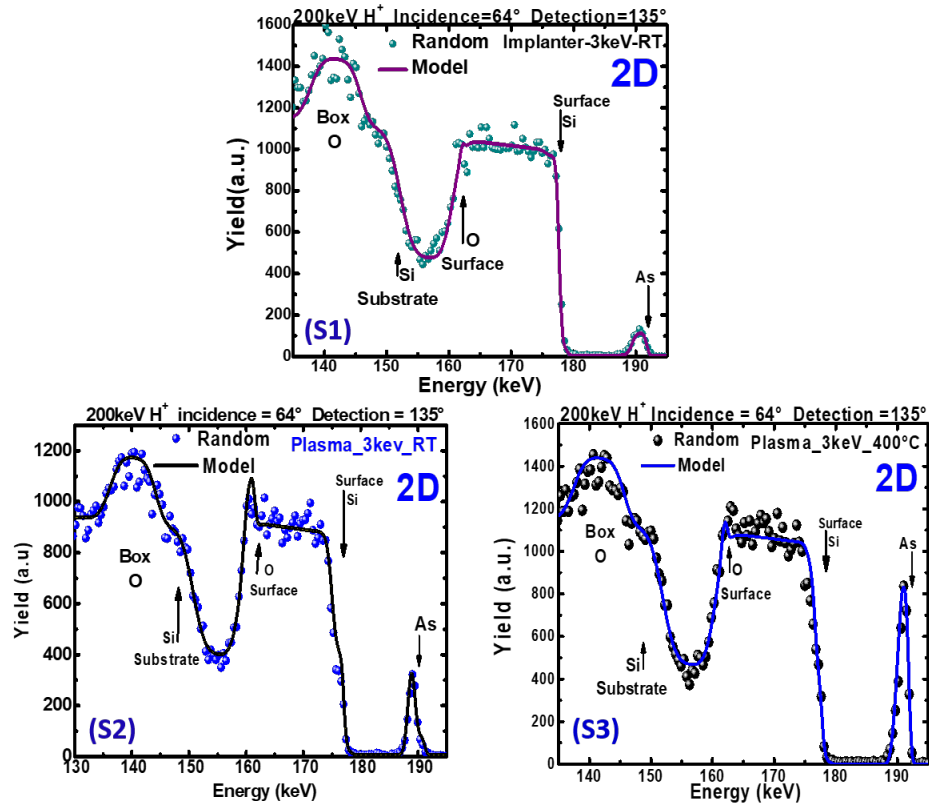


FIGURE 3.1: MEIS measurements on the samples implanted with arsenic ( $\text{As}^+$  – S1) and arsine ( $\text{AsH}_3^+$  – S2, S3) with the associated fits. The incidence and scattering angles were  $64^\circ$  and  $135^\circ$ , respectively. The implantation methods are indicated in each graph. Samples S2 and S3 have been implanted by PIII at room and high ( $400^\circ\text{C}$ ) temperatures, respectively.

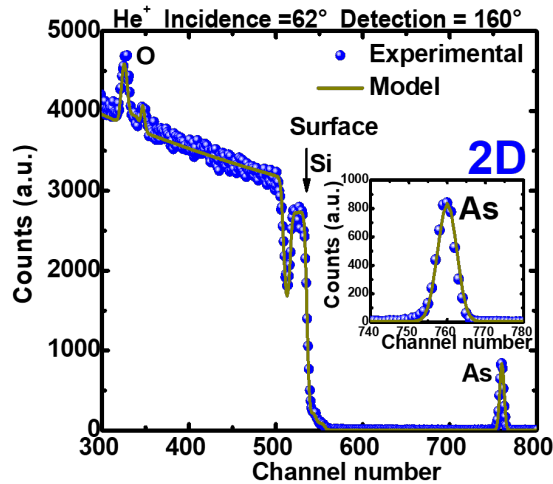


FIGURE 3.2: RBS experimental result with the associated fit, obtained on the arsine ( $\text{AsH}_3^+$ ) implanted sample. The incidence and the scattering angles were  $62^\circ$  and  $160^\circ$ , respectively.

The MEIS spectra were simulated by using the MEISanalyser.exe software already presented in the previous chapter. The RBS spectrum was simulated using the SIMNRA software[90]. The concentration of arsenic displayed in Table 3.1 shows a good agreement

IM = Implanter PL = Plasma	Experimental Techniques	
	RBS	MEIS
	Arsenic_Dose ( $\times 10^{15}$ at/cm <sup>2</sup> )	Arsenic_Dose ( $\times 10^{15}$ at/cm <sup>2</sup> )
Samples		
IM-3keV-RT (S1)	$0.9 \pm 0.1$ = targeted ( $1 \times 10^{15}$ )	$1 \pm 0.04$ = targeted ( $1 \times 10^{15}$ )
PL-3keV-RT (S2)	$1.95 \pm 0.5$ < targeted ( $5 \times 10^{15}$ )	$2.1 \pm 0.04$ < targeted ( $5 \times 10^{15}$ )
PL-3keV-400°C (S3)	$4.8 \pm 0.5$ ~ targeted ( $5 \times 10^{15}$ )	$4.5 \pm 0.06$ ~ targeted ( $5 \times 10^{15}$ )

TABLE 3.1: Comparison of the implanted arsenic doses measured by RBS and MEIS. The values obtained with the MEIS technique were computed through the simulations of the experimental spectra with the respective densities:  $6.9 \times 10^{22}$  mol/cm<sup>3</sup> (for Si<sub>0.36</sub>O<sub>0.64</sub>),  $2.3 \times 10^{22}$  mol/cm<sup>3</sup> (for SiO<sub>2</sub>) and  $5 \times 10^{22}$  mol/cm<sup>3</sup> (for Si).

between the MEIS and RBS measurements. Indeed, RBS is a technique widely used to quantify the chemical species into solid matrices thanks to its good capability of counting the scattered ions of different charge states (positive, negative and neutrals). The detection system used in MEIS is of electrostatic type, i. e. capable to only detect the charged ions. Therefore, for an efficient quantification with this technique, the fraction of the singly charged ions exiting the sample has been taken into consideration during the simulations, based on the work of Zalm et al. [73].

One observes that the computed dose is as targeted in the sample implanted by the conventional method. The difference between the targeted and measured doses in the sample implanted by PIII at room temperature, verified by the two experimental techniques, may arise from experimental issues. In contrast, in sample S3, the table indicates that one tends to implant the total targeted dose within the crystal by plasma immersion at 400°C.

### 3.2.2 Implanted depths of the dopants

Figure (3.3) (S1) shows the MEIS spectra of arsenic measured in two different geometries to analyze the spectra of arsenic, one in normal incidence and the other in inclined incidence (64°). The energy axes were converted into depth and it shows that the maximum quantity of the dopants is located at the extreme surface. The comparison of the experimental spectra of sample S1 with the SRIM simulations shows the agreement concerning the projected ranges.

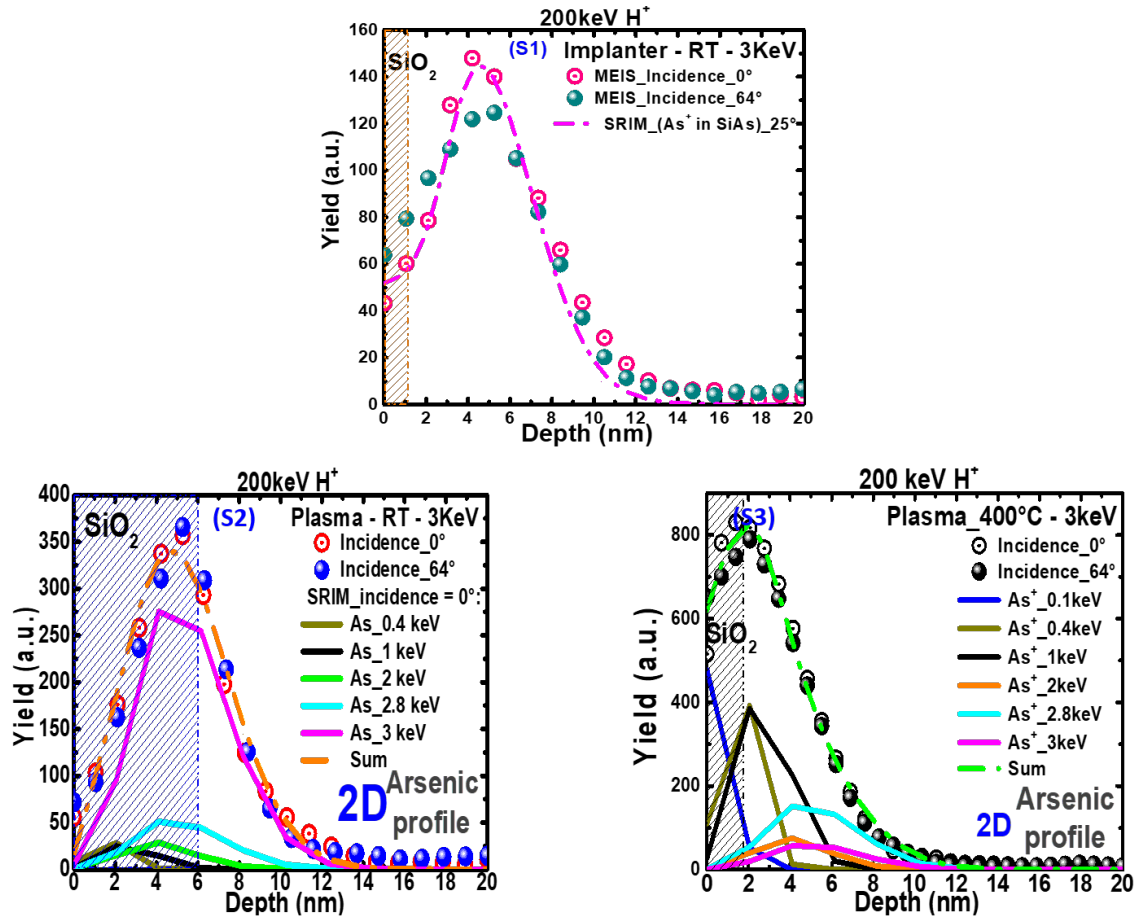


FIGURE 3.3: MEIS experimental spectra of arsenic measured in the samples implanted by the conventional (S1) and plasma (S2 & S3) methods at 3 keV. The spectra were acquired in normal (open dotted circles) and off-normal ( $64^\circ$  - filled circles) incidences. The SRIM simulations of the arsenic spectra in the conventional implantation were carried out with mono-energy ions. However, those for the plasma methods were carried out by using the arsenic ions of multiple energies. The gridded parts represented in the graphs indicate the surface oxide's thicknesses.

The species used in the PIII implanted samples S2 and S3 were molecules ( $\text{AsH}_3^+$ ) instead of single atoms ( $\text{As}^+$ ) as in the case sample S1. Therefore, for a given energy used for the implantation, each atom constituting the molecule is supposed to move with its own kinematic energy once it penetrated the wafer. Which supposes that at the contact with the wafer surface, the compound splits into single atoms. With the relationship  $E = \frac{1}{2}MV^2$ , one can determine the velocity  $V$  of a species, with a mass  $M$  (amu) and kinematic energy  $E$ . If the molecule  $\text{AsH}_3^+$  is accelerated at 3 keV for instance, the energies of the As and H atoms are 2.885 keV and 0.0385 keV, respectively. Due to the distribution of the kinetic energy of the incident projectiles, the arsenic ions of several energies were considered so as to compare the SRIM simulations with their MEIS spectra as shown in Figure (3.3) (S2 & S3). One observes with this approach that a significant quantity of As implanted at 3 keV and only a few ions were accelerated at multiple and lower energies in sample S2. This can be explained by the distribution of potentials arising from the

different rises and drops of the pulsed voltage. The spectra of sample S2 and S3 show that arsenic extends at a depth of about 9.5 nm (S2) and 8 nm (S3). However, the graph S2 shows that the thick oxide layer presents at the surface of this sample is considerably rich in arsenic.

### 3.3 Conformity assessment by MEIS in the 3D sample implanted by the conventional method

#### 3.3.1 Simulation approach

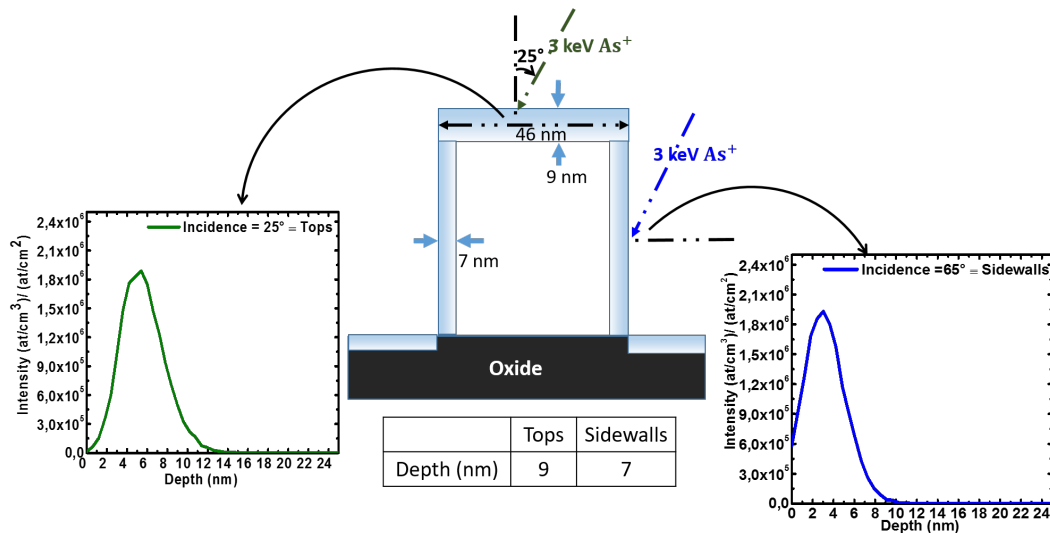


FIGURE 3.4: Schematic illustration of the tops and sidewalls doping from a bidimensional SRIM simulation approach. The estimated implantation depths are indicated in the table. The implantation conditions as well as the nature and the energies of the dopants are indicated in the graph and the drawing.

As depicted in Figure (3.4), the idea is to determine what could be the penetration depths of the implants in the tops and sidewalls by relying on the implantation conditions. For the tops surfaces, SRIM shows in the left graph of Figure (3.4) that arsenic penetrates at a depth up to 9 nm. By performing the simulations with the incidence angle of  $65^\circ$ , one can estimate the depth at which they implanted in the side of the Fins. The results displayed in Figure (3.4) show that the depth corresponding to the implantation in the sidewalls is around 7 nm. These results will be compared to those determined by MEIS analyses and the other techniques.

### 3.3.2 Calculations of the expected doses in the conventional implanted 3D sample.

We are interested in knowing how the dose distributes in each part of the nanostructure according to the implantation conditions adopted to dope this sample by using the conventional method. This can fuel the discussions about the doping conformity in the nanostructure implanted by this method. The calculations will be based on geometrical considerations. Therefore, the dimensions of the patterns constituting the line grating need to be known. These parameters can be obtained by Transmission Electron Microscopy (TEM) in scanning mode for instance. Prior to carry out the TEM analyses, a sample preparation was performed by focused ion beam (FIB) milling. The analyses were performed on a FEI Titan Themis transmission electron microscope operating at 200 kV. It is equipped with a probe corrector and 4 SDD - EDX detectors. High angle annular dark field scanning TEM (HAADF-STEM) image gives access to morphological information relative to the Fins and one can measure their dimensions. The results are presented in Figure (3.5).

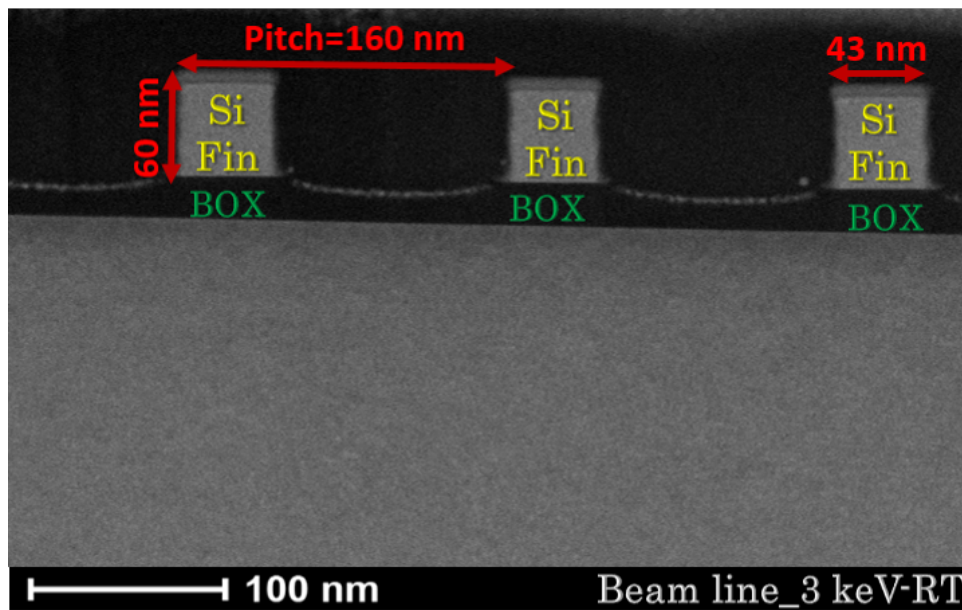


FIGURE 3.5: Cross-sectional Transmission Electron Microscopy (TEM) images in scanning mode acquired on the 3D-nanostructured sample (S1) implanted with arsenic. The image shows the Si-Fins, buried oxide (Box) and the Si-bulk stacking and the dimensions.

The schematic drawing of Figure (3.6) illustrates the implantation conditions in the patterns of dimensions provided by TEM analyses. The implanted depths of arsenic predicted by SRIM simulations were used in the drawing. Knowing the total projected dose per unit area ( $D_{\text{tot}} = 1 \times 10^{15}$  at/cm<sup>2</sup>), the incident angle ( $\theta = 25^\circ$ ) and by considering the patterns of unit length (in cm), it is possible to calculate the local dose in each part

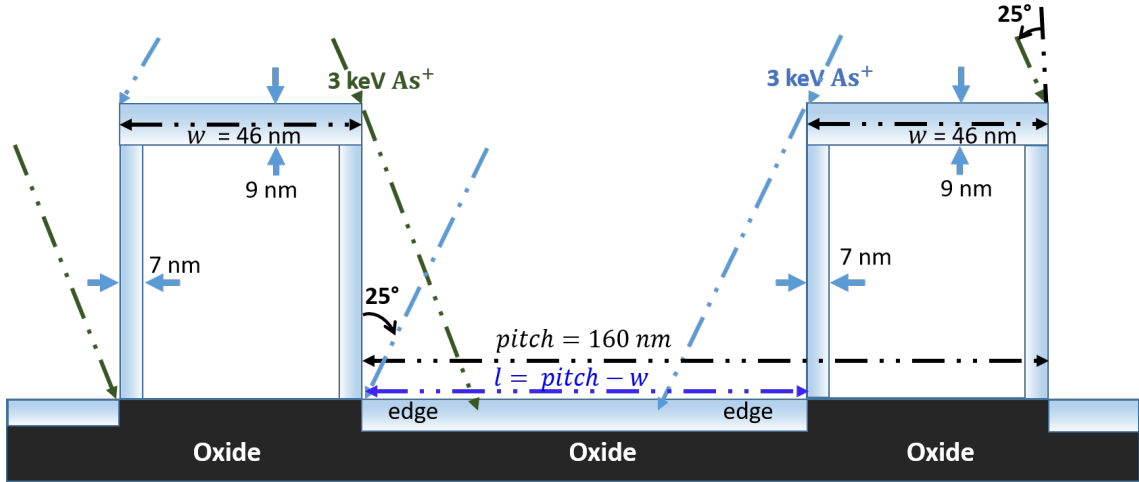


FIGURE 3.6: Schematic illustration showing the geometrical projections of the implantation of As in the Fins of dimensions as indicated in the TEM image of Figure (3.5). The figure represents the sample (S1) implanted by using the conventional method, the width is represented by considering the presence of a native oxide. The estimated implanted depths in the tops (9 nm) and sidewalls (7 nm) are those deduced from the SRIM [25] simulations illustrated in Figure (3.4).

of the nanostructure. It is the dose really received by the tops, sidewalls and bottoms of the patterns. Its calculations necessitate the determination of the fractions ( $p$ ) of the implanted dose in each of these parts. These dose fractions in turn depend on the implantation conditions. The relationships allowing their determinations are provided in equation (3.1).

$$\left\{ \begin{array}{l} p^{Tops} = 2 \times \left( \frac{w}{pitch} \times \frac{D_{tot}}{2} \right) \\ p^{Sidewalls} = \left( \frac{h \times \tan(\theta)}{pitch} \times \frac{D_{tot}}{2} \right) \\ p^{Bottoms} = 2 \times \left\{ \frac{[(pitch - width) - h \times \tan(\theta)]}{pitch} \times \frac{D_{tot}}{2} \right\} \end{array} \right. \quad (3.1)$$

The factor 2 in the expression of  $p^{Tops}$  derives from the fact that the tops received twice the half of the total projected dose, i.e.,  $2 \times 5.10^{14}$  at/cm<sup>2</sup> since the implantation was carried in two steps. The sidewalls have received the half of the total projected dose per step. Because of the shadowing effects caused by the neighboring Fins, the edges of the bottoms are twice less implanted than the middle. The relationships used to compute the local dosages ( $D_{Loc}$ ) are given in equation (3.2).

$$\left\{ \begin{array}{l} D_{Loc}^{Tops} = \frac{P^{Tops}}{S^{Tops}} ; \text{ with } S^{Tops} = \frac{w}{pitch} \\ D_{Loc}^{Sidewalls} = \frac{P^{Sidewalls}}{S^{Sidewalls}} ; \text{ with } S^{Sidewalls} = \frac{h}{pitch} \\ D_{Loc}^{Bottoms} = \frac{P^{Bottoms}}{S^{Bottoms}} ; \text{ with } S^{Bottoms} = \frac{pitch - w}{pitch} \\ \text{and } p^{Bottoms} = \frac{h \times \tan(\theta) + [pitch - w - 2 \times h \times \tan(\theta)]}{pitch - w - h \times \tan(\theta)} \end{array} \right. \quad (3.2)$$

The terms  $p^{Tops}$ ,  $p^{Sidewalls}$  and  $p^{Bottoms}$  are provided in equation (3.1).

Faces:	Tops	Sidewalls	Bottoms
Dose Fractions	0.275	0.175	0.55
Local dose $\times 10^{15}$ (at/cm <sup>2</sup> ):	1	0.23	0.76

TABLE 3.2: Calculated dose fractions and the expected local doses in the sample implanted by the conventional method. They were determined by considering the implantation conditions and the geometry of the sample.

Table 3.2 shows the theoretical values of the dose fractions and the local doses computed using equations (3.1 & 3.2). Despite their small surface, one realizes that the tops have locally received the largest dose. It corresponds to  $2 \times 5.10^{14}$  (at/cm<sup>2</sup>) for the two implantation steps. As shown in the first line of equation (3.2), the tops do not suffer from the angle effects comparatively to the sidewalls and bottoms. Indeed, the sidewalls that have the larger surface are expected to host the lower local dose. Because they suffer the most from the angle effects in contrast to the bottoms. This can be justified by the fact that the parts lighted by the implants' beam in the bottoms during the two implantation steps are of important length ( $(pitch-w)-2h \times \tan(25) = 60$  nm).

### 3.3.3 Calculations for the conformal implantation in the conventional implanted 3D sample.

We define an implantation as conformal when the tops and sidewalls have locally received the same dose and the thickness of the implanted areas is the same. According to this definition, Table 3.2 indicates that the implantation is not conformal. The value that one should obtain in the tops and sidewalls is  $0.61 \times 10^{15}$  at/cm<sup>2</sup>, determined from the geometry of the sample. With a nanostructure of such dimensions, the ideal implantation angle at which the tops and sidewalls receive the same local dose ( $1.10^{15}$  at/cm<sup>2</sup>) is given in equation (3.3), by noting that  $D_{Loc}^{Tops} = D_{tot} = 1.10^{15}$  at/cm<sup>2</sup>.

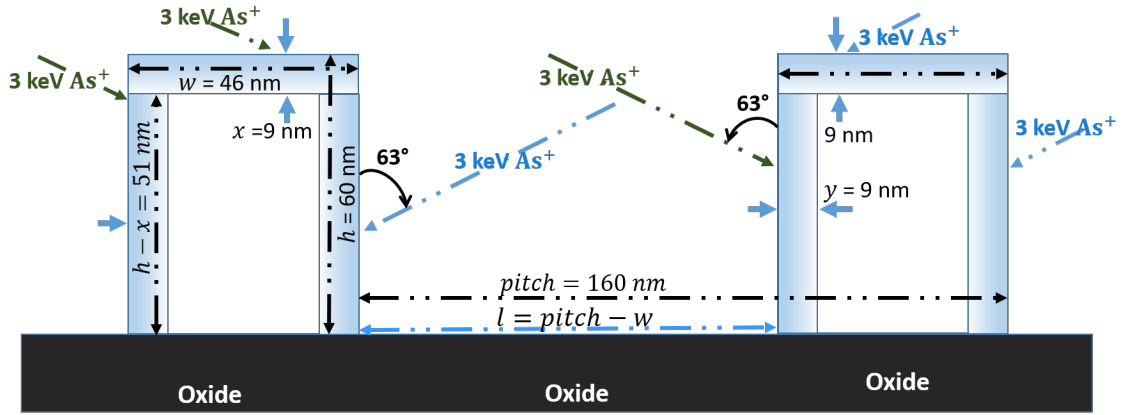


FIGURE 3.7: Illustration of a conformal implantation of arsenic ( $\text{As}^+$ ) by using the conventional method. The thicknesses  $x$  and  $y$  of the implanted layers in the tops and sidewalls are considered as the same.

$$\frac{h \times \tan(\theta) \times D_{\text{Tot}}}{2 \times \text{pitch}} \times \frac{\text{pitch}}{h} = D_{\text{loc}}^{\text{Tops}} \Leftrightarrow \theta = \arctan(2) = 63.4^\circ \quad (3.3)$$

Remark:

The final expression of the incidence angle  $\theta$  determined in equation (3.3) does not depend on the dimensions of the patterns. At this implantation angle, the bottoms remain undoped.

### 3.3.4 Measurements on the conventional implanted 3D sample

The MEIS measurements were carried out in random mode by using a 200 keV  $\text{H}^+$  beam, the experiments were performed at inclined and normal incidences. These analyses are done by simulating the MEIS spectra by using the PowerMEIS software[30]. During the measurements, the sample was oriented with respect to the detector so that the analyzed scattered projectiles were those detected laterally to the Fins. An illustration is provided in Figure (3.8).

The simulation of the MEIS spectra with PowerMEIS requires the modeling of the nanostructure by considering its shape, dimensions and compositions. To do so, the TEM image is very useful for a good representation of the line grating in the model, which is actually a matrix. As described in the previous chapter, the simulation of the peak of the dopants implanted within the matrix is done by introducing a certain number of layers of fixed density, thickness and stoichiometry. It helps observe how each chemical element constituting the nanostructure contributes in the obtention of the whole simulated 3D MEIS spectrum.

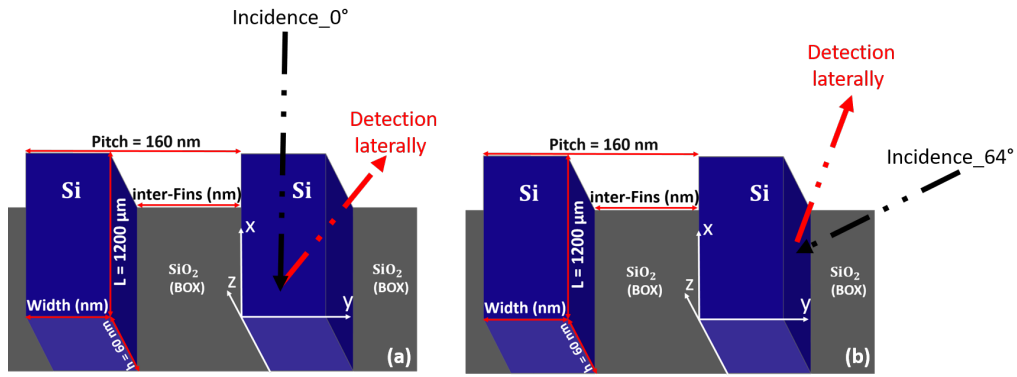


FIGURE 3.8: Schematic illustration of the geometry where the scattered projectiles are detected laterally with respect to the silicon (Si) Fins during the analyses in inclined incidence (a) and in normal incidence (b).

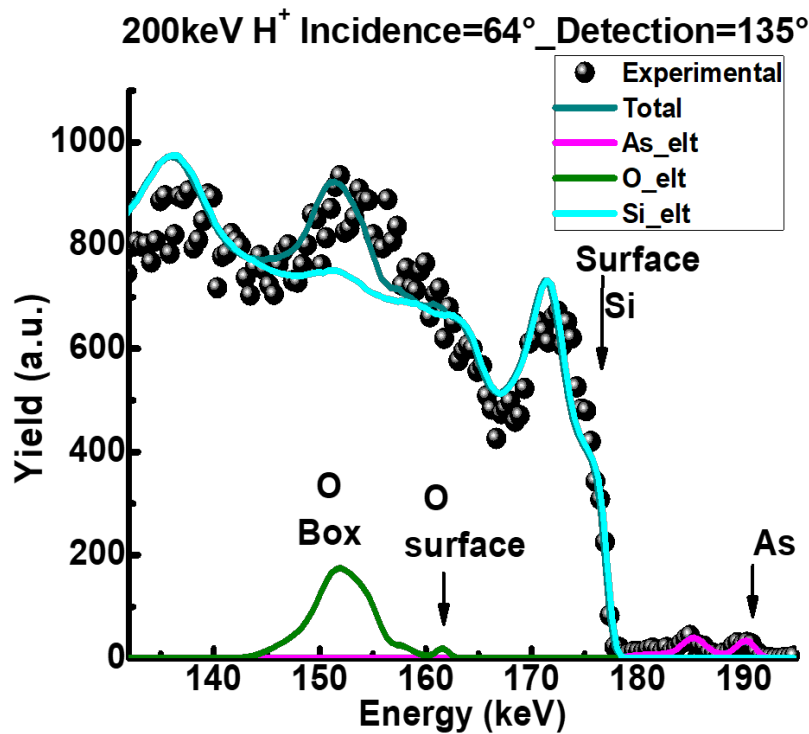


FIGURE 3.9: Illustration of the PowerMEIS simulations of a MEIS experimental spectrum with the contribution of all the chemical elements (Si, O, As) constituting the matrix. The incidence and scattering angle are indicated on top of the graph.

An example comparing the experimental spectrum and the simulated one is shown in Figure (3.9). For a same analysis mode (random), the MEIS spectrum acquired on a 3D structure is very different from that measured on the ultra-thin layers (non-patterned 2D samples shown in Figure (3.1)). One observes a particular contribution of arsenic. Instead of having a single peak, the 3D spectrum displays two peaks. This double contribution is highlighted because of the analysis geometries. They were developed in order to discriminate the peak of the dopants implanted in the Fins from that of the

dopants implanted in the bottoms. The whole spectrum of silicon is the convolution of the silicon's signals of the Fins and that of the oxide.

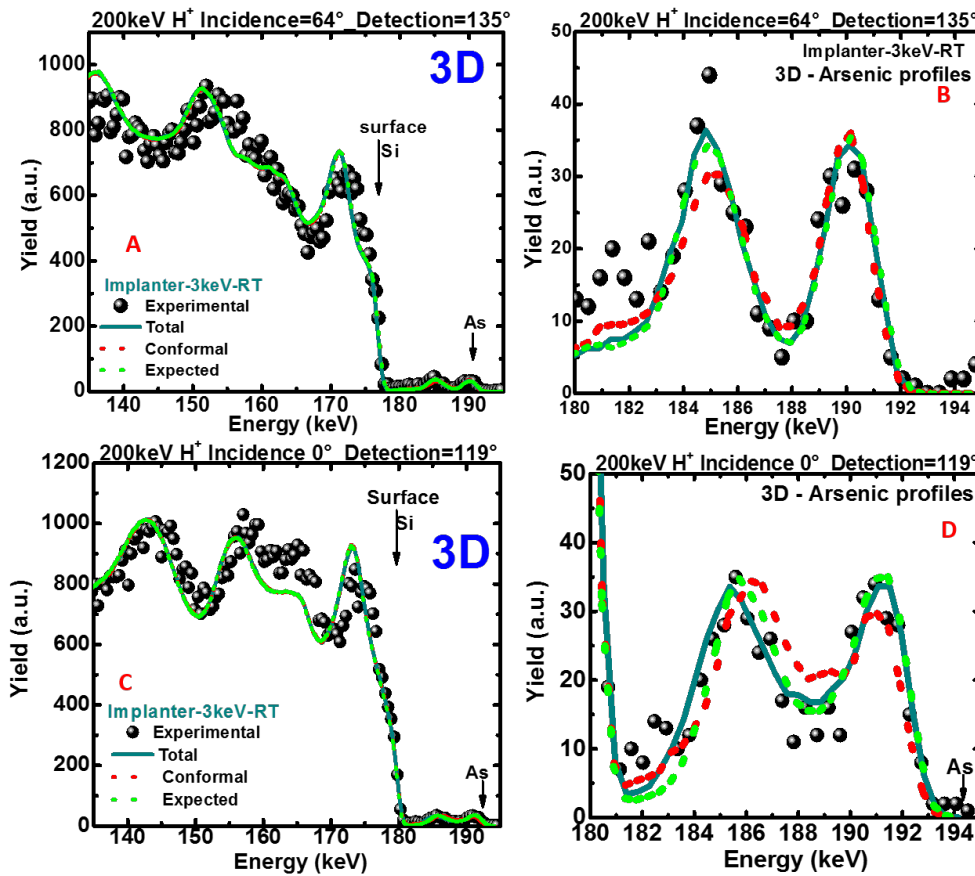


FIGURE 3.10: Presentation of the MEIS experimental spectra and their associated PowerMEIS simulations, obtained on the sample (S1) implanted with arsenic by using the conventional method. The incidence and scattering angle of the 200 keV projectiles are indicated on top of each graph. The orientation of the line grating on the wafer was such that the scattered ions exit laterally with respect to the Fins (see Figure (3.8)). The best fit (Total) is represented by the solid curve. The simulation of the spectrum corresponding to a conformal implantation (red-dashed) and the one expected from the implantation conditions (green-dashed) are illustrated. The double peaks of arsenic in the patterns are highlighted in the top and bottom-left graphs (B & D).

Figure (3.10) displays the experimental spectra measured by MEIS in inclined (3.10(A & B)) and normal (3.10(C & D)) incidences on the sample implanted by the conventional method. The top and bottom-left graphs show the zooming of the double peaks of the arsenic spectra. One observes that the best fit of the experimental data (solid curve) is different from the simulated curve of a conformal implantation (red-dashed curve). To understand how the tops and sidewalls contribute in the formation of the first peak, and to verify that the second one results from the bottoms' contribution, further analyses were performed by providing the simulated spectrum of As implanted at each single part of the nanostructure. The comparison of the features of the arsenic spectra in the two

geometries are presented in Figure (3.11). The simulations of a conformal implantation are also provided in Figure (3.12).

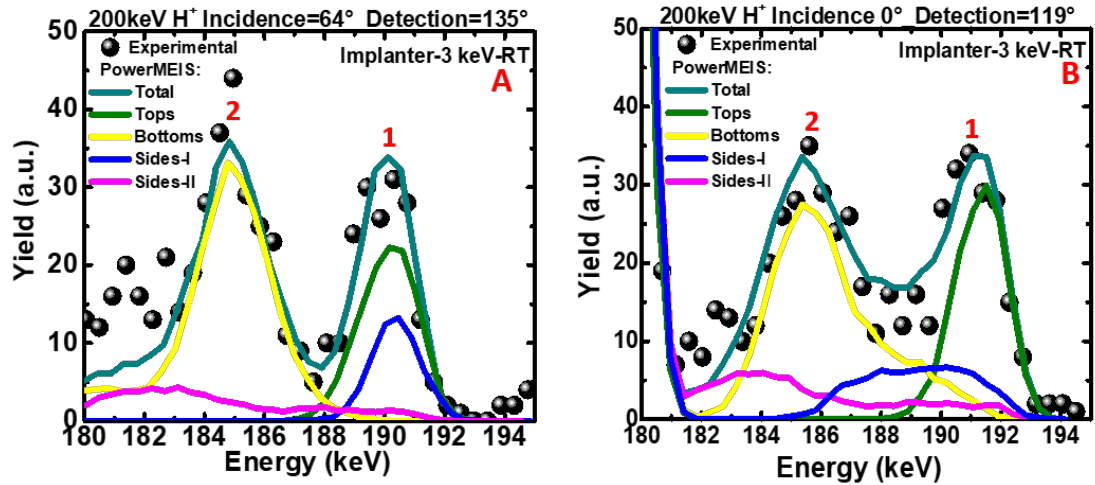


FIGURE 3.11: 3D deconvolutions of the arsenic spectra in the two analysis geometries. The first peak is labelled as 1 and the second as 2.

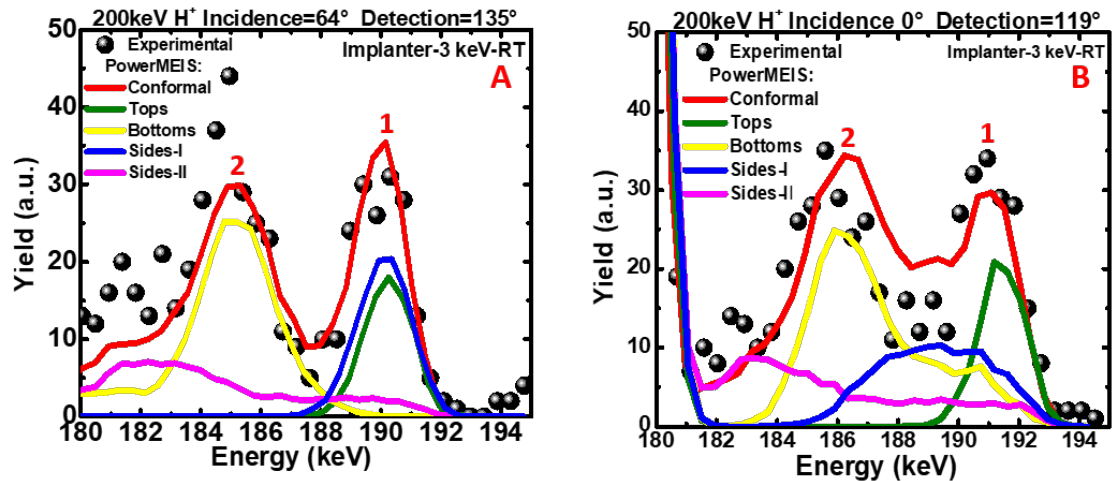


FIGURE 3.12: Illustration of the 3D deconvolutions of the simulated spectra for a conformal implantation, in the two geometries. The first and second peaks are also labelled as 1 and 2.

The 3D deconvolutions of the total fit of the experimental spectra are provided in the two analysis geometries (normal and inclined incidences). The generation of each sub-spectrum requires a representation of the corresponding matrix model (explained in appendix A). Thus, the analyses presented in Figure (3.11) and Figure (3.12) confirm that:

- The peak 1 really emanates from the contribution of the tops and sidewalls, in other terms, the contribution of the Fins.

- The bottoms majoritarilly contributes to the formation of the peak 2.
- The analyses in inclined incidence ( $64^\circ$ ) optimizes the scattering peak of arsenic implanted in the sidewalls (as explained in chapter 2 and in the lines below).
- The analysis in normal incidence ( $0^\circ$ ) optimizes the scattering peak of arsenic implanted in the tops.

Another importance of the 3D deconvolutions depicted in Figure (3.11) and Figure (3.12) is that, they help better understand how each of the two sidewalls at either side of the Fins participate in the obtention of the whole arsenic spectrum. Whether on the simulations of the measured spectra of arsenic or on those illustrating a conformal implantation, one notes different features in sidewalls – I and sidewalls – II in the two geometries. In the one at  $64^\circ$ , the arsenic spectra in the sidewalls - I appear peaked, while those of sidewalls – II spread along the energy axis. The schematic drawing shown in Figure (3.13) is provided for clarifications.

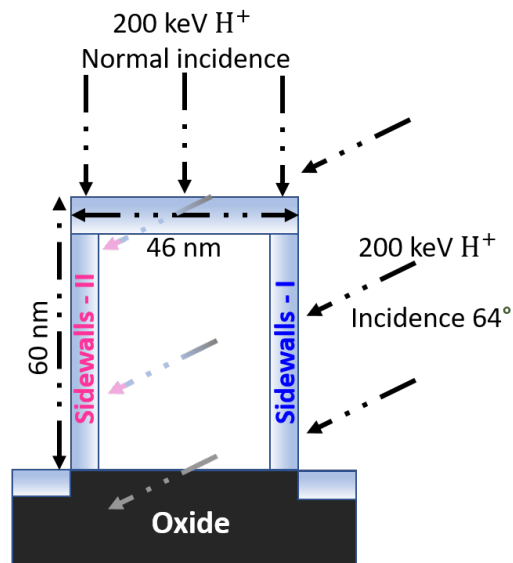


FIGURE 3.13: Illustration of the sidewalls - I and Sidewalls – II of the Fins. In inclined incidence ( $64^\circ$ ), the projectiles penetrate the Fins from the side directly facing the beam (sidewalls - I), then lose energy when crossing the core of the Fins, before reaching the sides opposite to their entrance (sidewalls – II).

In this geometry, the projectiles hit the tops at  $64^\circ$  with respect to their surfaces' normal, while they simultaneously hit the sidewalls' surface at an angle of  $90^\circ - 64^\circ = 26^\circ$  relatively to their surface normal. It is expected that the signal of arsenic display a peak at the extreme surface of the sidewall – I but not for sidewalls – II. Because the incident projectiles lose energy during their crossing of the Fins' core before reaching the arsenic atoms inserted in that part. The reason why the arsenic spectra of sidewalls – I and sidewalls – II appear flattened in Figure (3.11 - B) and Figure (3.12 - B) is related

to the analysis geometry in normal incidence. Indeed, when the beam is parallel to the sidewalls, it only sees a thin implanted layer at either side of the Fins which is extended all along their height (60 nm).

Computed doses and dopants distribution in the conventional implanted 3D sample.

dosages: $\times 10^{15} \text{ (at/cm}^2\text{)}$	Methods		Fins		Bottoms
			Tops	Sidewalls	
S1 Implanter-3 keV-RT	Local doses	Expected	1	0.23	0.76
		Measured	0.94	0.38	0.71
		Conformal	0.61	0.61	0.61

TABLE 3.3: Comparison of the normalized local dosages in the sample. The values of the measured and expected ones from calculations, as well as those deduced by simulations in the situation of a conformal doping are provided.

In the first line of Table 3.3, one observes that the distribution of the local dose is different from a conformal one. The expected and measured values follow the same trend and are comparable. The tops have received the largest local dose. The sidewalls are less doped than all the other parts. The bottoms are more heavily implanted than the sidewalls. From the measured local doses shown in Table 3.3, one can say that the implanted dopants did not uniformly distribute in this sample.

### 3.4 Conformity assessment by MEIS in the plasma implanted 3D sample at room temperature

Similar analyses were carried out on a sample implanted by plasma immersion. In contrast to the previous method where the implants have a unique trajectory, in PIII, their trajectories are distributed. Consequently, the calculations carried out in the conventional implantation method do no longer hold in PIII so as to allow the estimation of the expected doses. Only the geometry of the structure and the targeted dose can be exploited for the determination of the real doses. Firstly, we will present the image acquired by TEM analyses from which the dimensions can be measured. Figure (3.14) shows that the width, height and pitch of the patterns of sample (S2) are of dimensions 46 nm, 59 nm and 160 nm, respectively. The values corresponding to the local implanted doses can be calculated from these dimensions.

Figure (3.15) displays the experimental spectra measured in inclined incidence (A & B) and normal incidence (C & D) associated with the corresponding simulations. The zooming of the double peaks of the arsenic spectra are presented in Figure (3.15) - (B

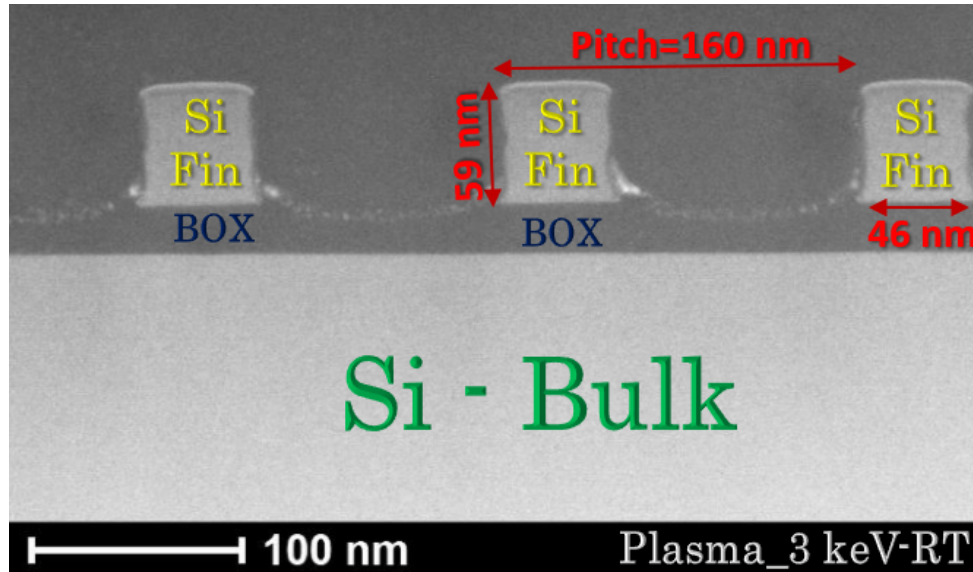


FIGURE 3.14: Cross-sectional Transmission Electron Microscopy (TEM) image in scanning mode of the 3D-nanostructured sample (S1) implanted with arsenic. The image shows the Si-Fins, buried oxide (Box), the Si-bulk and the dimensions of the patterns.

& D)). The simulated MEIS spectra corresponding to a conformal implantation are highlighted. For this sample, one observes that the best fit of the experimental data (blue solid curve) is by far different from that of the simulated conformal implantation. As shown by the red – dashed curves in the two – left graphs, the difference with the experiment is revealing a non – uniform distribution of the dopants in this sample. The double peaks measured in S2 look different from those observed in the sample implanted by the conventional implanter method (see Figure (3.10)). The yield of the first peak is higher than that of the second one. It has been observed from the 3D deconvolutions of the double peak of arsenic in Figure (3.11) that the peak 2 represents the signature of the doping in the bottoms. One can therefore say, from the analyses in sample S1, that the distribution of arsenic in sample S2 is also different and the quantity in the bottoms is inferior to that in the Fins. It remains to understand how the tops and the sidewalls contribute in the formation of the peak 1. In doing so, the analyses were expanded by providing the simulated MEIS spectra of the arsenic implanted in each single part of the nanostructure as well. The comparison of the measurements in the two geometries and the simulated spectra are presented in Figure (3.16), in association with the simulations of the conformal implantation presented in Figure (3.17).

The interpretation provided for the 3D deconvolutions of Figure (3.11) and Figure (3.12) hold for Figure (3.16) and Figure (3.17) as well. Indeed, one observes in Figure (3.16 - (B & D)) that the bottoms' peak is roughly 28.5 % lower than that of the tops. It should normally be slightly higher as indicated in Figure (3.17). The intense peak of the tops surface obviously shows that they host a quantity of dopants larger than in the bottoms.

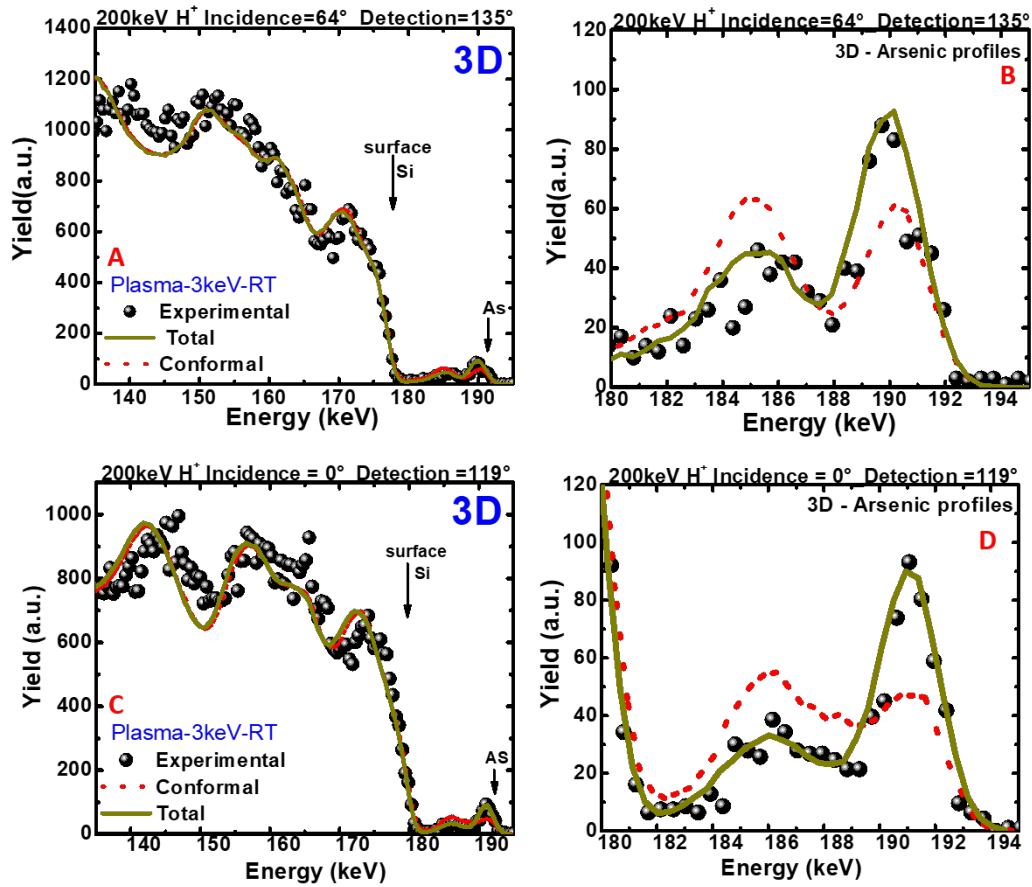


FIGURE 3.15: Presentation of the experimental spectra with their associated Power-MEIS simulations, obtained on the sample (S2) implanted by the plasma method at room temperature. The incidence and scattering angles of the 200 keV proton projectiles are indicated on top of each graph. The best fit (Total) is represented by the blue – solid curve. The simulation of the spectrum corresponding to a conformal implantation (red – dashed curve) is illustrated. The double peaks of arsenic in the patterns are highlighted in the top and bottom-left graphs (B) and bottom (D). The orientation of the line grating was such that the scattered ions exit laterally to the Fins (see Figure (3.8)).

If the concentration of arsenic in the Fins was similar to that in the bottoms, the peak 1 of the experimental spectra in the two geometries should be lower as shown by the simulation of the conformal implantation. Therefore, the experimental spectra should be looking like the red-dashed curves in Figure (3.16 - (A & B)). The contribution of the two sidewalls in the formation of the first peak is very low, despite their optimization with the geometry in inclined incidence. Their low yields show that they host the smallest dosage compared to the tops and bottoms. The computed doses in this sample are provided in Table 3.4.

The values obtained by measurements indicate that the tops host the maximum of the local doses (1.74 at/cm<sup>2</sup>) which is four times greater than that of the bottoms and more than eight times larger than in the sidewalls. The distribution of the local dose is different

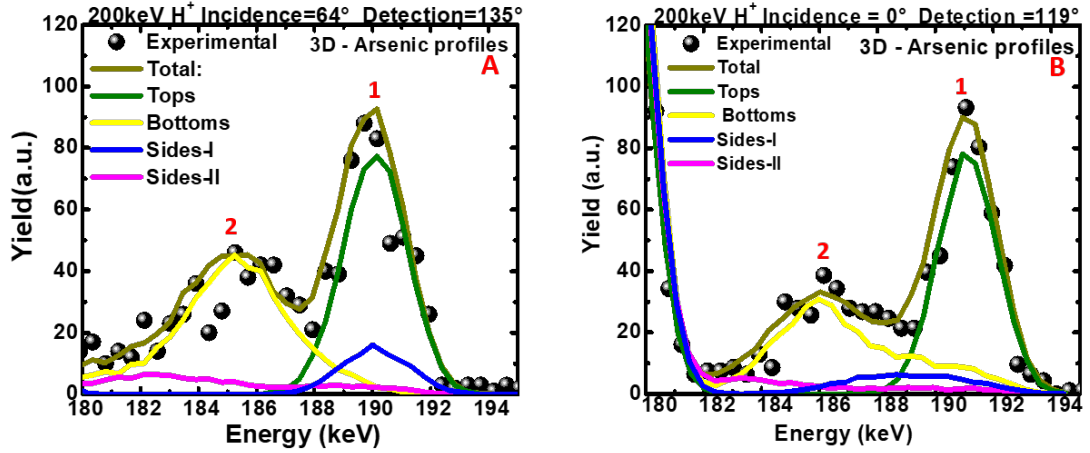


FIGURE 3.16: 3D – deconvolutions of the arsenic spectra of the sample implanted by plasma at 3 keV - room temperature. The first peak is labeled as 1 and the second as 2. The deconvolutions are performed in the two analysis geometries.

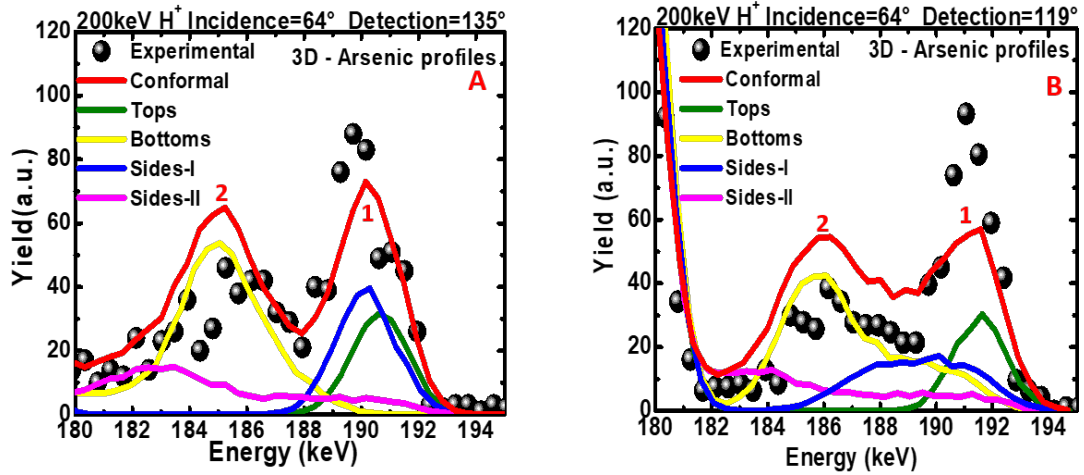


FIGURE 3.17: Simulations by 3D – deconvolutions of the arsenic spectra considered as conformally implanted by PIII at 3 keV - room temperature in each part of the nanostructure. The first peak is labeled as 1 and the second as 2. The deconvolutions are performed in the two analysis geometries.

dosages $\times 10^{15} \text{ (at/cm}^2\text{)}$	Methods		Fins		Bottoms
			Tops	Sidewalls	
S2 Plasma-3 keV-RT	Local doses	Measured	1.95	0.24	0.45
		Conformal	0.62	0.62	0.62

TABLE 3.4: Comparison of the normalized local doses measured in the sample implanted by plasma at 3 keV – RT, with those deduced from the simulations based on the assumption of a conformal doping.

from a conformal one, as observed in Table 3.4. It is interesting to see what is the impact of the temperature on the spectrum of arsenic. The analyses have thus been carried on

a sample heated at 400°C during its implantation by plasma immersion.

Measurements on the high temperature (400°C) plasma implanted 3D sample

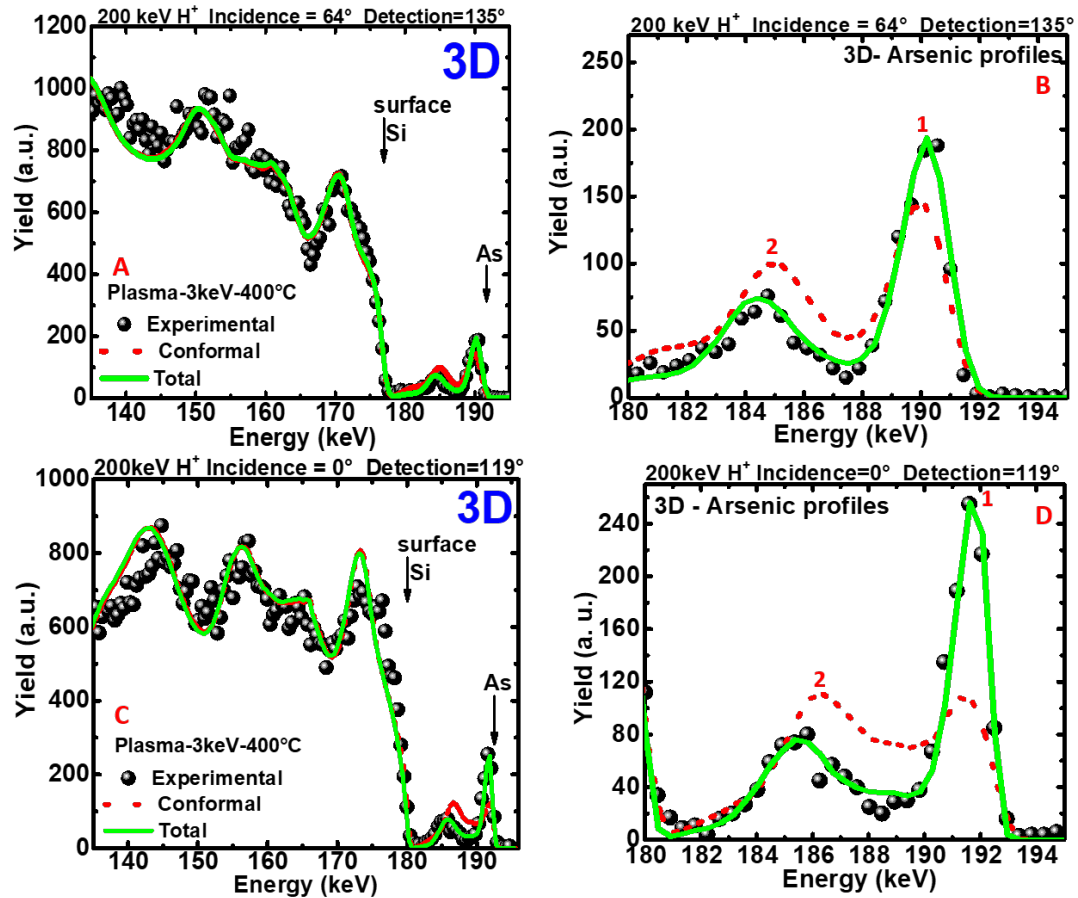


FIGURE 3.18: Presentation of the experimental spectra with their associated PowerMEIS simulations, obtained on the sample (S3) implanted by the plasma method at 400°C. The incidence and scattering angles of the 200 keV proton projectiles are indicated on top of each graph. The best fit (Total) is represented by the green-solid curve. The simulation of the spectrum corresponding to a conformal implantation (red – dashed curve) is illustrated. The double peaks of arsenic in the patterns are highlighted in the top and bottom – left graphs (B & D). The orientation of the line grating was such that the scattered ions exit laterally to the Fins.

The results of the measurements carried out on this sample are presented in Figure (3.18) with the associated simulations. The spectra of the arsenic implanted in each part of the nanostructure, obtained by 3D-deconvolutions of the total fit of the experimental spectra are provided in Figures (3.19 (A & B)). Figure (3.20) illustrates the case when the implantation is considered as conformal. Their interpretations are similar to those of Figures (3.10 - 3.12) and Figures (3.15 - 3.17). The doses measured are displayed in Table 3.5.

In Table 3.5, it is also observed that the tops have received the largest dosages and the sidewalls host the smallest. However, there is an interesting aspect to focus on. Indeed,

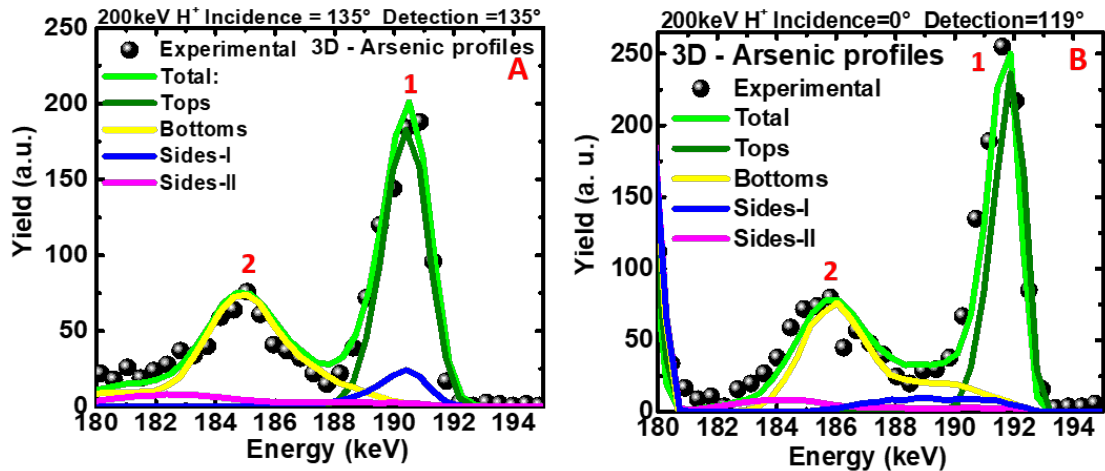


FIGURE 3.19: 3D – deconvolutions of the arsenic spectra implanted in each single part of the nanostructure by plasma at 400°C, in the two analysis geometries. The first peak is labelled as 1 and the second as 2.

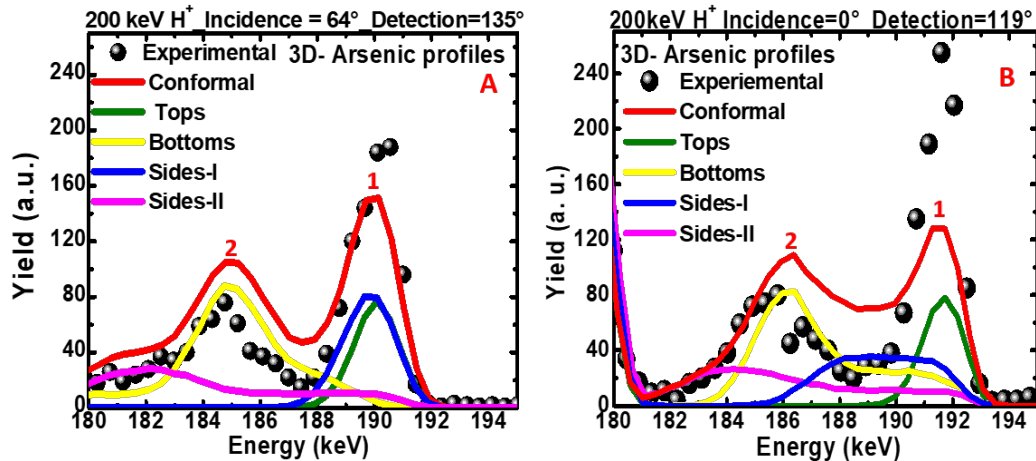


FIGURE 3.20: Simulations by 3D – deconvolutions of the arsenic spectra for an implantation by PIII at 400°C considered as conformal. The spectra are provided in the two analysis geometries. The first peak is labeled as 1 and the second as 2.

dosages $\times 10^{15}$ (at/cm <sup>2</sup> )	Methods		Fins		Bottoms
			Tops	Sidewalls	
S3 Plasma-3 keV-400°C	Local doses	Measured	1.81	0.19	0.56
		Conformal	0.62	0.62	0.62

TABLE 3.5: Comparison of the normalized local doses measured in the sample implanted by plasma at high temperature (400°C) – 3 keV, with those deduced by the simulation of a conformal implantation.

by looking at the measured values of the local doses in the sidewalls and bottoms of this sample, one remarks that there are similitudes with those of sample S2 in terms of dopants' distribution (see Table 3.4). One can remark that in all the 3D plasma

samples studied in this section, the maximum dose is concentrated in the tops and the minimum in the sidewalls. It is therefore interesting to gather all the values of the local doses determined in the three samples in Table 3.6 in order to have a clear vision on the dopants' distribution and appreciate the influence of the processes and temperatures.

Samples	Methods	Local Doses $\times 10^{15}$ ( $at/cm^2$ )		
		Fins		Bottoms
		Tops	Sidewalls	
S1 Implanter-3 keV-RT	Measured	0.94	0.38	0.7
S2 Plasma-3 keV-RT	Measured	1.95	0.24	0.45
S3 Plasma-3 keV-400°C	Measured	1.81	0.19	0.56

TABLE 3.6: Comparison of the normalized local doses measured in the three samples.

The results of the measurements of the local doses presented in Table 3.6 display considerable variations. The distribution of As in the plasma samples is different from that in the conventionally implanted one (S1). By confronting the MEIS experimental technique and PowerMEIS simulations, it is observed that there is no doping conformity in the samples. It is more marked in the plasma implanted ones. Indeed, comparatively to the other parts, the tops are the most doped ones in the three samples. The sidewalls of sample S1 contain the largest local doses compared to the sidewalls of samples S2 and S3 that are lowly doped. The local dose computed in the sidewalls of the room temperature plasma implanted sample is larger than that of the 400°C implanted one. Regarding the bottoms' doping, those of the sample implanted by the conventional method (S1) host a dose that is roughly 1.56 times greater than those of the plasma sample S2 and 1.25 times greater than those of S3. A hypothesis to explain the significant focusing of the dopants on the tops of the Fins, as observed in the PIII samples, can be the dopants' repulsion. It may be due to possible charging effects in the insulating oxide. One can notice that the implanted species hit the same patterned area, but experience two different materials: silicon (which is a semi-conductor) and the oxide (which is an insulator). It was reported in literature [91] that a high fluence or high density  $AsH_3^+$  plasma doping of an oxide can lead to its charging.

A third analysis geometry in the case when the scattered projectiles exit longitudinally to the line gratings have also been conducted by pure simulations (see Figure (3.21)). The aim is to observe the contributions of the tops, sidewalls and bottoms in the formation of the arsenic's spectrum, then compare with the previous measurements.

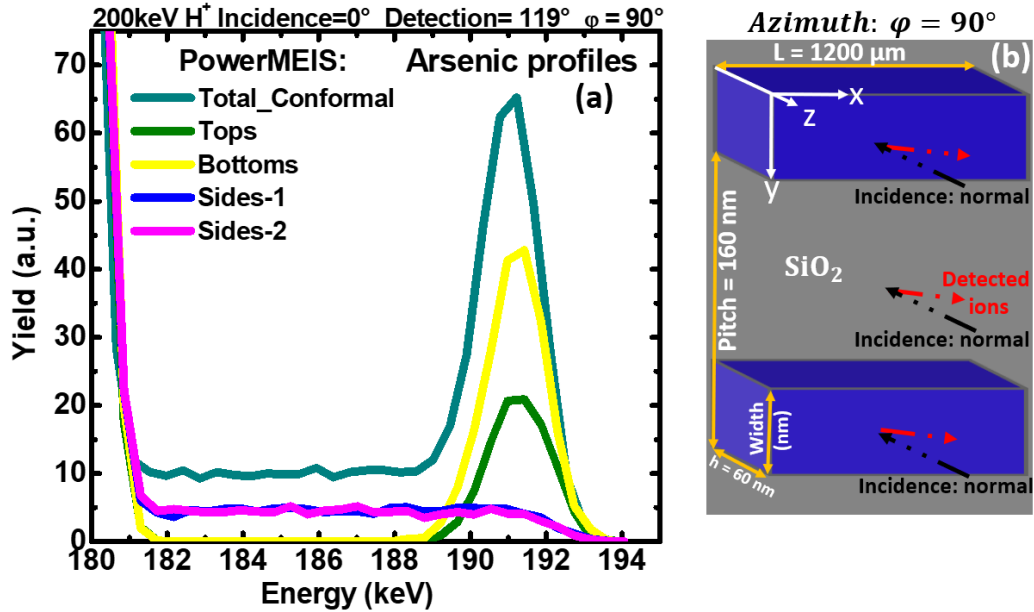


FIGURE 3.21: (a): Simulations of the arsenic spectra in the tops, sidewalls and bottoms of the patterns, when the scattered projectiles exit along the lines. (b): schematic illustration of the Fins where the azimuth  $\varphi = 90^\circ$  is their orientation in the plane of the sample holder during the analyses.

For the detection of the scattered projectiles along the Fins as shown in Figure (3.21), one observes only a single peak of arsenic in the spectrum of the overall nanostructure because the peak of the bottoms is no longer shifted back, it has moved towards the energy position of the tops. This allows to obtain a part of the spectra of arsenic entirely attributed to the sidewalls. It is not exactly the case with the two previous geometries because the peak of the bottoms is mixed with those of the sidewalls (see Figure (3.8)). The arsenic spectra in the two sidewalls appear spread along the energy axis because of the prolonged path length of the projectiles, mostly during their exit from the patterns. Therefore, Figure (3.8) and Figure (3.21) show that three geometries are sufficient to a full analysis of the 3D doping as well as the spectra of the implants in such nanostructure with MEIS.

The second experimental technique that will be used, x-ray diffraction (XRD), cannot evaluate the distribution of the dopants in the 3D structures. In contrast, it can be used to measure the dimensions of the non – implanted crystal regions. Knowing the dimensions of the overall nanostructures obtained by electron microscopy image and used in the PowerMEIS simulations, one can compute the difference between the dimensions of the overall nanostructure and that of the crystal regions to get access to the thickness of the implanted areas on the tops and the sidewalls.

### 3.5 Dimensions of the crystal and damaged areas by x-ray diffraction and TEM analyses

The analysis of the crystal quality in the core of the Fins is important because this region actually represents the active part of the triple gate transistors from where the charges flow through the 3D channel. The experiments were carried out on the bending magnet BM32 beamline of the European Synchrotron Radiation Facilities (ESRF). The grazing incidence x-ray diffraction (GIXRD) measured at the reciprocal coordinate  $q = (220)$  of the lines is able to provide the information related to the widths of the crystal areas in the patterns (see Figure (3.22)). The notation (220) refers to the Miller indices (hkl) of the probed crystal planes and the momentum  $q$  can be expressed in  $\text{Angstrom}^{-1}$ . The measurements in the (220) planes do not give a direct access to the information concerning the height of the crystal area because it is a dimension measured out of the planes. In contrast, the x-ray reflectivity (XRR) carried out by scanning along the  $z$  axis of the reciprocal lattice coordinate  $q_z$  of the lines allows to determine it. The height will be in turn used in the modeling of the experimental diffractograms in order to extract the information related to the width. The XRR results measured along the lines of the 3D samples studied above are presented in Figure (3.22).

The observed oscillations are called thickness fringes. They result from the interferences of the x-rays reflected by the atomic planes as they penetrate deeper in the crystal. Their broadening is related to how thick is the crystal. The smaller the period of the fringes the larger the thickness of the crystal region, as observed in Figure (3.22). The penetration depth of the x – photons, corresponding to the film's thickness or the height ( $h$ ) in the core of the Fins, is determined by using the expressions  $h=2\pi/\Delta q_z$  where  $\Delta q_z$  is the period between the consecutive fringes. Thus, the value of the height of the crystal areas within the line gratings is indicated in the graphs of each sample. The period of the fringes in sample S1 is larger, traducing a smaller height (50.6 nm) of the crystal area compared to that of the reference sample (55.5 nm) or sample S2 (52.3 nm). The fringes in sample S3 have the smaller period, hence the largest height of the crystal areas compared to S1 and S2.

The experimental spectra acquired along the (220) reflexion by the GIXRD method are provided in Figure (3.23). They represent the transverse scans where the in – plane incidence angle  $\omega(^{\circ})$  was swept over a fixed interval of the detector angle  $\varphi(^{\circ})$ . Such spectra are also called rocking curves because they were acquired by varying only one detector angle. After that, the angular coordinates were converted into the momentum of the reciprocal coordinates  $q_x$  ( $\text{Angst}^{-1}$ ).

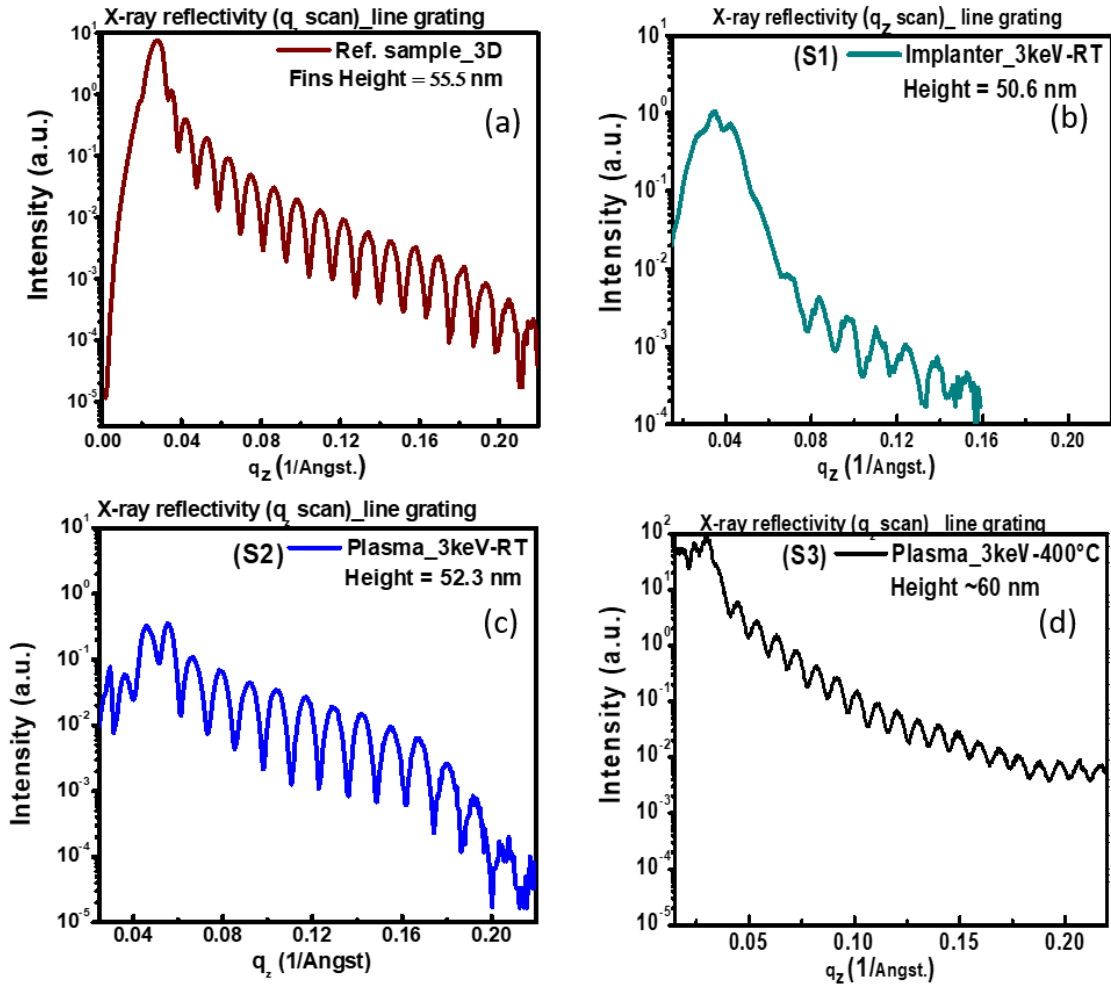


FIGURE 3.22: X-ray reflectivity measurements carried out in the line grating of the samples around the (220) reflexion. The energy of the x – photons was 12 keV and the wavelength 0.103532 nm. The reference sample was obtained from a slot different from that of samples S1, S2 and S3, which could explain a thickness of the crystal area 55 nm  $\neq$  60 nm.

The transformations into the momentum of the reciprocal coordinates allow to compare several spectra in the same graph and to get rid of errors in angular coordinates. The central peaks at  $q_x = 0$  are called Bragg's peaks or the zero order reflexion. The small peaks observed at either side of the central ones are the satellite peaks. Such transverse scans can give access to the real dimensions of the nanostructures [88, 92, 93], namely the width (form factor) and the period or pitch (structure factor) of the patterns. However, the pitch can be determined by computing the period of the satellites. By looking at the different spectra of Figure (3.23), one observes some discrepancies. There are fluctuations of the lateral dimensions of the structures that influence the spectra. Therefore, the fitting of the whole envelop of each spectrum will allow to extract the width. To do this, the mathematical model proposed by T. Baumbach and D. Lübbert [94] was used to calculate the diffracted intensities with their attenuations and they were confronted to the experimental measurements. This model is based on the first order Distorted Wave

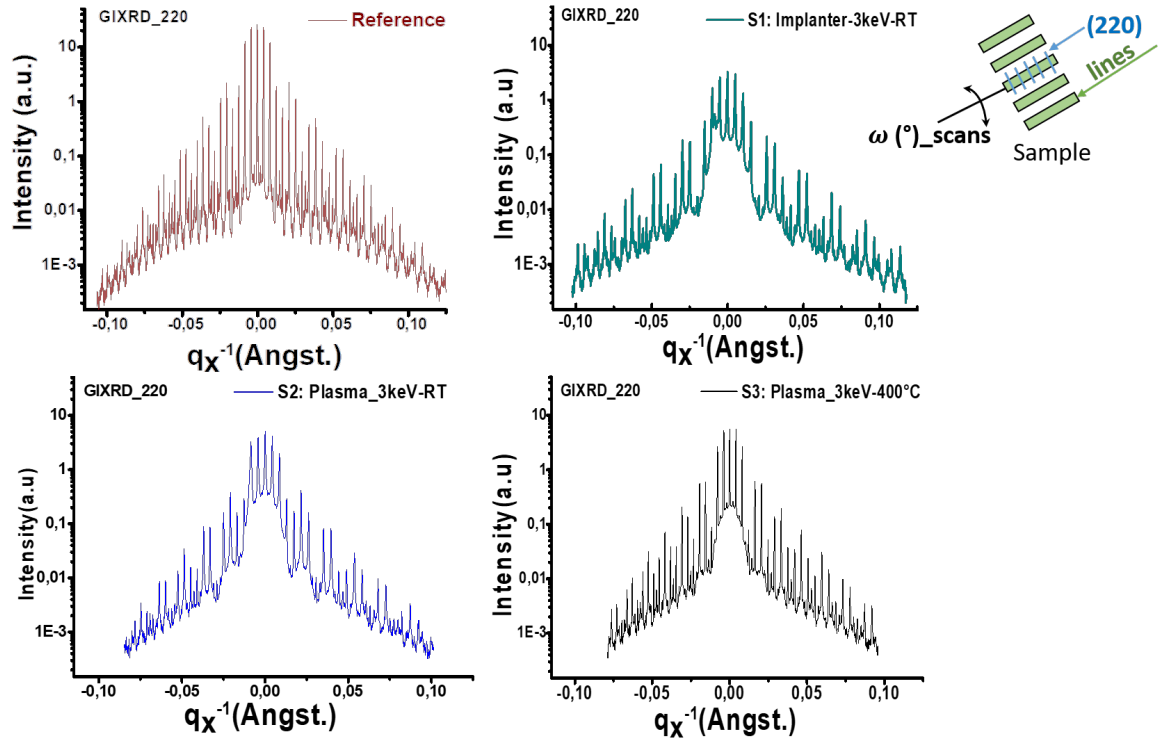


FIGURE 3.23: Raw experimental spectra measured by x-ray diffraction in grazing incidence (GIXRD) mode around the (220) reflexion. They were acquired on the samples implanted with arsenic by the conventional implanter and plasma immersion ion (PIII) methods, then compared with a non-implanted reference. The top-right drawing illustrates the geometrical conditions of the measurements. The wavelength of the x-photons was 0.103532 nm with an energy of 12 keV.

Born Approximation (DWBA). A simplified analytical formula of this model adopted to fit the experimental spectra was developed by using a Mathematica code v. 11.3. The calculations take into consideration the input parameters related to the measurements and the dimensions of the patterns: the incidence and exit angles, wavelength, period (pitch, determined by TEM imaging), the height (calculated from the XRR curves). The schematic diagram of the grating represented in the model is illustrated in Figure (3.24).

The comparison of the calculations of the diffracted intensity and the measurements on a reference non-implanted sample are provided in Figure (3.24). The initial value of the height and the pitch were 55.5 nm and 160 nm respectively, they were used to obtain the best fit presented in Figure (3.25). The width deduced from the calculations is 43.4 nm with a null sidewalls angle.

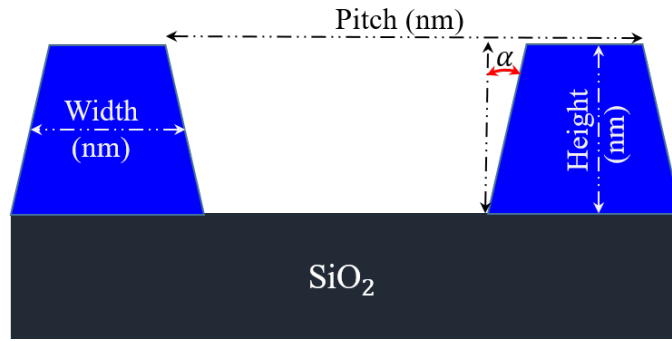


FIGURE 3.24: Model of the FDSOI line gratings used to calculate the diffracted intensities of the reference and the implanted samples. The term  $\alpha$  represents the sidewalls angle to take into consideration a possible non-rectangular shape of the patterns.

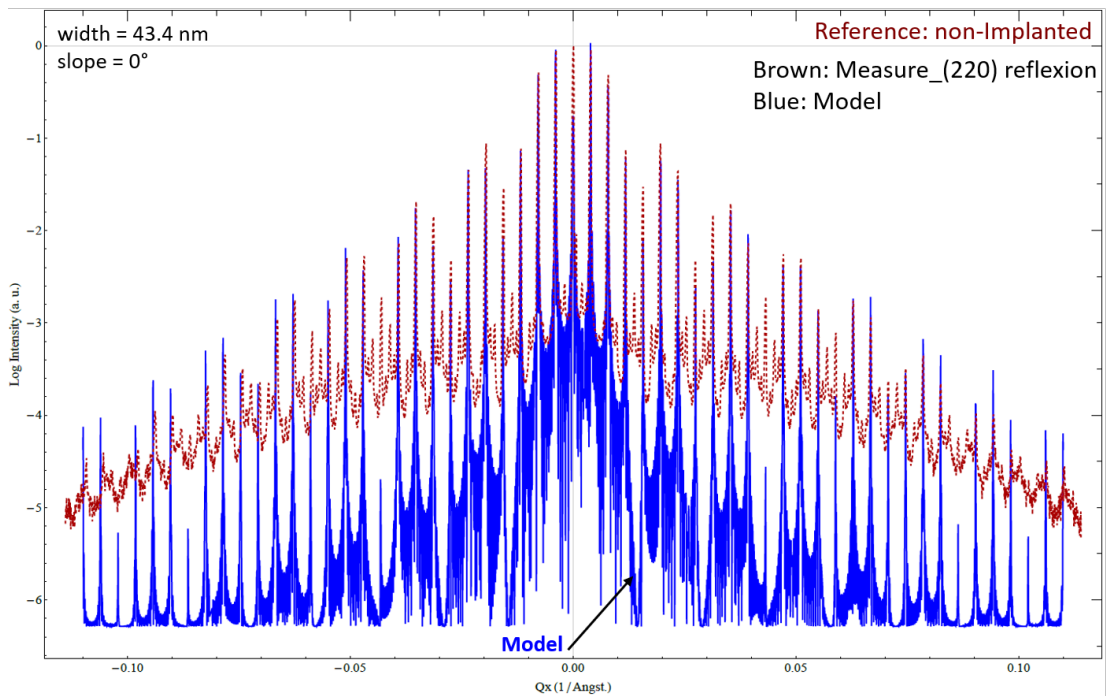


FIGURE 3.25: Comparison of the measured and calculated transverse scan profiles around the (220) reflexion of a non – implanted reference sample. The initial values of the height and the pitch are 55.5 nm and 160 nm, respectively. The width and the sidewalls angle determined by the calculations are indicated in the graph.

### 3.5.1 Case of the sample (S1) implanted at room temperature by using the conventional method

The overlaying of the calculations of the diffracted intensity and the measurements effectuated on this sample are presented in Figure (3.26). The width and the sidewalls angle thus deduced are 37.3 nm and  $0.3^\circ$ , respectively. This width corresponds to that of the non-implanted regions. It is smaller than that of the overall patterns. The determination of the thicknesses of the damaged-implanted areas will be done as explained in the previous lines. However, from a bidimensional approach, one can use the SRIM calculations

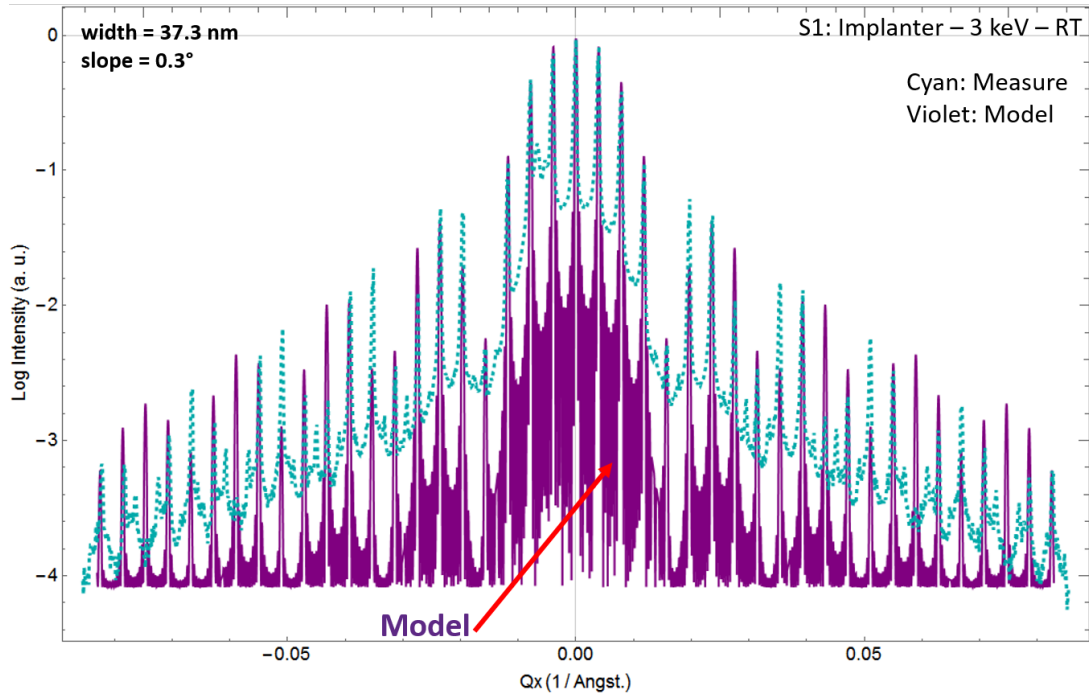


FIGURE 3.26: Comparison of the measured and calculated transverse scan profiles around the (220) reflexion of a sample implanted with arsenic at room temperature by using the conventional implanter. The energy, temperature conditions and parameters corresponding to the best fit are indicated on the graph. The values of the height and the pitch used for the calculations were 50.6 nm and 160 nm respectively.

to estimate at what depths could extend the damages in the tops and sidewalls surfaces. The results show in Figure (3.27) that one should expect roughly 9.5 nm in the tops and 6.5 nm in the sidewalls. The zooming of a pattern of this sample presented in Figure (3.28) indicates that the region implanted and amorphized with arsenic in the tops is about 7.5 nm, but it is tricky to evaluate that of the sidewalls from that image. Table 3.7 nevertheless compares the results obtained with the other analysis techniques.

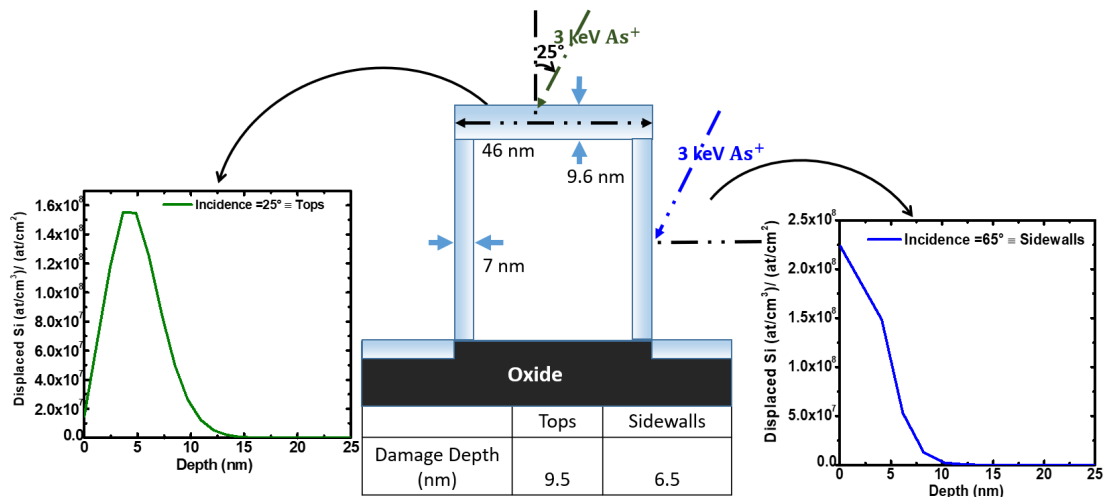


FIGURE 3.27: SRIM profiles of the displaced silicon atoms. They are used to estimate the damaging depths in the tops and sidewalls.

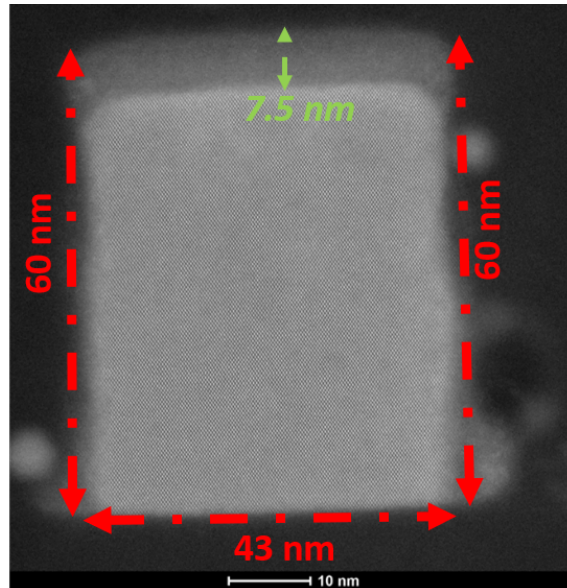


FIGURE 3.28: HAADF image of an isolated Fin of the sample implanted with arsenic at 3 keV-RT by the conventional method. The thickness of the implanted area on the top, the height of the pattern as well as the width of the crystal area are indicated.

Techniques	3D Sample S1: Implanter 3 keV – RT_Pitch = 160 nm					
	Overall dimensions (nm)		Damaged – implanted areas (nm)		Crystal area (nm)	
	Height	Width	Tops	Sidewalls	Height	Width
MEIS PowerMEIS	60	46	8.5	4.5	51.5	37
XRR	-	-	9.4	-	50.6	-
GIXRD	-	-	-	4.4	-	37.2
TEM	60	-	7.5	-	52.5	43
SRIM	-	-	9.5	6.5	50.5	33

TABLE 3.7: Comparison of the vertical and lateral dimensions of the crystal and damaged-implanted areas in the patterns. The values determined by each technique are indicated, the dimensions of the overall nanostructures are provided as well.

The thickness's values of the damaged-implanted areas measured by MEIS and XRR analyses in the tops only differ of 1.1 nm. They are comparable with that predicted by SRIM simulations, which estimate a damaged region of 9.5 nm thickness in the tops of the patterns. The contrast on the TEM image did not allow the identification of the damaged-implanted area on the tops with good accuracy because of the encapsulation of the patterns with an oxide during the sample preparation. One can nevertheless say that the value estimated by TEM (7.5 nm) for the tops' surfaces is close to those measured in MEIS (8.5 nm) and XRR (9.4 nm). Thus, as predicted by SRIM, the x-rays have detected larger implanted and damaged areas in the tops. The discrepancies observed in the dimensions of the damaged areas automatically influence the size of the crystal

regions within the core of the patterns. Their dimensions are indeed deduced from those of the areas damaged by the implantation. The three measurement techniques and SRIM do agree on their height, varying from 50.5 – 52.5 nm.

The values of the width of the crystal regions determined by grazing incidence x-ray diffraction (GIXRD) and MEIS is compared with the SRIM simulations as well. According to Table 3.7, the former technique sees that the damaged areas at the sidewalls are of thicknesses nearly 68% smaller than that predicted by SRIM simulations. However, the conditions in which the patterns were prepared for TEM analyses, make tricky the determination of their overall width. An estimation of the thickness of the damaged-implanted areas in the sidewalls is not easy as well. Thereby limiting the comparison with the other techniques. Only GIXRD and MEIS detect the crystal regions of comparable widths (37.2 nm and 37 nm). In contrast to the height, it is not obvious to establish a coherence between MEIS, GIXRD and SRIM for the width of the crystal regions. A possible hypothesis to explain it is that, the simulations by a purely bidimensional approach with this software are actually not sufficient for the analysis of the sidewalls. A SRIM simulation with a three dimensional structure would be more convenient. From what emerges from the previous discussions, there really exist implanted areas in the sidewalls of this sample that are very damaged. Therefore, the conventionally implanted and damaged regions surrounding the Fins (tops & sidewalls) are nearly totally amorphized since XRD analyses did not sense any orders in these parts of the crystal.

### 3.5.2 Case of the samples implanted by using the plasma immersion ion implantation method.

The next group of samples that will be presented in the following lines concerns those implanted by plasma immersions ion implantation (PIII) with the same energy (3 keV) as the previous sample. An image displaying an isolated pattern of the sample (S2) implanted at room temperature is provided in Figure (3.29), where the implanted-damaged areas containing arsenic on the tops are estimated at a depth of about 6 nm. The encapsulation of the patterns with an oxide during the sample preparation for TEM analyses, makes difficult the determination of any presence of a surface SiO<sub>2</sub>. Thereby limiting an accurate determination of all the dimensions. The GIXRD analyses results obtained on this one are presented in Figure (3.30) and those obtained on the sample (S3) implanted at 400°C are presented in Figure (3.31).

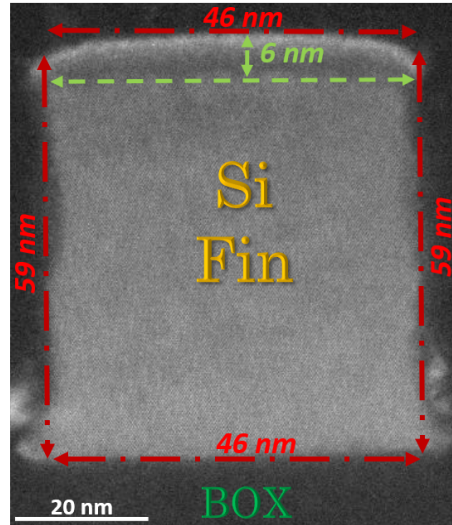


FIGURE 3.29: HAADF image of an isolated Fin of the sample implanted with arsenic at 3 keV-RT by plasma. The dimensions as well as the thickness of the implanted areas on the top ( $\sim 6$  nm) are indicated.

(A)

Dimensions of the overall patterns (Fins)						
Samples (Pitch = 160 nm)	S2: Plasma 3 keV – RT_AsH3			S3: Plasma 3 keV – 400°C_AsH3		
	Techniques & Modeling Tools:	Height (nm)	Width (nm)	Slope $\alpha$ (°)	Height (nm)	Width (nm)
MEIS PowerMEIS	60	49	0°	60	48	0.48°
TEM	59	-	0°	-	-	-

(B)

Techniques	S2: Plasma 3 keV – RT_AsH3_Pitch = 160 nm				S3: Plasma 3 keV – 400°C_AsH3_Pitch = 160 nm			
	Damaged – implanted areas (nm)		Crystal area (nm)		Damaged – implanted areas (nm)		Crystal area (nm)	
	Tops	Sidewalls	Height	Width	Tops	Sidewalls	Height	Width
MEIS PowerMEIS	7.5	6	52.5	37	7.3	5	52.7	38
XRR	6.7	-	52.3	-	$\sim 0$	$\sim 0$	$\sim 60$	-
GIXRD	-	1.25	-	46.5	$\sim 0$	$\sim 0$	-	49
TEM	6	-	53	46	-	-	-	-

TABLE 3.8: Comparison of (A): the vertical and lateral dimensions of the entire patterns used in the MEIS simulations and determined by TEM imaging. There are not TEM data available for sample S3. (B): the damaged implanted and the crystal areas within the line grating of the two samples.

The dimensions of the overall patterns determined by the TEM analyses and those used in the MEIS simulations are provided in Table 3.8– (A). It shows that the total dimensions of sample S2 determined with the two techniques are comparable. Table 3.8 - (B) displays the values of the width of the crystal areas obtained by GIXRD, compared to those determined by MEIS and TEM. In sample S2, the damaged implanted areas measured by XRR and TEM in the tops surfaces are small and comparable (6 nm and 6.7

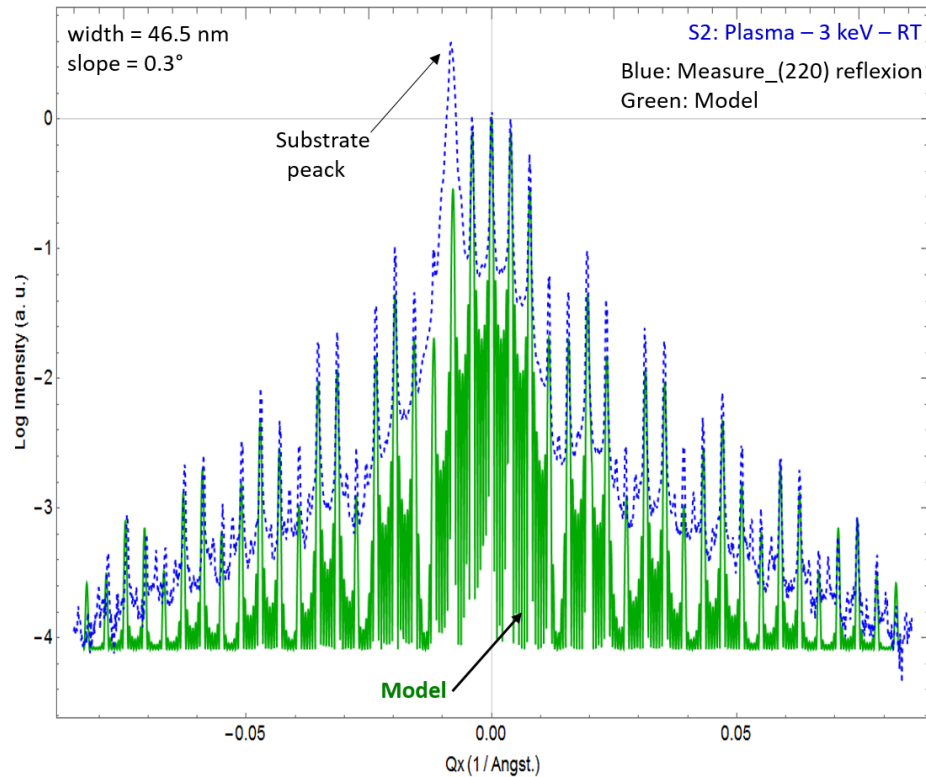


FIGURE 3.30: Comparison of the measured and calculated transverse scan profiles around the (220) reflexion of a sample implanted with  $\text{AsH}_3^+$  at room temperature by using the plasma method. The energy, temperature conditions as well as the parameters corresponding to the best fit are indicated on the graph. The values of the height and the pitch used for the calculations were 52.3 nm and 160 nm, respectively.

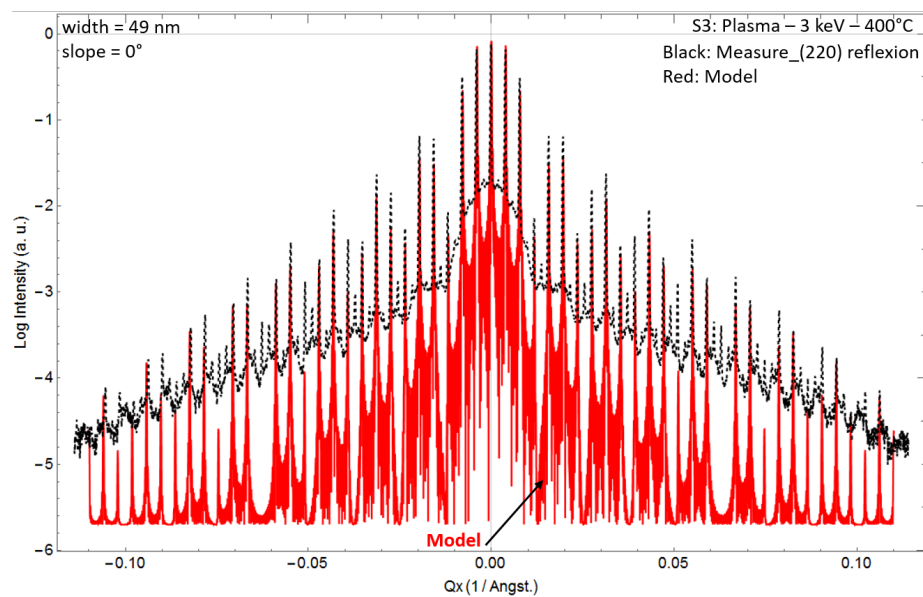


FIGURE 3.31: Comparisons of the measured and calculated transverse scan profiles around the (220) reflexion of a sample implanted with  $\text{AsH}_3^+$  at 400°C by using the plasma method. The energy, temperature conditions as well as the parameters corresponding to the best fit are indicated on the graph. The values of the height and the pitch used for the calculations were 60 nm and 160 nm, respectively.

nm). Yet, the MEIS measures a slightly larger thickness (7.5 nm). Concerning the sidewalls of S2, the GIXRD technique senses very few crystal disorders, despite the important implanted depth indicated by MEIS (6 nm). Thus, the dimensions of the crystal regions determined by GIXRD being close to those measured by TEM, the obvious interpretation is that there was no total amorphization of the implanted areas in this sample. Except the non fully amorphized areas in the tops, deduced by confronting the GIXRD data with those of MEIS and TEM. Regarding sample S3, the analysis of the x-ray data from which the height (60 nm) and width (49 nm) were extracted, show that they are comparable to those of the entire patterns. The discrepancies between the widths of the crystal areas measured by MEIS and GIXRD in S3 are considerable. As conclusion to these observations, one can say that in spite of the in – depth extension of the implanted regions, they are not fully amorphized, as felt by the x-rays. Even though damaged by the implantation, GIXRD sees the overall patterns as crystal. These observations concerning the amorphization levels of the implanted areas around the patterns can be confronted to the MEIS analyses carried out on the ultra-thin layers implanted with the same method and conditions.

### 3.5.3 Confrontation with the MEIS measurements on ultra-thin layers

This section aims at correlating the observations concerning the amorphization levels of the damaged implanted regions within the 3D patterns investigated by x-ray analyses. They can be evaluated with MEIS by overlaying the spectra acquired in channeling and random modes. An easiest way of doing this is to carry out the measurements on the non – etched area of the wafer as shown in Figure (3.32). The channeling mode being mostly sensitive to crystal disorders, it can highlight the existence of damages when the projectiles are aligned along a major crystal axis. Therefore, for a sample implanted at certain depth relatively to its surface, the host atoms are displaced due to the insertion of the foreign atoms. The ions cannot be fully channeled in this region because they interact with the displaced atoms and scatter. Consequently, one observes a peak of high yield on the part of the spectrum corresponding to the implanted – damaged region called damaged peak. If this yield is equivalent to that of the random spectrum presented in Figure (3.32), it means that the implantation has amorphized the area. Thus, the amorphization rate can be evaluated from the ratio of the yield of the damage peak to that of the random mode. The graphs (S1), (S2) and (S3) in Figure (3.32) show the energy spectra acquired on the non-etched areas of the piece of wafers hosting the implanted 3D line gratings studied above.

The notation 2D-S1, 2D-S2 and 2D-S3 will be chosen in order to distinguish the ultra-thin layers from the 3D patterned ones. One observes on Figure (3.32) that the yield

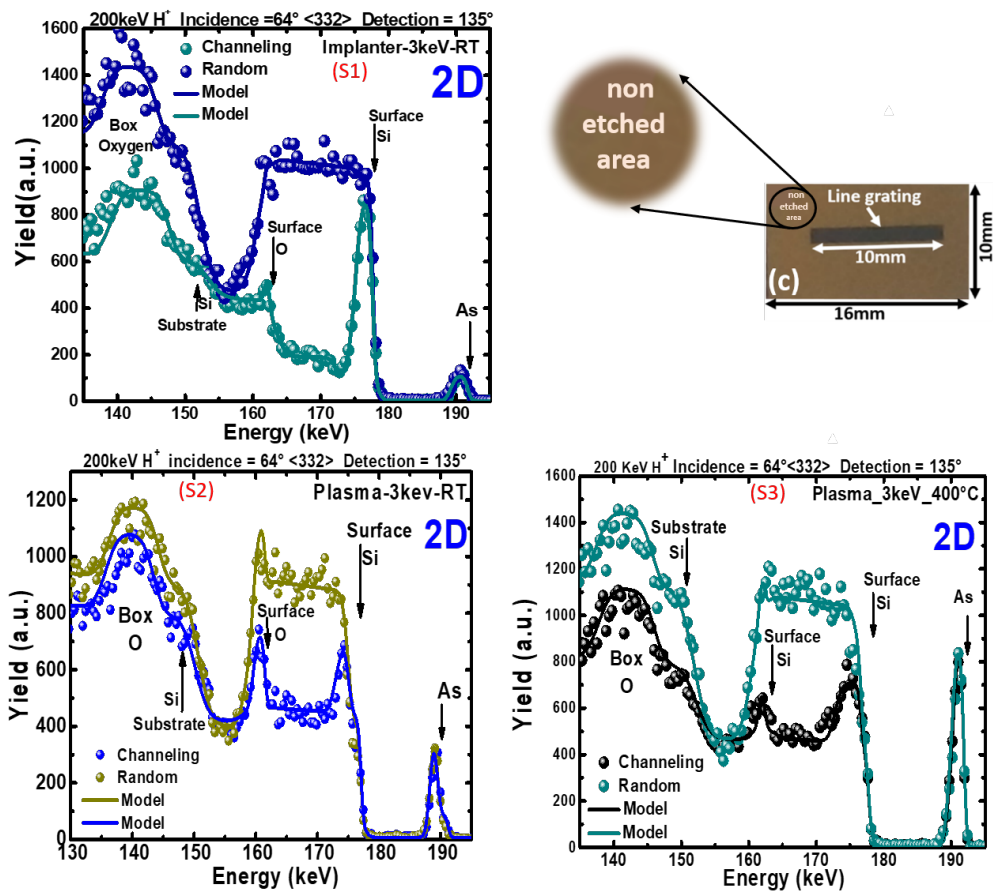


FIGURE 3.32: MEIS experimental results acquired in channeling and random modes on the samples implanted with the conventional implanter (S1) and by plasma – room temperature (S2) and 400°C (S3). The yield of the surface silicon damaged – peak in channeling mode serves to evaluate the amorphization level relatively to the yield in random mode. The top – right drawing shows the non-etched (2D) area on which the measurements were carried out.

of the damaged peak of the sample implanted by the conventional implanter method (2D-S1) is close to that of the random one. As said before, the corresponding area is nearly totally amorphized with the rate of 86 %. This is coherent with the x-ray analyses carried out on the 3D patterns of the same wafer. They showed that the dimensions of the crystal regions are smaller than those of the entire patterns. It is certainly due to the amorphization of an important part along the vertical and lateral directions of the implanted regions. However, the scattering yields of the damaged peaks measured in the 2D areas of sample 2D – S2 and 2D – S3 are very low comparatively to their associated random levels. The amorphization rate in sample 2D – S2 (74 %) is nearly comparable to that in sample 2D – S3 (71 %). These rates correspond to the sensitivity threshold of the x-rays in silicon. The measurements show that these plasma implanted samples are by far not amorphized. This once again agrees with the previous x-ray analyses carried out on the 3D patterns of the same respective wafers.

It has been observed that the height of the non-implanted crystal regions in sample S2 is 52.3 nm. This value is nearly similar to that determined by TEM (53 nm). It corresponds to the non-implanted areas which are not oxidized. The value obtained by MEIS is also similar, since the implanted and oxidized areas are comparable as well. Concerning the width, the TEM and GIXRD are analogue (46 nm & 46.5 nm) because the oxidation revealed by the TEM image is lower at the sidewalls ( $\sim 1.5$  nm) than at the tops ( $\sim 6$  nm). The X-rays are thus sensitive to the crystallized or partially crystallized areas of the patterns, but not sensitive to the implanted ones because they are fully disordered. In contrast, MEIS detects the crystal areas of smaller width, due to the fact that it sees the implanted and oxidized areas as disordered. When it comes to the 3D sample S3, the dimensions of the crystal regions seen by x-ray analyses are the same with those of the overall Fins. In S2 for instance, the MEIS technique sees a crystal area of smaller width ( $\sim 38$  nm) for the same reasons as provided above. Therefore, the MEIS appears as the only technique which is sensitive to the implanted areas in the two PIII samples. While the x-rays do not detect them due to the residual order that still remain.

### 3.6 Summary

The doping conformity in 3D structures has been investigated with medium energy ion scattering (MEIS). The preliminary studies carried out on the ultra-thin layers corresponding to their non-etched areas have served to calculate the dosage and evaluate the implantation depths. The Rutherford Backscattering Spectrometry (RBS) and MEIS agree on the fact that the dose is as targeted in the conventional implantation method, but inferior in PIII – room temperature. The implanted dose is close to the targeted one in PIII – 400°C (see Table 3.1). In the 3D structures, the implantation conditions adopted for the conventional method did not allow a uniform distribution of the implants. It has also been observed that the plasma immersion doping in different temperature conditions gave rise to a different distribution of the implants, compared to the conventional method. One has observed a considerable plasma doping in the tops of the patterns comparatively to the sidewalls. The analyses have revealed that the sidewalls doping in samples S2 and S3 is about 2 times lower than in S1. Therefore, improvements are still required to reach a good doping conformity in the Fins, more remarkably in those implanted by the plasma methods. The bottoms of the plasma implanted 3D samples that are likely to receive comparable implants with the tops surfaces, are lightly doped. A first attempt to explain it, may be the deformations of the potential surfaces due to the geometrical effects of the nanostructures. Another explanation approach is as follows. If the hypothesis of the possible repulsions of the incoming ions due to charges trapped in the oxide is verified, the plasma doping may difficultly lead to a conformal distribution

of the dopants into the FDSOI nanostructures. The method adopted to determine the dimensions of the implanted areas by combining the XRD, TEM and MEIS analyses have shown its efficiency for the sample (S1) implanted by the conventional method. Regarding the plasma implanted samples (S2 & S3), only the MEIS technique provides us with relevant information.

## Chapter 4

# Investigation of structural damages in ultra thin layers

### 4.1 Introduction

In the previous chapter, it was observed that the distributions of arsenic in the two doping methods, as well as its implanted depth are different from one sample to another. Which have drawn our attentions and made us questioned about what can be their contributions in the generation of structural damages. This chapter thus aims at discussing about the modifications into the silicon crystals after their implantation with  $\text{As}^+$  and  $\text{AsH}_3^+$ . It was performed by using the conventional implanter and plasma immersion methods. Heavy ions like arsenic are one of the most used elements for n-type doping of Si after phosphorus (P) because of their low diffusivity and shallow depth penetrations [72]. Due to their large mass, one can expect a total amorphization of the regions where they are located in the crystal. This can be explained by the several collisions cascades they induce during their insertion. Such damages can be considerable at high doses (e.g. in the range  $10^{15}/\text{cm}^2$  or above). The thermal budget should therefore be affordable for the post-implantation annealing in order to favor a rapid recrystallization. Hot implantations are thus considered as good alternatives because they allow the reduction of the amorphization depths[95]. The investigations of the damages in the samples will be therefore carried out with a particular emphasis on the crystal qualities of the areas beyond the implanted ones. The fact of associating the hydrogen to arsenic will be analyzed by focusing on the hydrogen profiles in the RT and  $400^\circ\text{C}$  PIII methods. The medium energy ion scattering analysis technique has been the principal technique used to achieve these studies. It has been associated to the Time-of-Flight Secondary Ion Mass spectrometry (ToF – SIMS) in order to help determine the origin of the anomalies

in the crystals. The results will be commented by taking into consideration the doping conditions in the two different methods.

## 4.2 The MEIS experimental results on ultra thin layers

The two analysis geometries used for the measurements on 3D structures in the previous chapter were also adopted for the non-patterned ones. The experimental results are presented in Figure (4.1) for the incidence at  $64^\circ$  with respect to their surface normal along the  $\langle 332 \rangle$  crystal direction, and for the normal incidence along  $\langle 001 \rangle$ . The implantation methods of each samples are indicated in the figure as well. There are two experimental spectra in each graph of Figure (4.1) associated to their respective simulations. One is acquired in channeling mode and one in random mode. The description of those acquired in random mode and a partial description of the spectra in channeling mode are provided in chapter 3. Therefore, only additional information concerning these spectra will be detailed in this section. The yields of the spectra in channeling and random modes are at the same levels in the buried oxide (Box) because of its amorphous structure. The peaks at energies 161.2 keV (left-column) and  $\sim 165.8$  keV (right-column) are from the scattering off oxygen (O) atoms of the surface oxide. The broader ones at energies  $\sim 146.5$  keV (left-column) or  $\sim 148$  keV (right-column) are from the scattering off oxygen atoms of the Box. The high yields resulting from the scattering off Si atoms in the bulk substrate are indicated.

It worth recalling the doses (in  $\text{at}/\text{cm}^2$ ) computed by MEIS in samples S1, S2 and S3, which are  $1 \times 10^{15}$ ,  $2.1 \times 10^{15}$  and  $4.5 \times 10^{15}$ , respectively. The implanted areas are the parts containing the dopants, they are highlighted in Figure (4.1) by the damaged surface silicon peaks. One observes that their broadenings and yields relatively to the random levels are not the same. These peaks relate on the different surface states of the implanted areas. One of the interests of simulating the measured spectra is to extract of the information related to the thicknesses of the parts damaged by the implantation. Thus, it has been found that the implanted areas extend to the depths of about 11 nm in sample S1 (nearly totally amorphised) and 12 nm in S2 and S3 (not totally amorphized). By looking at the experimental spectra of Figure 1, one realizes that the minimum yields ( $\chi_{\min}$ ), which is computed after the damaged peaks, are different in the two geometries. For each of them, the computed values are different from the measured ones. These parts of the spectra from where the  $\chi_{\min}$  are computed actually represent the non – implanted areas in the samples. We were interested in knowing why these discrepancies, and the cause of the large increase of the  $\chi_{\min}$  when the incoming projectiles are channeled

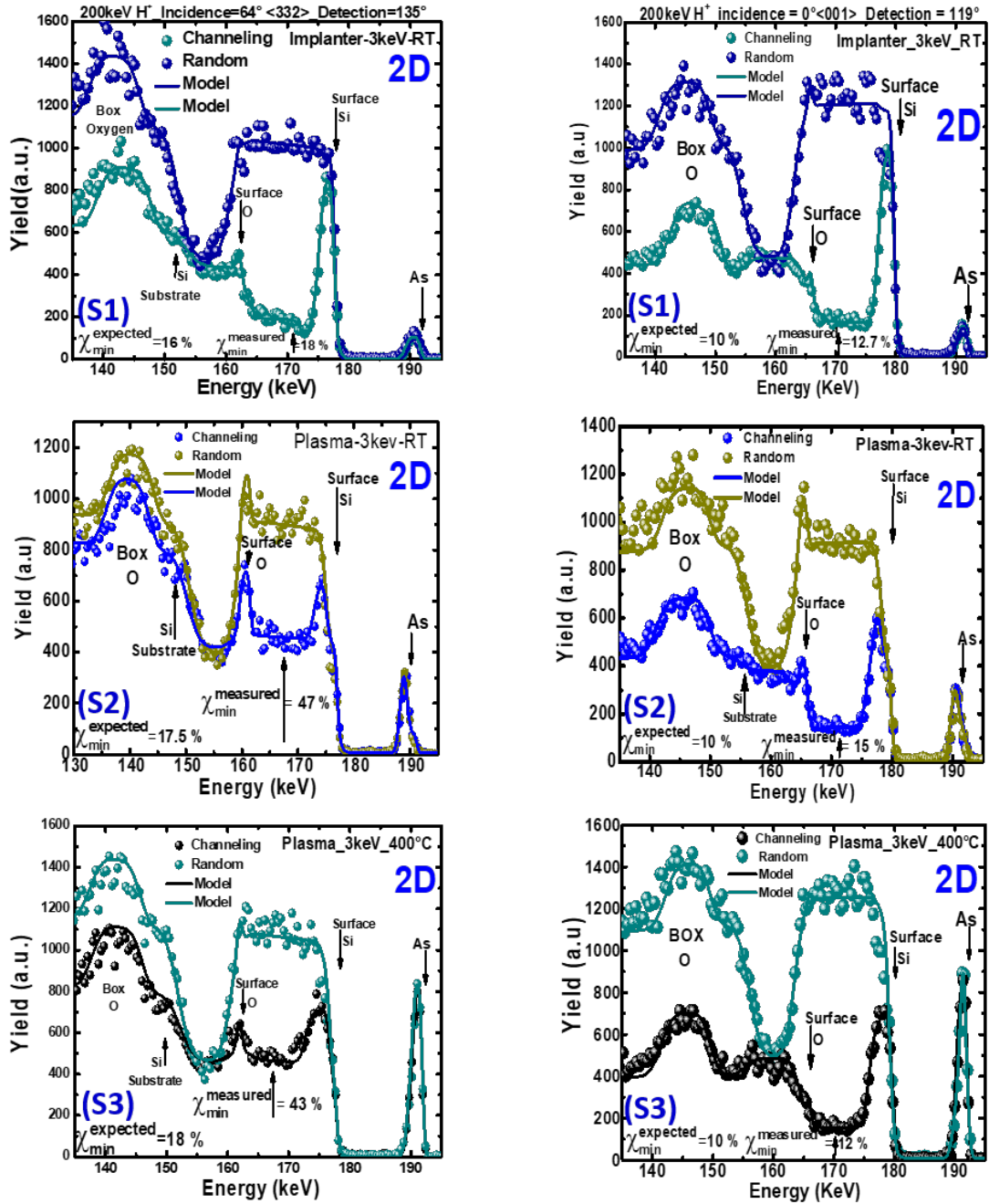


FIGURE 4.1: Experimental results with the associated models obtained on the arsenic ( $\text{As}^+$ : S1) and arsine ( $\text{AsH}_3^+$ : S2 & S3) implanted samples. The spectra of the left – column were acquired at an incidence angle of  $64^\circ$  so as to align the projectiles along the  $\langle 332 \rangle$  crystal axis and detect the scattered ones at  $135^\circ$ . Those of the right – column were measured at an incidence angle perpendicular to the sample’s surfaces (normal incidence  $\equiv \langle 001 \rangle$ ) with the scattering angle of  $119^\circ$ .

along the  $\langle 332 \rangle$  direction. Which brought us analyze the crystal qualities on the non-implanted areas in the samples.

### 4.3 Assessment of the crystal qualities in the non-implanted areas by MEIS

The minimum yield has been exploited to achieve these studies. Since the incident ions traverse a layer damaged by the implantation, they interact with the displaced atoms (defects). When they closely approach the nuclei, they are dechanneled from their ingoing direction and scatter. In the presence of anomalies in the crystal regions unreached by the dopants, the projectiles ions will undergo supplementary scattering. The direct consequence is that the  $\chi_{\min}$  augments in these regions of the crystal. The illustrations of the implantation-induced damages in the crystal silicon with the corresponding examples of their MEIS spectra in channeling and random modes are provided in Figure (4.2).

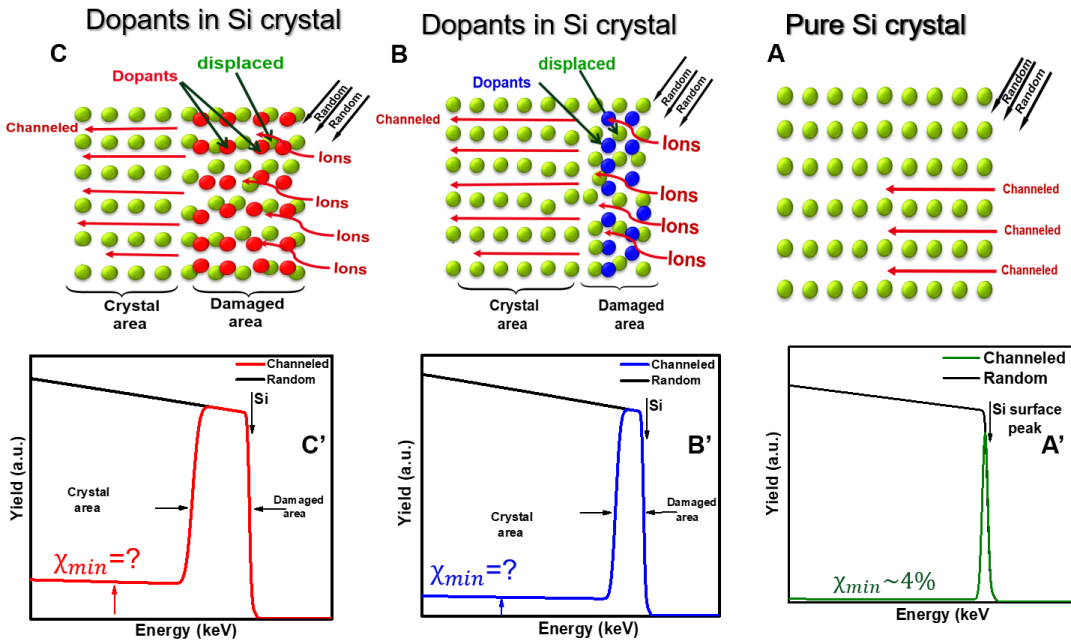


FIGURE 4.2: Illustrations of how the existence of crystal damages lead to the increase of the yield in the Si-crystal region, due to the dechanneling of the ingoing projectiles which affects the minimum yield ( $\chi_{\min}$ ). The example of the corresponding MEIS spectra in channeling and random modes are illustrated. The graphs A & A' depict the case of a pure (virgin) crystal silicon, graphs B & B' are for an implanted silicon showing that the increase of the  $\chi_{\min}$  is related to the thickness of the implanted area. Graphs C & C' are similar to those of graphs B & B', with the only difference that the damaged area is thicker.

When the incident projectiles are channeled along a given axis of a virgin crystal Si, the spectrum only displays a sharp surface peak (graph A' - green curve) resulting from the scattering off Si atoms of the extreme surface. The presence of a native oxide at the surface will also contribute to the formation of that peak in the silicon's signal. As the ions penetrate the crystal, they flow between the atomic rows, guided by the electric field of the nuclei. The  $\chi_{\min}$  is therefore very low in this case because they do not meet

any defects in the crystal. In the situation when the crystal is implanted, the variation of the minimum yield relatively to the thickness of the damaged layers, as illustrated in the graphs (B & B') and (C & C'), can be a reliable parameter to investigate the existence of crystal damages such as defects and deformations. Figure (4.3) presents the normalized MEIS spectra of the damages plotted in function of the depth. The zone – A represents the damaged areas studied in the precedent section and the zone – B is the one of interest for the analyses.

It presents three different case figures explaining the increase of the minimum yield. The graphs A & A' concerns a pure crystal silicon showing a non-null  $\chi_{\min} \sim 4\%$ , resulting from the dechanneling due to the thermal vibrations of the host atoms. The graphs B & B' are provided for an implanted crystal silicon at a certain depth with the associated damaged peak. The  $\chi_{\min}$  represented in the graph varies with respect to the damaged layer traversed by the ingoing projectiles. If the damaged – implanted layer is thicker, the dechanneling also increases as the ions traverse it, thereby inducing a large  $\chi_{\min}$  as depicted in the graphs C & C'. Since the depth extension of the damaged – implanted layer influences the minimum yield, we have therefore produced a graph (Figure (4.3)) showing its evolution in function of the thickness of the damaged layer traversed by the incident projectiles. The explanations on how to obtain it were already provided in chapter 2. As can be seen, the evolution of  $\chi_{\min}$  follows a linear law which is valid in the case of simple collisions and for ultra-thin layers.

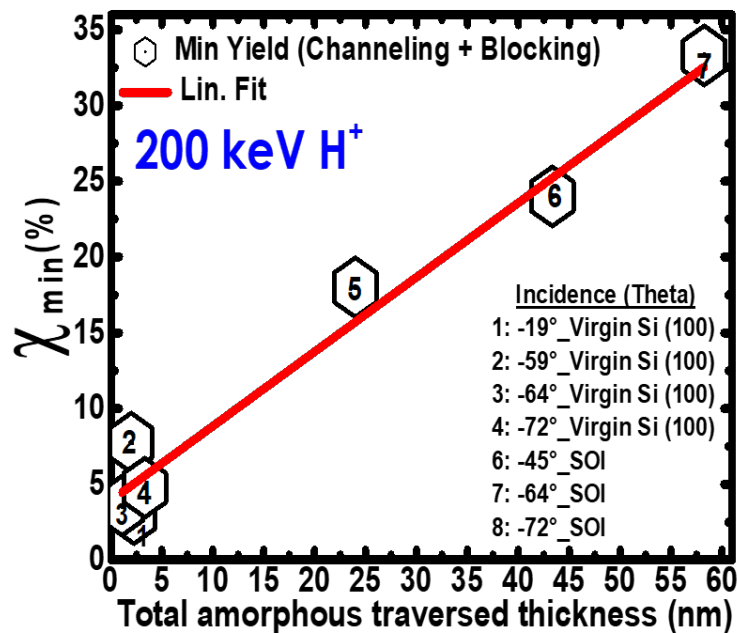


FIGURE 4.3: Evolution of the minimum yield with respect to the amorphous layer traversed by the incident projectiles in the silicon crystal.

When the incident projectiles are channeled along a given axis of a virgin crystal Si, the spectrum only displays a sharp surface peak (graph A' - green curve) resulting from the scattering off Si atoms of the extreme surface. In the presence of a native oxide at the surface will also contribute to the formation of that sharp peak in the silicon's signal and one also observe a sharp oxygen peak in the spectrum. As the ions penetrate inside the crystal, they flow between the atomic rows, guided by the electric field of the nuclei. In this case, the  $\chi_{\min}$  is very low because they do not meet any defects in the crystal. In the situation when the crystal is implanted, the variation of the minimum yield relatively to the thickness of the damaged layers, as illustrated in the graphs (B & B') and (C & C'), can be a reliable parameter to investigate the existence of defects in the crystals. Figure (4.4) presents the normalized MEIS spectra in channeling mode, plotted in function of the depth. The zone - A is representative of the damaged areas in the samples and the zone - B is the one of interest for the analyses in this section.

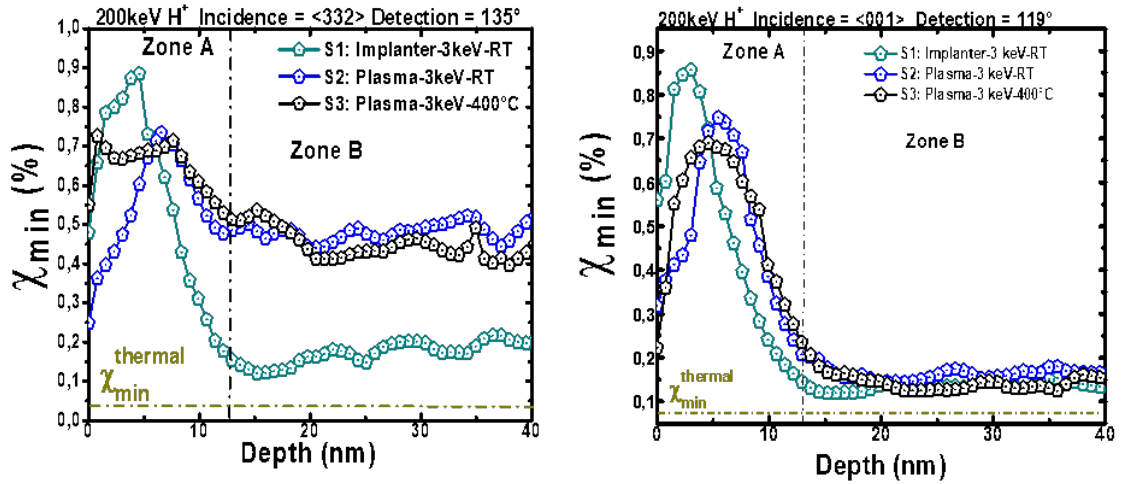


FIGURE 4.4: Normalized MEIS spectra of the damages in channeling mode, represented by the  $\chi_{\min}$  plotted in function of the depth. They derive from the spectra of Figure (4.1) measured along the  $\langle 332 \rangle$  channeling direction ( $64^\circ$  incidence) and in normal incidence ( $\langle 001 \rangle$ ). The Zones A and B refer to the implanted and non-implanted regions in the Si crystal. The  $\chi_{\min}$  corresponding to thermal vibrations of the Si atoms is indicated.

In Figure (4.4), the minimum yields computed in the 'zones B' for the geometry in off-normal incidence (left - graph,  $64^\circ \equiv \langle 332 \rangle$ ) are higher than those computed for the geometry in normal incidence (right - graph,  $\langle 001 \rangle$ ). The reason is that, the incident projectiles do not penetrate the crystal in the same way. For example, for a crystal in which the atomic planes are stretched along a given axis due to the effects such as deformations, the lattice parameter also augments along this axis (see Figure (4.5) (A)). When the projectiles penetrate it at an inclined incidence along a channeling direction like  $\langle 332 \rangle$ , they are very sensitive to these deformations and become partially channeled. The consequence is that the minimum yield augments because of the important deviation

from their ingoing direction. In contrast, for an incidence along the normal or vertical direction (e.g.  $\langle 001 \rangle$ , Figure (4.5) (B)), the incident projectiles are not sensitive to these vertical deformations. Consequently, they do not experience supplementary scattering within the crystal, after they have traversed the area containing the dopants and damaged by the implantation. This can explain why the minimum yields measured along the  $\langle 001 \rangle$  axis is very lower than those measured along the  $\langle 332 \rangle$  direction. However, this needs to be demonstrated with further details.

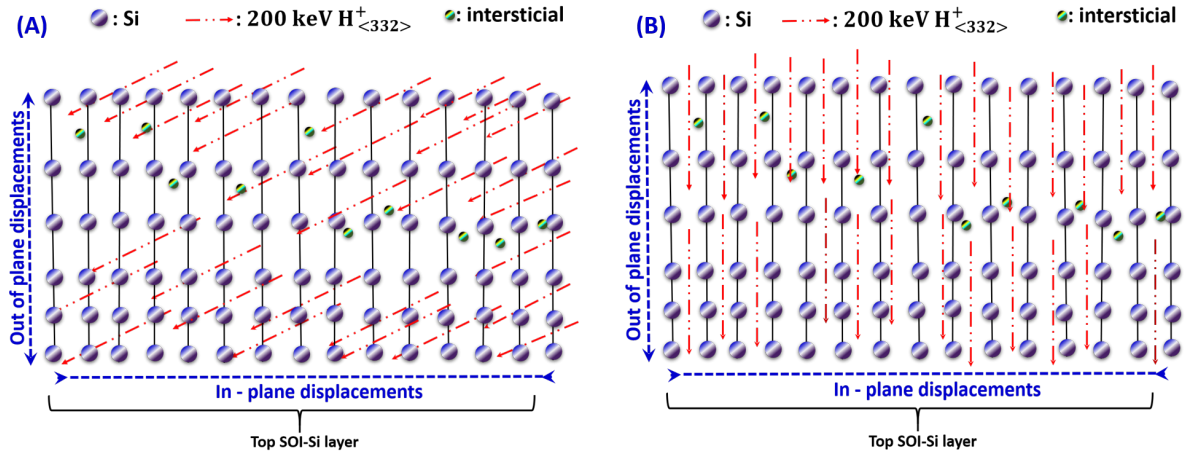


FIGURE 4.5: Illustrative examples of how the incident projectiles penetrate a crystal containing different types of damages such as displaced atoms, distortions, interstitials, when they are channelled along an inclined  $\langle 332 \rangle$  direction (A) and a vertical  $\langle 001 \rangle$  crystal axis (B).

#### 4.3.1 Highlight of the presence of defects in the crystal by using MEIS

The line predicting the evolution of  $\chi_{\min}$  with respect to thickness of the damaged layers has been used to compute its expected values in function of the thicknesses of the implanted areas. The example illustrating the principle of the computations is presented in Figure (4.6). It has been obtained on two samples displaying different values of the measured  $\chi_{\min}$ . The first sample is the one implanted with As – 3 keV – RT by using the conventional method (S1) and the second (S2) is implanted with AsH<sub>3</sub><sup>+</sup> – 3 keV – RT by using the plasma immersion method.

As shown in Figure (4.6) the expected values computed along the vertical crystal axis  $\langle 001 \rangle$  in the two samples are low (10 %). The small discrepancy between the theoretical and the measured values in sample S1 (2 %) show that its crystal has low defects. Consequently, it is of good quality. In contrast, the differences of 5 % in S2 is non-negligible. The Following comparisons and reasonings will be adopted to study the crystal of the sample implanted by plasma at high temperature (400°C). The results

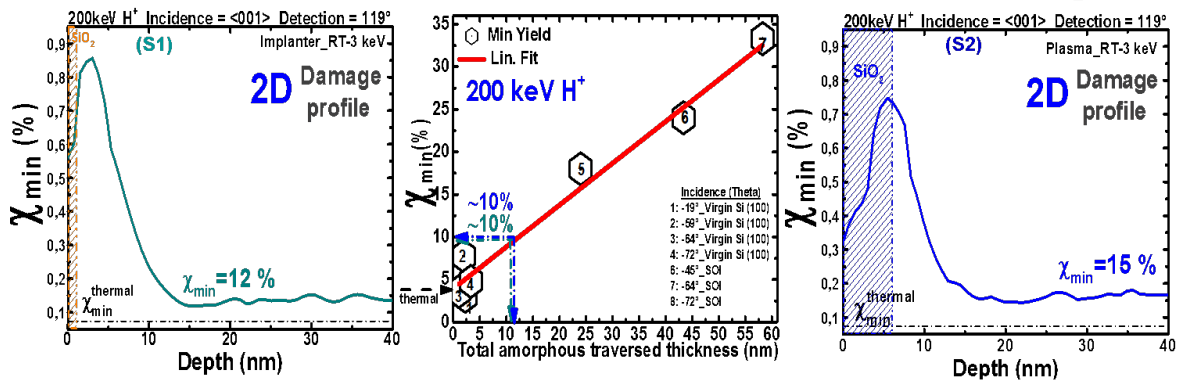


FIGURE 4.6: Determination of the expected min by using the calibration line giving the evolution of the minimum yield with respect to the amorphous thickness. The computed  $\chi_{\min}$  in normal incidence ( $\langle 001 \rangle$ ) are equivalent for the two samples (10%). The experimental values are indicated in their respective spectra.

comparing the expected and measured values of the minimum yields along  $\langle 001 \rangle$  in the three samples are thus regrouped in the bar charts of Figure (4.7).

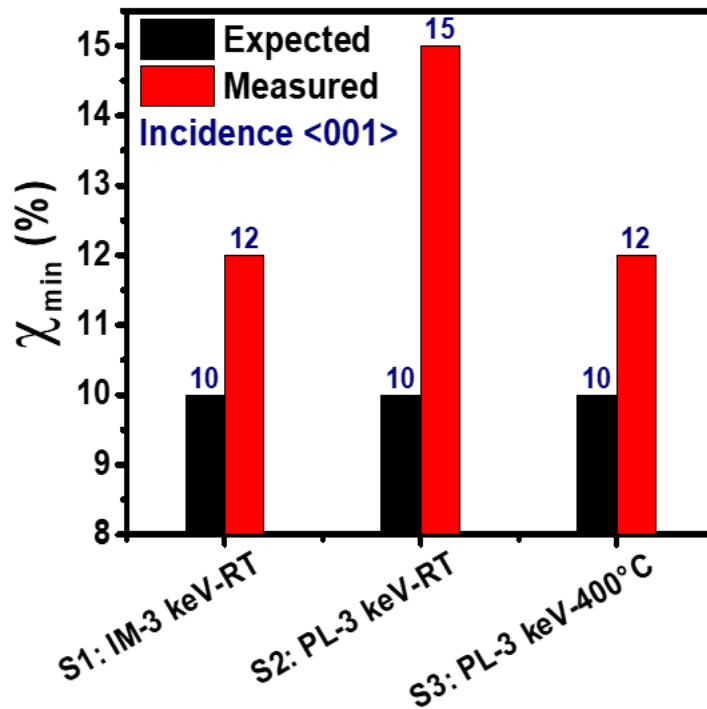


FIGURE 4.7: Comparison of the values of the measured minimum yields (obtained from the experimental spectra) and those extracted from the calibration line in normal incidence ( $\langle 001 \rangle$ ). The notation IM refers to implanter method and PL refers to plasma method.

Figure (4.7) shows that the discrepancies between the expected and measured values of  $\chi_{\min}$  are low. However, one observes that the expected  $\chi_{\min}$  in the three samples are the same. This can be explained by the fact that their implanted areas crossed by the ions are

of comparable depths. In particular, the difference between the expected and measured values of  $\chi_{\min}$  in S3 is comparable to that of S1. This indicates that the defects' rate in the sample implanted by PIII at 400°C is also low. However, for a good comparison, one should compute the differences between the measured and expected values of  $\chi_{\min}$  represented as  $\Delta\chi_{\min}$ . It gives the real rate of defects within each crystal.

The  $\Delta\chi_{\min}$  along the  $\langle 001 \rangle$  axis can be interpreted as the signature of structural defects revealed by the projectiles scattered in the corresponding regions inside the crystals, when they probe them in that direction. As announced by Figure (4.6) they are low. Except in sample S2 that displays a  $\Delta\chi_{\min}$  which is slightly increased (5 %). One observes how the high temperature plasma implantation reduces the rate of defects. It indicates that there is only a small contribution of defects in the dechanneling process of the incident projectiles. In Figure (4.7), the MEIS technique thus highlight its capability of determining the existence of defects within the crystal Si regions. It shows in general that they are of good qualities after the implantation.

#### 4.3.2 Highlight of the existence of deformation gradients into crystals by MEIS

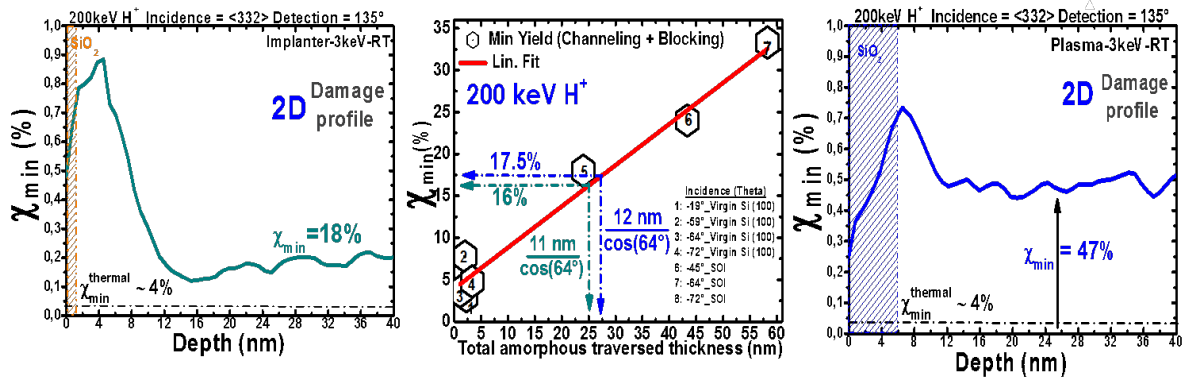


FIGURE 4.8: Determination of the expected  $\chi_{\min}$  by using the calibration line giving the evolution of the minimum yield with respect to the amorphous thickness. The incidence angle of the projectiles was 64° ( $\langle 332 \rangle$ ) with respect to the sample's normal.

The same procedure as the one employed to characterize the defects within the non-implanted crystal regions has been carried out to investigate the presence of the deformation gradients. According to Figure (4.8), a  $\chi_{\min}$  of 16 % was expected in S1 and 17.5 % in S2, when the incident projectiles penetrate their respective non-implanted areas after they have traversed the damaged ones at 64°. Yet, the measured values are larger. The raw results of the expected and measured values of  $\chi_{\min}$  along  $\langle 332 \rangle$  for the three samples are compared in Figure (4.9). One can also observe a large  $\chi_{\min}$  in sample

S3, measured along the same direction. The fact of having large minimum yields measured along  $\langle 332 \rangle$  indicates that the supplementary scattering yield of the projectiles is mostly due to something else than defects. Because, if there were considerable defects in the non-implanted crystal regions, the  $\chi_{\min}$  measured in normal incidence would be comparable to the values displayed in Figure (4.9). Which is not the case. Therefore, it is possible that the deformations be responsible of the large values of the minimum yields.

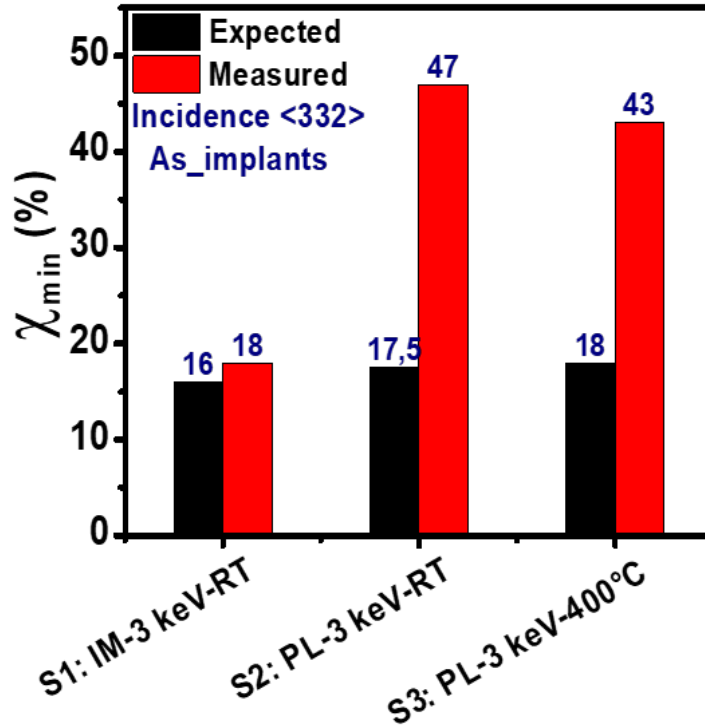


FIGURE 4.9: Comparison of the values of the measured minimum yields (obtained from the experimental spectra) and those extracted from the calibration line in inclined incidence ( $\langle 332 \rangle$ ). The notation IM refers to implanter method and PL refers to plasma method.

#### 4.4 Investigation of the co-implanted elements by ToF – SIMS

Given that  $\text{AsH}_3^+$  was used as precursor gas in the PIII method, the possible implantation of hydrogen (H) inside the crystal in order to cause anomalies is not excluded. Mostly if it is accelerated at a sufficient energy. It is therefore relevant to assess its possible responsibility in the generation of crystal disorders. Thus, the co-implantation of the hydrogen ions with  $\text{As}^+$  in the plasma immersion methods has been studied with a particular emphasis on their in-depth penetrations. Due to their low atomic number ( $z = 1$ ), their detection in medium energy ion scattering is not possible. The analyses by

time of flight – secondary ion mass spectrometry (ToF – SIMS) were therefore carried out in order to probe the depth profiles of hydrogen in the three samples. The negative depth profiles were acquired using a 0.5 keV Cs<sup>+</sup> sputter beam and a pulsed 25 keV Bi<sup>+</sup> analysis beam. A low energy (20 eV) electron flood gun was used for charge compensation. The measurements were conducted in ultra-high vacuum conditions ( $<5 \times 10^{-10}$  mbar). The depth calibration was performed by profiling boron deltas in a silicon reference sample. A hydrogen - implanted sample ( $6 \times 10^{16}$  H/cm<sup>2</sup> in Si) was used as a reference for quantification. The results are compared in Figure (4.10).

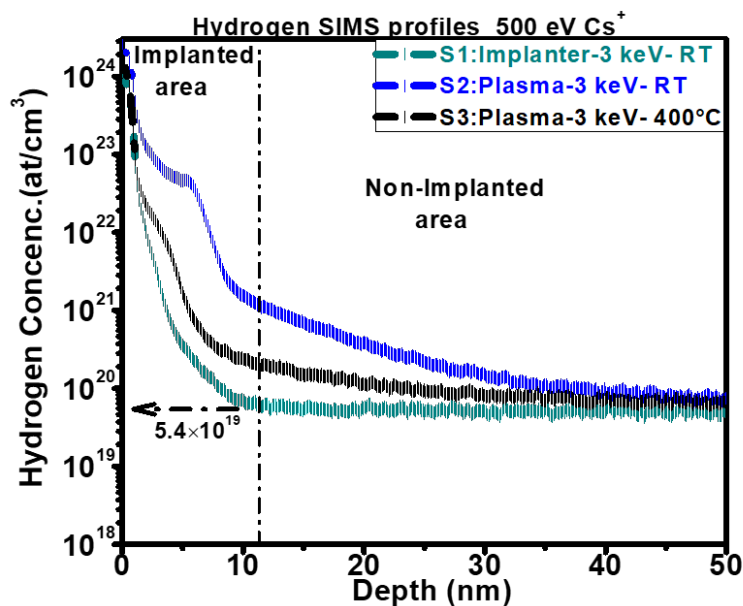


FIGURE 4.10: Comparison of the ToF-SIMS profiles of hydrogen, measured in the AsH<sub>3</sub><sup>+</sup> – implanted samples at 3 keV. A Cs<sup>+</sup> beam of energy 500 eV was used for the abrasion and the elements were analyzed with a Bi<sup>+</sup> beam of 25 keV. The depth calibration was performed by profiling boron deltas in Si (the deltas being measured by TEM). The implanted and non-implanted areas are those determined by MEIS.

Except the sharp and intense peaks displayed by the three spectra at the depths corresponding to the near surface regions (0 – 4 nm), one observes a continuous decrease of hydrogen with the depth. It is worth recalling that sample S1 has been implanted with single arsenic atoms rather than with AsH<sub>3</sub><sup>+</sup> molecules like in S2 and S3. This signifies that S1 should normally not contain hydrogen. The constant concentration of H in the non-implanted film of S1 is assimilated to the residual level in the analysis chamber. Thus, any H profile above that level should be considered as the real implanted hydrogen. In Figure (4.10), the concentrations of H in the PIII samples are above that of the conventionally implanted sample (S1) from the near surface area until beyond. The same figure shows that the significant quantities of hydrogen implanted in S2 at room temperature, is considerably reduced at high temperature (sample S3). Its large concentration at greater depths means that some fractions penetrated beyond the implanted areas with large energies. To verify this, the SRIM simulation of an H profile at 3 keV is confronted

to the experiments as illustrated in Figure (4.11). It is observed that the SRIM simulations of hydrogen overlay with their SIMS experimental profiles in samples S2 and S3 at depths above 40 nm. The energy actually possessed by a hydrogen atom associated to the  $\text{AsH}_3^+$  molecule accelerated at 3 keV is 0.028 keV. At these values, they cannot account for the SIMS experimental profiles as close as when they are simulated with an energy of 3 keV. It is only with 3 keV that one can better approach the experiments.

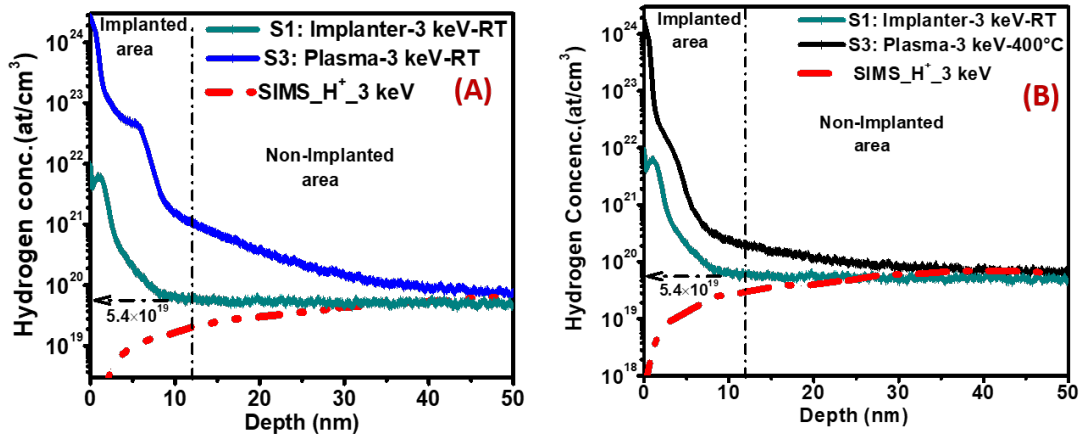


FIGURE 4.11: ToF-SIMS profiles of hydrogen in the 3 keV (A, B) PIII implanted samples with the associated SRIM simulations. The energies of the H ions used in the simulations were 3 keV. The concentrations corresponding to the residual contamination in the SIMS chamber are indicated by the arrows. The implanted and non-implanted areas are those determined by MEIS.

The hydrogen content measured in the PIII samples with a concentration superior to that of the natural contamination have impacts in the crystals, mostly beyond the implanted areas. Even though they are very few defects in all the samples, the deformation gradients exist in the plasma implanted ones. The  $\chi_{\min}$  measured along  $\langle 332 \rangle$  which can be attributed to the presence of deformation gradients, is larger in the RT plasma implanted sample (30% - S2) than in the one implanted at 400°C (25 % - S3). These high rates may probably arise from the existence of a concentration gradient of hydrogen in these samples. By looking at Figure 10 and Figure (4.11), one can realize that this gradient is more considerable in sample S2 than in sample S3. Hence a coherence with the evolution of the minimum yields. Even though they follow the same trend, one can note that the evolutions of the  $\chi_{\min}$  and the hydrogen concentration are not proportional. The explanation is as follows. The incident beam only channels if its orientation with respect to the local crystal direction is inferior to the critical angle. It does not follow a linear law since its variation in the presence of a deformation gradient also depends on the depth.

From these observations, one can say that the existence of deformation gradients essentially results from the implantation of hydrogen. The implanted dose of arsenic at 400°C is more than the double of that at room temperature. Yet, beyond the implanted areas,

the concentration of hydrogen at high temperature is more than two times smaller than that at room temperature. Therefore, implanting by PIII at high temperature reduces the hydrogen contamination due to its desorption.

## 4.5 Summary

This chapter was consecrated to the investigation of the post-implantation structural damages within the crystals, by using medium energy ion scattering (MEIS) as principle technique. The investigations have shown that the damaged-implanted areas are shallow, extending to the depths 11 – 12 nm. The amorphization rate in the PIII implanted sample at room temperature is larger than at 400°C. In contrast, it has been observed that the conventionally implanted sample was nearly totally amorphized. A particular attention has been consecrated to the crystal Si beneath the implanted areas. It has been observed that there are very few defects in the samples. The crystal of the samples implanted by the plasma method are deformed, however, with a reduction at 400°C. By correlating the MEIS with the ToF-SIMS analyses, it has been found that the element mainly responsible to the presence of the deformation gradients is hydrogen. An important effect to note is that, the PIII implantation with  $\text{AsH}_3^+$  at 400°C significantly reduces the quantity of hydrogen presents within the crystal underneath the implanted regions. This diminution is followed by the reduction of the rate of deformation gradients that they induce. It could be interesting to assess the effects of rapid thermal processes on the implanted depths, defects and deformation gradients.

## Chapter 5

# General conclusion & future works

The aim of the studies was to investigate the doping into the structures of three dimensional (3D) architectures. Several state-of-the-art experimental techniques based on ion beam (MEIS), x-rays and electron microscopy have been used. The doping in question has been performed by using the conventional implanter (or beamline) and plasma immersion ion implantation (PIII) methods. The nature of the dopants utilized are single arsenic ions ( $\text{As}^+$ ) and arsine ( $\text{AsH}_3^+$ ).

The low lateral resolution of the MEIS beam was not adequate to analyze the model systems adopted for the investigation of the 3D doping. In order to circumvent this difficulty so as to probe the patterns locally, a suitable protocol has been developed. It encompasses a set of three different geometries from which one can localize the information on the dopants inserted in each part. The simulated MEIS spectra of the arsenic implanted in the tops, bottoms, sidewalls have been provided by the use of adequate codes and the PowerMEIS software. Each geometry provides the information related to the arsenic located in these three parts of the line gratings. However, each part contributing differently. In the geometry where the scattered projectiles are detected laterally with respect to the patterns, the signal of arsenic implanted in the bottoms is separated from those of the sidewalls and tops. While in the geometry where the scattered projectiles are detected longitudinally, the signal of arsenic in the tops and bottoms are mixed but discriminated from the those of the sidewalls. One can therefore deconvolute the conformity in the 3D doping by using MEIS with three different analysis geometries.

The MEIS has demonstrated its efficiency in extracting the crucial information concerning the dosage in these types of 3D structures. The possibility of determining the quantity of the dopants in each parts of the patterns as we did, is very important in the sense where, it stands as the key criteria to appreciate the conformity. We have observed that the local dose implanted in the tops of the patterns by using the conventional method

is comparable to that expected, which is a good result. In contrast, unexpected results were obtained in the 3D structures implanted by PIII. Indeed, significant discrepancies have been observed in the distributions of the dopants, with large concentrations in the tops and few in the oxide and sidewalls. The geometry of the nanostructures of such dimensions can induce effects such as the derivations of the potential surfaces mainly at the corners of the patterns. The consequence on the doping is the deviation of the trajectories of the incoming ions so as they cannot reach the sidewalls and bottoms. This can be a possible explanation of the non-uniform distribution of the dopants inside the structure, but these effects are weak. They cannot justify the considerable discrepancies observed. Because the low bottoms doping was not observed in the 3D sample implanted by the conventional method, but only in those implanted by plasma. As suggested, the charge accumulations in the oxide could explain it, due to the repelling of the incoming ions from penetrating into the oxide and therefore focus them in the tops. Even though the plasma implantation was not conformal in the samples studied here, we also claim that this method is the good alternative to achieve large scale and fast 3D dopings with high throughput. However, the type of the nanostructure may influence the outcomes, namely the SOI materials.

It was interesting to determine the thicknesses of the implanted areas surrounding the Fins. The combination of the x-ray analyses, namely grazing incidence diffraction (GIXRD) and reflectivity (XRR) in correlation with MEIS and TEM provided us with relevant results. They have shown that the areas of ultra-thin thicknesses implanted by the conventional method are nearly totally amorphized. Similar investigations could be carried out by MEIS in channelling mode by deconvoluting the contribution of the tops and sidewalls in the formation of the surface peak. This is an open problem since there is not yet a tool with which one could process the spectra acquired on such structures in channeling mode. Nevertheless, one can note from these analyses that MEIS can be correlated to XRD for an efficient investigation of the implanted layers into the 3D structures.

The assessment of the post-implantation crystal qualities has been another way of studying the impacts of the different doping processes on the samples by using MEIS. It has been found that the rate of defects in the non-implanted crystals of all the samples are very low. With a significant diminution in the sample implanted by plasma at 400°C. The ToF-SIMS analyses have revealed that there is no hydrogen in the crystal of the conventionally implanted sample. Which is not the case for the plasma implanted ones where the quantity of hydrogen is considerable in RT, but significantly reduced at 400°C. The MEIS technique has also highlighted the existence of deformation gradients in the non-implanted crystals, as the main responsible of the dechanneling of the incidence projectiles along  $\langle 332 \rangle$ . Thanks to the ToF-SIMS measurements, it has been found

that the co-implantation of hydrogen is the main responsible of their presence. Since they diminish at 400°C, rapid thermal annealings can be good alternatives to cure the crystals after the implantation. From what comes out of the above discussions, there is a clear evidence illustrating that the MEIS analyses are of course powerful, but has to be correlated to other complementary techniques as well. Without forgetting the major modeling and simulation tools required.

## Future works

In chapter 3, the structures that have been studied are of same Pitches and heights. It could be interesting to investigate those of different dimensions in order to check if there is an influence on the dopants' distribution, hence on the conformity. Because of the unique energy used in the two doping methods, the impacts of the different implantation energies on the conformity was not possible to assess. The impact of the different implantation energies on the doping conformity can be explored as well.

It has been hypothesized that the charging effects are more likely to occur during the plasma doping of SOI nanostructures. Which represent a challenge to overcome if there are evidenced. We only relied on our results to propose the possible existence of these phenomena. Nevertheless, we think that an experimental process to verify the existence of the charging effects, is to carry out measurements on two different patterned samples hosting the line grating of same dimensions (pitch, width, length). However, they have to be elaborated from two different types of wafer: one issued from the bulk silicon technology and the other from SOI. They should simultaneously be implanted with the same dose, energy and in the same temperature conditions. The comparison of the results would help find out the appropriate doping conditions for each types of nanostructures. The combination with the x-ray analyses by using a synchrotron source will give access to the implanted areas. Thus, the association of the MEIS and x-ray analyses techniques within the method that we named 'X-MEIS' stand as a relevant one for the investigations of the doping of the 3D structures. Alongside the experimental processes, another way of investigating the existence of the charging effects can be done by 3D molecular dynamics simulations.



The dimensions and shape of the patterns in each sample were conserved when generating their respective models. The layers built from the surface until at certain depth within the patterns are introduced in the in order to take implantation of the dopants into account. A same number of layers of same total thicknesses were used. The different stoichiometries were introduced from the simulation files used in PowerMEIS.

The procedure of the 3D - deconvolution is such that the simulated spectrum of arsenic inserted in each part of the structure derives from the simulated spectrum of the total structure. Therefore the models corresponding to each of these spectra should derive from that of the overall 3D structure as well. The example of the matrix models that were generated in order to simulate the single implantations at the tops, bottoms, sidewalls – I and sidewalls – II are illustrated in figure (A.2). An interpretation of these images is as follows. If the implantations were performed in only one of the respective parts of the Fins as illustrated, we would have had the corresponding spectra shown in chapter 3.

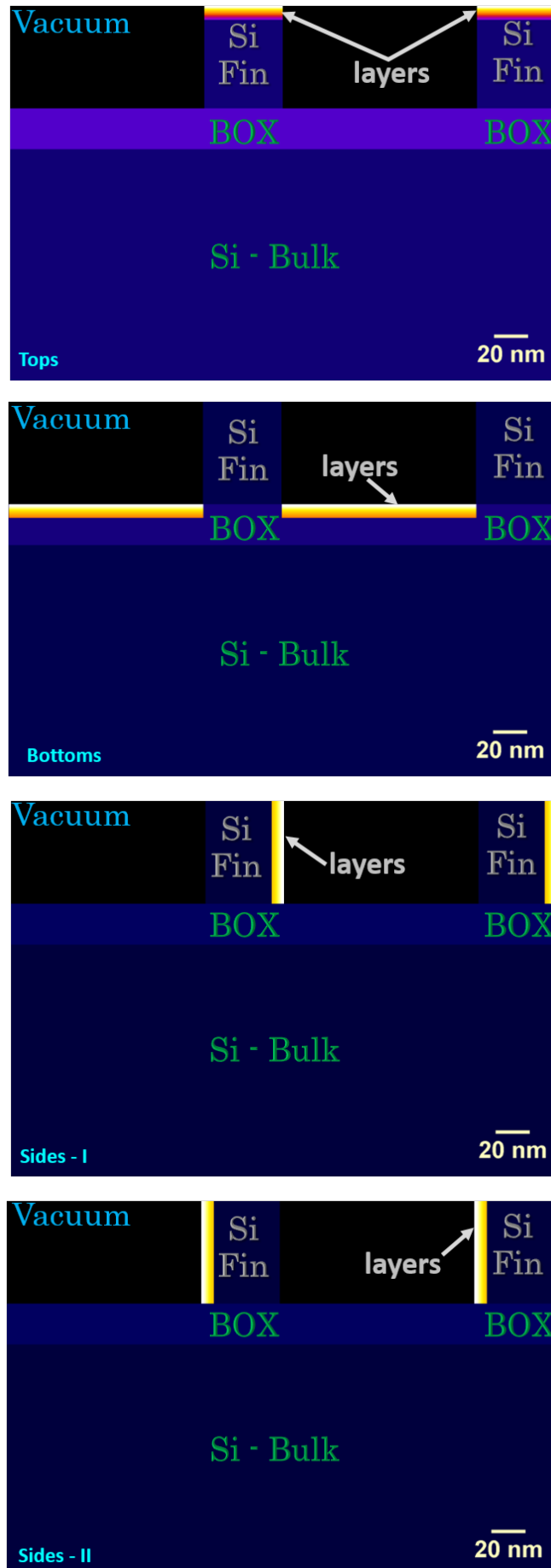


FIGURE A.2: Representation of the matrix models of the nanostructures utilized to simulate the implantation of arsenic in the: tops, bottoms, sidewalls-I and sidewalls-II.

## Appendix B

# Analysis Electron Microscopy (AEM)

### Transmission Electron Microscopy (TEM)

In 1927 G. P. Thomson demonstrated that it was possible to obtain the diffraction pattern of electrons into a solid crystal[96], if they are accelerated at energies in the kV range (e.g. 50 kV). Then it was shown that by focusing them into a narrow probe beam, the sample can be imaged with good spatial resolution using appropriate lenses. This is what lead to the invention of TEM. In order to make the functionalities of TEM effective, the firsts lenses were developed in 1931 by Ernst Ruska in Berlin. The imaging at the atomic scale thus consists in aligning the atomic rows of the sample so that they can be imaged through the incident electrons. An example is depicted in figure(B.1)[97].

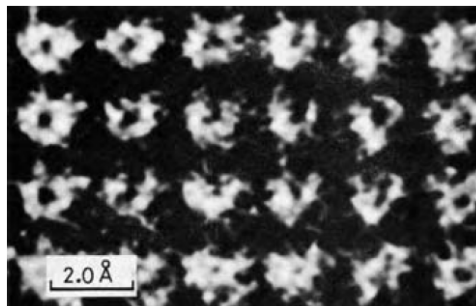


FIGURE B.1: TEM image of the atomic columns represented by the white dots.

The principle of a conventional TEM is as presented at the left hand side of figure(B.2). In that figure, the incident beam is fixed. The electrons extracted from the source at high temperature are parallelly oriented onto the sample. The image is formed through the objective lens by the electrons that have been scattered, diffracted or transmitted when

striking the sample. The two firsts phenomena are exploited in this technique because of the wavy-corpiscular nature of electrons. Indeed, if the electrons can be scattered as 'particles' when passing through a material, they can also be diffracted as 'waves', within the same material.

There are many types of electron sources (or electron guns). Those that are frequently used are made of tungsten(W), LaB6 or of field emissions types. Some of the required characteristics for a good source are the coherency, the brilliance and a narrow probe size. The other mode of performing a specimen imaging by using the same TEM instrument is to scan across it. This second mode of is thus defined as 'Scanning- Transmission Electron Microscopy (STEM)', presented in the next subsection.

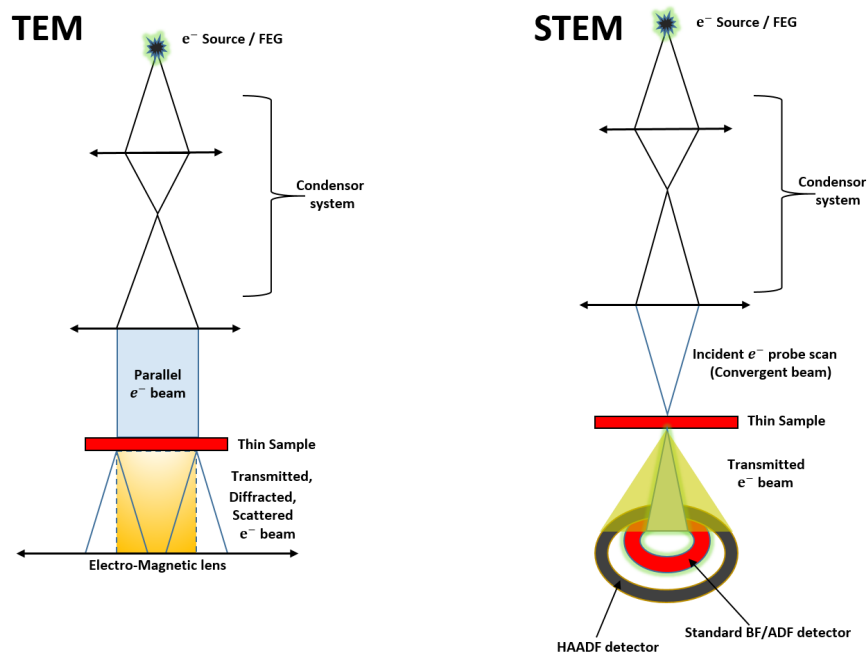


FIGURE B.2: Schematic principles of the TEM (left) and STEM (right) analysis techniques.

## Scanning Transmission Electron Microscopy (STEM)

In STEM mode, the incident electron beam is focused within a small probe beam onto a thin sample. The image is obtained point by point from the scans carried out with the help of the beam deflectors. The spatial resolution is expected to be better than in TEM mode because of the focused probe which expands the resolution limit[98]. In general, the spatial resolution of electron microscopes is by far better than that of light microscopes, because electrons have smaller de Broglie wavelength than photon. The schematic principle of STEM is presented in the right hand side of figure(B.2).

## The electron microscope detectors.

The characteristics of the detector utilised on the TEM/STEM instruments differ from one to another. The choice of a given detector mostly depends on the type of signal we want to observe and the expected information. There are different types of detectors as indicated in figure(B.3):

- Bright Field (BF) detector: for the transmitted and first rings of the diffracted beams. The bright field image is formed by the direct beam.
- Annular Dark Field (ADF) detector: for the diffracted beam. The dark field is formed by all the electrons that are not in the direct beam.
- High Angular Annular Dark Field (HAADF) detector: affords the detection of the diffracted electrons beam at large angles with a good z-contrast. This is also achievable in thermal diffuse scattering.  $z$  represents the atomic number of a given chemical element.

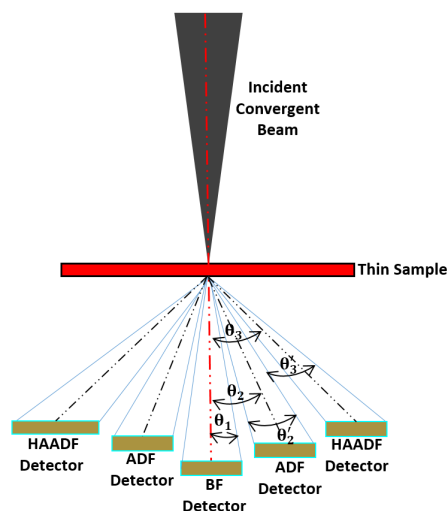


FIGURE B.3: Different detectors utilised in (S)TEM. The different angles  $\theta$  correspond to the deviations with respect to the direct transmitted beam, and also to the limits of the detection angle with the other systems.

## Energy dispersive x-ray spectroscopy

The STEM instrument can in turn be employed for further complementary analyses. For example, it is possible to perform a chemical profiling, by investigating the energy of the x-rays emitted by the host atoms when the electron beam hits the sample. Through the detection of those x-radiations, one can find out which chemical elements they are emitted from. This is achieved through the technique called energy dispersive x-rays

(EDX) analysis. However, it is important to notice that EDX suffers from unavoidable presence of artifacts resulting from possible contaminations that limit the precisions in the evaluations of the results or the mappings. Nevertheless, one can perform a qualitative elemental analysis in a short period of time[28]. First of all, one needs to execute the imaging of the areas of interest in the sample in (S)TEM mode. An example of the EDX imaging in cross-section is presented in figure(B.4) showing the 3D-profile of three chemical elements (Si, As and O) in a Fin-shaped Si nanowire.

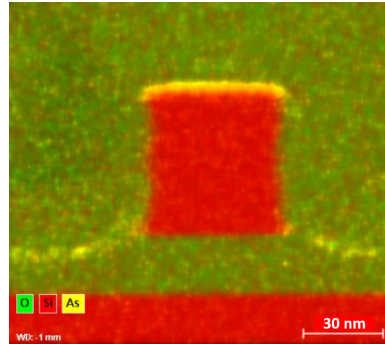


FIGURE B.4: Example of an EDX image showing the chemical profiles of Si, As and O acquired on a 3D Fin-shaped silicon nanowire.

## Sample preparation for (S)TEM imaging

There are several preparation methods for (S)TEM analysis techniques. Each of them depends on the information we want, as well as the constraints related to the type of the sample[28]. Some of the methods that can be cited are: the thinning by polishing, ions milling, cross-section preparation, cliving, lithography, focused ion beam (FIB), etc. We will provide few details on the last method since it is the one which has been adopted for the preparation of the samples studied in this project. FIB can be considered as a scanning electron microscope (SEM) coupled with a built-in ion mill, which the gallium (Ga) ions constitutes the sputtering beam. An image showing the double gun setup for FIB and SEM is provided at the left hand side of figure(B.5). An illustration example of the steps undertook to obtain a thin specimen is as presented at the right hand side of figure(B.5):

- A: the region to be cut is delimited by the markers,
- B: protection of that region when sputtering the sample with the ion beam,
- C,D: cutting of the trenches,
- E: final cutting of the either lateral sides of the trenches,

F: a final polishing is required before the extraction of the specimen for the analyses.

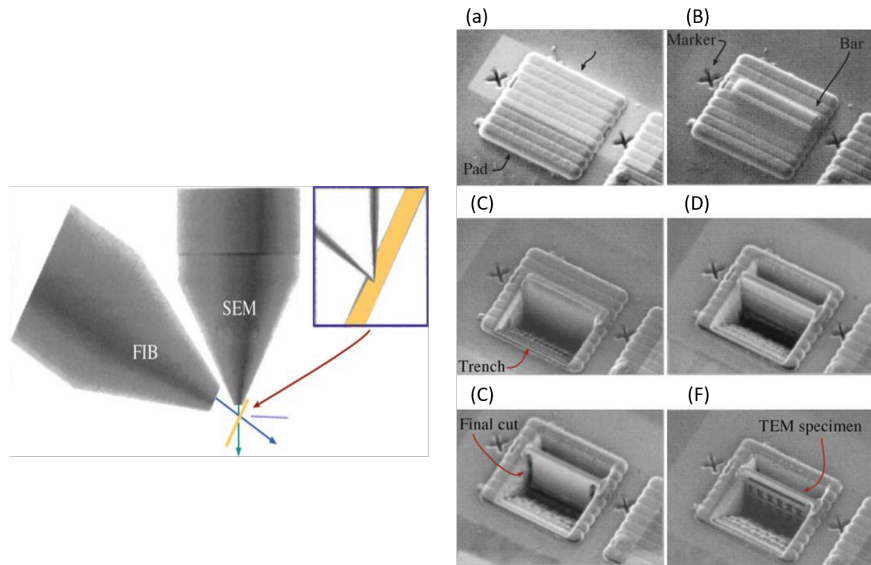


FIGURE B.5: Left: Zoom of the two beams system of the sample preparation (the FIB gun generates  $\text{Ga}^+$  for the sputtering and the SEM gun can be used for imaging the sputtered region. Right: preparation steps for the FIB cuts in question[28].

### The sample holder

The sample holder dedicated to the (S)TEM experiments is displayed in figure(B.6) where the essential parts are highlighted. This image shows the sample introduced into a vacuum box. The jewel bearing made of sapphire, placed at the extremity of the rod, is settled into a second jewel such that a comfortable manipulation of the stage can be performed. The holder inside the vacuum TEM environment is isolated from the exterior part by an O-ring.

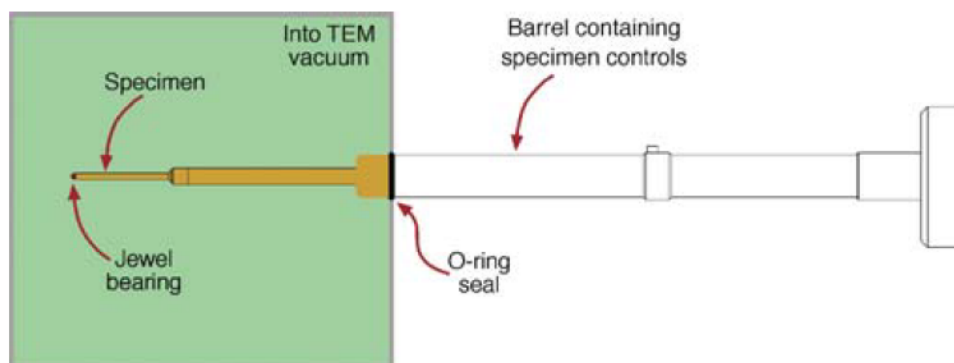


FIGURE B.6: Image of the traditional side-entry holder[28].

The experimental setup which has been utilized for the investigation throughout this work was a Titan Themis TEM/STEM microscope. It affords the possibility to perform the

three imaging methods (TEM, STEM and EDX) by keeping the sample environment. The image of the setup including the associated details of the microscope column is provided in figure(B.7)

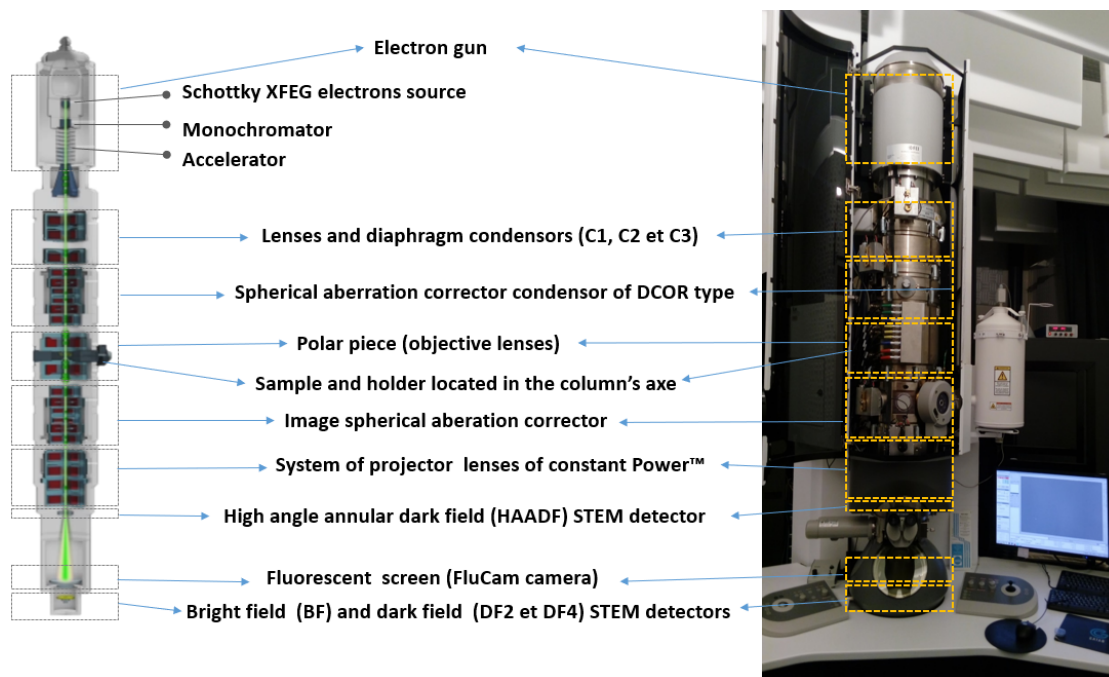


FIGURE B.7: Image of the FEI Titan Themis (S)TEM microscope column utilised for the analyses, available on the Leti's nano characterization platform (PFNC).

# Bibliography

- [1] Robert X. Cringely. Breaking moore's law. techreport, October 2013. URL <https://www.cringely.com/2013/10/15/breaking-moores-law/>.
- [2] Fikru Adamu-Lema. *The scaling of MOSFETs, Moore's law, and ITRS*. University of Glasgow, University of Glasgow, Glasgow, G12 8LT, UK. \*Email: fikru@elec.gla.ac.uk, 2017. URL [http://userweb.eng.gla.ac.uk/fikru.adamu-lema/Chapter\\_02.pdf](http://userweb.eng.gla.ac.uk/fikru.adamu-lema/Chapter_02.pdf).
- [3] H.-N. Yu V.L. Rideout E. Bassous R.H. Dennard, F.H. Gaensslen and A.R. Leblanc. Design of ion-implanted mosfet's with very small physical dimensions. *IEEE Solid State Circuits*, 9(5):256, 1974.
- [4] Francis BALESTRA. *Nouveaux Matériaux et Dispositifs pour la Nanoélectronique*. IMEP-LAHC, Grenoble INP-Minatec.
- [5] Toru Kaga Digh Hisamoto and Eiji Takeda. Impact of the vertical so1 "delta" structure on planar device technology. *IEEE TRANSACTIONS ON ELECTRON DEVICES*, 38(6):1419–1424, June 1991.
- [6] Xuejue Huang, Wen-Chin Lee, Charles Kuo, Digh Hisamoto, Leland Chang, Jakub Kedzierski, Erik Anderson, Hideki Takeuchi, Yang-Kyu Choi, Kazuya Asano, Vivek Subramanian, Tsu-Jae King, Jeffrey Bokor, and Chenming Hu. Sub-50 nm p-channel finfet. *IEEE TRANSACTIONS ON ELECTRON DEVICES*, 48(5):880–886, May 2001.
- [7] Intel. Intel-standards-22nm-3d-tri-gate-transistors-presentation. techreport, Intel, April 2011.
- [8] Sławomir Prucnal. *Fundamentals of Nanoelectronics: Basic Concepts*. Helmholtz Association, November 20014. URL [www.hzdr.de](http://www.hzdr.de).
- [9] Flatresse P. Magarshack, P. and G. Cesana. Utbb fd-soi: A process/de- sign symbiosis for breakthrough energy-efficiency. In *Design , Automation & Test in Europe Conference & Exhibition* ,, pages 952–957, Grenoble,, March 2003. URL <https://doi.org/10.7873/date.2013.200>.

- [10] Cesana G. Technology for very high-speed and energy efficient soics. In *FDSOI Forum*, 2014. URL <http://www.soiconsortium.org/fully-depleted-soi/presentations/september-2014-fdsoi-forum/TP2521%20The%20FD-SOI%20technology%20for%20energy%20eff.pdf>.
- [11] Bo Cui. *Microfabrication and thin film technology*. University of Waterloo,. URL <http://ece.uwaterloo.ca/~bcui/>.
- [12] Julian DUCHAINE. *Confidential*. PhD thesis.
- [13] P. Eyben et al., editor. *Analysis and optimization of new implantation and activation mechanisms in ultra-shallow junction implants using scanning spreading resistance microscopy (SSRM)*, volume 912, 2006. Materials Research Society.
- [14] Mody, editor. *3D-Carrier profiling in finFETs using Scanning Spreading Resistance Microscopy*, 2011. IEDM, IEDM.
- [15] Dick James and Michael Current. *Analytical Techniques for Ion Implantation*, chapter 16, pages 1–48. Siliconics, Ottawa, Canada, dickjames@siliconics.ca ; Current Scientific, San Jose, CA USA, currentsci@aol.com. URL <https://www.researchgate.net/publication/330357013>.
- [16] D. Blavette and S. Duguay. Investigation of dopant clustering and segregation to defects in semiconductors using atom probe tomography. *Journal of Applied Physics*, 2016.
- [17] Ajay Kumar Kambh, Arul Kumar, Antonios Florakis, and W. Vandervorst. Three-dimensional doping and diffusion in nano scaled devices as studied by atom probe tomography. *Nanotechnology*, 24:1–7, June 2013. doi: doi:10.1088/0957-4484/24/27/275705.
- [18] Andre A. Budrevicha and Wilfried Vandervorst. *SIMS Analysis on the Transistor Scale: Probing Composition and Dopants in Nonplanar, Confined 3D Volumes*. Copyright © 2016 Pan Stanford Publishing Pte. Ltd, 2016. ISBN 978-981-4669-78-8.
- [19] S. Qin. Challenges of 2-d (3-d) device doping process and doping profiling metrology. In *International Workshop on Junction Technology*, pages 91–97, 2016.
- [20] Denis Jalabert, Ian Vickridge, and Amal Chabli. *Swift Ion Beam Analysis in Nanosciences*. John Wiley & Son, (2017). ISBN 9781119005063. doi: 10.1002/9781119005063. URL <http://www.wiley.com>.
- [21] Brett W. Bush. *Metal and Alloy Surface Structure Studies Using Medium-energy Ion Scattering*. PhD thesis, Rutgers, The State University of New Jersey, May 2000.

- [22] J. F. Ziegler H. H. Andersen. *Hydrogen Stopping Powers and Ranges in All Elements*, volume 3. Pergamon Press, 1977. ISBN 0-08-021605-6.
- [23] J. F. Ziegler. *Helium Stopping Powers and Ranges in All Elements*. Oxford, 1977.
- [24] Wei-Kan Chu. Calculation of energy straggling for proton and helium ions. *Phys. Rev. A*, 13(0):2054–2060, June 1976. ISSN 6. doi: 10.1103/PhysRevA.13.2057. URL <https://link.aps.org/doi/10.1103/PhysRevA.13.2057>.
- [25] James F. Ziegler. URL [www.srim.org](http://www.srim.org).
- [26] D.R. Rueda M.C Garcia Gutiérrez. *Bases of Synchrotron Radiation and Light Sources*, chapter 1: Bases of Synchrotron Radiation, Light Sources, and Features of X-Ray Scattering Beamlines, pages 1–22. Number 776. Springer-Verlag, 2009. doi: 10.1007/978/-3-540-95968-7\_1.
- [27] What is a synchrotron? Synchrotron science, The European Synchrotron, . URL <http://www.esrf.eu/about/synchrotron-science/synchrotron>.
- [28] David B. Willaims and C. Barry Carter. *Transmission Electron Microscopy. A text book for maerial sciences*. Springer, 2009. ISBN 978-0-387-76500-6.
- [29] M. A. Sortica, P. L. Grande, G. Machado, and L. Miotti. Characterization of nanoparticles through medium-energy ion scattering. *J. Appl. Phys.*, 106:1–7, 2009. ISSN 114320.
- [30] UFRGS. Powermeis simulation software. URL <http://tars.if.ufrgs.br/>.
- [31] G. E. Moore. Cramming more components onto integrated circuits. *Electronics*, 38 (8), April 1965.
- [32] H. MORICEAU, France F. FOURNEL CEA, LETI, and INAC France F. RIEU-TORD, CEA. *Materials and manufacturing techniques for silicon-on-insulator (SOI) wafer technology*, volume 3. Elsevier Ltd, 2014. doi: 10.1533/9780857099259. 1.3.
- [33] *Smart cut: a promising new soi material technology*, 95CH35763, October 1995. Proceedings IEEE International SOI Conference, IEEE.
- [34] M. Nakano T. Abe and T. Ito. *Silicon-On-Insulator Technology and Devices*. Number 61. Pennington, ed. d.n. schmidt edition, 1990.
- [35] EUROSUI+, editor. *INFORMATION AND COMMUNICATION TECHNOLOGIES*, number FP7-216373, June 2011. European Platform for Low-Power Applications on Silicon-On-Insulator ACM, Monthly Publication of Electronic Newsletter Collecting the Main Advances of SOI Technology (Updated Version 30/06/11).

- [36] . URL [https://fr.wikipedia.org/wiki/Dopage\\_\(semi-conducteur\)](https://fr.wikipedia.org/wiki/Dopage_(semi-conducteur)).
- [37] Claude CHABRO. *Implantation ionique*. Service traitement de surface, UNIREC (Usinor-Sacilor Group).
- [38] T. Sakamoto H. Kawaura and T. Baba. Observation of source-to-drain direct tunneling current in 8 nm gate electrically variable shallow junction metal–oxide–semiconductor field-effect transistors. *Applied Physics Letter*, 76(25): 3810–3812, 2000.
- [39] P. Packan S. Thompson and M. Bohr. Mos scaling: Transistor challenges for the 21st century. *Intel Tech. J.*, Q3:1–19, 1998.
- [40] Harb A. Deltimple N. Mohsen, A. and A. Serhane. 28-nm utbb fd-soi vs. 22-nm tri-gate finfet review: A designer guide - part i. *Circuits and Systems*, 8:93–110, 2017. ISSN 2153-1293. doi: <https://doi.org/10.4236/cs.2017.84006>. URL <http://www.scirp.org/journal/cs>.
- [41] F. Andrieu C. Buj-Dufournet F. Allain P. Scheilin J. FOucher N. Daval D. Lafond L. Tosti L. Brevard O. Rozeau C. Fenouillet-Beranger M. Marin F. Boeuf D. Delprat K. Bourdelle B-Y. Nguyen O. Weber, O. Faynot and S. Deleonibus. High immunity to threshold voltage variability in undoped ultra-thin fdsoi mosfets and its physical understanding.
- [42] A. Asenov. *VLSI*, page 86, 2007.
- [43] A. Cathignol et al. *EDL*, page 609, 2008.
- [44] A. Vandooren et al. *IEDM*, page 975, 2003.
- [45] D. G. Armour W. Vandervorst E.H.J. Collart R.D. Goldberg P. Bailey T. C. Q. Noakes M. Werner, J. A. van den Berg. Damage accumulation and dopant migration during shallow as and sb implantation into si. *Nuclear Instruments and Methods in Physics Research B*, 216:64–74, 2004. doi: 10.1016/j.nimb.2003.11.022.
- [46] J. A. van den Berg, D.G. Armour, S. Zhang, S. Whelan, , and H. Ohno et al. Characterization by medium energy ion scattering of damage and dopant profiles produced by ultrashallow b & as. into si at different temperatures. *J. Vac. Sci. Technol. B*, 20(3), May 2002. doi: 10.1116./1.1477420.
- [47] Cheung Chang Bunji Mizuno Paul K. Chu, Nathan W. Cheung and Othon R. Monteiro. *HANDBOOK OF PLASMA IMMERSION ION IMPLANTATION AND DEPOSITION*. 99-89627. JOHN WILEY & SONS, John Willey & Sons. Inc. 605 Third Avenue New York, 2000. ISBN 0-471-24698-0.

- [48] P. Boulenc C. Tavernier F. Olivié Z. Essa, F. Cristiano. Modélisation tcad des prols et fuites de jonctions ultra-minces dans les technologies cmos avancées.
- [49] P. Pichler. *Intrinsic Point Defects, Impurities, and their diffusion in Silicon*. Springer Wien. New York, 2004.
- [50] Matthew Werner. *Damage formation and annealing studies of low energy ion implants in silicon using medium energy ion scattering*. PhD thesis, Institute for Materials Research (IMR) School of Computing, Science and Engineering (CSE) The University of Salford, UK., March 2006.
- [51] M . SCHARFF(t) J. LINDHARD and H . E. SCHIØTT. Range concepts and heavy ions ranges. *Matematisk-fysiske Meddelelser, Dan. Vid. Selsk.*, 33(14):1–40, 1963. NOTES ON ATOMIC COLLISIONS, II.
- [52] P. EYBEN, W. VANDERVORST, D. ALVAREZ, and an M. FOUCHIER M. XU. *Probing Semiconductor Technology and Devices with Scanning Spreading Resistance Microscopy*, chapter 2, pages 31–87.
- [53] W. Vandervorst and M. Meuris. 29, 1994. ISSN US-5369372.
- [54] W. Vandervorst and M. Meuris. 15, January 1992. ISSN EP-466274.
- [55] Katharina Grella. Assessment of spreading resistance measurements by local probe microscopy. mathesis, Grenble INP, DRT/CEAGre/LETI/DPFT/SMCP/LASIPFNC, December 2008.
- [56] M. Pawlik. *Journal of Vac. Science and Technology*, 10(1):388–396, 1992.
- [57] R.G. Mazur et al. *Journal of the Electrochemical Society*,, 113(3):255–259, 1966.
- [58] A. Budrevich and J. Hunter, editors. volume 449, 1998. AIP Copyright © 1998 Pan Stanford Publishing Pte. Ltd.
- [59] R. G Wilson, F. A. Stevie, and C. W. Magee. *Secondary Ion Mass Spectrometry*. Springer, 1989.
- [60] P. Bailey, T.C.Q. Noakes, C.J. Baddeley, S.P. Tear, and D.P. Woodruff. Monolayer resolution in medium energy ion scattering. *Nuclear Instruments and Methods in Physics B 183*, pages 62–72, 2001.
- [61] Denis Jalabert. *Analyse de nanostructures semi-conductrices par faisceau d’ions*. Hdr, UNIVERSITE GRENOBLE I – JOSEPH FOURIER, October 2012.

- [62] H. Renevier B. Daudin M.-H. Cho K. B. Chung D. W. Moon J. M. Llorens N. Garro A. Cros A. García-Cristóbal D. Jalabert, J. Coraux. Deformation profile in gan quantum dots: Medium-energy ion scattering experiments and theoretical calculations. *PHYSICAL REVIEW B*, September 2005. doi: 10.1103/PhysRevB.72.115301.
- [63] N. Angert. Ion sources. *IAEA Collection*. URL [www.iaea.org/inis/collection/NCLCollection/Store/\\_Public/26/001/26001458.pdf](http://www.iaea.org/inis/collection/NCLCollection/Store/_Public/26/001/26001458.pdf).
- [64] HAMAMATSU. *MCP (microchannel plate) AND MCP ASSEMBLY*. HAMAMATSU PHOTONICS, HAMAMATSU PHOTONICS K.K., Electron Tube Division, 314-5, shimokanzo, Iwata City, Shizuoka Pref., 438-0193, Japan, January 2016. URL <https://www.hamamatsu.com/jp/en/3008.html>.
- [65] Marc-A. Nicolet Wei-Kan Chu, James W. Mayer. *Backscattering spectrometry*. Harcourt Barce Jovanovich, Publishers, 1978. ISBN 0-12-173850-7.
- [66] S. Thomas Picraux Leonard C. Feldman, James W. Mayer. *Materials analysis by ion channeling submicron crystallography*. Hartcourt Brace Jovanovich, 1982. ISBN 0-12-252680-5.
- [67] N. Bohr. *Mat. Fys. Medd Dan. Vid. Selsk*, 18(8), 1948.
- [68] K. Dan. Vidensk. Selsk. Lindhard, J. *Mat.-Fys. Medd.*, 34(14), 1965.
- [69] Dokl. Akad. Nauk SSSR Tulinov, A. F. *Sov. Phys.-Dokl*, 10(463), 1965.
- [70] D. S. Gemmell and R. E. Holland. *Phys. Rev. Lett.*, 14(945), 1965.
- [71] Donald S. Gemmell. Channeling and related effects in the riotion of charged particles through crystals. *Rev. Mod. Phys.*, 46(1), January 1974.
- [72] M Dalponte, H Boudinov, L V Goncharova, E Garfunkel, and T Gustafsson. Meis study of antimony implantation in simox and vacancy-rich si(100). *Journal of Physics D: Applied Physics*, 40(14):4222, 2007. URL <http://stacks.iop.org/0022-3727/40/i=14/a=017>.
- [73] P. C. Zalm, P. Bailey, M. A. Reading, A. K. Rossall, and J. A. van den Berg. Quantitative considerations in medium energy ion scattering depth profiling analysis of nanolayers. *Nuclear Instruments and Methods in Physics Research B*, (387):77–85, October 2016. doi: <http://dx.doi.org/10.1016/j.nimb.2016.10.004>. URL <http://creativecommons.org/licenses/by/4.0/>.
- [74] Dario F. Sanchez Agenor Hentz Mauricio de A. Sortica, Pedro L. Grande and Gabriel Marmitt. *PowerMEIS 2.0 User's Manual*. Universidade Federale do Rio Grande do Sul, Instituto de Fisica, Laboratorio de Implantação Iônica, March 2013.

- [75] Dario. F. Sanchez Mauricio de A. Sortica, Pedro L. Grande. *PowerMEIS 2.0 User's Manual*. Universidade Federale do Rio Grande do Sul, Instituto de Fisica, Laboratorio de Implantação Iônica, manual1 edition, March 2010.
- [76] Leszek S. Wielunski. Edit Szilagyi and Geoffrey L. Harding. Multiple scattering effects in depth resolution of elastic recoil detection. The work was partially supported by Hungarian OTKA grant No. F019165.
- [77] Cristiane Marin Daniel L. Batista Gustavo de M. Azevedo Pedro L. Grande Dario. F. Sanchez, Gabriel Marmitt and Paulo F. P. Fichtner. New approach for structural characterization of planar sets of nanoparticles embeded into a solid matrix. *Sci. Rep.*, 3(3414), 2013. doi: 10.1038/srep03414. URL [www.nature.com/scientificreports](http://www.nature.com/scientificreports).
- [78] . URL [https://simple.wikipedia.org/wiki/J.\\_J.\\_Thomson](https://simple.wikipedia.org/wiki/J._J._Thomson).
- [79] Sigmund P. *Sputtering by particle bombardment I*, volume 47 of *1437-0859*. Springer, Berlin, Heidelberg, 1981. ISBN 978-3-540-38514-1. URL <https://doi.org/10.1007/3-540-10521-2>.
- [80] Marc AUCOUTURIER Evelyne DARQUE-CERETTI and Patrice LEHUÉDÉ. Spectrométrie de masse d'ions secondaires : Sims et tof-sims -principes et appareillages. *Technique de l'ingénieur*, 4:2618, 2014.
- [81] Marc AUCOUTURIER Evelyne DARQUE-CERETTI and Patrice LEHUÉDÉ. Spectrométrie de masse d'ions secondaires : Sims et tof-sims procédures d'analyse et performances. *Technique de l'ingéniere*, page 2619, 2015.
- [82] Thomas Grehl. *Improvements in TOF-SIMS Instrumentation for Analytical Application and Fundamental Research*. Westfälischen-Wilhelms Universität Münster, 2003.
- [83] Hitomi Satoh et al. Relative sensitivity factors for submicron secondary ion mass spectrometry with gallium primary ion beam. *J. Appl. Phys.*, 32(8):3616–3620, August 1993. Part 1.
- [84] URL <http://nobelprize.org/nobelprizes/physics/laureates/1901/rontgen-bio.html>.
- [85] FriedrichW., Knipping P., and Von Laue M. Sitzungsber. *Math. Naturwiss., Munchen*, pages 303–322, 1912.
- [86] S. Takagi. Dynamical theory of diffraction applicable to crystalss with any kind of small distortion. *Acta crystallogr.*, 15(12):1311–1312, December 1962.

- [87] Martin Emrich and Detlef Opper. *XRD for the analyst Getting acquainted with the principles*. PANalytical B.V., Lelyweg 1, 7602 EA Almelo, P.O. Box 13, 7600 The Netherlands, 2 edition, 2013. ISBN 978-90-809086-0-4. URL [www.panalytical.com](http://www.panalytical.com).
- [88] Sophie Baudot. *Strained MOSFETs on SOI : strain analysis by X-ray diffraction and electrical properties study*. Theses, Université Joseph-Fourier - Grenoble I, December 2010. URL <https://tel.archives-ouvertes.fr/tel-00557963>.
- [89] ESRF in brief and key figures. Press room, The European Radiation Synchrotron ESRF, . URL <http://www.esrf.eu/about/press-room/intro-esrf-journalists>.
- [90] Matej Mayer. *SIMNRA User's Guide*. Max-Planck-Institut für Plasmaphysik. URL <http://www.simnra.com>.
- [91] Shu Qin, James D. Bernstein, Zhuofan Zhao, Wei Liu, and Chung Chan. Charging effects in plasma immersion ion implantation for microelectronics. *J. Vac. Sci. Technol. B*, 5(13):1994–1998, September 1995.
- [92] Q. Shen and Stefan Kycia. Determination of interfacial strain distribution in quantum-wire structures by synchrotron x-ray scattering. *Physical Review B*, 55(23):15791–97, 1997.
- [93] B. Weselak Q. Shen, C. C. Umbach and J. M. Blakely. X-ray diffraction from a coherently illuminated si(001) grating surface. *Physical Review B*, 48(24):17967–73, 1993.
- [94] T. Baumbach and D. Lübbert. Grazing incidence diffraction by laterally patterned semiconductor nanostructures. *J. Appl. Phys. D*, 32:726–740, 1999.
- [95] F. Torregrosa, Y. Spiegel, J. Duchaine, T. Michel, G. Borvon, and L. Roux. Recent developments on pulsion® piii tool: Finfet 3d doping, high temp implantation, iii-v doping, contact and silicide improvement, amp; 450 nm. In *2015 15th International Workshop on Junction Technology (IWJT)*, pages 1–5, June 2015. doi: 10.1109/IWJT.2015.7467061.
- [96] Ray F. Egerton. *Physical Principles of Electron Microscopy: An Introduction to TEM, SEM, and AEM*. Springer, Ray F. Egerton Department of Physics, University of Alberta 412 Avadh Bhatia Physics Laboratory Edmonton, Alberta, Canada T6G 2R3, 2005. ISBN 0-387-25800-0. URL [www.springeronline.com](http://www.springeronline.com).
- [97] Hashimoto et al. *Journal of the Physical Society of Japan*, 1977.
- [98] *Microscopie électronique en transmission : MET (ou TEM)*. Phelma, Geenoble INP, 2016.